The influence of turbulence on the aerodynamic optimisation of bluff body road vehicles

This item was submitted to Loughborough University's Institutional Repository by the/an author.

Additional Information:

- A Doctoral Thesis. Submitted in partial fulfilment of the requirements for the award of Doctor of Philosophy of Loughborough University.

Metadata Record: https://dspace.lboro.ac.uk/2134/14381

Publisher: © P.S. Newnham

Please cite the published version.

The Influence of Turbulence on the Aerodynamic Optimisation of Bluff Body Road Vehicles

By P.S. Newnham

Doctoral Thesis

Submitted in partial fulfilment of the requirements

for the award of

Doctor of Philosophy of Loughborough University

May 2007

Abstract

In order to promote further understanding of the effects of the atmospheric environment encountered by road vehicles in the real world, a wind tunnel based investigation was conducted into the effect of small scale turbulence on the road vehicle optimisation process. An initial investigation was carried out using a 1-box model with variable leading edge radii from 10mm to 100mm. Measurements of time averaged forces were made over a range of Reynolds numbers from 200,000 to 1,300,000 (based on the square root of frontal area) and free stream turbulence levels from 0.2% to 5.1%. The transcritical Reynolds number based on edge radius was established as a basis for comparison between turbulence levels. Centreline pressures and PIV vector fields are presented to provide information on separation and reattachment. The investigation was extended to a more representative 2-box model using the same radii as before and a reference model at full scale, where the edge radii varied from 25mm to 150mm and turbulence intensity from 1.8% to 4.3%. It was shown that there is a strong reduction of separation under increased turbulence, and a small increase in skin friction.

A further experiment was carried out to investigate the influence of freestream turbulence on the characteristic effect of changing backlight angle on lift and drag. It is shown that there was a reduction in drag due to the action of turbulence on the separation over the backlight, which may be driven by an effect on vortex strength. Tests were also carried out on two full scale vehicles to investigate the effect of increasing turbulence intensity on front and rear spoilers, cooling drag, and A-pillar vortex flows. The observed changes were small but would often be cumulative in their effect, so that optimising a vehicle in a significantly different turbulence level could produce a difference in the total forces acting on the vehicle.

These experiments have shown that the primary effect of the additional freestream turbulence introduced by grids is on the boundary layer, as was expected from the literature. The results showed that increasing the turbulence intensity made separated regions smaller, and suggested that vortices become weaker and less well defined. The work provides a basis for continuing to investigate the effect of freestream turbulence on the process of optimising the aerodynamics of road vehicles.

Acknowledgements

"Big whorls have little whorls,
Which feed on their velocity;
And little whorls have lesser whorls,
And so on to viscosity
(in the molecular sense)."
– Richardson [1]

Table of Contents

Table of Figures

Table of Tables

Nomenclature

δ^{99}	boundary layer thickness calculated as the point where U=99% of freestream (mm)
δ^{*}	boundary layer momentum thickness (mm)
ε_U	error in U (m/s)
$\varepsilon_{u'}$	error in u' (m/s)
η	non-dimensional edge radius based on the square root of frontal area
λ	wavelength (m)
ρ	density (kg/m^3)
σ	standard deviation
A	frontal area (m^2)
C_D	drag coefficient
C_{Dtcrit}	trans-critical drag coefficient
C_L	lift coefficient
C_{LF}	front lift coefficient
C_{LR}	rear lift coefficient
C_p	pressure coefficient
C_{pb}	base pressure coefficient
f	frequency (Hz)
L	macrolength scale (m)
L_M	model length (m)
p	local static pressure
p_∞	reference static pressure
PIV	Particle Image Velocimetry
r	front edge radius (m)
Re_A	Reynolds number based on the square root of frontal area
Re_{crit}	critical Reynolds number
Re_r	Reynolds number based on front edge radius
Re_{rtcrit}	transcritical Reynolds number based on front edge radius
Re_{tcrit}	transcritical Reynolds number
T	integral time scale (from autocorrelation) (s)
Tu	turbulence intensity (%)
U	time averaged windspeed (m/s)
U	fluctuating component in the U direction (m/s)
U'	r.m.s. of u (m/s)
$\bar{U}_{mass}$	average centre of mass of recorded velocities in a PIV vector field (m/s)
Z	constant relating to the confidence interval of a statistical error

Chapter 1

Introduction

There is a continuing requirement to improve the aerodynamic design of road vehicles to reduce drag, improve fuel consumption, reduce carbon dioxide output, and provide a more refined driving experience. To this end it is desirable to investigate improvements to testing methods to more accurately simulate conditions on the road. A better understanding of the real world aerodynamic environment and its effect on the flowfield around a moving vehicle, and the consequent forces it experiences, could positively influence the design process and provide the engineer with new tools for optimising road vehicles.

This thesis reports on a wind tunnel based investigation into the effect of small scale turbulence on the road vehicle optimisation process. To gain an insight into how raised levels of turbulence might affect the decisions made over small detail changes, an investigation was carried out using a simple 1-box model with variable leading edge radius. Measurements were made of the forces acting on the model over a range of Reynolds numbers and turbulence levels. Centreline pressures were recorded and PIV was used to provide information on separation and reattachment and some insight into the time varying separated flows around smaller radii. The edge radius experiment was extended to investigate the effect of turbulence on a more representative 2-box model and a well known automotive reference model at full scale. Having established that there is a strong effect of turbulence on separated flows, and a weaker effect on skin friction, further parametric tests were carried out to look at using the same technique on other commonly used detail changes, such as the back angle on a fast back type model, and front and rear spoilers on various models at full scale. The back angle model showed an effect of turbulence on vortex strength, which was also investigated by means of flow visualisation techniques on the A-pillar of a production road vehicle. It was found that additional turbulence does have an effect on the time averaged forces on the vehicle, which arise through changes in separations, vortex strengths and skin friction. These changes are often small, and individually inconsequential, but also often cumulative in their effect, so that optimising a vehicle in a significantly different turbulence level could produce different design decisions, which could add up to a valuable difference in the overall forces acting on the vehicle. The additional turbulence could also be useful in informing the aerodynamicist about problem areas of the car, for example wind noise around the A-pillar. These experiments have provided a basis for

continuing to investigate the effect of freestream turbulence on the process of optimising the aerodynamics of road vehicles.

1.1 The vehicle optimisation process

The aerodynamicist has a number of tasks to fulfil in vehicle design, some conflicting, some complementary, and some separate. They must try to improve the performance, for maximum speed and fuel economy, provide air for cooling the engine and brakes, for the engine to breathe, and to provide comfort to the passengers. They must ensure that the vehicle is aerodynamically stable, especially at high speed, with low wind noise and good control of spray and dirt deposition on the side glass and backlight. To achieve these varied objectives, they must work closely with other engineers to ensure that they hit their targets, whilst also satisfying the targets of safety, packaging, powertrains and HVAC, for example, and maintaining a vehicle shape that satisfies the style constraints and customer expectations.

Aerodynamic optimisation is therefore not undertaken in isolation but as a highly integrated part of the vehicle development process. There are not infinite variations available in shape or size, and the aerodynamicist must achieve the best possible compromise for the vehicle as a whole. A typical vehicle design process begins with early styling models made of clay. Once surface geometries are available, foam cut models are produced which are used by the aerodynamicist to evaluate the performance of the different concepts under consideration. The aerodynamic targets are set very early to ensure that the performance criteria set by marketing can be achieved [2]. These scale models are then developed by streamlining and refining of details, to produce a first choice candidate design. The winning concept(s) then moves forward to full scale styling bucks, some of which are used by the aerodynamicist. Work is then done on changes to the fine detail, in order to preserve the look of the vehicle whilst respecting all the other engineering targets that the vehicle must meet. For most new car projects, the desirability and therefore saleability of the vehicle is paramount. The market for new cars is very competitive, and the major selling point of any one vehicle over another can often be the first impression it creates. A car that does not have the right look, but that has great performance, will often be outsold by a beautiful car with only average speed and fuel economy for the class, even for a sports car – the BMW Z8

being a notable example of a well-engineered and fast car which did not sell well because it was unappealing.

For the aerodynamicist, the most important parameter, and the one to which the most effort is devoted, is the reduction of vehicle drag, for reasons of straight line performance, fuel economy and carbon dioxide emissions. The modern approach of refining the small details to achieve the required drag target is described by Hucho et al. [3]. Hucho started with the styling model, and built an aerodynamically shaped fairing onto the front, that would ensure fully attached flow. The design was based on an aircraft nosecone fairing. Having measured the drag of the model with this fairing, it was assumed that this was the minimum possible drag for an ideally optimised road vehicle nose built onto the styling buck. The fairing was removed, and a series of tests were made with parametric changes to angles of the radiator grill, or radius of the bonnet, for example. These fundamental tests indicated the correct direction to take for the final shape, which was then defined, including the grill detail and cooling air flow. It was shown that it is possible to use rounding, chamfering, and other small shape changes to reduce the drag to a value approaching, or equal to, the drag of the vehicle with fully aerodynamic fairings. The flow over the bonnet was also considered, as a fully attached flow here not only reduces drag, but provides a high pressure region at the base of the windscreen, forcing air into the heating, ventilation and air conditioning (HVAC) system. The final results were achieved without significantly affecting the sharp, angular style that was required by the stylists at the time. In a more complete analysis of a vehicle, the modifications will often be a compromise between conflicting effects on drag, lift, and lateral effects, and interference effects where a small increase in drag on the vehicle at one point is necessary in order to make a larger saving at another point. It may also not always be possible to achieve the ideal lowest possible drag due to styling constraints [2].

While Hucho's modifications were mostly achieved by testing small incremental steps, selecting the modifications that made improvements and discarding those that moved the results away from the target, this method has since been developed further. Cooper [4] demonstrated an approach to front edge rounding where a range of edge radii were tested over a range of Reynolds numbers, and an optimum edge radius selected based on the results. Cooper's experiment used a model scaled to represent a generic truck,

4

but with all the detailing removed, so that it became a rectangular cuboid with an additional front section that had radiused top and side leading edges. This section was replaceable. The experiment showed that there is a large Reynolds number effect on the ideal front edge radius, and Cooper recommended that a revised (from the SAE standard) minimum Reynolds number Re_A of $2*10^6$ (based on the square root of frontal area) should be used if model scale testing is to be used to optimise edge radius. In practice, however, model scale testing is used to provide information about the relative merits of different body schemes, and detailed optimisation is carried out using full scale models. Cooper also examined the effect of changing the edge radius on transcritical Reynolds number, where transcritical Reynolds number is defined as the lowest Reynolds number, following the critical value, at which the C_D becomes approximately a constant. The critical Reynolds number is defined as the point where the separated laminar boundary layer becomes unstable and begins to undergo transition to turbulent flow (Hoerner [5]). Pre-critical flow is therefore undesirable, as it describes a condition where there is a separated laminar boundary layer on the radius, and hence a high drag coefficient. Figure 1 shows the identification of the critical and transcritical Reynolds numbers (Re_{crit} and Re_{tcrit}) for a sphere.
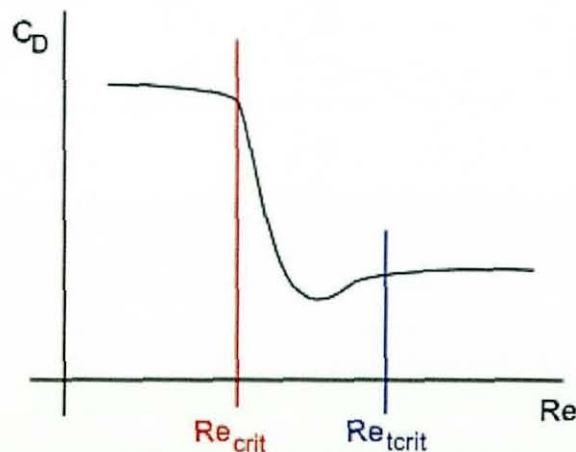
Figure 1 Typical variation of drag coefficient with Reynolds number for a sphere

The results showed that it was possible to collapse the results for transcritical Reynolds number onto a constant value by recalculating the Reynolds number based on front edge radius. This approach will be repeated in this work, and the effect of turbulence on the constant value examined. Cooper used the results to determine an optimum value for the edge radius at model scale, and claimed that the results would be comparable to full scale, although the maximum Reynolds number tested was $2.6*10^6$. Examination of the graphs shows that there exists the possibility that smaller radii could undergo

transition to fully attached flow at a higher Reynolds number, and it would appear that in fact to validate Cooper's claim for a correct optimum radius, the experiment would have to be done on the same model at full scale. However, it is not the aim of this project to demonstrate a valid optimum edge radius at model scale, but to understand the mechanisms and trends in the data in order to produce methods for full scale testing. It should be noted that one of Cooper's key assumptions is that the optimum radius is the smallest one that undergoes transition to fully attached flow. This may be an old fashioned view, driven by the predominant styling of cars when the paper was originally written in 1986 – for example, the vertical leading edge radii on the Land Rover Discovery 3 were made quite large without compromising the bluff styling language. Current vehicle design tends towards more complex curved bodies, for aerodynamic and pedestrian safety reasons as well as a modern aesthetic that regards flowing surfaces and lines more favourably than in the '70s and '80s. Therefore, the effect of a more realistic onset flow, such as with elevated levels of freestream turbulence, is of just as much interest for cases of large radii with attached flow as it is when considering tight radii or sharp edges where there may be separation.

Barnard [6] notes that even more drag reduction can be achieved by giving the bonnet a smooth continuous curve from the stagnation point upwards, and this can be seen on many current road cars, where the grill at the front above the bumper is often largely decorative and less than half the area is actually used for under-bonnet flows, if any at all. Examples of this technique include the 2006 Honda Civic, where the grill that would usually be at the front of the bonnet was entirely replaced by a clear plastic styling feature that bears the company logo, and so the bonnet radius sweeps up continuously from the numberplate.

At the rear of the car, large reductions in vehicle drag can be realised by adjusting the backlight angle for minimum drag. In Buchheim's [7] parametric study of general alterations over a whole vehicle, the most significant factors affecting drag were backlight angle and rear end height, which are related. It was shown that there is a clear minimum drag coefficient, at around 15 degrees, and a pronounced maximum, at around 30 degrees, for the model used.

This effect was explained in some detail by Ahmed [8] who investigated the flow structures over the backlight of a simple bluff body (the Ahmed model). A similar peak

6

in drag at 30 degrees was recorded, and a general form of flow structure for this high drag case was described. A pair of longitudinal vortices is formed on the C-pillars (in this document, the C-pillar refers to the rear pillar) and persists into the wake flow. The longitudinal vortices cause a downwash that helps the flow to stay attached, or to reattach if it separates. When there is separation, a semi-circular or semi-elliptic recirculation zone forms on the backlight between the vortices and the reattachment point. On the base of the vehicle, two opposing zones of recirculation form laterally across the base, one above the other. When the angle becomes too great, the downwash is no longer sufficient to cause reattachment and the flow breaks down, with no trailing vortices and a separation at the top edge of the backlight. Ahmed backed up this view of the flow with data from wake surveys and flow visualisation studies on the backlight.

Howell[9] also showed the effect of backlight angle on a more realistic automotive bluff body (the Windsor model), and repeated Ahmed's result of a high drag "critical" angle at 30°. Howell also showed that rounding on the roof-backlight edge (100mm radius) and C-pillars (25mm radius) changed the aerodynamic characteristics and raised the critical back angle for drag. The rounded C-pillars raised the peak yaw moment by around 25%, and shifted the back angle where this peak value occurred from 30° to 20°.

In a further study of the effect of longitudinal vortices on road vehicles, Bearman [10] showed that the drag and sideforce on the vehicle can be calculated from a wake survey, but that the lift could not. The results confirmed that the maximum drag value coincides with the maximum strength of the C-pillar vortices, which was controlled by the backlight angle. The reason it was not possible to calculate the lift was that a component of lift results from the local acceleration of the air underneath the vehicle; since this does not shed vorticity downstream, it is not possible to measure it using a wake survey.

1.2 The effect of turbulence

Whilst using established procedures, the vehicle aerodynamicist is optimising the vehicle for a single onset flow; that found in the wind tunnel being used. The outside environment is not the same as the inside of a wind tunnel, and so it is important to understand first how it is different, and second whether an improved simulation of the real world might make any difference to the detailed decisions being made during the optimisation process. Some improvements have already been made, for example by

using improved blockage corrections, moving belts and rotating wheels, but until recently the question of turbulence has not generally been considered.

1.2.1   Turbulence in the real world

The headline wind tunnel drag coefficient, as generally quoted by manufacturers and the press, is normally a measurement of drag in clean, low turbulence, homogenous onset flow at 0° yaw. In the real world such conditions are unlikely to prevail. The atmospheric boundary layer is generally turbulent, the flow angularity may be different for different parts of the car, and there will often be a side-wind component that causes different effective yaw angles at different heights on the car. This yaw angle variation has been considered for a long time, for example by Watkins [11] who shows that due to the velocity profile of the atmospheric boundary layer, an incident sidewind will have a distinct velocity profile over a vehicle height. This profile means that when the sidewind velocities are added to the road velocity, the total wind velocity relative to the car is of different magnitude and direction over the vehicle height. In the real world there are topographical features such as trees, bridges, railways, etc. and other vehicles, all of which have an effect on the aerodynamic environment. It is therefore possible that shape optimisation performed under ideal conditions may not provide optimal results for the vehicle on the road. As there is now such a strong emphasis on reducing CO_2 emissions, this is an area worth investigating to see if any useful gains can be made.

The atmospheric conditions encountered by a vehicle have been discussed by many authors. Watkins [11] discusses the turbulence levels typically found on the road. Longitudinal intensities of 2.5% to 5% and lateral intensities of 2% to 10% are quoted for results from stationary and moving vehicles. The lower figures related to roads where there were few roadside features, and the higher figures to roads with significant housing or trees near the side of the road. In both cases the surrounding countryside was open and flat. The higher lateral intensities appear, from the data presented, to have been an isolated cluster of datapoints, with most of the results lying between 2% and 5% as for the longitudinal case. It was pointed out that some of the low frequency energy was filtered out by a 0.1Hz high pass filter, used to ac couple the data from the hotwire, with the rationale that eddies larger than 10s could be assumed to be quasi steady.

8

In a further review paper, Watkins [12] examines the work of wind engineers looking at the effect of time of year, surface roughness and terrain on the turbulence intensity and turbulence energy spectrum of the atmospheric boundary layer. A clear conclusion is that the length scales of the turbulence and the fluctuations in yaw angle and average flow velocity make realistic simulation in the wind tunnel difficult. Watkins also noted that much of the data on atmospheric turbulence recorded by wind engineers is measured at 10m above the ground and upwards. This may be appropriate for civil engineering applications but is unlikely to capture the environment experienced by road vehicles.

Additional data on atmospheric turbulence can be found in the ESDU database. The minimum height above the ground is generally 3m, but some interesting trends are shown with respect to surface roughness. Roughnesses presented range from very low (snow covered farmland, flat arid desert) to very high (city centres, forests), and trends are drawn of turbulence intensity and integral length scale. The results are measured and averaged over one hour long samples at an average wind velocity of 20m/s at 10m height. They show that increasing the roughness increases the turbulence intensity at 3m from approximately 11% for the lowest roughness to more than 36% for the highest (based on wind velocity). However the length scale decreases with increasing roughness, from a maximum of 100m down to just over 1m at the lowest. The effect of changing average windspeed over a range from 10m/s to 40m/s is identified in the data, but the effect of further reducing the height above the ground is not.

The range of turbulence intensities described in the above literature is quite large and indicates that for specific application to automotive aerodynamics, more data is required. It would be useful to establish a set of test cases that represent the conditions encountered by cars on faster moving roads, where aerodynamic drag is most important. Watkins' data [11], showing turbulence intensities of 2-5% (based on resultant velocity), examined the conditions on two driving routes in Australia, one on a road without trees or bridges, and one on a road with multiple trees and bridges included. Neither route had much traffic, and the surrounding terrain was open and flat. Conditions on a UK motorway surrounded by wooded hills and multiple large bridges and with heavy traffic could be considerably different, indicating that data collected may produce test cases whose application is limited to a particular country or continent.

Clearly the ideal would be to create a catalogue of data at multiple locations around the UK and Europe if the results are to be aimed at the European automotive industry, but a limited set should allow some trends to be drawn that would then show whether further data is necessary. There is also a continuing need to identify those types of turbulence that affect aspects of vehicle design, and what the likely impact is, for example a change in drag, or stability, or wind noise.

This decision will be influenced by studying recorded turbulent spectra as well as simple intensities or integral length scales. Richards et. al. [13] examined the variation in turbulence at heights of 10m and below, down to a minimum height of 0.115m. 3-component ultrasonic anemometers were used to produce spectra and coherence information in order to compare data sampled at different heights and different frequencies, and to generate spectral models for the atmosphere at low levels. It is stated that the local turbulence generation occurs in a range of frequencies termed the intermediate frequency sub-range, from around 0.001Hz to 10Hz, with the highest energy levels shown between 0.01Hz and 1Hz. The results also show that there is significant variation in the turbulence intensity spectra (spectral density as a ratio to the local mean speed) between 10m and 1m. As height reduces, there is a very small increase in the intensity spectra for u and v components between 0.01Hz and 0.1Hz, and a larger increase between 0.1Hz and 10Hz, despite a known attenuation of the windspeed data at high frequencies due to the transfer function of the anemometers. That the data are relative to the local mean speed indicates that the larger turbulent eddies actually decrease in size as the mean speed drops near the ground, in line with the boundary layer profile, which fits a simple logarithmic profile described in the paper. The increase seen in the high frequency component closer to the ground appears to indicate a transfer of energy from large scale to smaller scale turbulence (e.g. as inferred from Bradshaw [14]). The w component data shows that the spectra for vertical turbulence is significantly reduced between 0.01Hz and 1Hz and increased between 1Hz and 10Hz. This appears to be an intuitive change, as the vertical turbulent length scale must tend to zero at the ground. The vertical component is only weakly coherent between 10m and 1m, and the u and v components are strongly coherent at low frequency and weakly coherent at high frequency. Since there is a significant amount of turbulent energy in the high (>0.1Hz) range, it is therefore necessary to make these kinds of measurements at 1m in order to get an accurate picture of the environment

encountered by road vehicles, rather than relying on data for higher levels such as 3m or 10m.

In a review of the state of knowledge on the environment experienced by road vehicles, Howell [15] advocated the use of wind-averaged drag. Wind averaged drag is an integrated drag coefficient over the full range of yaw angles and wind speeds experienced by a vehicle on the road, and it was shown that turbulence intensity affects the total wind velocity and yaw angle experienced by the vehicle. Howell uses UK Meteorological Office data for average windspeeds, taken at 10m height above the ground and extrapolated downwards. It is observed that a correct estimate of turbulence intensity is very important both in obtaining an accurate measure of the variation of yaw, and also in measuring the C_D values at different yaw angles.

Whilst it is clear that the environment experienced by a road vehicle has not been measured in a comprehensive fashion, the above data provides some basis for experimentation. An understanding has been developed of turbulence intensities ranging from 2% to 5%, excluding those eddies generated at frequencies lower than 0.1Hz. Richard's data shows that this excludes a significant proportion of the local turbulence, but the relationship between the size of the turbulent eddies and the size of the vehicle is important.

1.2.2   Dividing the micrometeorological scale

Wind turbulence events fall on a meteorological scale based on their frequency. Low frequency events, such as those generated by an area of low pressure moving across a country, are commonly referred to as macrometeorological, and higher frequency events, from large gusting wind down to everything that a vehicle aerodynamicist would recognise as free stream turbulence, are referred to as micrometeorological. When authors such as Watkins and Saunders [12] have discussed modelling real world turbulence in the wind tunnel, they have usually considered the likely effects of the whole micrometeorological scale, or, most of it, excluding gusts and large crosswind stability type effects. Watkins considered that turbulent eddies over 10s long could be considered as quasi-steady flow phenomena.

The concept of comparing the length scale directly to the vehicle size was introduced by Bearman [16] who reviewed several studies on the effect of free stream turbulence on

11

the flow around bluff bodies, looking in detail at the effects of intensity and length scale, and it was noted that the effects were often separate. Although combined turbulence parameters had been determined in some cases, by Taylor [17] and also by Bearman and others, they were not universal, and depended on the nature of the experiment. Various results showed that the length scale itself is not as important as the ratio of length scale to a characteristic dimension of the bluff body in question. Bearman suggests that if the length scale is very large in comparison to the body, then it is seen as a correlated unsteady mean flow of varying amplitude and dimension. If it is small in comparison to the body, then although it will tend to decay rapidly over the length of the body, and it will also be distorted by the streamline curvature, it will interact with the boundary layer, and it may affect the mean flow field around the body.

This gives rise to the concept that it would be reasonable to break down the micrometeorological scale, examining the effect of length scales smaller than the size of the body separately from those of a greater size. The effect on body forces of the small scale turbulence, that strongly affects the boundary layer, could then be examined in detail, and another method sought for the development of an understanding of larger scales.

1.2.3   Wind tunnel testing with turbulence generation

1.2.3.1   Generic shapes

Several studies have focused on the effect of free stream turbulence on the flow over simplified generic shapes. Bearman [16] considered the effect of the free stream turbulence on thin laminar boundary layers, and stated that they undergo transition to turbulent at lower Reynolds numbers than for a smooth freestream. This is due to increased mixing with the freestream, and pressure fluctuations in the freestream. It was seen that separated shear layers also undergo transition earlier due to free stream turbulence, implying that where they are associated with a separation bubble and reattachment, a separation bubble should be smaller in the presence of freestream turbulence, as the turbulent boundary layer tends to reattach to the surface earlier. The turbulence also tends to increase skin friction in the attached boundary layer. The effect of increased free stream turbulence on overall drag and lift forces was not found to be predictable, in some cases increasing drag, in some decreasing it, and in others not affecting the drag at all, depending on the configuration of the body. Changes in length

12

scale were also unpredictable, sometimes increasing the effect due to turbulence, sometimes reducing it, and sometimes having no effect. Bearman gives data for 3D flows over blunt short bodies with no reattachment, and smooth fronted long bodies. Automotive bodies tend to be long and blunt, and where separations exist on the forebody they tend to be small and reattachment is expected. This study will use an automotive type body to add some data in this gap.

Hillier and Cherry [18] reported work on a 2 dimensional flat plate with a significant thickness, where the effects of turbulence intensity and length scale on reattachment length, pressure distribution, and fluctuating pressures were measured. The body was 1.37m long and 38mm thick with sharp edges, ensuring separation and reattachment along the length. It was reported that turbulence intensity has a strong effect on the pressure distribution and reattachment length, tending to reduce the size of the separation bubble. The size of the separation bubble is stated to be controlled by an equilibrium between the fluid being entrained into the shear layer at the separation point from inside the separated volume, and the fluid being recirculated into the separation region by the reattaching shear layer. Additional freestream turbulence may affect the start of transition, affecting the bubble at the leading edge, or it may change the structure of the already turbulent portion of the shear layer. Hillier and Cherry state that the start of transition occurs very close to the separation point even in the clean flow, so the most likely effect is on the development of the turbulent free shear layer as it moves downstream. It was also found that the pressure distribution and reattachment length were not significantly affected by changes in length scale. The ratio of length scale to the thickness of the model varied from 0.36 to 1.95. Increasing the length scale did increase the fluctuating pressures, and a correlation was found between the fluctuating pressures normalised against the turbulence intensity and the body dimension divided by the integral length scale.

Li and Melbourne [19] investigated the effect of turbulence on the pressure distribution over a three dimensional flat plate with rectangular cross section. The aspect ratio of the plate was 32. Measurements were made of the centreline pressure distribution and showed that raising the turbulence intensity reduced the size of the separation bubble and increased the suction near the leading edge of the plate. For the largest turbulence intensity of 12%, the minimum Cp value was almost double the value for the smooth

flow (for which a turbulence intensity was not quoted). It was also shown that, for length scales of the order of the thickness of the plate (50mm) and up to 4 times that value, the length scale did not make any significant difference to the pressure distribution. However, when larger length scales were tested at the same turbulence intensity, the suction was reduced and the size of the separation bubble increased. This would seem to reinforce Bearman's argument [16] that the smaller scales affect boundary layer growth and separation more, because when the turbulent energy is concentrated in the smaller scales, the boundary layer reattaches sooner. This is a significant finding, because it adds weight to the concept that generating smaller scales and omitting the larger scales is an acceptable test method for modelling part of the real world as experienced by a road vehicle.

Li and Melbourne [20] also considered the effect of turbulence on the fluctuating pressures. It was shown that the time averaged results are dominated by intensity, while increasing the length scale acted to reduce the suction by a small amount at the leading edge. The effect on the fluctuating pressures inside the separation bubble was much more marked – increasing the length scale from around half the thickness of the flat plate to 12 times the thickness more than doubled the fluctuating component of the pressure coefficients. It is noted that the intensities and scales were determined by the interest of the authors in the aerodynamics of buildings and are therefore considerably larger than those of interest to the automotive engineer.

Xia and Bearman [21] examined the flow characteristics of a series of bluff cylindrical bodies with elliptical fronts and slanted bases. The base slant angle and the fineness (length/diameter) ratio of the bodies were varied and the effects on C_D, base pressure distribution, and wake vortices were examined. The effect on base pressure of variations in the level of freestream turbulence was also examined. As in previous studies referenced in the paper, two flow regimes are defined – regime I, "a recirculating wake with uniform pressure over the base" and regime II, "a wake flow dominated by two longitudinal vortices forming from the leading edge of the slanted base". Xia and Bearman found that the critical backslant angle between regime I and regime II, where the drag coefficient is at its highest is around 45 degrees, although other authors have found higher angles, for bodies of revolution. The difference from the conventional value of around 30 degrees (from the horizontal) for a road vehicle is

not explained but is probably down to the difference in model geometry – a circular cross section rather than rectangular, lack of additional details such as bonnet, windscreen etc., and an aspect ratio of one – and also to the installation of the model in the centre of the tunnel, whereas Ahmed's result was for a road vehicle in ground effect. A strong effect of back angle on the vortex shedding from the model was seen, as well as a reduction in pressures at the edges of the slanted rear face as the critical back angle approached. The effect of four levels of turbulence on base pressure was investigated. It was shown that there was not a significant effect of turbulence on the base pressures for turbulence intensities from 0.03% up to 6.2%. It was speculated that there might be an effect on the critical back angle but it was not investigated further.

1.2.3.2   Automotive based tests

Some study has been made of comparisons between wind tunnel data using grids and real world drag reduction, including by Watkins [22]. The difference between the drag reduction gained from using a spoiler on a lorry cab as measured in the wind tunnel and as measured on the road was examined. Four turbulence grids were used to give five different levels of turbulence in the tunnel, including the baseline. It was shown that the road results do not match the tunnel results, but that using higher turbulence levels in the tunnel gave a better match at high yaw angles. It was observed that the turbulence intensities and length scales measured on the road did not match the conditions in the tunnel tests, but the wide variability of all factors, such as driving style, traffic levels, average speeds, vehicle loading etc. make it difficult to draw useful conclusions from this data. Measuring fuel flow and windspeed in order to make comparison between different modifications to the lorry cab would seem to introduce far too much noise. This highlights one of the problems in simulating real world turbulence, in that widely varying on-road conditions can generate large variations in aerodynamic drag. Close examination of the data for the body fairing test shows that for small yaw angles the on-road value of ΔC_D (from the baseline without the drag reduction device) varies more than the values obtained from the wind tunnel using 5 different turbulence levels between 1.3% and 3.7%. It is therefore difficult to make use of this data for practical development tests.

Wiedemann [23] investigated the effect of turbulence on what was termed "effective Reynolds number", by performing Reynolds number sweeps in a model scale wind

tunnel and measuring drag coefficient. "Effective Reynolds number" was defined as the Reynolds number where the drag coefficient fell to 0.3, with the turbulence grid installed. Over the range of Reynolds numbers tested, the drag coefficient was reduced when the turbulence screen was used. Wiedemann's results show a trend that indicates that, if higher Reynolds numbers were investigated, the drag in the clean tunnel might reduce below the drag with turbulence, which becomes fairly constant. Wiedemann stated that the effective Reynolds number was almost doubled by using a turbulence grid producing an intensity of 2.8%, and suggested that higher increases would only require higher turbulence intensities. However, in the clean tunnel, the results did go from relatively high drag to lower drag, whereas, with the turbulence grids installed, the drag was more constant throughout the Reynolds number range tested, varying only by about 20 drag counts, as opposed to 100 (1 drag count is a C_D of 0.001). This indicates that there is also an effect of the turbulence on the trend of drag with Reynolds number. To try to combine the effects of turbulence and length scale, Wiedemann comments on the results when replotted as the Reynolds number for $C_D = 0.3$ against Taylor's turbulence parameter $Tu_x(L_M/L)^{1/5}$. It was noted that the results for the two models used give different trends against the parameter, due to model scale. The scale of the model causes changes due to problems with horizontal buoyancy and interactions between the model wake and the collector of the open jet tunnel used. However, the results for the individual scale models also do not form a straight line on this graph, indicating (as suggested by Bearman [16]) that the exponent of 1/5 is not valid for all bluff bodies with separations, although it is valid for spheres (Dryden [24]).

As an alternative to using grids, another method of generating turbulence in the wind tunnel was used by Passmore [25], based on a method by Bearman and Mullarkey. A pair of oscillating aerofoils were used to generate large scale turbulence over a range of different frequencies. Pressure tappings were used to calculate the forces on a bluff body in steady state flow and in the oscillating flow. It was found that the transient results did not match the quasi-steady predictions, even at the lowest frequencies tested, where the gust wavelength was in excess of 35 model lengths. This appears to contradict Bearman's supposition, in that the longer length scale turbulence expected from the low frequency oscillation is not seen as a correlated unsteady mean flow, although the tunnel and model may suppress the gust. The main difference in Bearman and Mullarkey's test was that they were only able to select a small number of different

16

frequencies, by changing springs in their oscillating wings, and so they varied tunnel speed to achieve lower frequencies. Their steady state measurements were taken at a single speed, so there may be some Reynolds number effects present in their data that causes it to correlate better at low frequency. In Passmore's test, the aerofoil sections could be oscillated at any frequency up to the maximum tested, and so the Reynolds number was kept constant. The aim of both of these experiments was to examine the difference between static and dynamic yaw testing, rather than to study the effect of turbulence.

Cogotti [26] has also conducted experiments with freestream turbulence, but at full scale. Using flapping "wings" installed in the Pininfarina wind tunnel that are wider at the bottom than the top, with the intention of introducing a velocity profile to the flow as well as turbulence. Cogotti found that the drag coefficient is always higher with turbulence than without, but noted that it was difficult to identify a reference velocity for the turbulent flowfield. Several options are given (at the height of the stagnation point, or the mean dynamic pressure in front of the car between 0 and 1.5m height) and it is stated that the difference in results is negligible. However, in order to predict trends under varying turbulence levels, and for comparison with other types of testing, it would appear that the reference velocity is indeed important. Current research at Pininfarina has therefore focused on building up a library of data on how cars perform relative to each other, in order to form a basis for comparison.

Another commonly used method of altering the separation around a radius was used by Cooper [4], testing with flow tripping strips on the leading edges of the model. This showed similar effects to the introduction of turbulence, including the different asymptotic drag coefficients. He also showed that particle size (and therefore surface roughness) and strip location made a considerable difference to the results. This result reinforces the idea that the additional levels of freestream turbulence are having the same effect, tripping the boundary layer as it flows over the radius. This method is useful to show the similarity of the effects, but setting the flow conditions by the use of turbulence generating devices in the tunnel results in a repeatable flow condition that is model independent.

1.2.4   Turbulence experienced by a vehicle following a vehicle

Investigations have also taken place into the effect of aerodynamic interference between vehicles following at close proximity, in attempts to reduce the drag of several vehicles travelling together by forming convoys. These experiments have focused on the drag reduction achievable by reducing the pressure drag on the front and rear faces of the vehicles in the convoy. In a convoy of 2, the front vehicle benefits from a reduction in drag from the rear face, and the following vehicle benefits from a reduction in the pressure drag on the front face. The effect is highly variable with following distance and most authors deal with spacings of below 2 car lengths (e.g. Hong [27]). These studies demonstrate one potential problem of developing vehicles in the wake of another vehicle, in terms of identifying the changes caused by the additional freestream turbulence, which is how to compare results between tests of a vehicle in a wake, and the isolated vehicle. This problem arises because the reference velocity and the pressure field at the front of the test vehicle are affected by the vehicle in front.

Other authors have looked in some detail at the wake of a vehicle in isolation. Baker [28] and others classify the wake into "near" and "far" wakes. The near wake is dominated by the recirculating flow where the body ends and the flow separates. As previously seen, it will also display trailing vortices if the backlight angle is less than approximately 30 degrees. The vortices cause additional drag, but the wake is also compressed in this case and tends to become smaller as it moves downstream (Sims-Williams [29]) which reduces the pressure drag due to the wake. For a squareback vehicle, the wake tends to only show weak trailing vortices, only a large separated turbulent wake that has recirculation near the body. The far wake is a highly turbulent flow, but tends to collapse towards the ground, although more slowly in the case without trailing vortices.

Some work has been done on wind tunnel studies of vehicles following vehicles, most notably by Cogotti [30], who placed two vehicles in line in the Pininfarina tunnel, at a spacing of approximately 6m (with the upstream vehicle completely in the nozzle of the wind tunnel). It was reported that the flowfield around the vehicle following was affected by the vortices of the vehicle in front. The effect of the upstream vehicle on the wind noise produced was also investigated. Cogotti noted that the exterior noise was increased, mainly in the region of the front wheels, and the interior noise was increased

18

at all frequencies measured. Previous studies have shown that the noise caused by turbulence is different to the noise in a conventional wind tunnel test, and Peric [31] has recommended that more effort be put into simulating the transient noise caused by turbulence in the wind tunnel.

One of the methods that could be used to measure the amount of wind noise is to try to correlate the strength of pressure fields, e.g. on the side glass, with the amount of interior noise. This method was demonstrated by Burnett [32] who showed that it was possible to measure trends in interior noise due to changing body details, e.g. 'A pillar' adjustments, in the MIRA full scale wind tunnel, even though the background noise in the tunnel is quite high. It may also be possible to make measurements in the Loughborough model scale tunnel along similar principles, which would then allow the generation of more data on noise caused by turbulence. Gilhome [33] showed that the peak pressure forces on a car door were significantly under-predicted by wind tunnel testing in comparison to on road tests, although the average values were over-predicted, which demonstrates a need for further investigations in this area. However, this is outside the scope of this project.

1.2.5   Summary of the effect of turbulence

It is clear that turbulence has an effect on the flowfield around a vehicle, and consequently on the forces acting on it. One of the most important conclusions arising from the literature has been that there should be a way of separating out different effects of the real world aerodynamic environment on the car, and then separating out the sources of these effects. Broadly, there are two categories; the first is gross crosswind or longitudinal gusts that lead to crosswind stability problems, potential lane-departure events due to induced side forces and yaw moments, and increased drag and/or lift due to increased vehicle velocity relative to the air. The second, smaller crosswind or longitudinal gusts that cause vibrations or wind noise refinement issues and increased drag due to turbulence in the freestream interfering with the flow over the vehicle. It is desirable to classify the turbulence intensities, length scales and frequencies that drive the latter effects and to attempt to simulate this kind of turbulence in the wind tunnel. Following the research of Bearman and others, it is intended to use grid generated turbulence as a simplified source of turbulence, that will provide some insight into the

effect of the small scale eddies that have been shown in the literature to have an effect on the boundary layer of the model.

1.3 Objectives

The overall objective of this work is to investigate the effect of grid generated turbulence on the shape optimisation process. This is done in several sections.

- Firstly, a simple 1-box model is used to provide fundamental information on the effect of the grid generated turbulence on the leading edge radii of the model. Five levels of turbulence are investigated over the range of 0.2% to 5.1%. Balance measurements are used to acquire time averaged forces, and base pressures and centreline pressure tappings were also recorded. At the lowest turbulence intensity, this model allows a comparison with Cooper's previously published data [4]. The turbulence intensities are chosen to correspond to Watkins' data on the turbulence experienced by a moving vehicle in open conditions [11]. The primary sponsor of the research is interested in 4x4 vehicles (also known as off-road vehicles, SUVs, SAVs etc., e.g. Land Rovers, BMW X5, Mercedes ML Class) for commercial reasons, and so the model has an aspect ratio that is typical of this vehicle type. However, the results are generally applicable and this decision came only from the early priorities for the work.

- In order to reinforce the conclusions made from measurements of the forces and pressures on the 1-box model, PIV is used to measure the flowfield around the leading edge radius.

- The experiment is expanded to examine a simplified 2-box model, also based on a typical 4x4 vehicle, to show that the principles established with the simplified 1-box shape transfer to a more car-like body. The same turbulence generating grids are used.

- A full scale test is conducted, using a generic car shape (the MIRA reference model) in the estate car configuration, in order to match the 2-box shape as closely as possible. The leading edge radius on the bonnet is modified, and Reynolds sweeps are conducted in three levels of turbulence, from 1.8% to

4.3%. Comparison between full scale and model scale tests is made on the basis of Reynolds number based on the edge radius, rather than the model dimensions.

- At model scale, a different generic shape (the Windsor model) is used to show the effect of turbulence on the flow at the rear of the model, by varying the backlight angle.

- Additional work is conducted at full scale to show the effect of raised freestream turbulence on other simple modifications, such as front and rear spoiler performance, cooling drag, and A-pillar vortex size and position (using flourescene). Tests are performed on the MIRA reference vehicle, and on a 2005 Jaguar XJ and a Land Rover Discovery 3.

In order to give a background to these experiments, the next chapter discusses the experimental techniques used, the method of generating turbulence at model and full scale, and a discussion of sources of error in the experiments.

Chapter 2
Experimental method

2.1　Details of the wind tunnels

2.1.1　The Loughborough model scale tunnel

The largest low speed wind tunnel in the Department of Aeronautical and Automotive Engineering is an open circuit, closed jet wind tunnel with a 1.32m * 1.92m working section. The working section was designed to accommodate a ¼ scale passenger car, or a ⅓ scale racing car. The tunnel was designed to have a standard test speed of 40m/s, but is capable of running at speeds of up to 45m/s with a ¼ scale model installed.
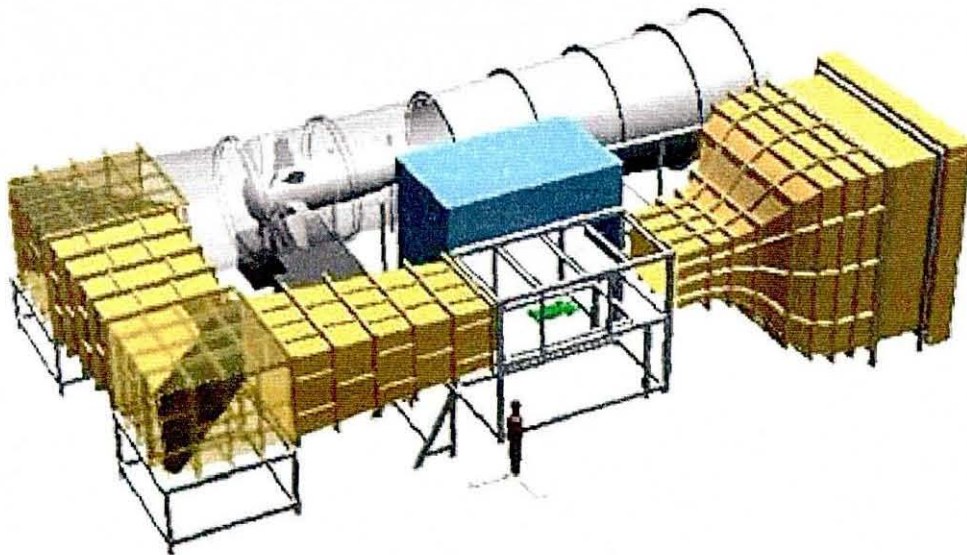
Figure 2 The 1.3m*1.9m wind tunnel (with a person to scale)

Figure 2 shows the tunnel layout. The tunnel draws air in from outside the building (through the yellow inlet shown bottom right), taking it through a contraction of ratio 7.4:1, followed by the working section, and then diffusing it down to the first of two corners, followed by another diffuser, the second corner, a shape change to accommodate the fan, and then the final diffuser which leads back to the outside. This arrangement was chosen because of the limited space available.

The clean tunnel turbulence intensity was measured by Johl, using a constant temperature anemometer, [34] as 0.15% at 40m/s, and the boundary layer thickness at the model position is 60mm (also at 40m/s). Further details of the design and performance of the tunnel can be found in Johl. The tunnel has an underfloor 6 component balance, with stated accuracies and ranges as shown in Table 1.

Component	Balance Load Ranges	Accuracy (% full scale)
Drag	+/- 120 N	0.010
Side Force	+/- 420 N	0.005
Lift	+/- 500 N	0.010
Roll Moment	+/- 150 Nm	0.010
Pitch Moment	+/- 60 Nm	0.010
Yaw Moment	+/- 45 Nm	0.015

Table 1 Balance range and accuracy

There are also six pressure transducers available. Five of them have a range of ± 250mmH$_2$O, and one has a range of ± 1000mmH$_2$O. One of the 250mmH$_2$O transducers is permanently connected to the main tunnel pitot static, and measures windspeed. All of the transducer full scale ranges can be reduced to improve accuracy where the pressures being measured allow.

The main tunnel data acquisition system, for signals from pressure transducers, or other analogue signals, consists of a PC with a 12-bit DAQ card. The card has 16 available channels, used in Referenced Single Ended mode, and is controlled using commercially available data acquisition software.

For turbulence measurements, a hotwire system is available, consisting of a Constant Temperature Anemometer system, connected to a dedicated PC with a 16-bit DAQ card (16 channels in Referenced Single Ended mode). Commercially available software is used to control the system, which has its own on-board signal conditioner, capable of applying offset, gain, and low pass/band pass filtering to the signals from the wire. There are two probe controllers allowing single or dual wire measurements to be made. A selection of hotwires are available, including standard single wires, 90° single wires for boundary layer measurements, and a dual axis thin film probe. There is a traverse for use with the hotwire system or other probes, capable of positioning a probe within the tunnel to an accuracy of ± 1mm.

A commercial PIV system is also available for making flowfield measurements, which is fully described in Chapter 4.

2.1.2 The MIRA full scale wind tunnel

The MIRA full scale wind tunnel is of open circuit, closed jet design and has a working section of 7.94m by 4.42m, a maximum speed of 36m/s, and a contraction ratio of

1.3:1. Time averaged forces and moments are measured using an underfloor 6 component balance.

2.2   Turbulence generation

2.2.1   Model scale

Four turbulence generating grids were used to increase the turbulence intensity in the wind tunnel. Two 50mm square grids using different gauge wire were used, one with 2.41mm wire and the other with 3.85mm wire. In addition two schemes of horizontal masking tape strips were used with the heavy gauge grid to further increase the turbulence intensity. It was expected from previous research [23, 35, 36] that mounted 30 mesh diameters upstream of the model (1.5m from the front face), the thin gauge grid would produce a homogenous turbulence intensity of around 1-1.5% at the front face of the model, and the heavy gauge grid slightly more. Vickery's consolidated data [36] showed a strong correlation between the distance from the grid divided by the bar size and turbulence intensity. Using masking tape strips on the heavy gauge grid[1], and based on Vickery's data, a scheme was devised, using two thicknesses of tape in the same pattern, for two higher turbulence grids. This tape scheme is shown in Figure 3, and is symmetrical about the tunnel floor to reduce the possibility of velocity overshoot. 25mm and 12mm tape widths were used, significantly raising the blockage ratio (to a maximum of 37%).
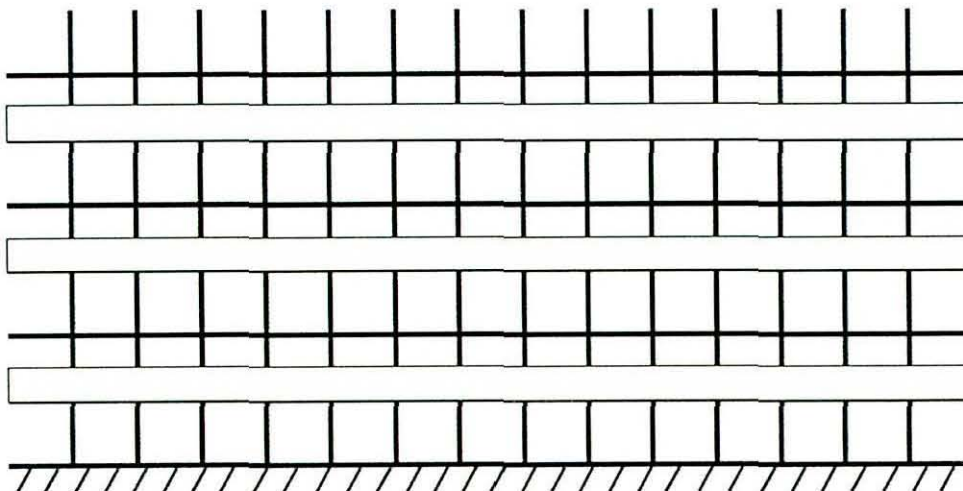
Figure 3 Bottom of grid showing 1" masking tape scheme

This caused a reduction in the maximum tunnel speed to 34m/s with the 25mm tape, and although wider tape could potentially produce more turbulence, reducing the tunnel

---

[1] Thanks to Simon Watkins for this suggestion.

speed further would compromise the maximum test Reynolds number and make comparison between results more difficult. The blockage ratio also raised the aerodynamic loading on the grid considerably, and so the grids were securely bolted to the floor and ceiling of the tunnel using small metal straps across the topmost and bottommost horizontal wires.

The turbulence intensities produced by the grids were measured with a constant temperature anemometer connected to a single hotwire. The wire was calibrated over the range of 5m/s to 45m/s, and turbulence measurements were taken at 30m/s, because the higher blockage grids restricted the tunnel speed to less than 40m/s. The sampling frequency was 10kHz, with a low-pass filter set at 3kHz to avoid aliasing problems. Higher sampling rates and cut-off frequencies (sampling at 25kHz and filtering at 10kHz) were also used to check that no significant turbulent energy was excluded from the results. A traverse was used to move the hotwire in a vertical line on the centreline of the tunnel, at the centre of the model mounting position, and readings were taken at vertical intervals to determine whether the turbulence was homogeneous. At each position, 1048576 ($=2^{20}$) samples were taken. These were then broken up into 8 blocks. Turbulence intensity, power spectra, autocorrelation and integral length scale results were calculated for each block and ensemble averaged over the 8 blocks at each point.
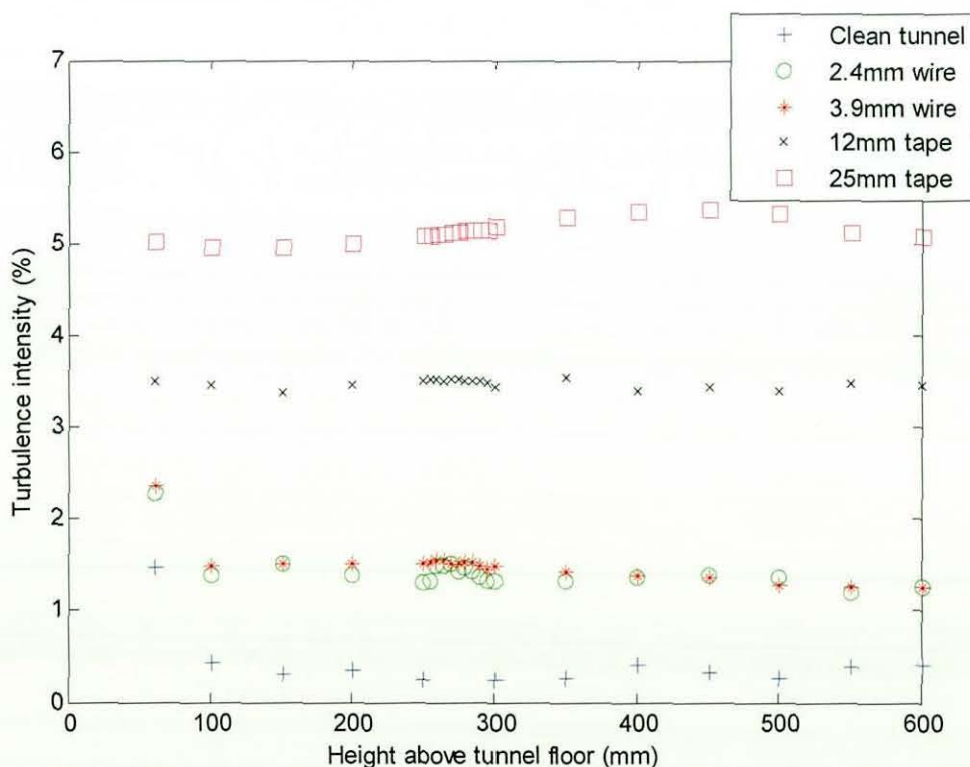
Figure 4 Tu for all turbulence levels on the tunnel centreline, model position centre, at 30m/s

27

The recorded turbulence intensities are shown in Figure 4 for the different grid schemes. The average turbulence intensities were 0.2% for the clean tunnel, 1.38% for the thin gauge grid, 1.45% for the heavy gauge grid, 3.41% for the 12mm tape and 5.13% for the 25mm tape. The figure shows that at 60mm, although the tunnel velocity remains mainly constant (Figure 5), the boundary layer has a strong influence on the turbulence intensity at the lowest height measured for the plain grids. Across the main part of the working section, the turbulence intensity is reasonably constant. Smaller steps were used between y=250mm and y=300mm in order to determine whether the wake effects of the wires persisted at the model location. It is clear that the turbulence intensity is reasonably homogeneous across the range of the data. The clean tunnel turbulence was measured between 0.15-0.3%; this is a little higher than that recorded by Johl at 40m/s but still low. The difference is most likely because the r.m.s. is driven by fluctuations from outside the tunnel and interaction between the outlet and inlet, and so not much reduced by changes in tunnel speed, and the mean speed by which it is divided is lower, giving a higher percentage turbulence intensity.

Figure 5 shows the spatial velocity variation across the tunnel height. The clean tunnel varies very little across the height. For the first two turbulence grids, the wire pitch was the same as the pitch of the traverse, apart from between 250-300mm. For the grids with tape, the pitch of the tape is double the pitch of the measurements, and the windspeed remained within acceptable limits All turbulence grids show some effect of the wake of the wires or the tape, but the variations are within ±0.5m/s, which is considered acceptable, given the limits of hotwire accuracy without correcting for variation in the ambient temperature. The tunnel air temperature varied by less than 2 degrees during the experiment, which contributed a small error in the average speeds recorded, and because the tunnel draws in air from the outside, there is a further possibility of small variations in tunnel speed due to atmospheric wind conditions. Since the model height is 380mm, it is expected that there should not be a noticeable difference in an area weighted average speed over the bottom of the model and another at the top.
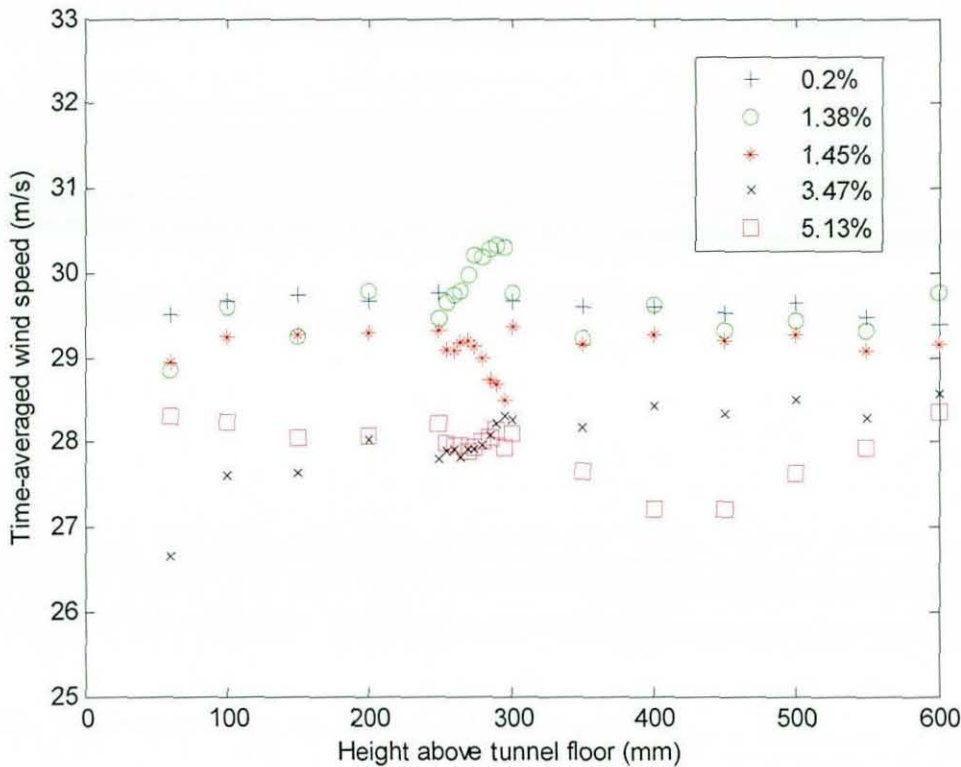
Figure 5 Variation in average windspeed with tunnel height at the centreline of the tunnel, centre of the model position, at about 30m/s

Conventionally, grid generated turbulence should follow Taylor's hypothesis, which states that the rate of decay of the turbulent eddies is slow, and therefore the autocorrelation function of the u component is the same as the spatial correlation in the x direction. This means that the integral length scale can be calculated by first computing the integral time scale (the integration of the autocorrelation function between $\tau=0$ and the first time that R_{xx} crosses the x axis), and then multiplying by the average freestream velocity U. However, for the data recorded, this method showed unusually large length scales in the clean tunnel, of the order of 20-50m in the freestream away from the wall. It is suspected that due to the open circuit design of the tunnel, taking air from outside the building, there may be some effects of both the ambient wind, and interference between the outlet and the inlet of the tunnel. Since the circuit length is approximately 50m, this may well be shown in the results. These pulsations in tunnel speed are very low energy, but clearly measurable, and they cause problems with measurement of the length scales from the grids. The turbulent length scales calculated for the grids were also clearly affected by these longer length scales. Normally it would be expected that the eddy size from a turbulence generating grid would be very small. Therefore, following Fransson [37], who reported a similar problem, it was decided to high pass filter the results to identify the turbulent

29

component as opposed to the total fluctuations in the tunnel. The cut-off frequency was chosen to ensure the inclusion of any eddies that could fit in the working section, both longitudinally and laterally. Since the working section is approximately 5m long (giving a wavelength λ of 5m), and the hotwire data was sampled at a windspeed of 30m/s, the cut-off frequency was calculated from the formula

$$f = U / \lambda = 6Hz \hspace{4cm} \text{Equation 1}$$

The filtered data gave slightly different turbulence intensities. For the clean tunnel, the intensity was 0.08%. For the grids, in the same ascending order, the intensities were 1.25%, 1.41%, 3.41% and 4.95%. The length scales were 205mm for the clean tunnel, and for the grids, 16mm, 15mm, 25mm and 37mm respectively. Fransson was more restrictive and chose a cut-off frequency based on the width plus the height of the tunnel, giving a higher frequency. For the Loughborough tunnel, using this criterion would give a frequency of 10Hz, which reduces the length scales slightly – for example the first turbulence grid then produces a length scale of 12mm instead of 16mm. However, the trend is not affected, and as a measure of the average eddy size that affects the model, the first values with the lower cut-off frequency are acceptable.

In order to further validate the results, the turbulence length scales were also calculated by fitting the Harris-Von Karman spectral model to the unfiltered data, as described by Li and Melbourne [20]. This method effectively correlates against the corner frequency between the turbulence generation and the Kolmogorov roll-off rate, meaning that the low frequency information is somewhat damped. The results are shown with the results from the high pass filtered autocorrelation in Table 2 and are almost identical. The length scale for the clean tunnel was calculated using the Harris-Von Karman method but is considered of little use, as the fit is very poor and the value still relates to the length of the circuit rather than the size of any turbulent eddies.

Unfiltered Tu	L (HP filtered autocorrelation)	L (Harris-Von Karman spectra)
1.38%	16mm	16mm
1.45%	15mm	15mm
3.41%	25mm	24mm
5.13%	37mm	37mm

Table 2 Length scales in the model tunnel

2.2.2   Full scale

In the MIRA full scale wind tunnel, due to concerns about aerodynamic loading, and distance from grid to model position, turbulence generating grid patterns were installed at the entrance to the contraction on the upstream face of the honeycomb section flow straightener. The honeycomb in the MIRA tunnel is large, with diamond sections approximately 300mm across and 1m deep, making it ideal for supporting the large grids, whilst unlikely to significantly reduce the turbulence generated. Several grid schemes were considered, all using only vertical bars as it was not practical to install horizontal bars across the 11m wide honeycomb. Two schemes were chosen to use for the tests, based along similar lines to the masking tape grid schemes used at model scale. Both consist of 9 4.4m long wooden strips mounted vertically at a spacing of 1.4m across the honeycomb, with the spacing reducing to 0.7m between the pieces of wood at the edges and the walls to give symmetry as with the masking tape schemes at model scale.

The first grid uses 200mm strips, and the second 300mm. Figure 6 shows the second of the grids from behind the model position with the traverse on the main turntable. The first grid was found to generate a turbulence intensity of 3.4%, and the second 4.3% (from unfiltered hotwire data). Hotwire measurements of the standard tunnel showed it to have a turbulence intensity of 1.8%. As a consequence of the practicalities of installing such a large grid, only vertical bars were used, which may have the fortunate result of being more representative of typical low-level turbulence. Normally, where there are both horizontal and vertical bars, grid generated turbulence is generally expected to decay towards isotropic and homogeneous turbulence. Using only vertical bars, it is probable that more longitudinal and lateral turbulence and less vertical is generated, although it is expected that it will still decay to isotropy eventually, but it was not possible to test this. However if this was the case then it would be a little closer to a realistic turbulence field with the w-component being reduced close to the ground (eg. as measured by Richards [13]). The homogeneity of the turbulence was measured using a hotwire mounted on a traverse at the model location and found to vary by ±0.3% for both the grids and the clean tunnel. The length scales given using the Von Karman method (detailed in Section 2.2) were 160mm for the 3.4% grid and 165mm for the 4.3% grid. The length scale for the clean tunnel was 250mm. Because of the practical constraints mentioned earlier, the grids are upstream of a 1.3:1 contraction,

31

which would be expected to affect the length scales and intensity. The turbulence intensities are only slightly lower than would be expected by comparison against the plot of grid generated turbulence in Vickery's study [36], but if it was decided to repeat this experiment in a different full scale wind tunnel, it would therefore be necessary to take account of this when designing grids to produce similar turbulence levels.
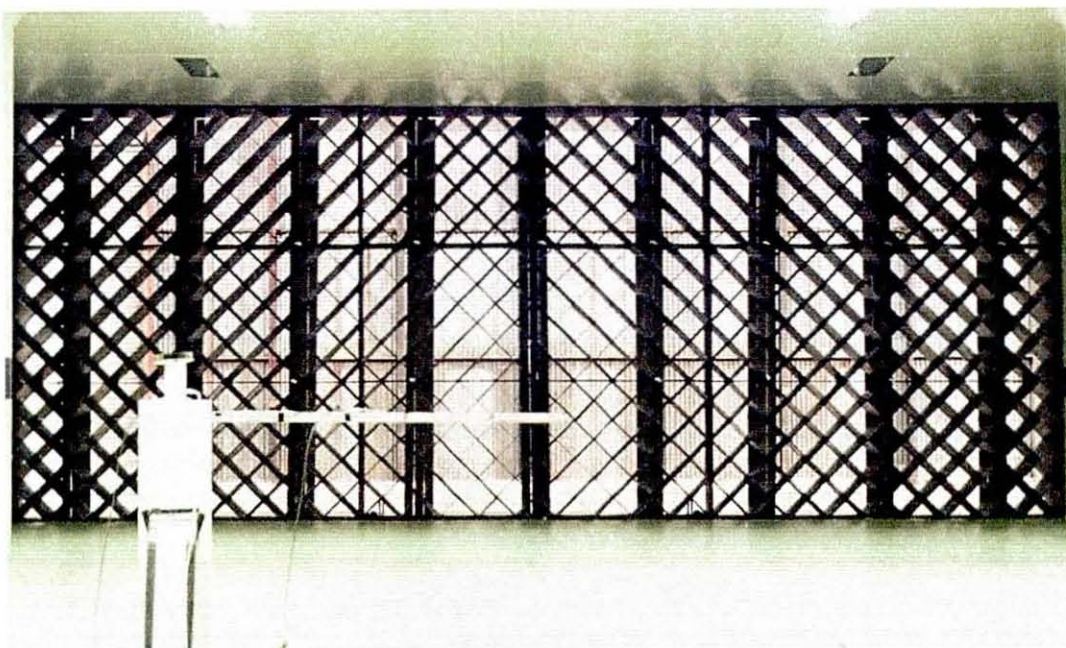
Figure 6 MIRA tunnel grid viewed from behind the model position (hotwire shown on turntable centre)

A correlation was conducted between the tunnel pitot and the model position with and without the turbulence grids. A small correction (approx. +0.14m/s static offset and -.22% scaling adjustment for the 3.4% grid, and +0.16m/s static offset and -.17% scaling adjustment for the 4.3% grid) was applied to the windspeed for all the turbulence grid results to allow for the blockage effect of the grid on the tunnel pitot.

2.3   Accuracy and repeatability

For all tests at model scale, all 6 forces and moments were recorded on the balance, and their coefficients calculated. The wind speed and Reynolds number values were corrected for blockage using a simple area ratio continuity formula:

$$U_{corrected} = U_{measured} * \frac{100}{100 - blockage}$$

Equation 2

where *blockage* = (model frontal area / tunnel working section area) * 100

32

The coefficients have been calculated using the blockage corrected wind speed. Reynolds numbers were also calculated based on edge radius, Re_r, as it is expected that the transcritical Reynolds number Re_r will be constant with edge radius (Cooper [4]).
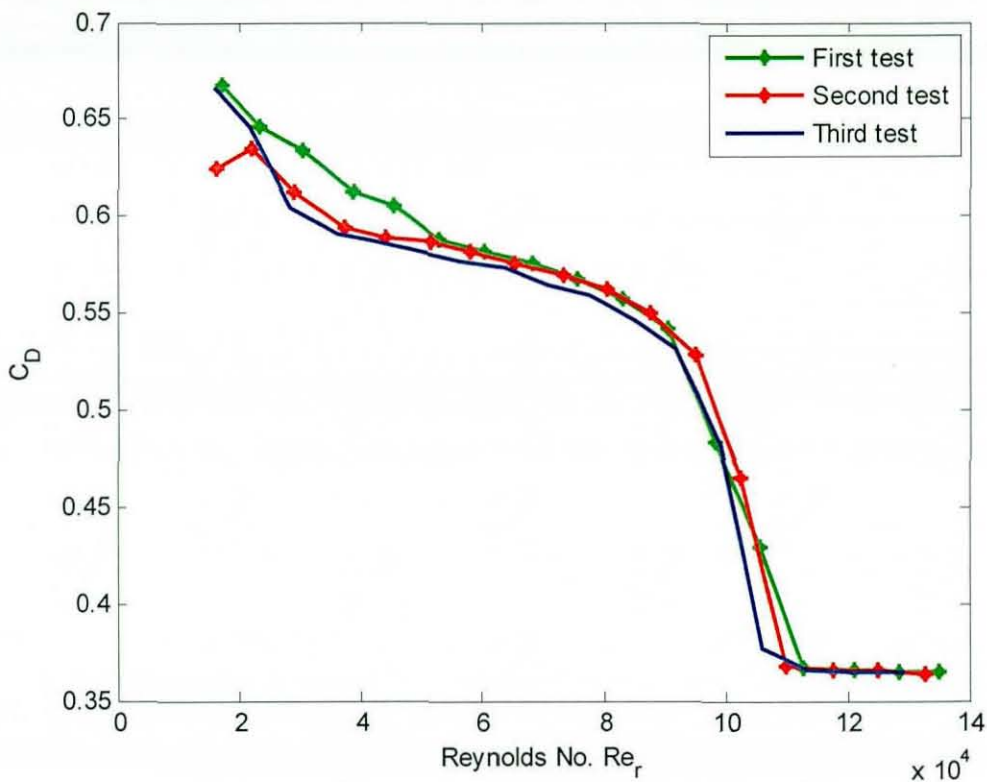
Figure 7 Drag coefficient repeatability test (40mm front at 0° yaw)

Figure 7 shows a repeatability check on the drag results at model scale, carried out over several separate test sessions, after removing and reinstalling the model. It is necessary during the tests to remove the model from the balance to change the front section, to avoid the possibility of damaging the balance. The three tests show a very good agreement for the important values of transcritical Reynolds number and post-critical drag coefficient, where the flow has become fully attached. In the post-critical region the variation is less than 2 counts of drag ($\Delta C_D < 0.002$). In the precritical region the variation is very high at the lowest Reynolds numbers, but reduces to approximately 9 counts as the Reynolds number increases and the separation bubble becomes more stable (as described in Section 4.4.2). The repeatability between the first and second test is much better, because although the model was removed, the experiment was not completely dismantled. This means that the repeatability within a single set of results is less than 3 counts of drag above a Reynolds number of approximately 50,000.

Figure 8 shows the results for the front and rear lift coefficients at model scale. The results show a similar effect to drag; the repeatability for the pre-critical region is around 9 counts of front lift or 5 counts of rear lift, but in the post-critical region the repeatability is better than 3 counts for front lift and 4 counts for rear lift. The repeatability of the front and rear lift is less than 5 counts within a single results set.
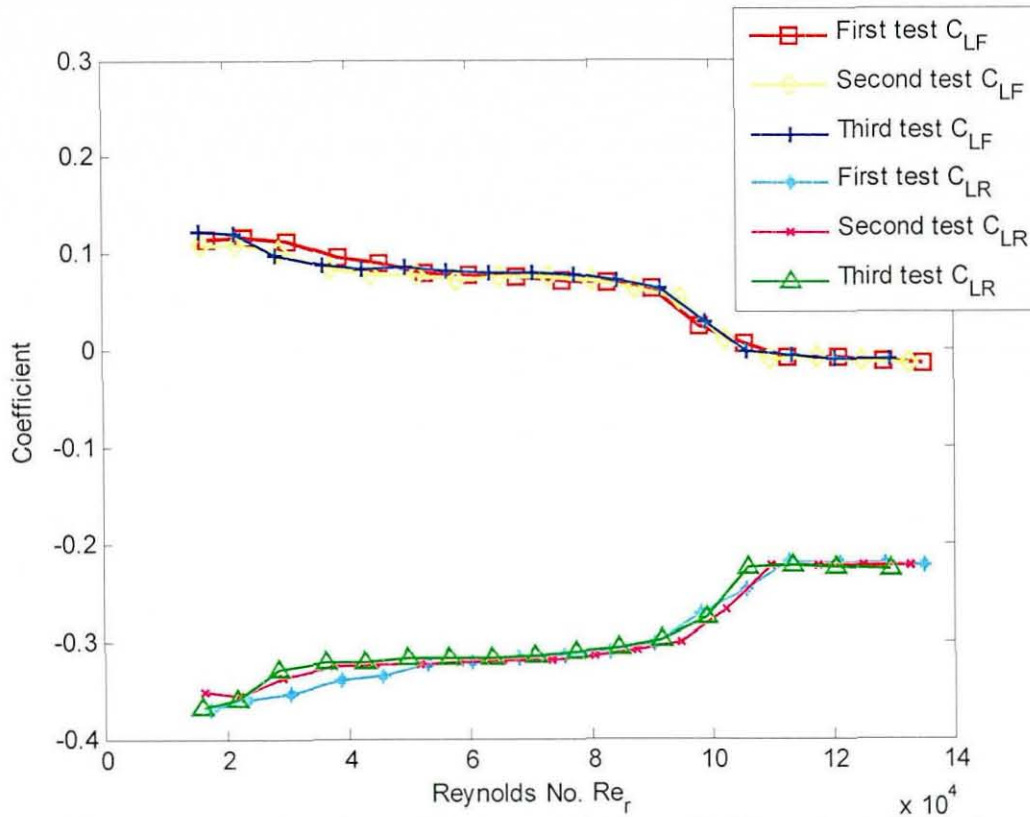
Figure 8 Front and rear lift coefficient repeatability results (40mm front at 0° yaw)

In the full scale tunnel the balance is also a 6-component mechanical balance that uses strain gauges. The overall accuracy is quoted as better than 3 counts of drag ($\Delta C_D = 0.003$) at the standard test speed of 28m/s.

2.4   Effect of the wind tunnel boundary layer

It is known that the fixed floor of a typical wind tunnel does not accurately simulate the ground as experienced by a moving vehicle. A flow is generated under the model that consists of two boundary layers close together, which will interact and may develop into a channel flow, depending on vehicle ground clearance. Since it will not be possible to test with a moving ground plane, the likely effect of additional turbulence on the tunnel floor boundary layer must be considered, as it will contribute to changes in the forces on the model.

Mason and Sovran [38] discussed the effect of the boundary layer thickness on the aerodynamic characteristics of a road vehicle, primarily to establish corrections that could be used to predict the on-road values. In these experiments, comparison will only be made between different results from wind tunnels with fixed floors, and so an extension to real world numbers will not be attempted. However, Mason and Sovran also examined the effect of variations in the displacement thickness of the boundary layer on the tunnel floor, and this could allow some estimation to be made of the effects of changes in the boundary layer thickness due to varying Reynolds number and turbulence intensity.

The model was mounted with the bottom of the model at 60mm above the tunnel floor in order to be clear of the boundary layer at 40m/s, but no correction due to the variation of the boundary layer thickness with speed was made.

An estimate of the boundary layer thickness at different windspeeds is made by modelling the flow into the working section as the flow along a flat plate, beginning from the point of inflection of the contraction. At this point in the contraction the boundary layer thickness is expected to reduce to almost zero (Johl [34]), and in the favourable pressure gradient it will grow more slowly in reality and thus the estimate is conservative.

The thickness of a turbulent boundary layer can be estimated from Equation 3 by assuming that the boundary layer follows Prandtl's seventh root law (Houghton and Carpenter [39]).

$$\frac{\delta}{x} = \frac{0.38}{\mathrm{Re}_x^{0.2}}$$
Equation 3

where x is the distance from the point of inflection of the contraction to the point of interest (mm), and δ is the boundary layer thickness (mm).

The displacement thickness δ^* of a turbulent boundary layer can be calculated as 1/8 of this value by substituting Equation 3 into the equation for the displacement thickness given by Houghton and Carpenter. The distance x to the front of the model is 4054mm, so the boundary layer thicknesses are approximately as shown in Table 3.

Wind speed (m/s)	Boundary layer thickness δ (mm)	Displacement thickness δ^* (mm)
10	79	9.9
20	69	8.7
30	64	8.0
40	60	7.5

Table 3 Boundary layer thickness variation with Reynolds number

In Mason and Sovran's experiment, the displacement thickness relative to ground clearance of the model was varied by using different model scales, in the clean tunnel and with one of two backward facing steps. The results showed how the lift and drag coefficients varied with boundary layer displacement thickness relative to ride height. Their model had wheels and a simplified underbody which was not flat. A range of δ^*/H of 5% to 70% was examined, and it was concluded that the presence of a ground plane boundary layer does has a significant effect on the measured forces. However, over a small range of displacement thicknesses such as that in the table, Mason and Sovran's results suggest that the increase in the drag coefficient with Reynolds number due to the thinning boundary layer is likely to be of the order of 10 counts for a similarly complex model. The models used at model scale in the present study all have a flat floor and no wheels, reducing the potential for interaction. Considering that the drag coefficient in of the 1-box model decreases by around 300 counts over the range of Reynolds numbers tested, this is a small additional error.

When the turbulence intensity in the freestream is raised, it is expected that there will be an interaction between the turbulent eddies and the boundary layer on the floor of the tunnel. The distance from the point of inflection of the tunnel to the grid mounting position is long enough that the boundary layer should be turbulent at the grid, and so the likely effects are a thickening of the boundary layer (Bearman [16]) and changes in the structure of the edge of the boundary layer (Bradshaw [40]). Bradshaw [40] noted in his review of the effect of freestream turbulence on boundary layer growth that it is very difficult to predict the effects accurately. The growth is dependent on the relationship between the scale of the turbulence and the thickness of the boundary layer; if the turbulent eddies are large, and the boundary layer thin, or the eddies small and the boundary layer is thick, then the interaction will be weaker than if the eddy size is approximately the same as the boundary layer thickness. Grid generated turbulence is known to decay with distance away from the grid [36], and Bradshaw states that the effect of this type of turbulence is less than if the flow was ideal with constant

turbulence along the length of the tunnel. The boundary layer is thicker at the model position (Table 3) than the Harris-Von Karman integral length scales previously established, and so the interaction must be at its strongest at some upstream point, and becoming weaker as the flow approaches the model. An in depth measurement of this effect has not been carried out in this study, but, in the hotwire measurements, there is no evidence of a boundary layer extending as high as 100mm from the tunnel floor, and, if anything, some evidence of a slight velocity overshoot near the floor for the grid scheme with 25mm tape.

Chapter 3
Edge radius optimisation of a simple model

In this chapter, the results are presented of an edge radius optimisation experiment using a simple 1-box model. The method is based on Cooper's leading edge radius experiment [4]. This involved a Reynolds sweep at each radius to characterise the response of the model using the balance. The experiment was extended by looking also at base pressures and centreline pressure distributions, and by varying the level of freestream turbulence. Cooper's result of a constant transcritical Reynolds number based on edge radius was used as a defining parameter to show the effect of turbulence on the flow over the models. In all, five levels of turbulence were used.

The 1-box model, similar in concept to Cooper's, is a single box shape with a replaceable front section with 10 different radii, scaled to represent a traditional 4x4 vehicle with a tall and relatively short body.

In vehicle development, the aim of the edge radius optimisation process is to achieve fully attached flow, giving a low drag coefficient. The flow around edge radii should therefore ideally undergo transition at a Reynolds number lower than that experienced by the vehicle at a representative road speed. The experiment was designed to investigate the transitional behaviour of the different edge radii under different turbulence conditions. The results are presented in the following sections, first investigating the effect of turbulence on the drag coefficient and base pressures, and then investigating the lift coefficient results. Finally the centreline pressure distribution is examined to give additional insight into the conclusions reached from the force measurements.

3.1   Model details and test procedure

Edge radii were selected that would cover a range from completely pre-critical flow at all Reynolds numbers possible in the model tunnel to fully developed post-critical flow at most Reynolds numbers tested. Cooper's data [4] was used to provide an estimate of the range required, and radii from 10mm up to 100mm in 10mm steps were selected. Wiedemann[23] suggested that increasing the turbulence would increase the effective Reynolds number, and therefore it was known in advance that some of the radii that only showed the high drag pre-critical flow in Cooper's tests could undergo transition under raised freestream turbulence.

The model frontal area was scaled to produce a blockage ratio of 6%, resulting in a model that is approximately 22% of full scale. Each replaceable front section had the same radius on the top and side front edges with radii ranging from 10mm to 100mm. The 40mm to 100mm radii can be seen in Figure 9. The underside and rear of the model were flat with no backslant. In Table 4 the model details are shown and for comparison the model details employed by Cooper are also included. For the 1-box model, the tunnel can produce Reynolds numbers from $Re_A = 0.4*10^6$ up to $Re_A = 1.5*10^6$, where Re_A is the Reynolds number based on the square root of frontal area.

	1-box	Model used by Cooper
Length L	845mm	1143mm
Width W	390mm	381mm
Height H	380mm	381mm
Front cross-sectional area A	$0.1478m^2$	$0.1161m^2$
Blockage ratio	5.953%	3.1%
Front edge radii	10mm - 100mm in 10mm steps	0mm - 85mm

Table 4 Details of 1-box model sizing
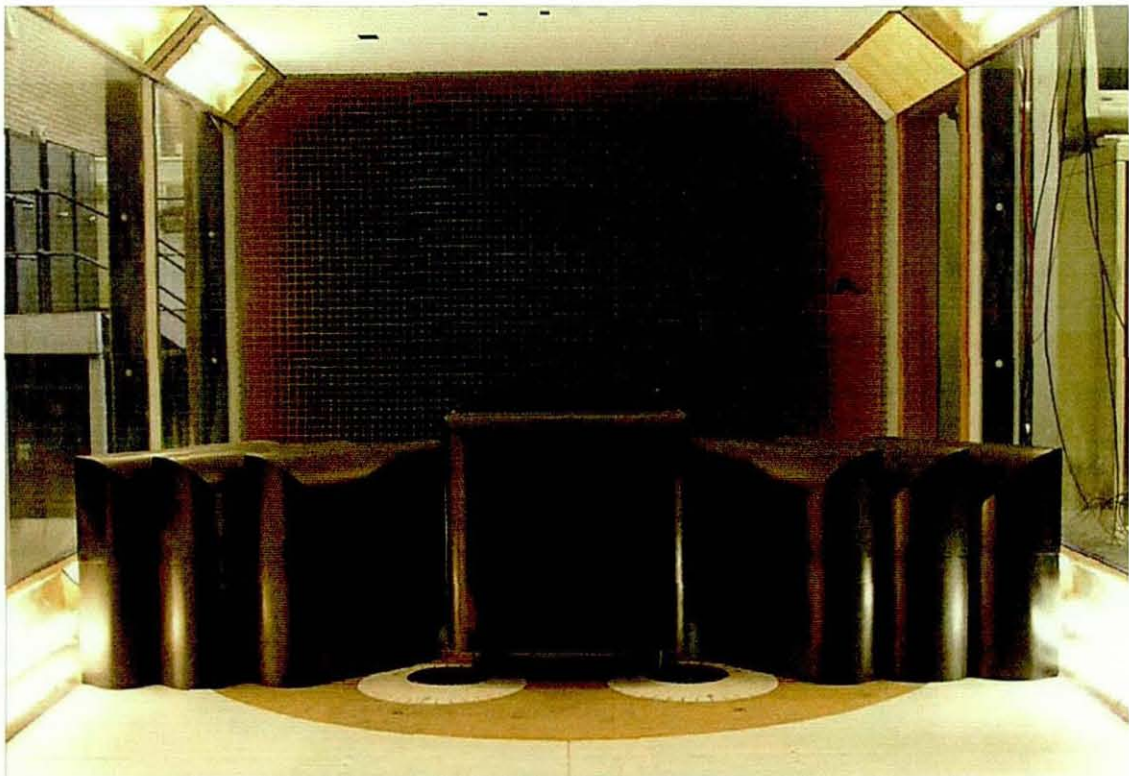
Figure 9 The 1-box model with 7 of the front sections (40mm-100mm)

Figure 9 shows the model with a selection of front pieces on either side. The model is mounted on threaded bar, which is connected to the underfloor balance. The ride height was set at 60mm, as the boundary layer thickness (δ^{99}) is approximately 58mm at 40m/s

41

with an empty test section. Figure 10 shows a dimensioned drawing of the model with the 70mm front section attached.
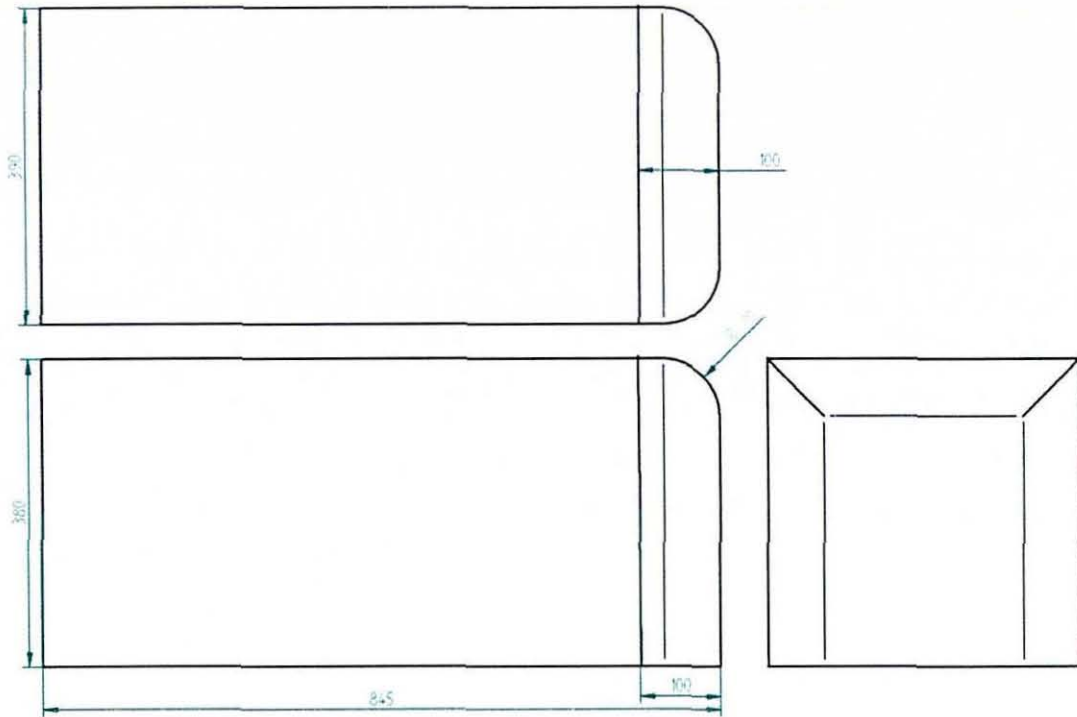
Figure 10 1-box model drawing with dimensions in mm (70mm front section fitted)

Base pressures were measured using 5 static tappings arranged in the centre of the back of the model, which were coupled together, and the pressures measured using a low range differential pressure transducer. Conventionally, the static reference is the tunnel pitot static, the same as is used to establish the reference velocity, but this was not possible. When a turbulence grid is in the tunnel, the normal tunnel pitot becomes unreliable, and wind speed is recorded by a pitot upstream of the grid, previously calibrated against the normal tunnel pitot in clean flow, i.e. with no grid installed. It is not possible to use this upstream pitot as a static reference, because the grid itself causes a static pressure loss. Therefore a roof static above the line of the back edge of the model provided the reference. This is significantly distant enough from the model not to be affected by it. It measures a static pressure related to the blockage corrected dynamic pressure and not the tunnel pitot dynamic pressure.

3.2 The effect of turbulence on drag

3.2.1 Clean tunnel drag results

Figure 11 shows the variation of drag coefficient at zero yaw for the 1-box model in the Loughborough model scale tunnel. The models were tested from 5m/s to 45m/s in

42

2.5m/s steps, and the results are plotted against Reynolds number based on the square root of frontal area (Re_A). The results show that for the smaller radii, the drag coefficient is quite high at low Reynolds numbers, of the order of 0.65. It drops slowly to begin with and then undergoes a rapid fall until it abruptly stops decreasing and becomes stable. For the medium and large radii (40mm+) transition to fully attached, low drag flow is clearly visible. The 3 smallest radii did not undergo transition before reaching the maximum safe operating load for the drag component (115N). This limited the maximum Reynolds number possible for these radii. It is probable that if higher Reynolds numbers could be reached, one or more of the smaller radii would also undergo transition to attached flow. Figure 11 shows good agreement with Cooper [4].
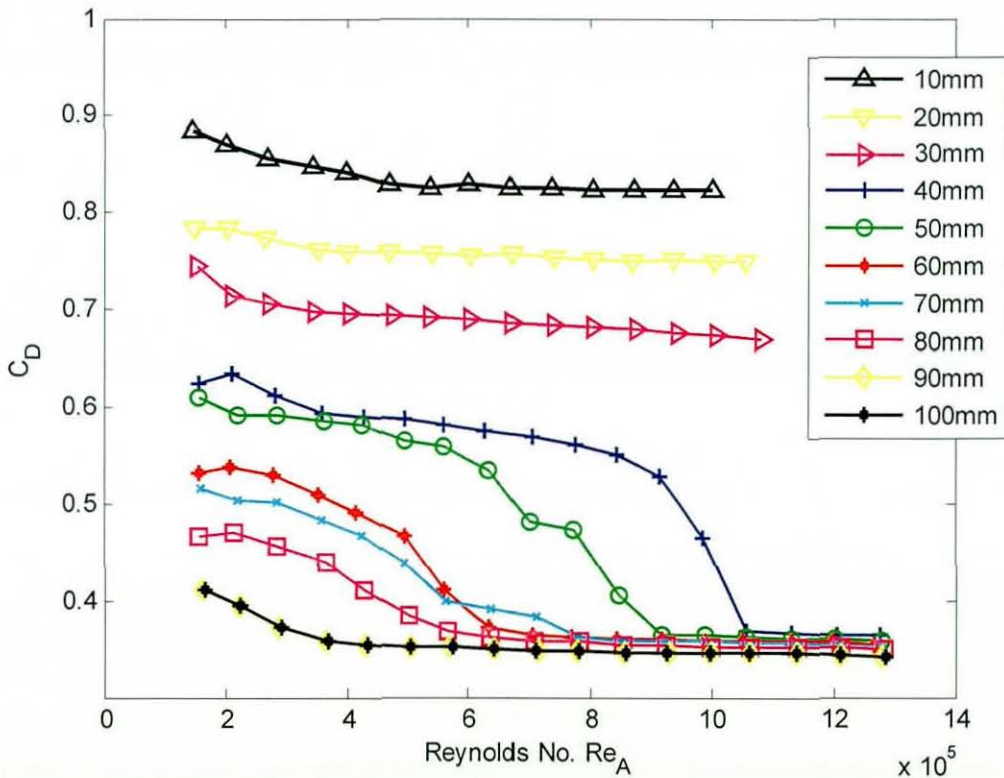
Figure 11 Variation of drag coefficient at 0° yaw with Reynolds number (Edge radius as a parameter)

The results for the 40mm front section are repeated in Figure 12 with the chronology of the experiment indicated by the arrows. As Reynolds number increases, the flow becomes attached and the drag reduces to a relatively constant minimum at a particular Reynolds number. However, as the speed is reduced the turbulent boundary layer, that is now established, persists at lower tunnel speeds so the subsequent rise in drag occurs at a lower Reynolds number. This effect is much more noticeable on the smaller radii because they are more prone to separated flow due to the increased curvature. It can be

seen from Figure 12 that the critical and transcritical Reynolds numbers (see below) are still relatively similar whether one chooses to use the data for velocity increasing or decreasing.
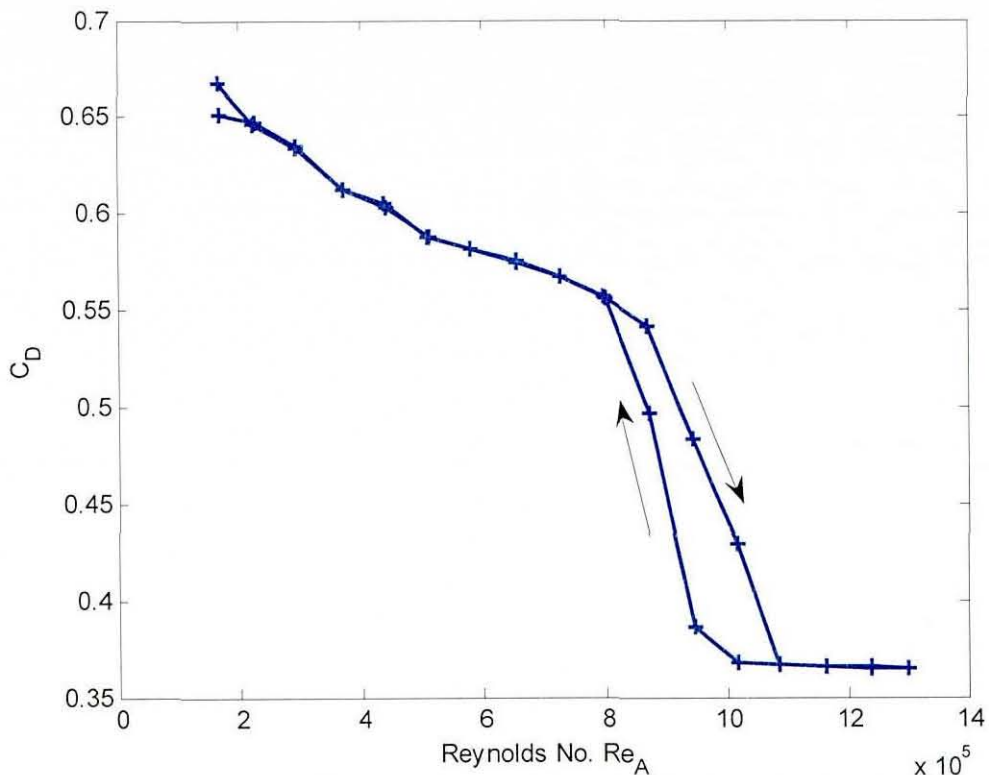
Figure 12 Variation of drag coefficient with Reynolds number for 40mm front section showing hysteresis loop

Figure 13 shows the result for the 40mm front with the hysteresis loop removed (velocity increasing only). At low Reynolds numbers, the high drag coefficient implies that there is separated flow around the front of the model. As the Reynolds number increases, the drag coefficient slowly reduces, indicating that the separation is a bubble that is reducing in size and the reattachment point is moving further forwards (as shown by Cooper [4] using wool tufts for the same Reynolds number region on his model). As Reynolds number increases further the critical Reynolds number is reached, which is defined as the point where the separated laminar boundary layer becomes unstable and begins to undergo transition to turbulent flow (Hoerner [5]). The flow becomes fully attached, and the drag drops dramatically, reaching a low and reasonably constant post-critical drag coefficient. The flowfield around the radius is examined further in Chapter 4.
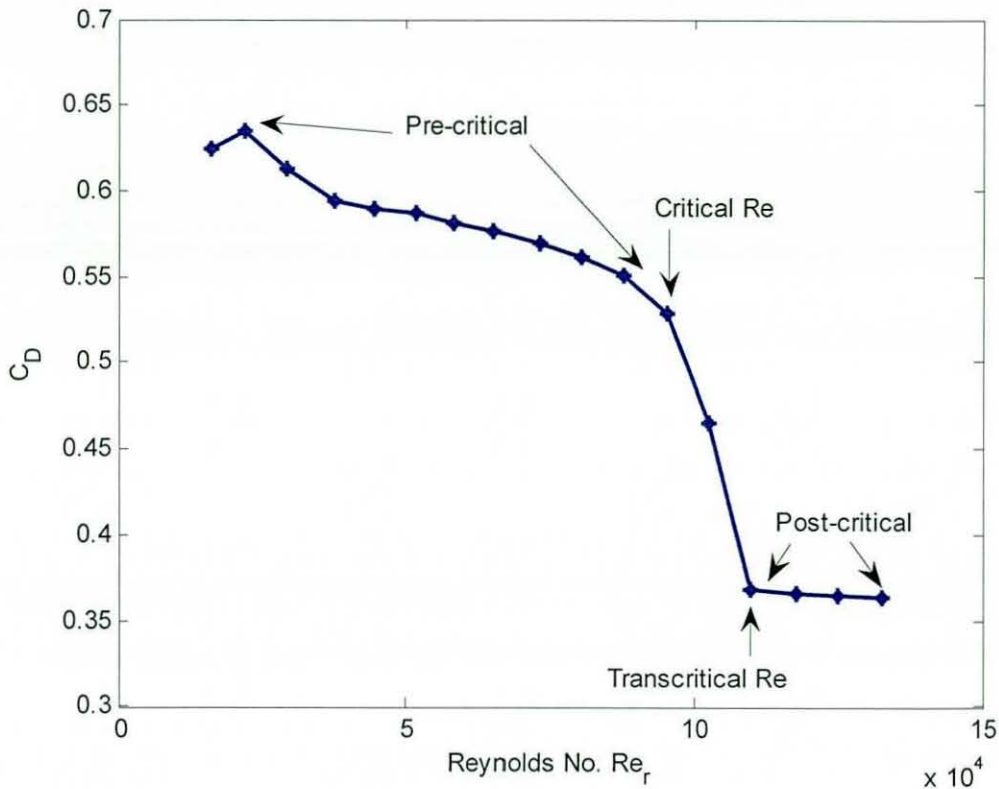
Figure 13 Variation of C_D with Reynolds number (40mm front only) showing flow regimes and transcritical Reynolds number

Also shown in Figure 13 for the purpose of defining terms are the transcritical Reynolds number Re_{tcrit}, which is defined as the point where C_D falls to a low and approximately constant value after the critical Reynolds number, the critical Reynolds number itself, and the pre-critical region.

The data from Figure 11 is represented in Figure 14 with the Reynolds numbers based on edge radius (Re_r), and without hysteresis loops shown (speed increasing only). The transcritical Reynolds number identified in Figure 13 is here seen to be relatively constant when based on edge radius (Re_{rtcrit}), repeating the result of Cooper [4].

The transcritical Reynolds number is therefore a useful parameter, because it represents the whole dataset for this model at this turbulence intensity. If the results at different freestream turbulence levels also produce a constant Re_{rtcrit}, it will be a way of directly identifying the effect of the turbulence. This will be shown later in this chapter.
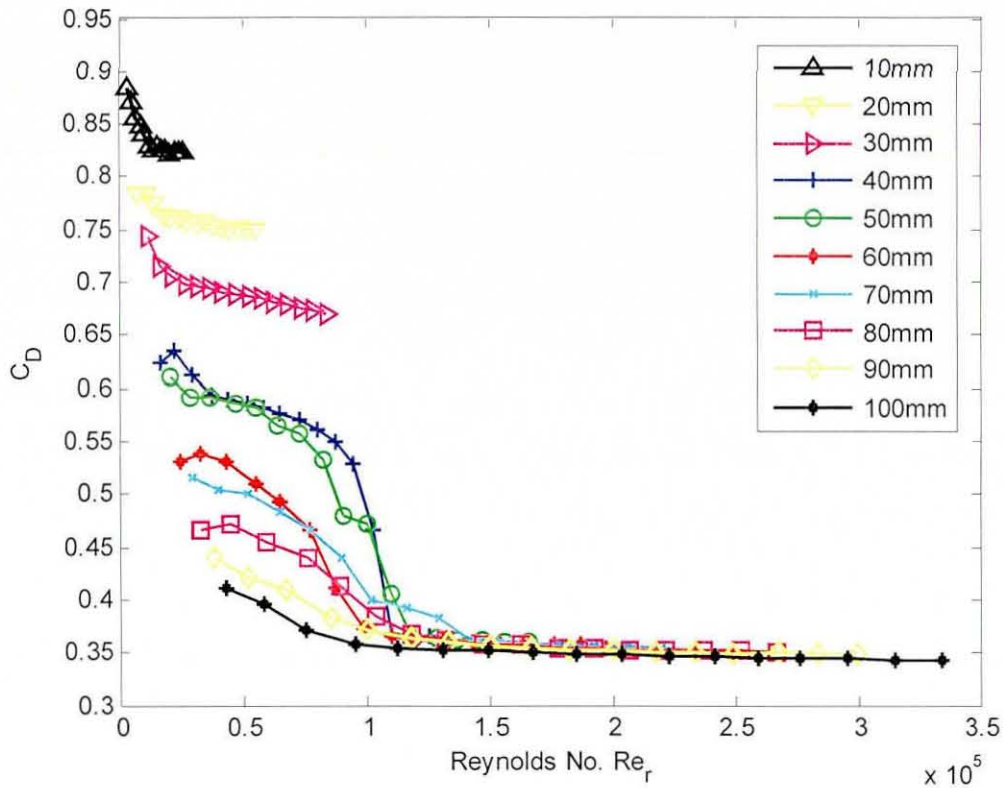
Figure 14 Variation of drag coefficient at 0° Yaw with Reynolds number based on edge radius (Edge radius as a parameter)

However, although it is easy to identify Re_{rtcrit} directly by eye for the 40mm radius, this is not the case for all radii, especially the largest, and so a consistent method is required. One method, as used by Newnham[41], was to fit a spline to the results, and identify the transcritical Reynolds number by eye using the first derivative of the spline to assist in identifying the correct point. This is more accurate for those curves that are less obvious, e.g. the 80mm or 90mm front sections, but it still requires user intervention.

An alternative method, not requiring intervention, involves identifying a linear best fit of the last 4 points recorded, and then, using a "Piecewise Cubic Hermite Interpolating Polynomial" (PCHIP) curve fit, the point where the curve deviates significantly from the line is picked out numerically. The last 4 points are used because, as shown in Figure 13, the 40mm front section (which is the smallest radius to undergo transition on the 1-box model) has only 4 points in the post-critical region, where C_D is reasonably constant and independent of Re. The PCHIP fit was used because it produces a result that closely fits the points with little overshoot (unlike the spline). The method was calibrated by testing different values of significant deviation and then selecting the value that gave answers that most closely matched the correct values for the curves where transcritical Reynolds number is readily identifiable by eye. In practice the

46

results for the different methods are not significantly different, but the final method can be applied automatically and objectively and is the most consistent.
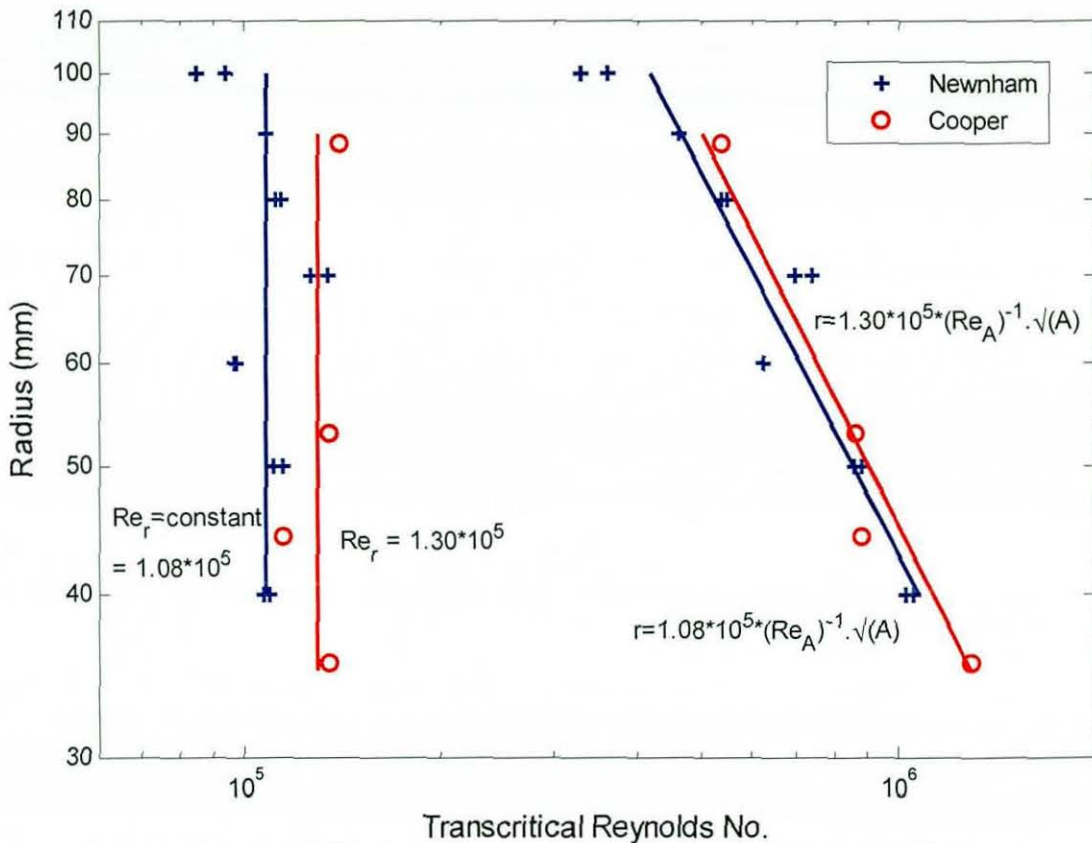
Figure 15 Collapse of data for clean tunnel at zero yaw and comparison with Cooper

Figure 15 shows the transcritical Reynolds numbers for all the edge radii against edge radius on a log-log scale. On the right hand side, the transcritical Reynolds numbers are based on the square root of frontal area, and the data is shown to fit a universal curve. On the left, the transcritical Reynolds numbers are based on edge radius, and the results are shown to be approximately constant. This is a repeat of Cooper's results, which are also plotted for comparison. In Cooper's paper the results are shown against non-dimensional edge radius, calculated using the equation:

$$\eta = \frac{r}{\sqrt{A}} \hspace{5cm} \text{Equation 4}$$

where r = radius (m), A = frontal area (m)

Cooper fitted the formula $\eta = const * (\text{Re}_A)^{-1}$ to the data on the right, but then multiplied both sides by $\sqrt{A}$ and rearranged to give $\text{Re}_r = const$, shown on the left. Since the constant is independent of the frontal area, a model with a different frontal area should still have approximately the same values of Re_{rtcrit} for a chosen radius, but a

47

different value of Re_{Atcrit}, because of the difference in A. Cooper's intention was to demonstrate an optimisation of a model scale vehicle that would still be optimal at full scale. In that case, scaling up to a 1:1 vehicle would give the same value of η as the model, and therefore the same Re_{Atcrit}. However, in the same turbulence conditions a 40mm radius on a 1:5 scale model will behave in a similar way, and give a similar Re_{rtcrit}, as a 40mm radius on a full size vehicle. In other words, this is not a scale model effect.

Instead of aiming to optimise a geometrically accurate vehicle at model scale, the focus in the present study is to examine the process of optimisation, and the effect of freestream turbulence on the flow around a radius of varying size. To show this, the results are all plotted against the radius in mm, and η is not used. The reason therefore for testing at full scale in Chapter 5 is to demonstrate the practicality of the technique, and to repeat the results shown at model scale and show that the same logic can be applied to both experiments.

3.2.1.1   Yaw sensitivity in the clean tunnel

Figure 16 and Figure 17 show the variation of C_D with Reynolds number Re_r for the 40mm and 70mm front sections respectively at different yaw angles. At 15° the 40mm front does not undergo transition, although it was possible to force low drag flow at high Reynolds number by first accelerating the windspeed with the model at 0° yaw and then yawing the model. It can be seen from the figures that the model is sensitive to yaw, in that there is an increase in drag coefficient across the range of Reynolds numbers tested. The transcritical Reynolds number appears constant for the 70mm front section, but there is less confidence in the result at 40mm, partly because of the reduced resolution at 10 and 15 degrees yaw for this radius. There is little evidence even at 40mm to suggest a trend in transcritical Reynolds number with yaw angle.
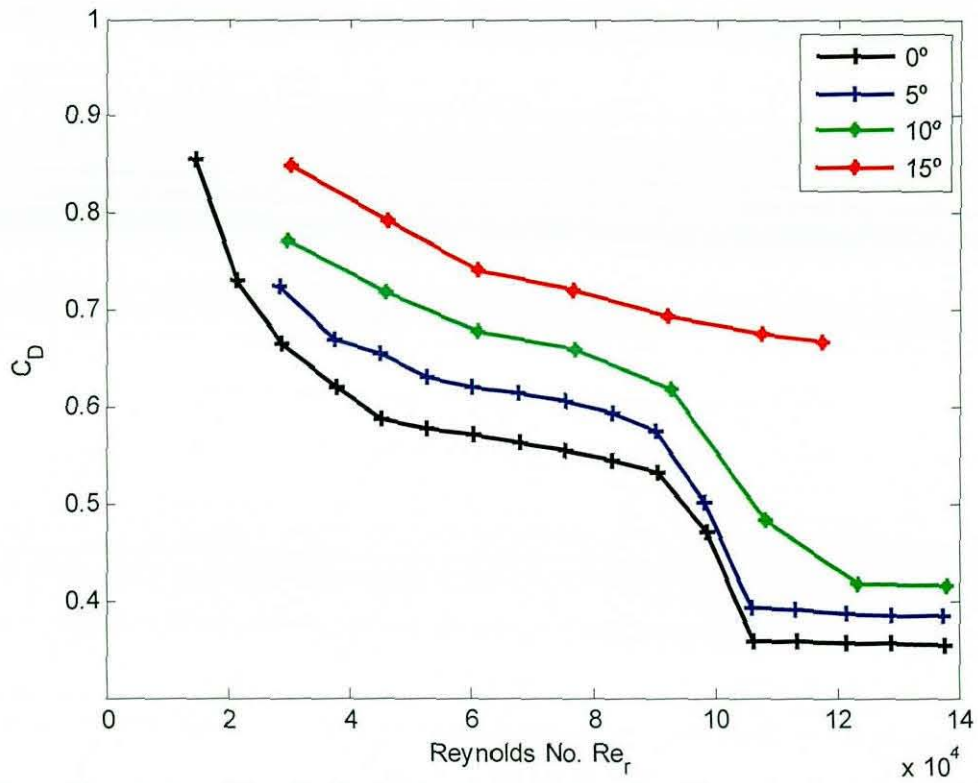
Figure 16 Variation of C_D with Re_r for the 40mm front section (Yaw angle as a parameter)
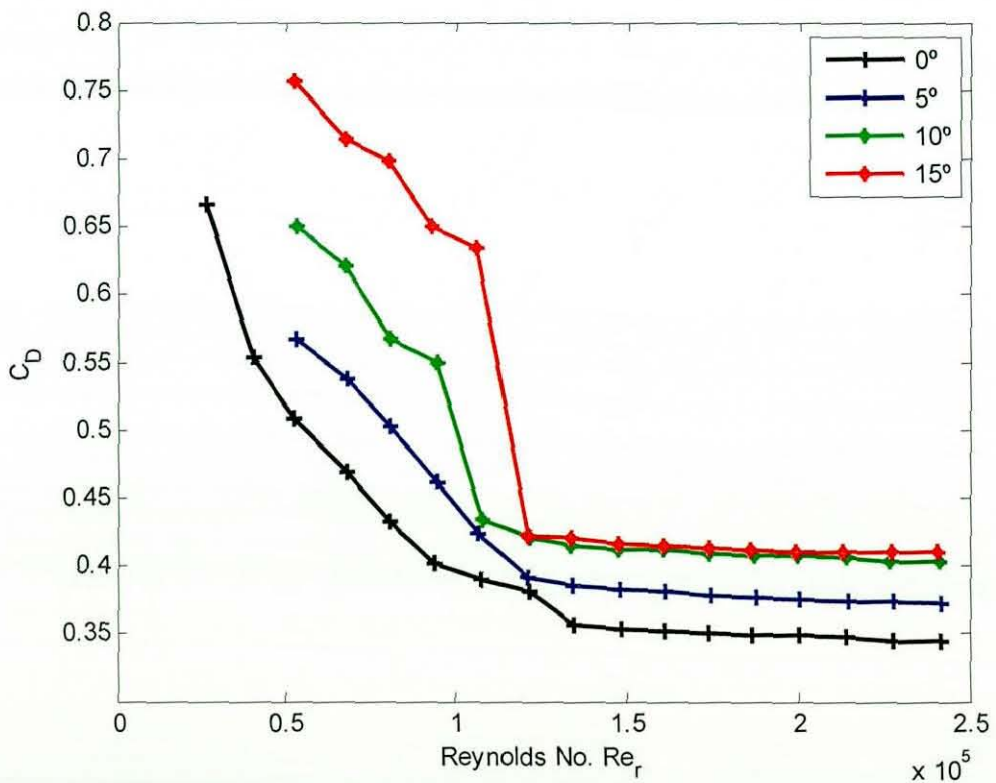
Figure 17 Variation of C_D with Rer for the 70mm front section (Yaw angle as a parameter)
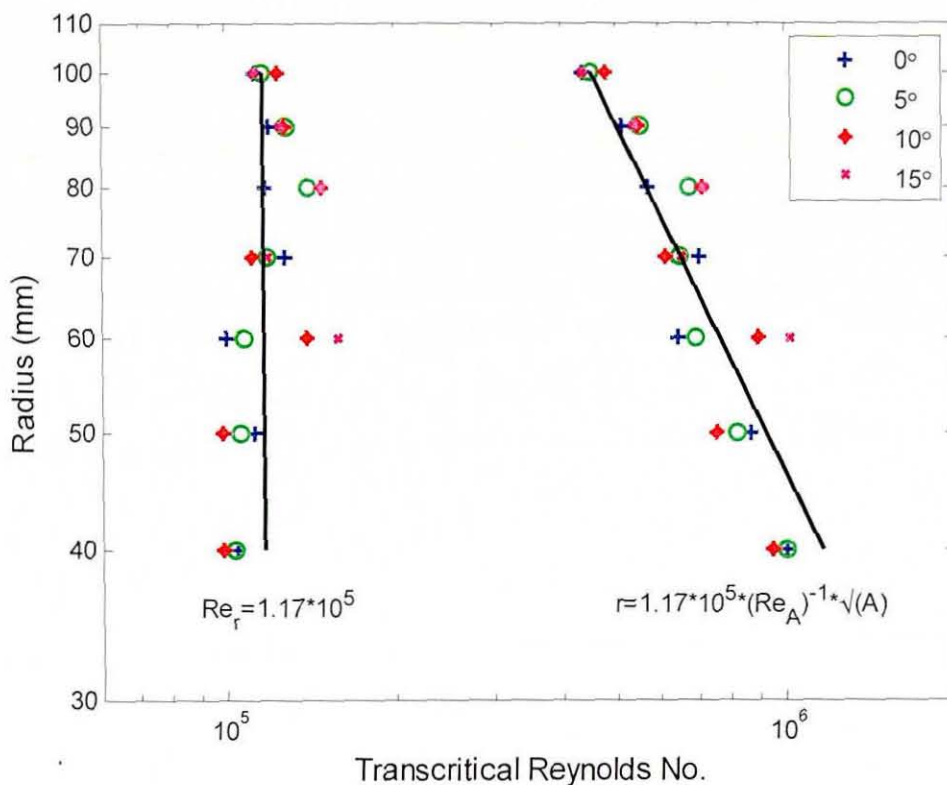
Figure 18 Collapse of drag data for the clean tunnel with all yaw angles

In Figure 18 the transcritical Reynolds numbers for the model at different yaw angles are plotted against edge radius, with results for Re_A on the right and Re_r on the left. The mean value of Re_{rtcrit} was determined to be $1.17*10^5$. Table 5 shows the variation in the constant against yaw angle. The differences in the data are very small – a difference between the maximum and minimum Reynolds number of only $7.6*10^3$, compared to the spread between maximum and minimum Re_{tcrit} at zero yaw of $4.9*10^4$. It is suggested that the overall effect of yaw is small with no significant trends.

Yaw angle	Transcritical Re_r
0°	$1.14 * 10^5$
5°	$1.18 * 10^5$
10°	$1.21 * 10^5$
15°	$1.15 * 10^5$

Table 5 Variation in average transcritical Reynolds number with yaw angle

Figure 19 shows the results for transcritical Reynolds number based on edge radius replotted against yaw angle. There is an increase in the spread of the data as yaw angle increases, but there is no significant trend present in the figure.
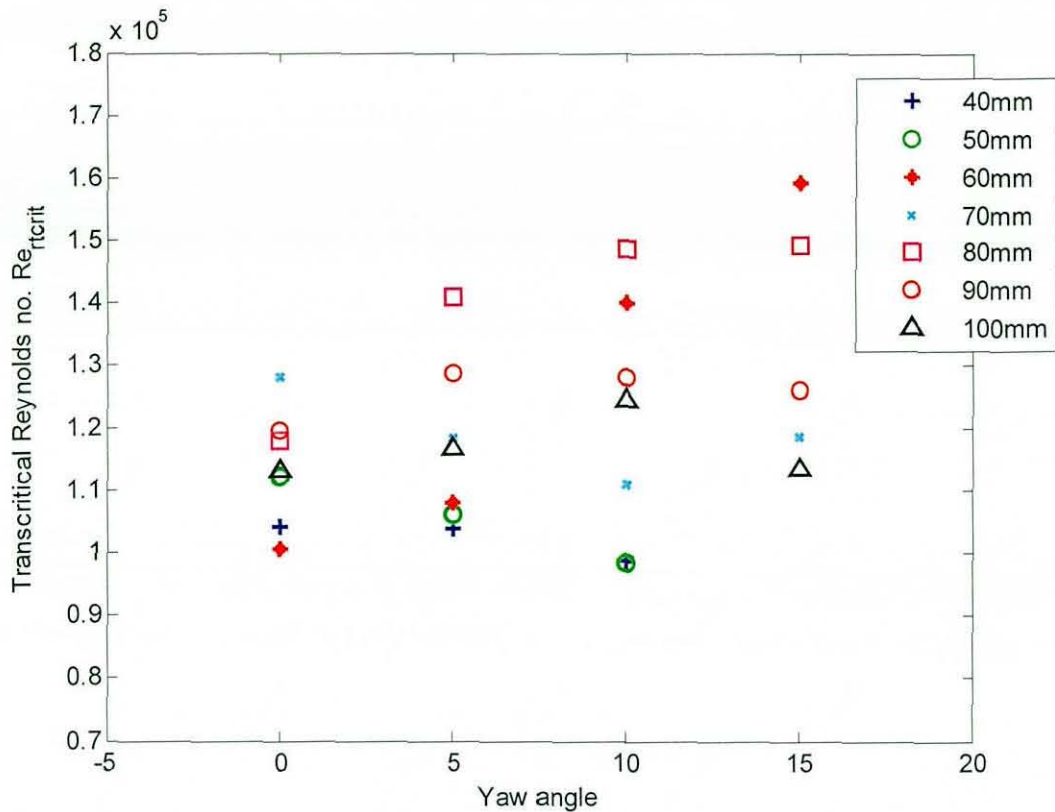
Figure 19 Variation of transcritical Reynolds number Re$_{rtcrit}$ with yaw angle, clean tunnel (edge radius as a parameter)

3.2.1.2   Base pressure results in the clean tunnel

The base pressure results were analysed by converting them to pressure coefficients using the equation

$$C_p = \frac{p - p_\infty}{\frac{1}{2}\rho U^2}$$

Equation 5

where p is the tapping static pressure (Pa), p$_\infty$ is the static reference pressure (Pa), ρ is air density (kg/m^3) and U is the tunnel speed (m/s)

Figure 20 shows the base pressure coefficient C$_{pb}$ for the clean tunnel. The first obvious characteristic is that the base pressure is not the same for each front section in the post-critical flow regime. It seems counterintuitive that the 100mm front section should cause the base pressure to be lower, implying that the base drag is greater in this case, although as will be seen in the pressure tapping results, the base pressure in the centre is not equal to the base pressure everywhere. There are some effects of transition apparent in the figure, which are shown more clearly in Figure 21, with the same data replotted against Reynolds number based on edge radius.
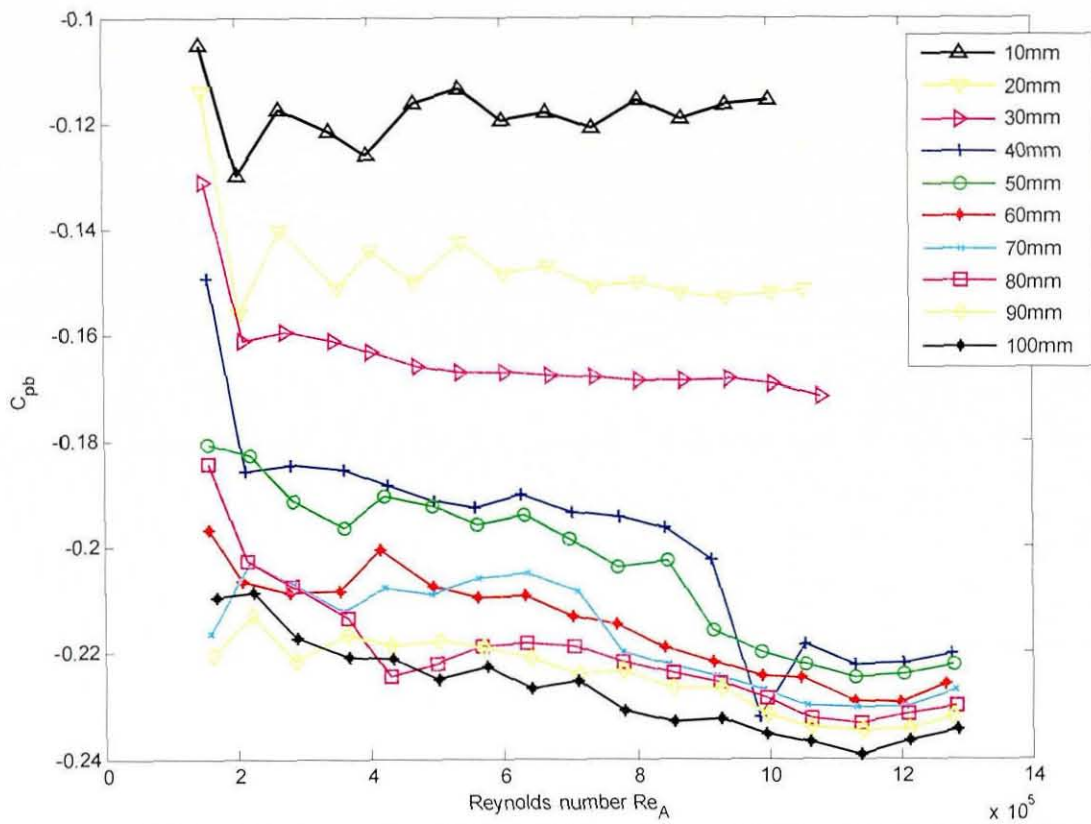
Figure 20 Variation of base pressure with Reynolds number based on frontal area (edge radius as a parameter)
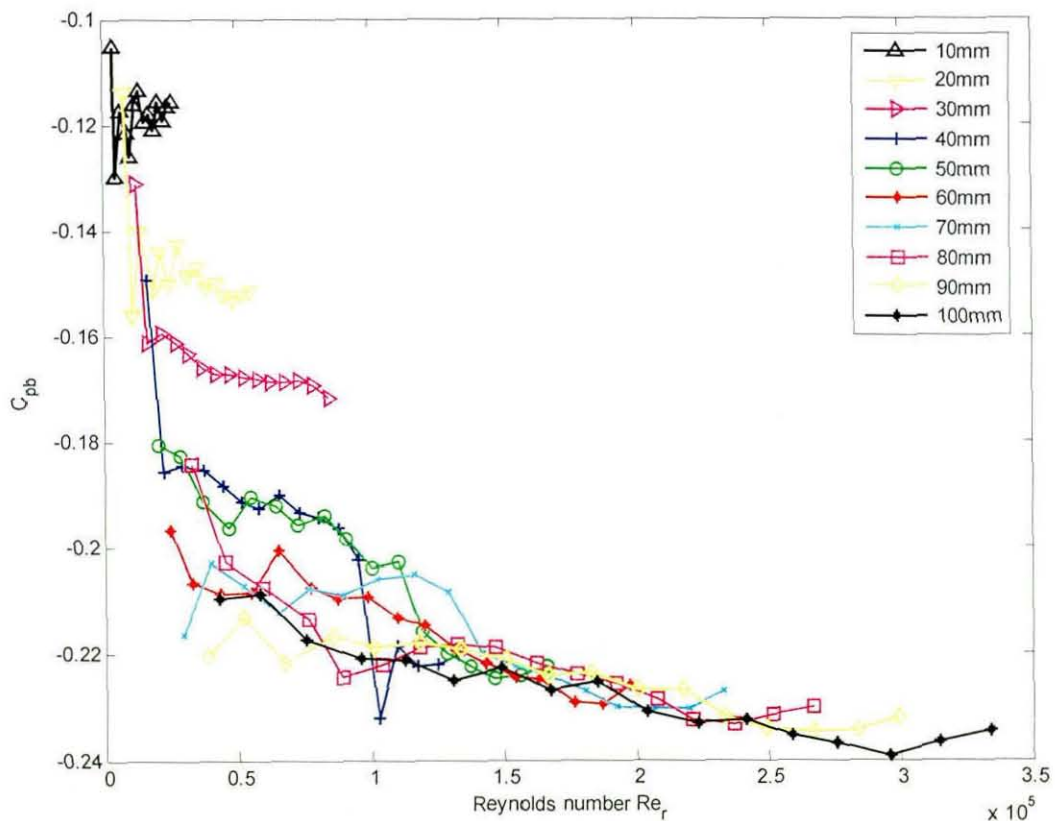
Figure 21 Variation of base pressure with Reynolds number based on edge radius (edge radius as a parameter)

The transcritical Reynolds numbers are much less clear on individual curves due to the variation in the results, but it is clear that overall there is a difference between the pre-critical flow, when the Reynolds number Re_r is less than approximately 108,000 (from the balance results), and the post critical flow, at higher Reynolds numbers. It is suggested that the front sections that show separated wakes at low Re_r have higher (less negative) base pressures because the separation at the front of the model causes a much larger boundary layer, as seen in the PIV results (Chapter 4). The opposite effect is seen for the large radii with fully attached flows – as the Reynolds number increases, the boundary layer at the trailing edge of the model becomes thinner (Equation 3) which should give a sharper separation and less mixing. This reduces the base pressure (more negative) giving more base drag.

3.2.2   Summary of clean tunnel drag results

- The 1-box results show that the transcritical Reynolds number based on edge radius is a constant. This repeats the result of Cooper [4]. The variability that is evident is largely caused by the unstable nature of the flow in the range of Reynolds numbers close to the critical and transcritical Reynolds numbers.

- It was shown that, because the constant Re_{rtcrit} is dependent only on the edge radius, the results can be treated as a test of edge radius optimisation without reference to the model scale. A 40mm radius should perform the same in a full scale wind tunnel as it does in the model scale wind tunnel, at the same Reynolds number based on edge radius.

- The drag of the model is shown to be sensitive to yaw, but the transcritical Reynolds number remained constant over the range of yaw angles tested (0 – 15°). This was also reflected in Cooper's results [4].

- The base pressures are also found to vary with Reynolds number, in a way that correlated to the presence of separation at the front of the model. The base pressure was considered to be controlled by the boundary layer thickness at separation.

3.2.3   Drag results with additional turbulence

The introduction of the turbulence grid reduces the maximum speed of the tunnel because of the additional pressure loss. The effect is small for the two lowest turbulence grids but at the highest level the maximum tunnel speed was reduced to 32m/s. This limits the maximum Re number achieved in the following results.
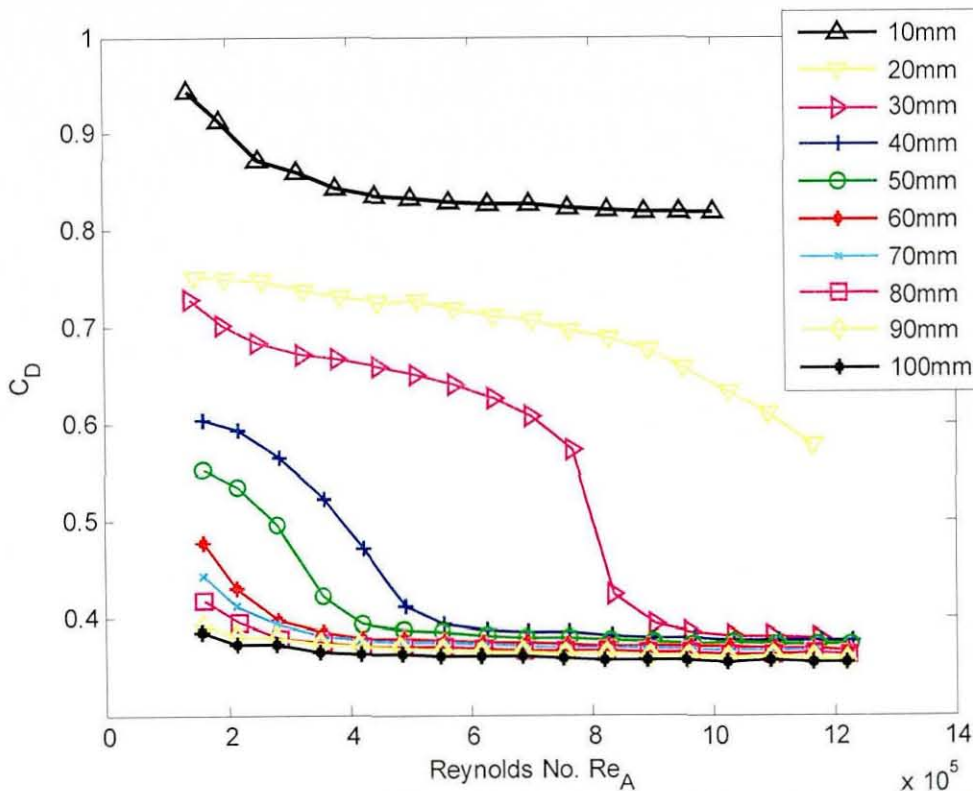
Figure 22 Variation of C_D with Reynolds number Re_A, Tu=1.38% (edge radius as a parameter)

Figure 22 shows the drag results with the freestream turbulence raised to 1.38%. It is clear in comparison with the clean tunnel results in Figure 11 that there has been a significant change in the pattern of transitions, and in the shape of some of the curves. According to Wiedemann's results [23], an increase in the effective Reynolds number (for the whole model) is expected, which is the analogy often used to describe how the additional turbulence has reduced the transcritical Reynolds number for a particular configuration. The 30mm radius now undergoes transition whereas in the clean tunnel it did not, and the drag coefficient of the 20mm radius reduces considerably more at high Reynolds numbers than it did when the background turbulence level was much lower. The maximum Reynolds numbers for the 10mm and 20mm radii are limited by the drag limit on the balance, as for the clean tunnel results.
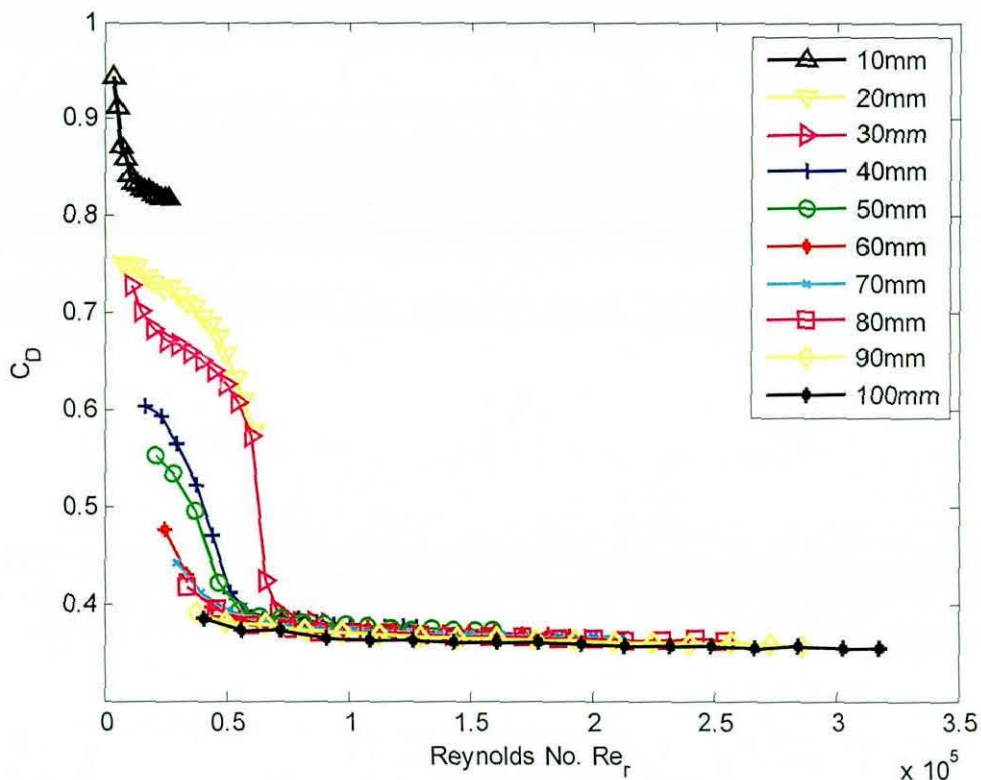
Figure 23 Variation of C_D with Reynolds number Re_r, Tu=1.38% (edge radius as a parameter)

Figure 23 shows the results for 1.38% turbulence replotted against Reynolds number based on edge radius. It can be seen in the figure that the transcritical Reynolds number, Re_{rtcrit}, is still approximately constant, but is much lower than it was in the clean tunnel. Using the same methodology as before, the average values of Re_{rtcrit} were calculated, and are reproduced in Table 6 for all levels of turbulence. The results show that the most significant change occurs between the very low turbulence case – the clean tunnel – and the lowest level of increased freestream turbulence. The results for 1.38% and 1.45% are effectively the same, and when turbulence intensity is increased further, the changes are small.

Turbulence intensity (%)	Average Re_{rtcrit}
0.2	$1.08 * 10^5$
1.38	$0.54 * 10^5$
1.45	$0.56 * 10^5$
3.41	$0.44 * 10^5$
5.13	$0.41 * 10^5$

Table 6 Variation in average Re_{rtcrit} with turbulence for the drag results at 0° yaw
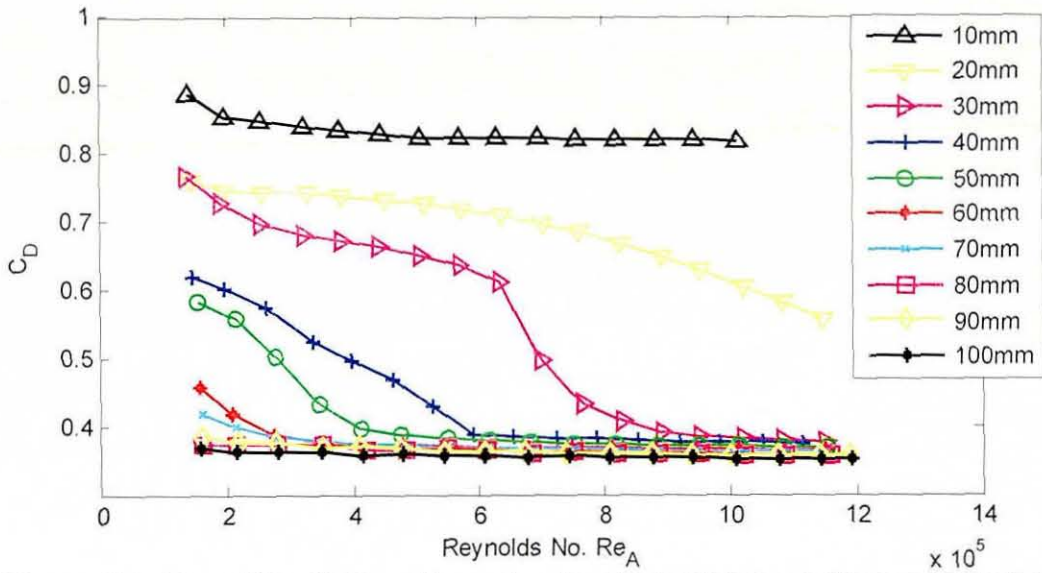
Figure 24 Variation of C_D with Reynolds number Re_A, Tu=1.45% (edge radius as a parameter)
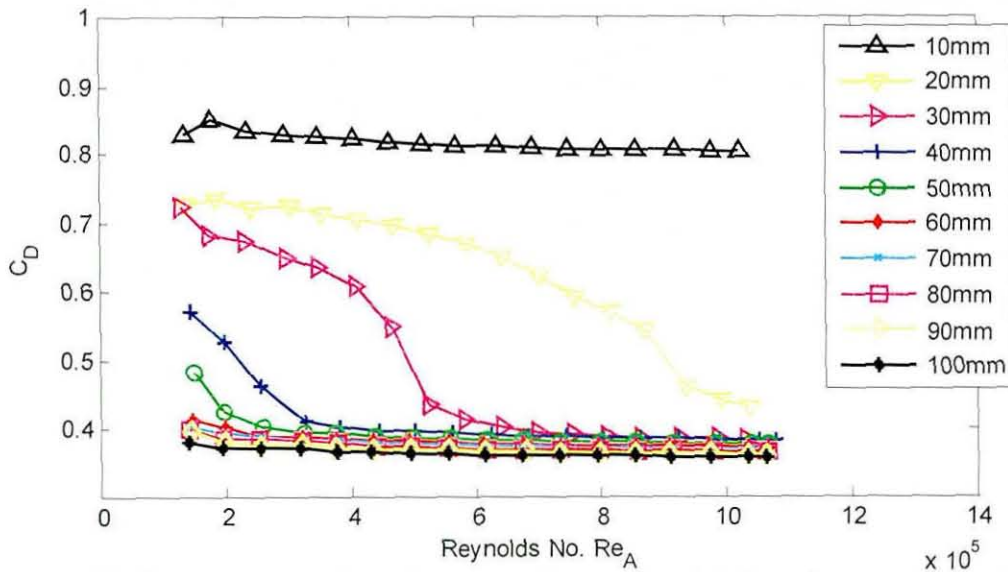
Figure 25 Variation of C_D with Reynolds number Re_A, Tu=3.41% (edge radius as a parameter)
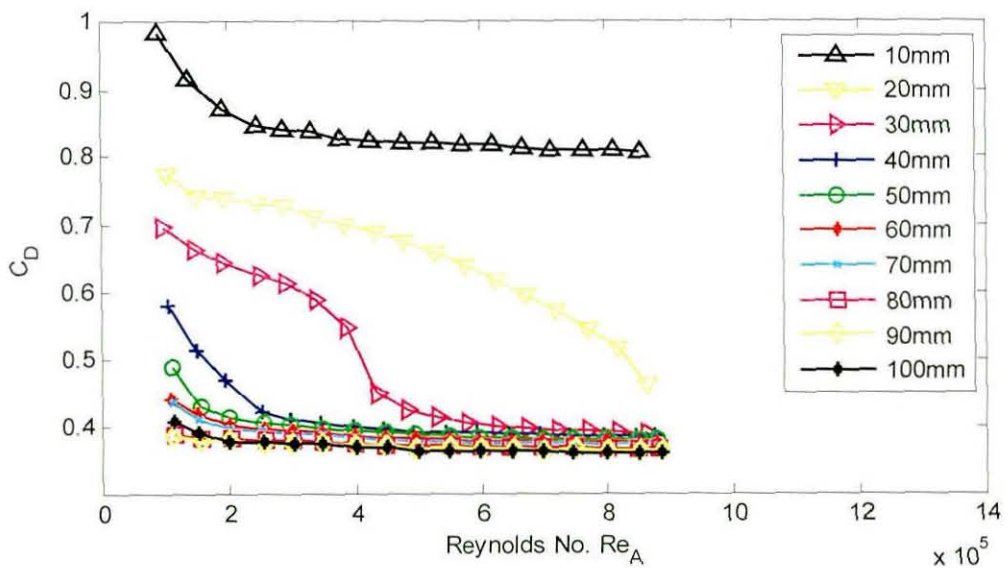
Figure 26 Variation of C_D with Reynolds number Re_A, Tu=5.13% (edge radius as a parameter)

Figure 24 to Figure 26 show the drag results as the level of freestream turbulence was increased. It is possible to see that the differences between the results at the raised turbulence levels are smaller than the difference between the clean tunnel results (Figure 11) and a small amount of additional freestream turbulence (1.38%, Figure 22).
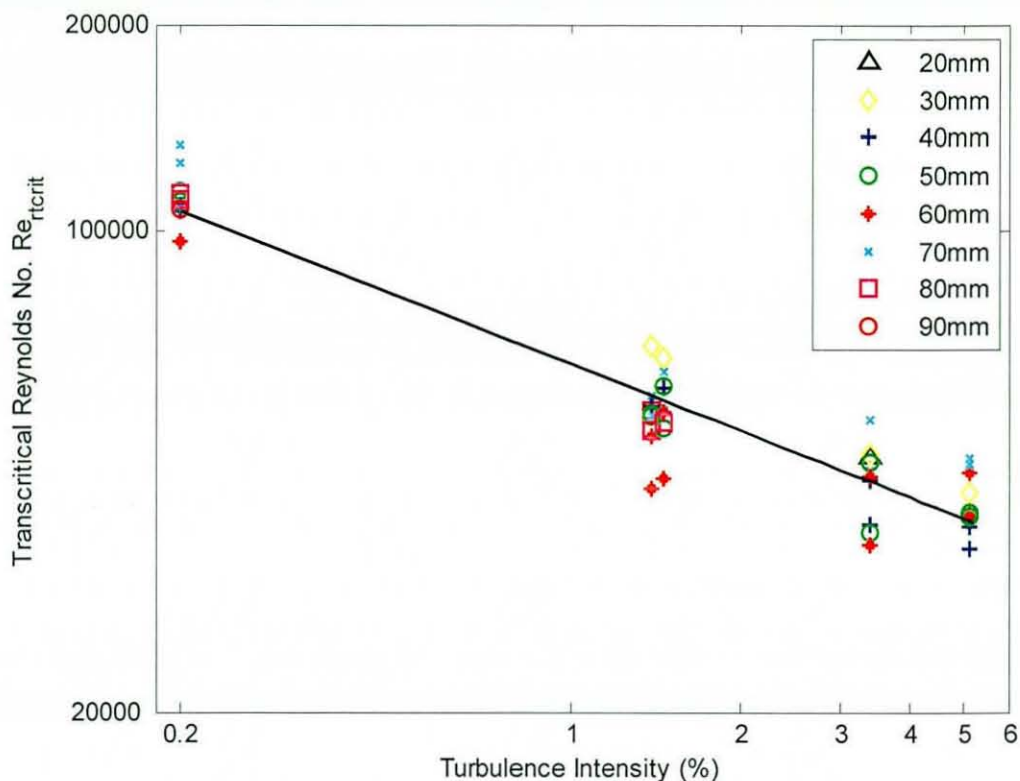
Figure 27 Comparison of transcritical Reynolds number at 0° yaw

The transcritical Reynolds numbers were calculated for all radii, where it was possible to accurately identify it, and the results plotted against turbulence intensity on a log-log scale in Figure 27. There is an inverse relationship between turbulence intensity and transcritical Reynolds number shown by the fit line, $Re_{rtcrit}=6.4*10^5*Tu^{-0.32}$. There are two sets of data for each grid on the graph, from two separate test weeks. Where data have not been plotted it is because the transcritical Reynolds number either did not exist, because transition did not occur for that radius in that turbulence intensity, or because the graph was so flat that it was not reasonable to claim to have identified a transcritical Reynolds number.

3.2.3.1   Effective Reynolds number

Wiedemann's argument [23] for the effect of turbulence is that it is analogous to a change in effective Reynolds number, and is based on finding the Reynolds number for a particular turbulence intensity where the drag coefficient of the model used fell to a

presented value (0.30). Wiedemann noted that the increase in turbulence intensity is likely to change the wall shear stresses, and thus increase the value of asymptotic C_D, although this was not seen in the results Wiedemann presented. It was shown that the magnitude of the change in effective Reynolds number was dependent on the scale of the model, and errors that moved the data away from the fit were either due to the model being too close to the grid, or due to interference with the collector of the open jet wind tunnel that was used. The argument of effective Reynolds number is intended to be an expedient way of testing a model scale vehicle under conditions that are analogous to full scale, by using raised levels of freestream turbulence. Wiedemann does not attempt to show that the change in effective Reynolds number is linear or valid over a range of Reynolds numbers, only that the model should reach the full scale drag coefficient at a lower Reynolds number than in the clean tunnel.

In the present study, the results presented in Figure 11 and Figure 22 to Figure 26 show that there is also an effect of turbulence on the way that C_D changes with Reynolds number, particularly in the transition region, where there is a change in the way the separation behaves, and the way transition to fully attached flow occurs. In the clean tunnel, there is a definite sharp corner point on the curve for the 40mm radius, which shows that the C_D falls quickly to the post-critical value and then becomes approximately constant from that point as Reynolds number increases. When the freestream turbulence level is raised, this transition becomes more gradual, more similar to the larger radii, where there is first a large fall in C_D and then a gradual reduction towards the post-critical value. The transcritical Reynolds number in these cases becomes more difficult to accurately identify.

Wiedemann aimed at optimising a vehicle at model scale, and stated that, using the freestream turbulence levels generated, it would be possible to optimise a vehicle as if at full scale at a Reynolds number (based on vehicle length) of $4.1*10^6$, using a 40% scale model. While this is not the aim of the present experiment, the fact that additional turbulence can be used to force transition for the 20mm radius (which would be 92mm if scaled up), as shown in Figure 25, would seem to back up this conclusion, although it is impossible to achieve such high Reynolds numbers in the Loughborough wind tunnel without causing significant blockage effects.

The change seen in the drag characteristic with Reynolds number leads to an alternative view, that of effective radius. It is highly unlikely that the curve for a particular radius in raised levels of freestream turbulence would match precisely to a different radius in the clean tunnel and so it is difficult to see how this concept could be used formally. However, ignoring the model scale and focusing on the Reynolds number based on edge radius as a point of comparison, it does appear that since both the transcritical Reynolds number and the characteristic have changed, that the change in effective radius is equal to the ratio of the constant transcritical Reynolds number Re_r between one level of freestream turbulence and another.

Taking the results for the clean tunnel and the first increased turbulence level, this would imply a doubling of effective radius, so that, for example, the 40mm front radius in the turbulent flow should show the same characteristic curve for drag with Reynolds number as 80mm front radius in the clean tunnel. Examining the figures shows that although the transcritical Reynolds numbers based on frontal area, the characteristic with Reynolds number and manner of transition are very similar, the C_D for the 40mm front is much higher in the pre-critical flow with increased freestream turbulence than the pre-critical C_D for the 80mm front radius in the clean tunnel. This is because of differences in skin friction and in the acceleration and pressure field around the radius. Therefore effective edge radius is not a complete explanation of the effect of increased turbulence, but it may be a useful concept for understanding how a particular radius will perform in increased freestream turbulence, even if the levels of C_D are not accurately matched.

3.2.3.2   Change in post-critical drag coefficient

To compare the effect of the freestream turbulence on the magnitude of C_D as Reynolds number changes, the results for all freestream turbulence levels for the 40mm front radius are shown in Figure 28. At low Reynolds numbers the addition of turbulence is seen to reduce the drag coefficient but above the transcritical value the drag coefficient is higher. Wiedemann [23] showed results that indicate that, where separations are reduced, there should be a reduction in C_D, and postulated that the wall shear stress would also increase, leading to an increase in asymptotic C_D. Cogotti [26] showed results for full scale vehicles that showed an increase in C_D when the level of freestream turbulence was increased, and Meier [42] also indicated that increased freestream

turbulence increases skin friction. Figure 28 indicates that for a simplified bluff body there is a reduction in C_D due to reduced separation at low Reynolds numbers, and an increase at high Reynolds numbers due to higher wall shear stresses.
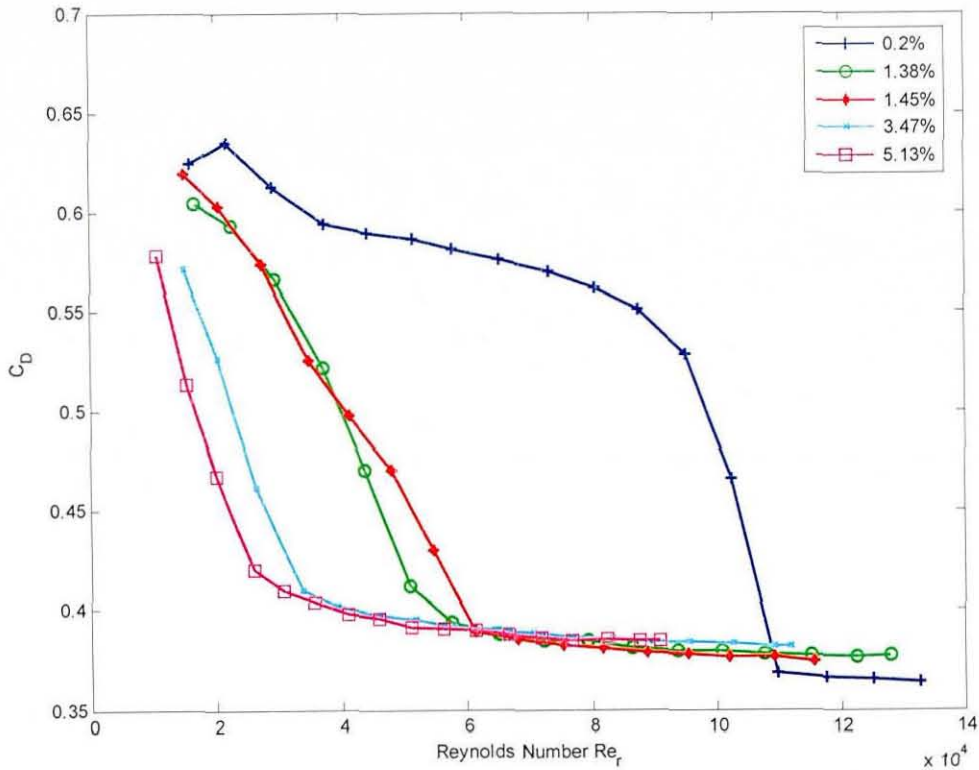
Figure 28 Comparison of drag coefficient variation at 0° yaw with Reynolds number based on edge radius (40mm front) (turbulence intensity as a parameter)

Figure 29 shows how the post-critical drag coefficient varies between different front sections in each turbulence case. It is clear that the larger the edge radius, the lower the drag, in all cases. As already discussed, the addition of freestream turbulence caused the post-critical drag to be higher. An important aspect of all the results is that increasing the freestream turbulence from 0.2% to the lowest additional level tested caused the largest change – the actual value of turbulence intensity over 1.38% only makes a small difference. From 0.2% to 1.38% is a factor of 7 times increase in turbulence, and from 1.38% to 5.13% is only a factor of 4 times increase, and so there is an indication in the results that the ratio of turbulence intensities is related to the change in post-critical C_D.

In Figure 30 the results are replotted as the change in drag coefficient over the clean tunnel value against turbulence intensity, which shows again that the lowest level of additional freestream turbulence makes the largest change to the results. It is of interest that despite having very similar turbulence intensities and length scales, the 1.38% and 1.45% grids produce consistently different results, with the 1.38% grid producing a

60

greater change than the 1.45% grid. The increase in post-critical C_D is shown to be reasonably independent of edge radius in the figure.
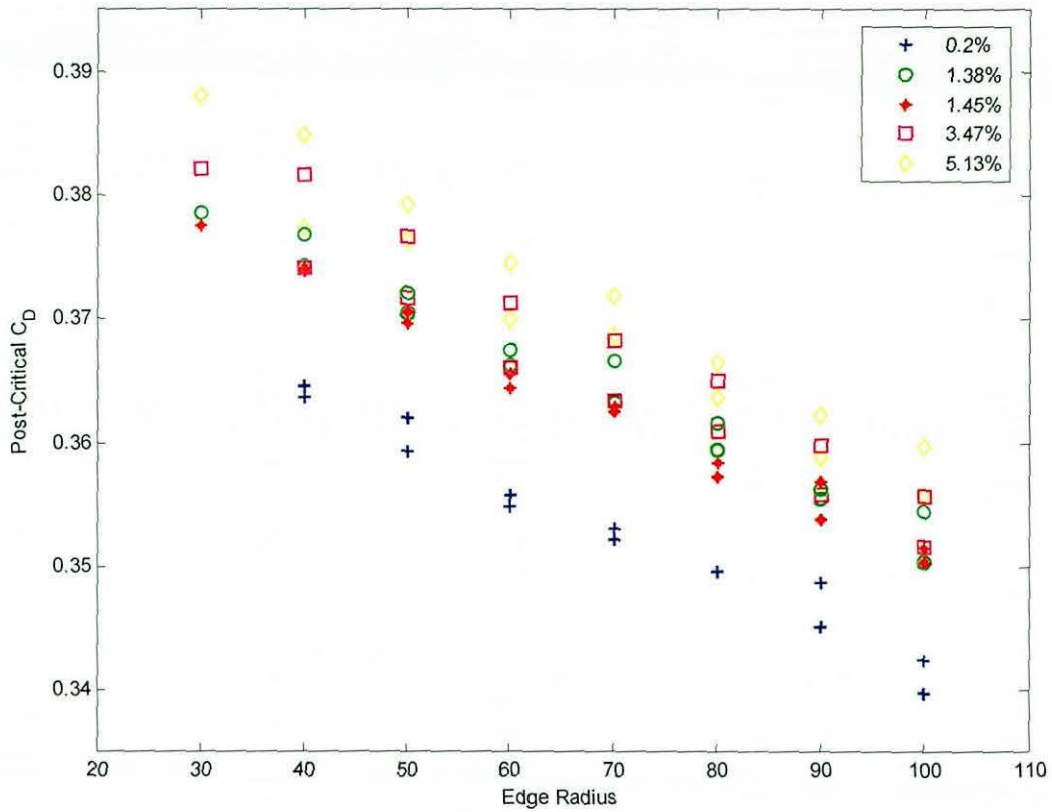
Figure 29 Variation of post-critical drag coefficient at 0° yaw with edge radius (Turbulence intensity as a parameter)
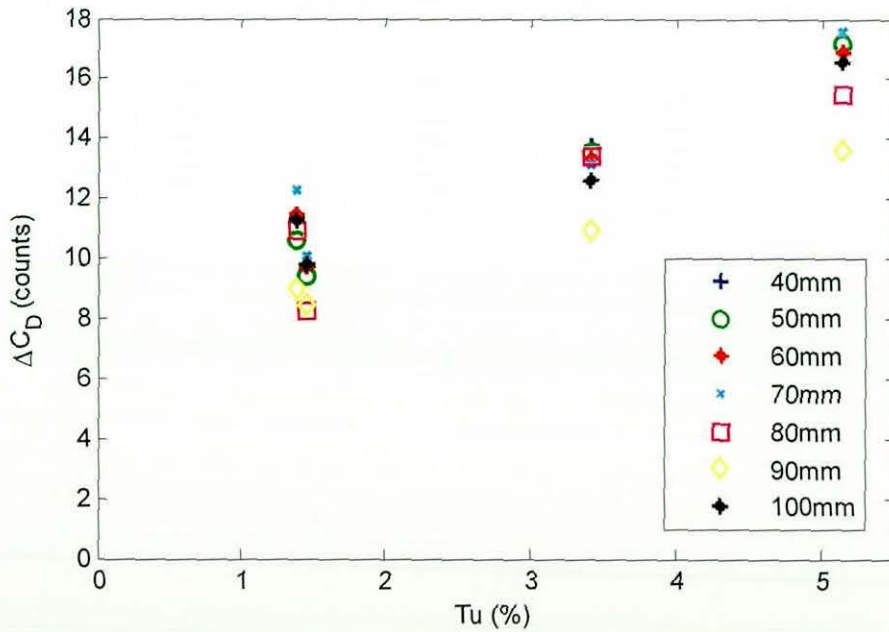
Figure 30 Change in post-critical drag coefficient with turbulence intensity (edge radius as a parameter)

3.2.3.3   Effect of yaw with additional freestream turbulence

Figure 31 shows the data collapse for all yaw angles for 1.38% freestream turbulence. The mean value of Re_{rtcrit} was recalculated to include all the data, and is slightly higher than for the zero yaw data only; $0.65*10^5$ instead of $0.54*10^5$.
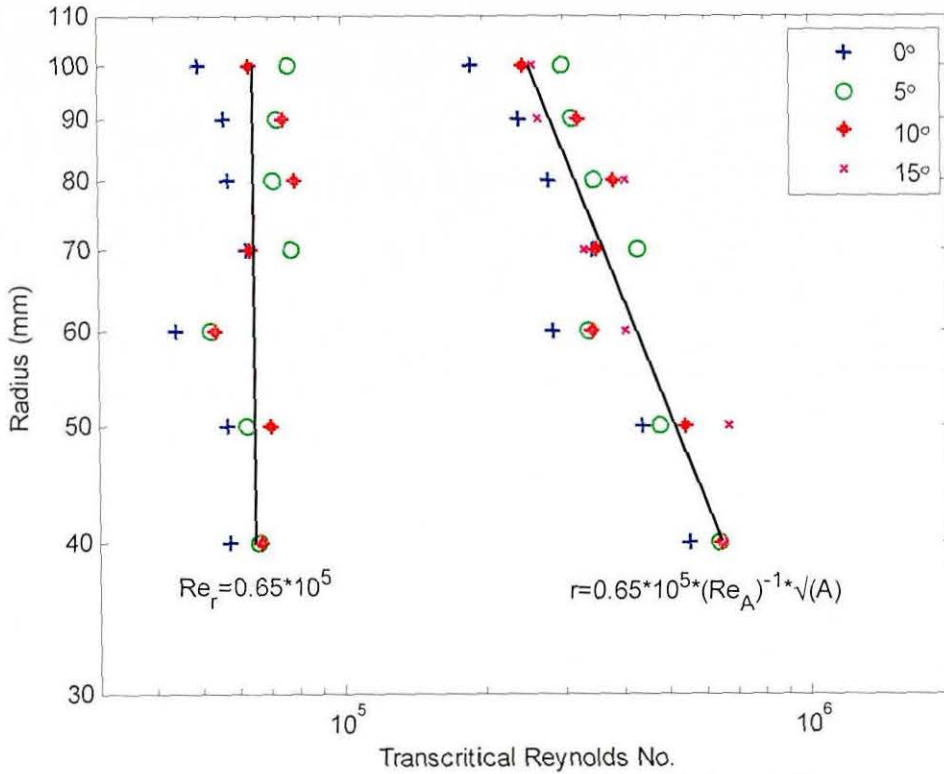
Figure 31 Collapse of drag data for the first turbulence grid
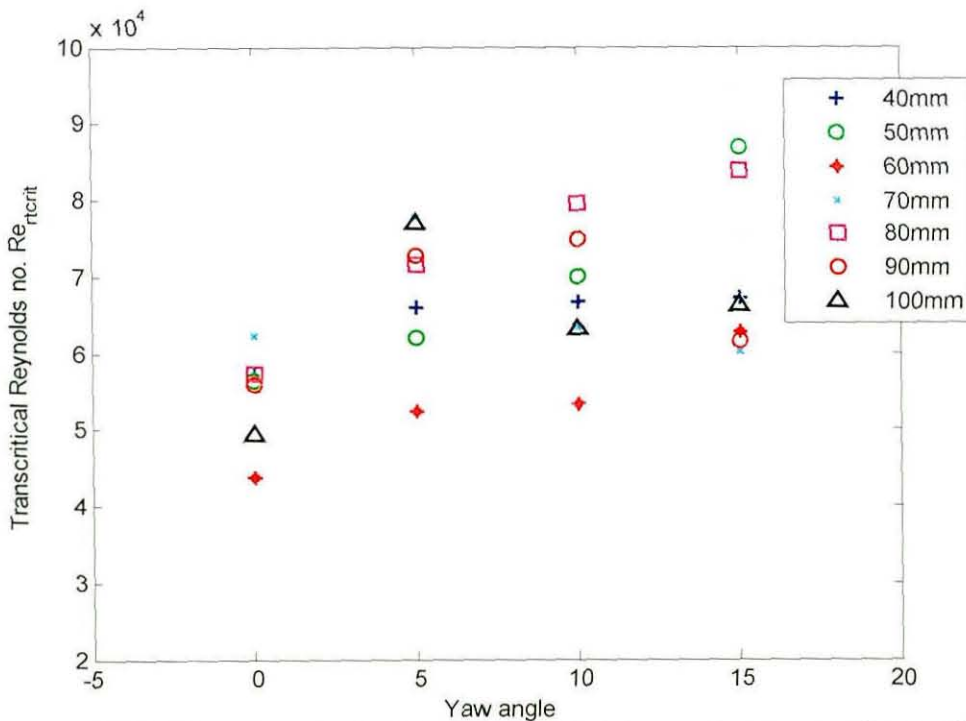
Figure 32 Variation of transcritical Reynolds number Re_{rtcrit} with yaw angle (Tu=1.38%)

62

Figure 32 shows the transcritical Reynolds numbers based on edge radius replotted against yaw angle. There is only a very weak trend in the results and it is not considered to be significant.

3.2.3.4 Hysteresis with additional turbulence

Figure 33 shows that the hysteresis loops that were very clear for the 40mm and 50mm front on Figure 11 are not evident even for the lowest level of additional freestream turbulence. This is another indication that the turbulence grid does not only increase the effective Reynolds number, but significantly alters the flow over the model. The PIV results in Chapter 4 clearly show the difference between increasing the turbulence level and increasing the Reynolds number. Hysteresis was not investigated for the smaller radii and they are therefore not included on this figure.
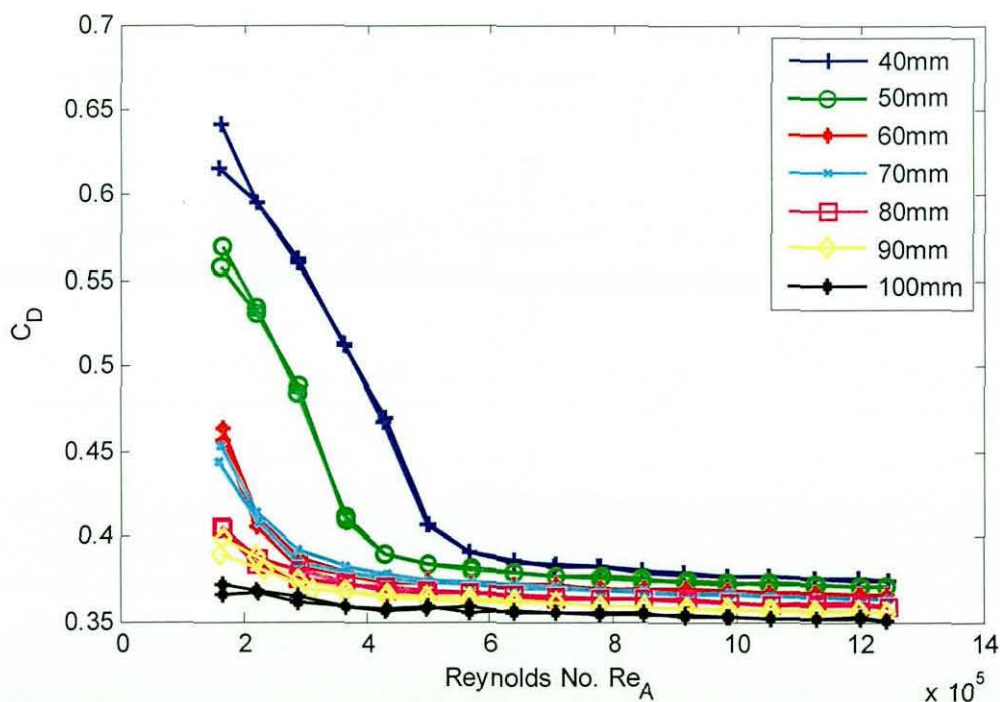
Figure 33 Variation of drag coefficient at 0° yaw with Reynolds number for the 1-box model, Tu=1.38% (Edge radius as a parameter)

It was suggested that the hysteresis was caused by the presence of a separated laminar boundary layer when increasing the Reynolds number, which then does not appear when Reynolds number is reduced, because the boundary layer tends to stay turbulent and attached when it has already been tripped by the higher speed running. With additional freestream turbulence, the shape of the graph is changed and there is no prolonged separation as Reynolds number increases for these radii.

3.2.3.5   Effect of raised freestream turbulence on base pressure

Increasing the freestream turbulence reduces the base pressure, contributing to the increase in post-critical C_D, as shown by the results for the 40mm front radius in Figure 34. Examining the other front sections shows the same effect, for example for the 30mm front radius in Figure 35. The 30mm front section undergoes a strong transition at all the raised turbulence levels, but increasing the turbulence intensity still reduces the post-critical base pressure, contributing to the rise in post-critical C_D.
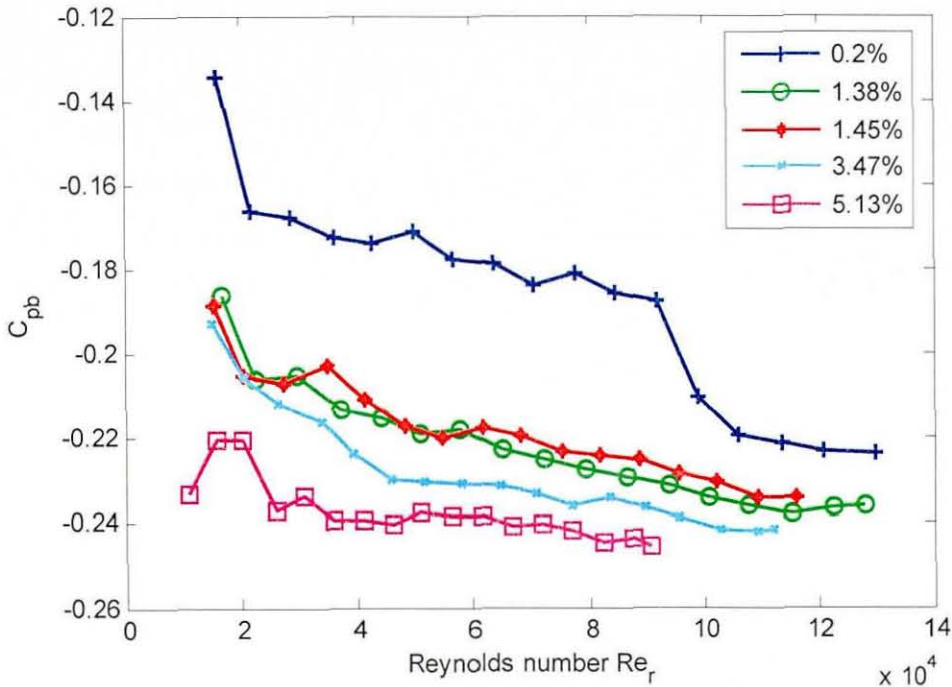
Figure 34 Base pressure comparison, 40mm front only, with turbulence intensity as a parameter

Figure 36 shows how the post-critical value of base pressure coefficient varies with turbulence intensity. There is a clear trend of reducing base pressure (increasing suction) with increasing turbulence, with the greatest reduction appearing on the smallest radii, and a greater additional change for the smaller radii as the turbulence intensity was increased. Bearman [16] reported that for a 3D body with a smooth front, there was no effect of turbulence on base pressure, and that where the body was short and blunt with separation, there was a reduction in the base suction (less negative). These results show an opposing effect, but the model is in ground effect, which will have a significant effect on the base pressure distribution when compared to the bodies in free air in Bearman's studies, and the PIV results (Chapter 4) show that when there is separation on the front of the model, there is also reattachment along the sides, which

was also not the case for Bearman's short blunt bodies. The base pressure distribution is further investigated in Section 3.4.2.
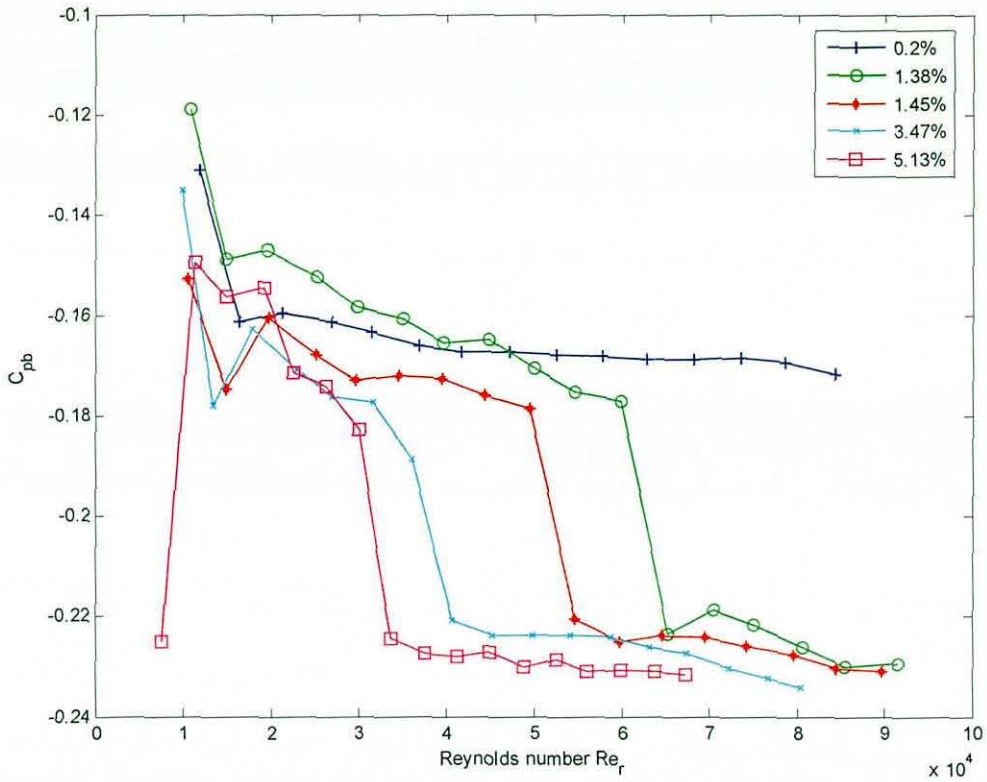
Figure 35 Base pressure comparison, 30mm front only, with turbulence as a parameter
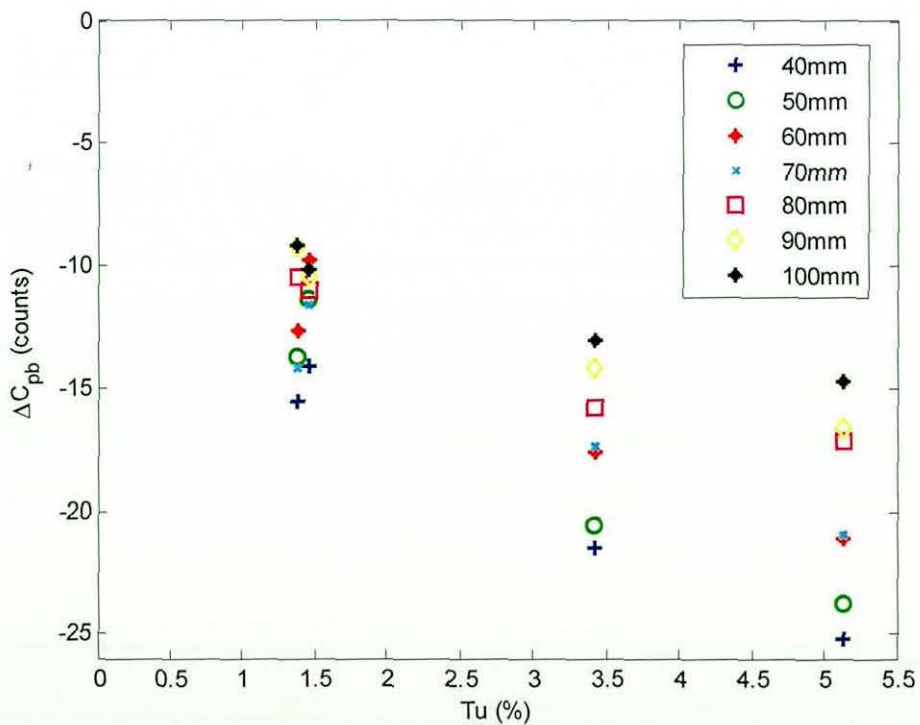
Figure 36 Change in post-critical base pressure coefficient with turbulence intensity

3.2.4 Summary of results with increased freestream turbulence

- The transcritical Reynolds number based on edge radius was found to remain constant for a particular level of freestream turbulence, but was reduced by increasing freestream turbulence. The inverse relationship $Re_{rtcrit}=6.4*10^5*Tu^{-0.32}$ was found to match the results.

- The concept of an effective Reynolds number was found to be an inadequate description of what happens when the freestream turbulence level is increased. Instead, effective edge radius was proposed as a more representative model. It was shown that this concept gave a fair representation of the change in the trend of drag with Reynolds number at different turbulent intensities, but did not capture the difference in the values of C_D between one radius at an increased turbulence intensity and its equivalent in the clean tunnel.

- The post-critical C_D was shown to increase with increasing turbulence intensity. The increase was reasonably independent of edge radius and was shown to depend on the ratio between turbulence levels.

- As in the clean tunnel, no significant trend in transcritical Reynolds number with yaw angle was seen.

- The hysteresis loops that were seen in the clean tunnel were damped out completely by increased turbulence.

- Increasing the turbulence intensity caused an increase in base suction (more negative base pressure) indicating that some of the increase in drag is caused by this change in the pressure field, as well as an increase in skin friction.

3.3 The effect of turbulence on lift

3.3.1 Clean tunnel lift results

Figure 37 shows the total lift coefficient (C_L) results at zero yaw. The curves are not as simple and distinctive as the drag coefficient results, and there is no obvious constant value for transcritical Reynolds number. It is possible that there may be competing effects between the front and rear of the model. In order to investigate this, and to look for a correlation with the drag results, the front and rear lift results are calculated using Equation 6.
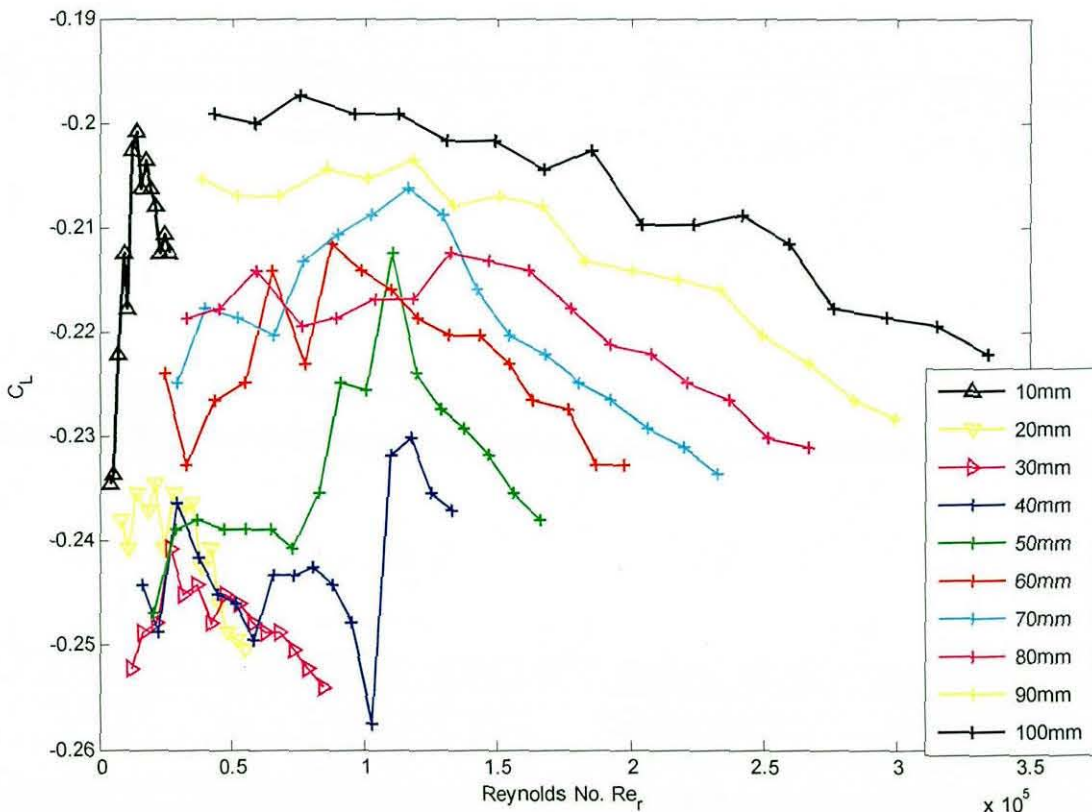
Figure 37 Variation of lift coefficient at 0° yaw with Reynolds number based on edge radius (Edge radius as a parameter)

$$C_{LF} = \frac{C_L}{2} + C_{MY} \qquad\qquad C_{LR} = \frac{C_L}{2} - C_{MY} \qquad\qquad \text{Equation 6}$$

where C_{LF} = front lift coefficient
C_{LR} = rear lift coefficient
C_{MY} = pitching moment

The transition from pre- to post-critical behaviour is now clear in both the front (Figure 38) and rear (Figure 39) lift results. It is possible to identify transcritical Reynolds numbers for the front lift coefficient (C_{LF}) using the same method as for drag. The rear lift coefficient (C_{LR}) shows a similar pattern of clear pre-critical, transitional and post-

67

critical flows. The smaller radii, 10mm-30mm, do not undergo transition, just as was the case for the drag results. However, they do follow the same pre-critical trend as the other radii, and, separated into front and rear lift coefficients, the results are relatively flat and consistent, while the overall lift coefficient trends appear less steady.
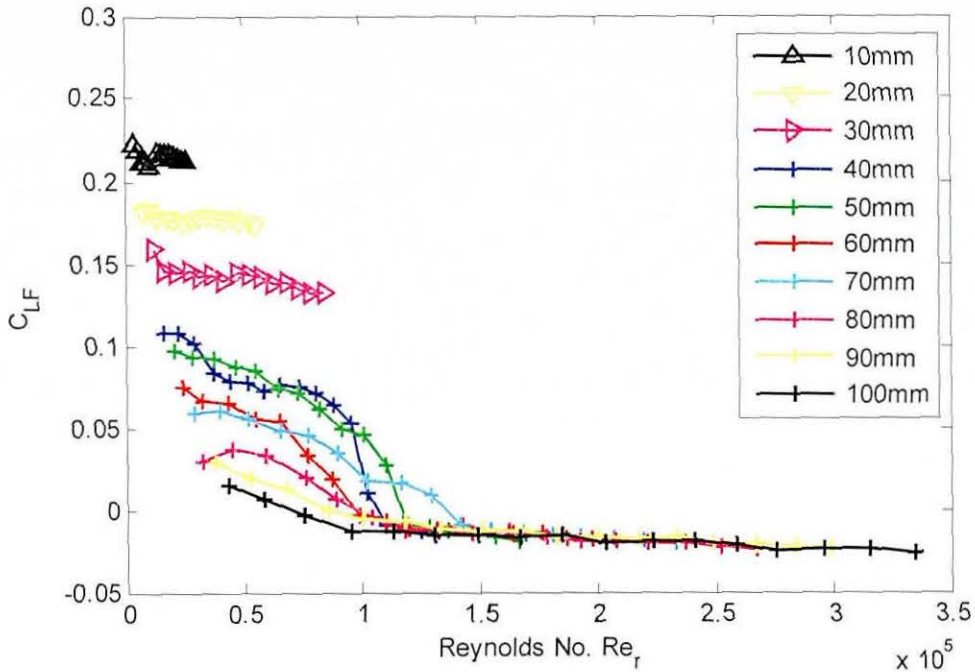
Figure 38 Variation of front lift coefficient with Reynolds number based on edge radius (edge radius as a parameter)
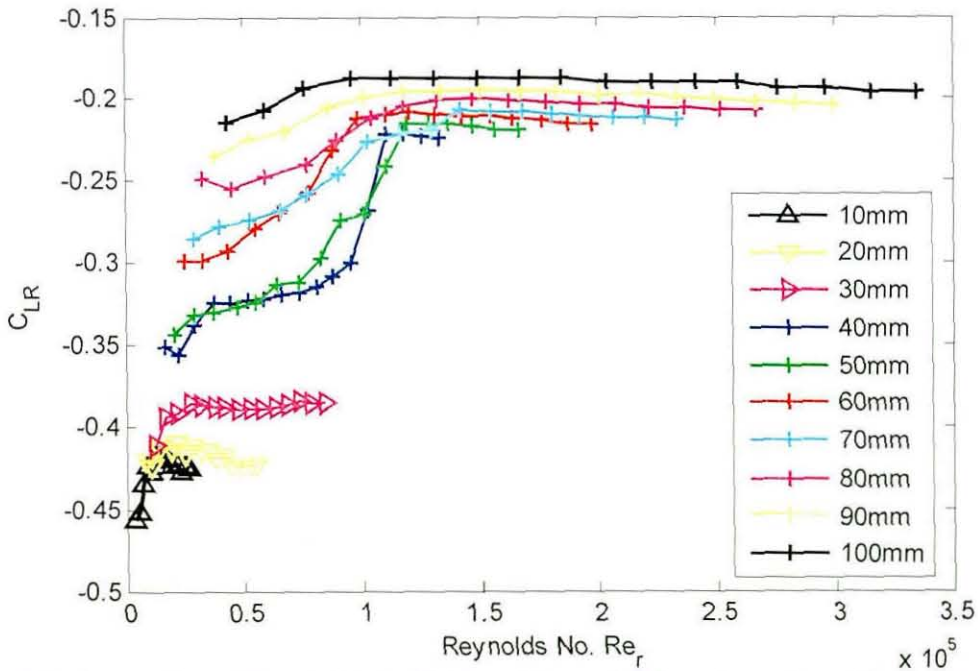
Figure 39 Variation of rear lift coefficient with Reynolds number based on edge radius (edge radius as a parameter)

The reduction in front lift with increasing Reynolds numbers must come from a change in the pressure recovery after the radius, and this is shown in the centreline pressure results in Figure 47.
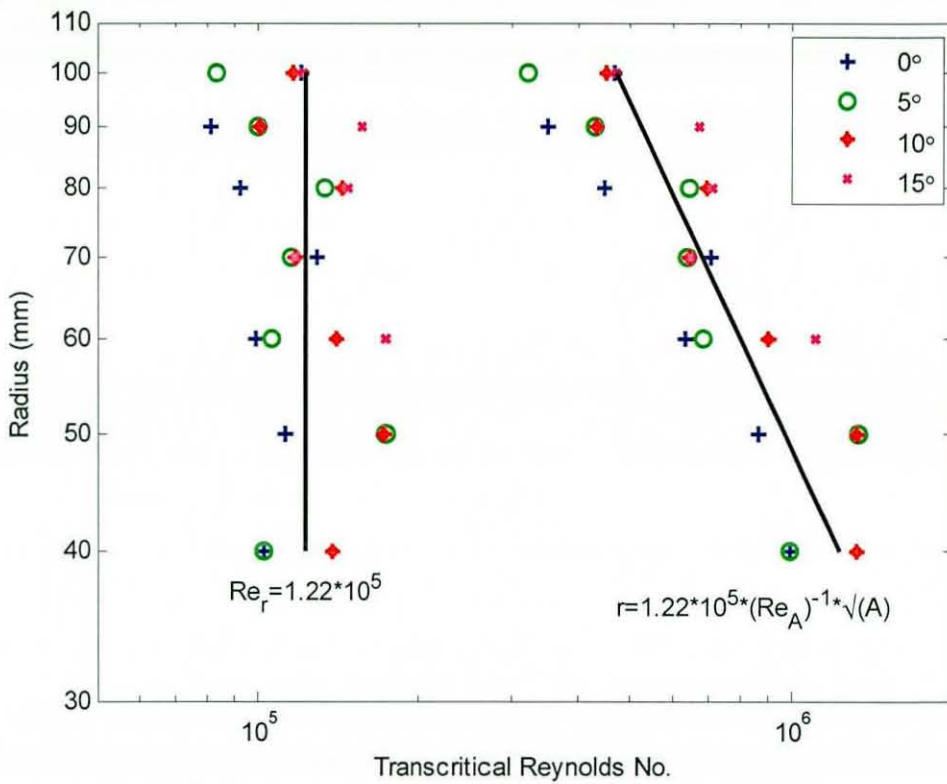
Figure 40 Collapse of front lift coefficient for the clean tunnel (C_{LF})
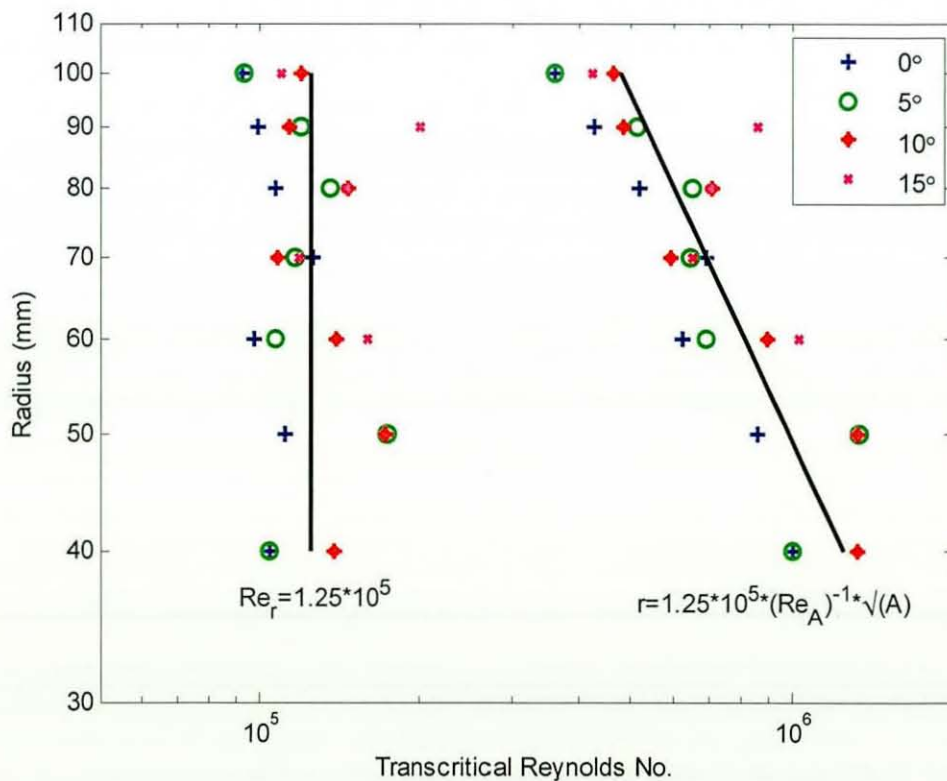
Figure 41 Collapse of rear lift coefficient for the clean tunnel (C_{LR})

Figure 40 and Figure 41 show the collapsed data for front and rear lift, for all yaw angles. In comparison with Figure 18, there is a similar amount of spread in the results, and many individual points on the drag results match with corresponding individual points in the lift results. This shows that the transition in the flow affects lift and drag for a given Reynolds number in a similar way.

The constant values obtained by least square analysis match well with those obtained for the drag data and are given in Table 7.

Coefficient	Least squares average Re_{rtcrit}
C_D	$1.14*10^5$
C_{LF}	$1.22*10^5$
C_{LR}	$1.25*10^5$

Table 7 Comparison of transcritical Reynolds numbers for drag and lift coefficients

3.3.2 Lift coefficient results with increased freestream turbulence

The results of the addition of turbulence for a single radius are shown in Figure 42, split as for the clean tunnel results into front and rear coefficient. The changes in front and rear lift are opposite in sign. The results show similar trends to the drag coefficient, in that additional freestream turbulence reduces the transcritical Reynolds number. The values of Re_{rtcrit} were calculated for all the radii using the same method as before, and the results are shown in Table 8. The results are similar to the drag results in Table 6.
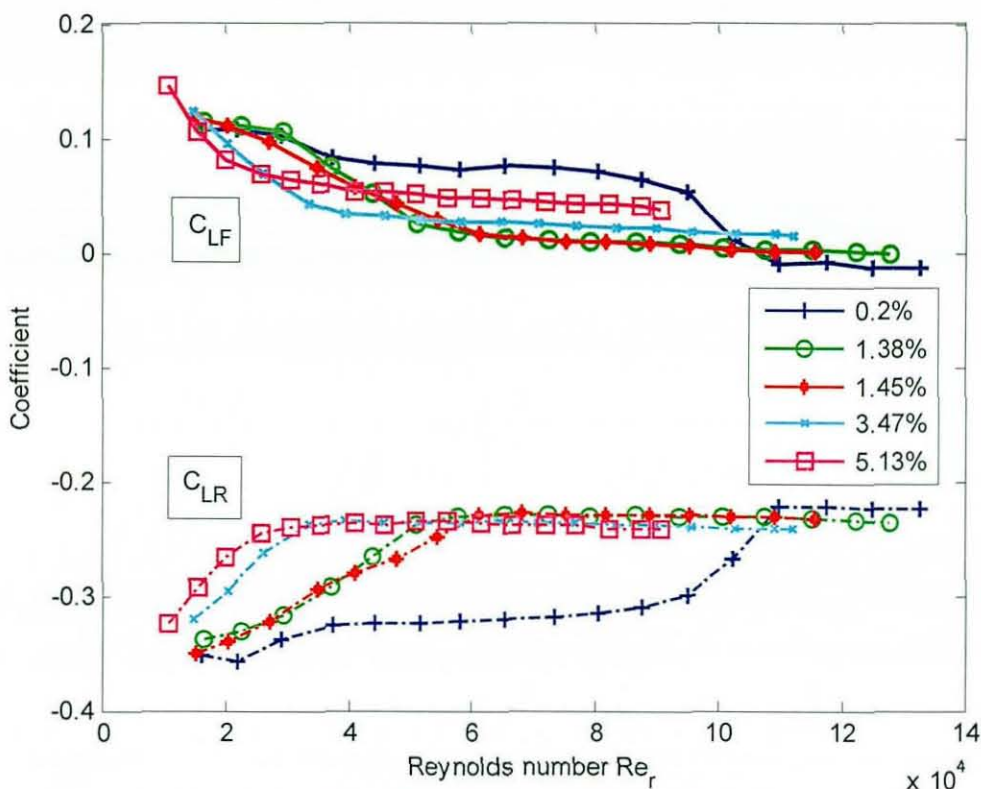
Figure 42 Comparison of front and rear lift coefficients at 0° yaw with Reynolds number based on edge radius (40mm front)

Tu (%)	C_{LF} Re_{rtcrit}	C_{LR} Re_{rtcrit}
0.2	$1.02*10^5$	$0.98*10^5$
1.38	$0.56*10^5$	$0.60*10^5$
1.45	$0.52*10^5$	$0.54*10^5$
3.41	$0.40*10^5$	$0.59*10^5$
5.13	$0.32*10^5$	$0.32*10^5$

Table 8 Variation in front and rear transcritical Reynolds number with turbulence at 0° yaw

There is also a clear change in the post-critical values of front and rear lift coefficient with additional freestream turbulence. Post-critical rear lift (Figure 44) is reduced by adding turbulence, and post-critical front lift (Figure 43) is increased – in other words, the magnitude of the coefficient always increases.
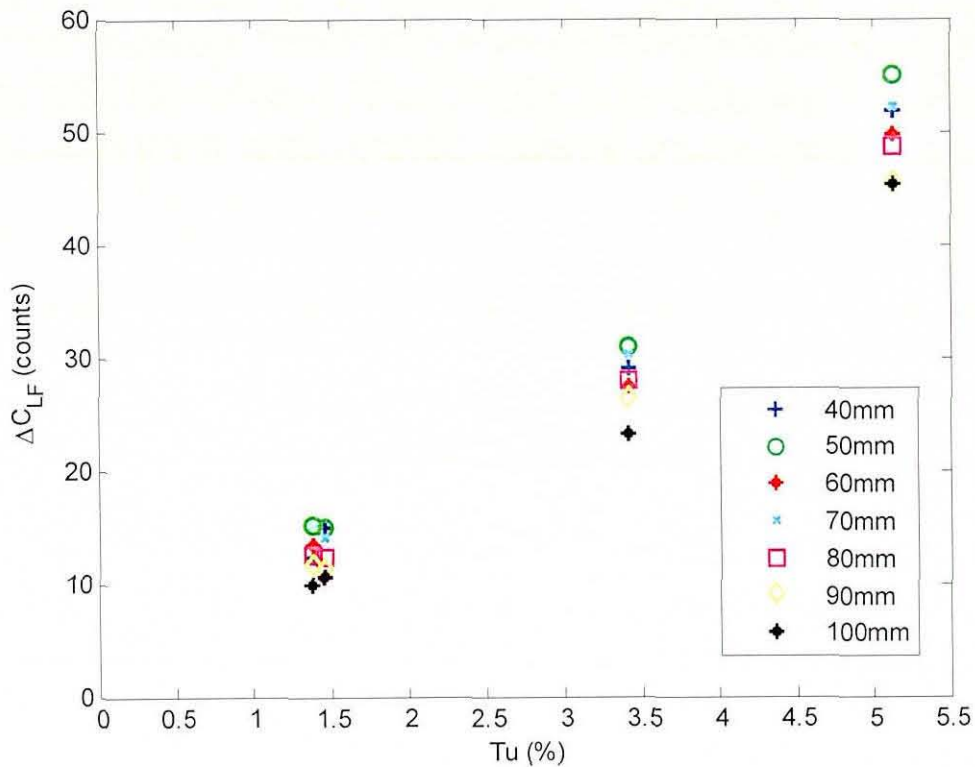
Figure 43 Change in post-critical C_{LF} with additional freestream turbulence

In the drag results, it was seen that adding any small amount of additional freestream turbulence made more difference than further increasing the turbulence level (Figure 30), but for the front lift this is not the case, as the changes are more progressive. The front lift is highly affected by changes in the flow around the top radius, and in the centreline pressure results it will be seen how the pressure distribution is affected by the additional turbulence.

The change in rear lift coefficient is much smaller with the largest change occurring when the turbulence was increased to 1.38% (although increasing it to 1.45% gives a significantly smaller shift over the baseline result), with further increases in turbulence only resulting in a small additional reduction, as was the case for the drag results. The changes at the rear are likely to be driven by changes in the front stagnation point.
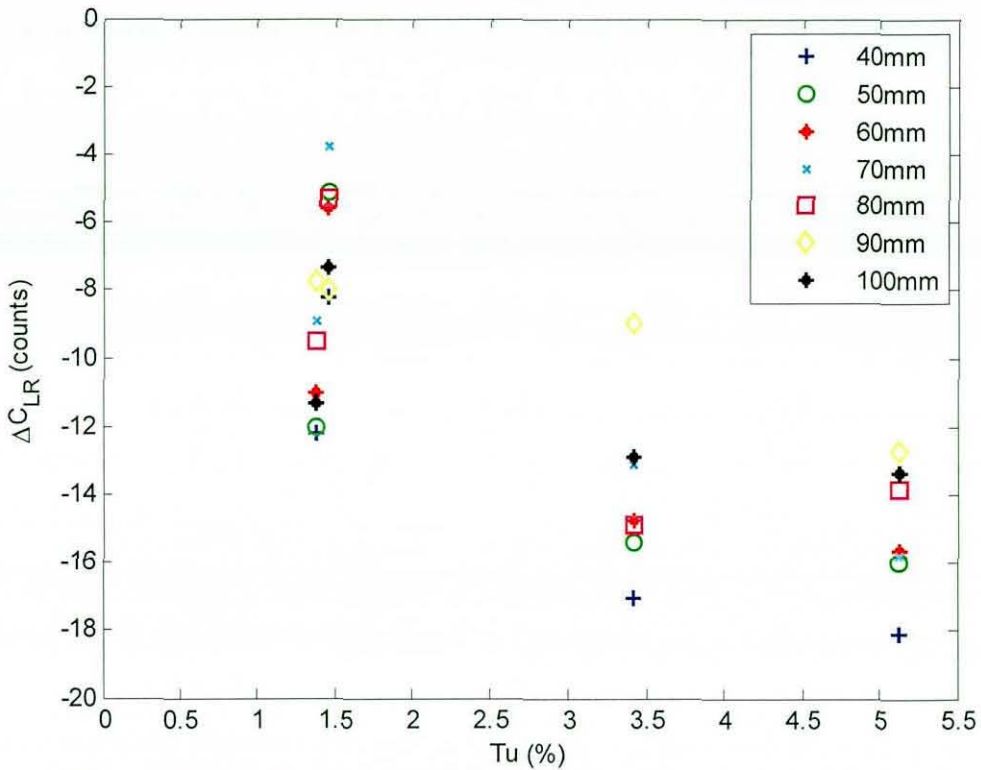
Figure 44 Change in post-critical C$_{LR}$ with additional freestream turbulence

3.3.3   Summary of the lift results

- In terms of the change in Re$_{rtcrit}$ and the effect of the additional turbulence on post-critical front and rear lift coefficients, the lift results broadly show the same effects as the drag results.

- The most significant effects occur around the front of the model, as would be expected, with additional effects at the rear of the model that most likely arise from shifts in the front stagnation point position.

3.4   The effect of turbulence on the centreline pressure distribution

A line of pressure tappings was installed on the centreline of the model, in order to capture the detailed pressure distribution around the radius, and the pressure recovery region on the roof. Tests were conducted on the 30mm, 40mm and 100mm radii, at 20m/s, 30m/s and 40m/s. The two small radii were chosen because they cover the full range of different flow regimes believed to exist on the model, and the 100mm front section provides a control result where no separation is expected – since the 100mm front section has shown very little variation in drag or base pressure trends, it should give similarly unaffected pressure curves. The tapping locations for the 40mm radius are shown in Figure 45. The static reference was located in the roof of the tunnel in line with the base of the model, because it was not possible to use the upstream pitot tube when it was upstream of a turbulence grid, due to the pressure drop across the grid. The pressure coefficients are therefore reported as blockage corrected values.
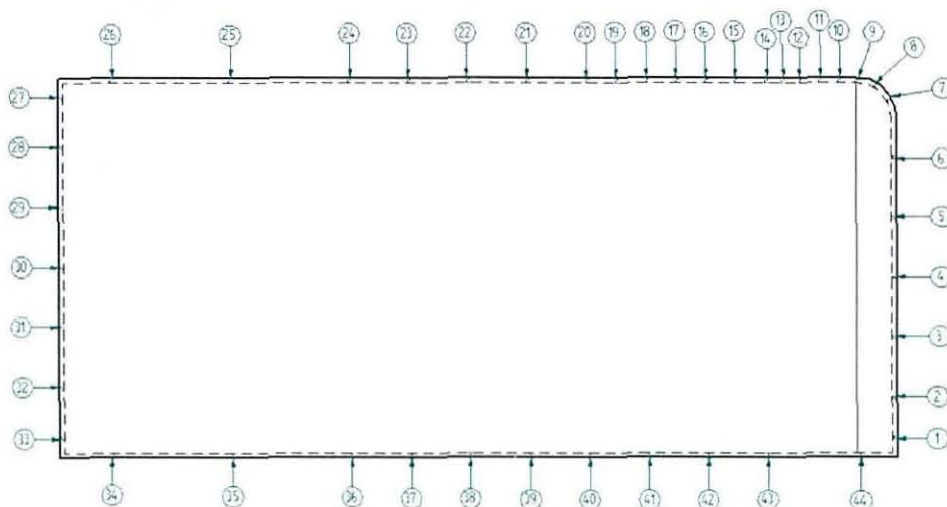
Figure 45 Tapping locations on the 1-box model with the 40mm front section installed

From the drag results (Figure 11, Figure 22, and Figure 24 to Figure 26) it was expected that the speeds chosen would show separated and reattached flows for the clean tunnel and turbulence grids, depending on the edge radius and Reynolds number.

3.4.1   Effect of turbulence on the top surface pressure distribution

Figure 46 shows the results for the 30mm radius in the clean tunnel. The drag results indicated separated flow, with a C_D of 0.69 at 20m/s, 0.68 at 30m/s and 0.67 at 40m/s. The pressure results show strong evidence for this, as can be seen by the shape of the distribution, which has a region of suction over a large length of the upper surface with a suction peak downstream of the edge radius itself.

74
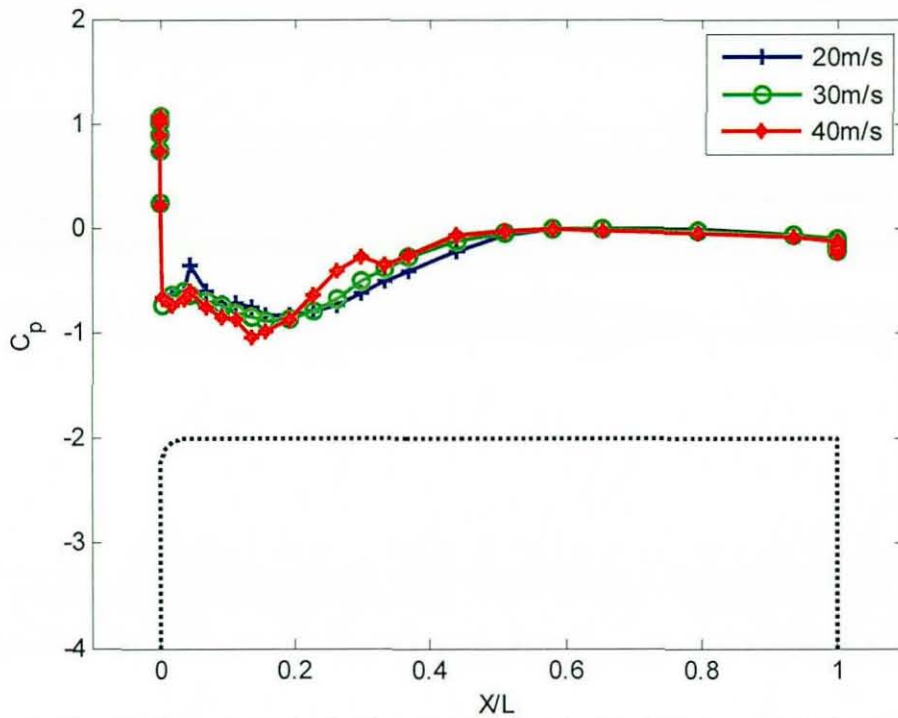
Figure 46 Top surface C$_p$ results for the 30mm radius in the clean tunnel (windspeed as a parameter)

Along with the relatively low magnitude of the peak suction (compared to the figures that follow), this general shape is a characteristic of the pressure distribution under deliberately separated flowfields that appear in the literature (e.g. Li and Melbourne [19]). It is not possible to determine the reattachment point from pressure results, but it can be clearly seen that the pressure recovery length reduces with increasing windspeed (and therefore Reynolds number). The peak recorded pressure coefficient on the front face of the model for this radius in the clean tunnel was slightly greater than 1, which is likely to be due to the static reference location and some experimental error.

Figure 47 shows the same radius but with the turbulence intensity raised to 1.45% (the results for 1.38% turbulence are very similar). Here, the separation still occurs at 20m/s, but by 30m/s there is a large suction peak on the radius. For comparison, the C$_D$ at 20m/s was 0.65, at 30m/s 0.43 (in the end of the critical region on the graph), and at 40m/s 0.38. Hucho [43] states that the suction peaks are much smaller for separated flows, so the deep suction at 30m/s indicates that a significant change has occurred in the flowfield, so that the flow is either fully attached or only intermittently separated. The pressure recovery length becomes much shorter after this strong suction, and does not change significantly with Reynolds number, but the peak suction increases at 40m/s.

There is, therefore, some further change in the flow around the radius that is indicated by the increase in suction and the decrease in C_D from 0.433 to 0.381.
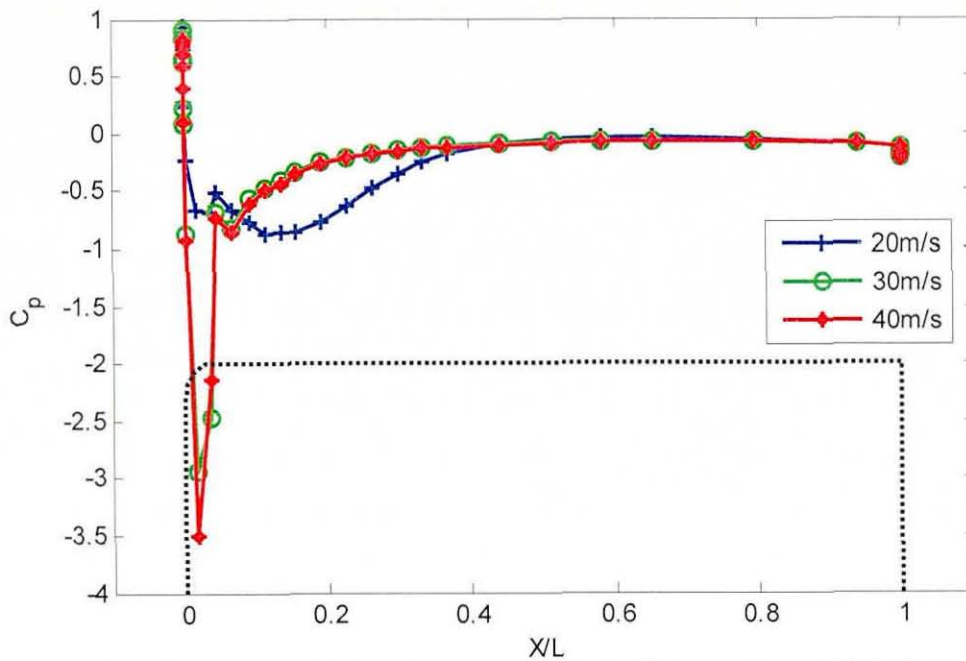
Figure 47 Top surface C_p results for 30mm radius with 1.45% turbulence grid (windspeed as a parameter)
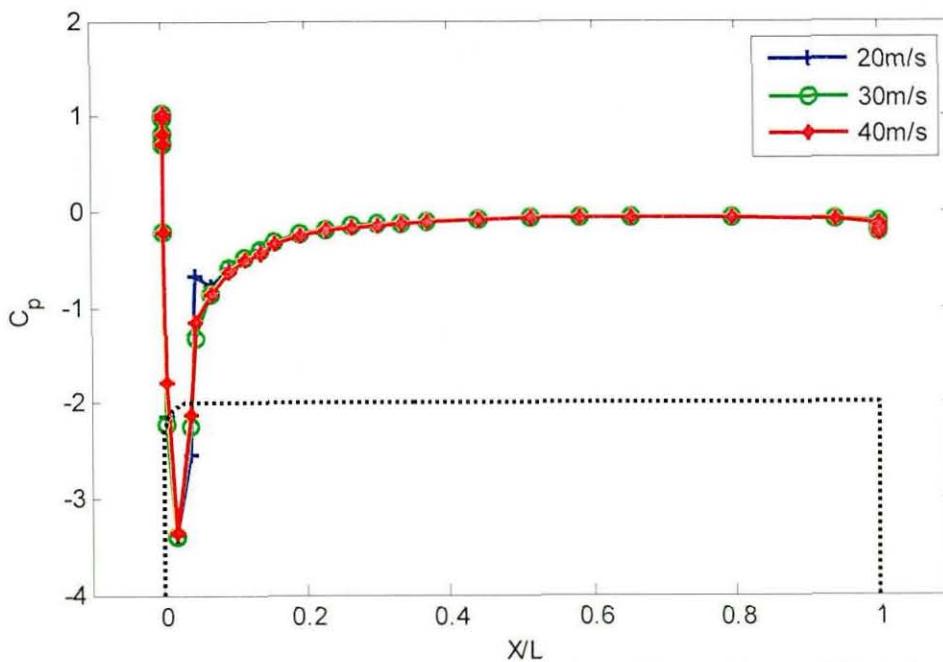
Figure 48 Top surface C_p results for the 30mm radius with 3.41% turbulence grid (windspeed as a parameter)

In Figure 48 the results are shown for the 3.41% turbulence grid. In this case there is a deep suction around the radius at all speeds indicating attached flow. There is a small kink in the curve just at the point where the radius finishes, when the speed was 20m/s, which is also shown in Figure 47 at 30m/s. The repeatability of this feature in different

turbulence conditions at different speeds indicates that it is not caused by a blocked tapping but is typical of a highly localised flow separation occurring where the radius stops and the flat top or side of the model begins. At this point on the model there is a discontinuity in the second derivative of the surface function.
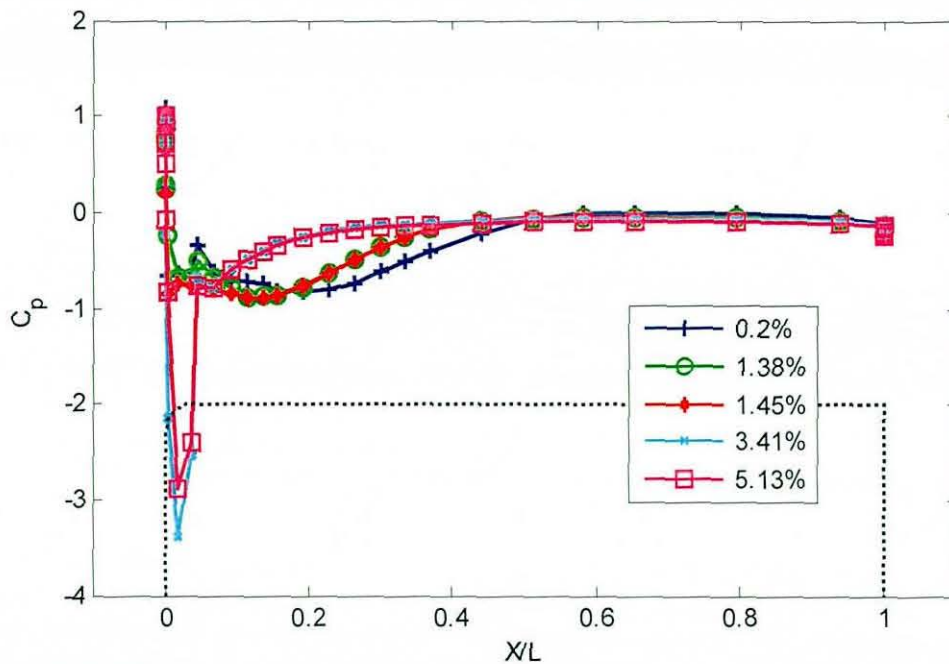
Figure 49 Top surface C_p results, 30mm radius at 20m/s with body profile shown (Tu as a parameter)

In order to directly compare the changes caused by different levels of freestream turbulence, Figure 49 shows the variation in C_p with longitudinal position at 20m/s for the 30mm radius with turbulence intensity as a parameter. The Reynolds number Re_r is $0.41*10^5$. In the separated cases (0.2% - 1.45% turbulence) the results follow those of Hillier [18], Saathoff [44], Li and Melbourne [19] and others, in that increased turbulence caused a reduction in the size of the separation bubble and an increase in the magnitude of the suction peak. Additional turbulence (3.41% and 5.13%) causes the flow to become fully attached around the radius, although as before it may display a small separation at the point where the radius stops.

For the same radius but at 30m/s (Figure 50) the Reynolds number is now sufficiently high ($Re_r=0.61*10^5$) that the flow is fully attached or only intermittently separated for all values of additional turbulence. The small kink at the end of the radius, that is characteristic of a local separation, appears for turbulence intensities of 1.38% 1.45%, and 5.13%, but not for 3.41%. For comparison, the drag coefficient was 0.433 at 1.45% turbulence, 0.390 in 3.41% turbulence and 0.392 in 5.13% turbulence. Some of the

reduction in C_D between 1.45% and 3.41% could come from this area of the model, but a change of 2 counts of drag is too small to draw a significant conclusion for the higher level of turbulence. There is also an increase in base suction (more negative) between 3.41% and 5.13% contributing to the drag change that will be shown in the next subsection.
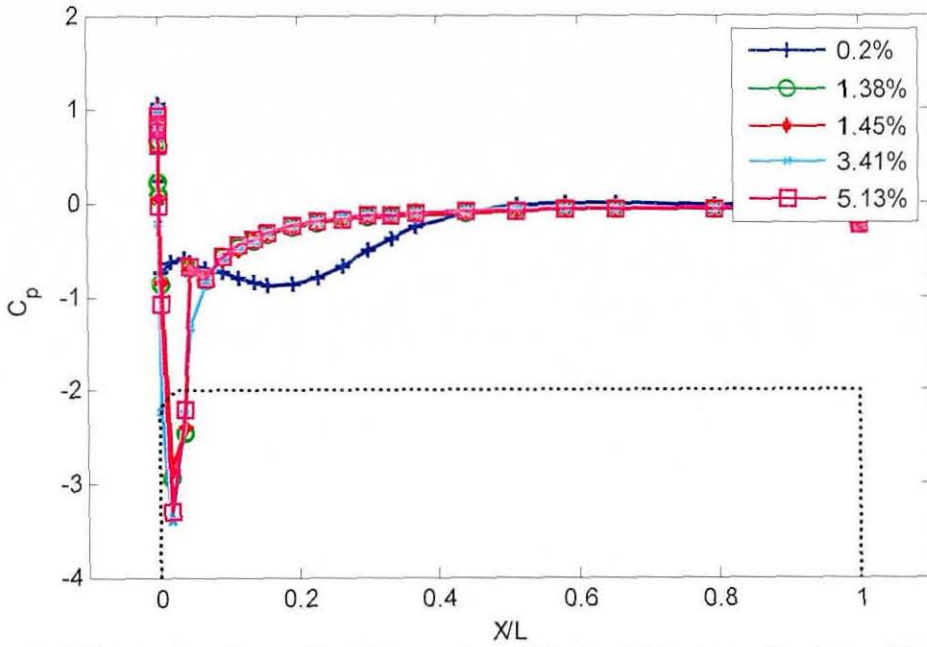
Figure 50 Top surface C_p results, 30mm radius at 30m/s with body profile shown (Tu as a parameter)
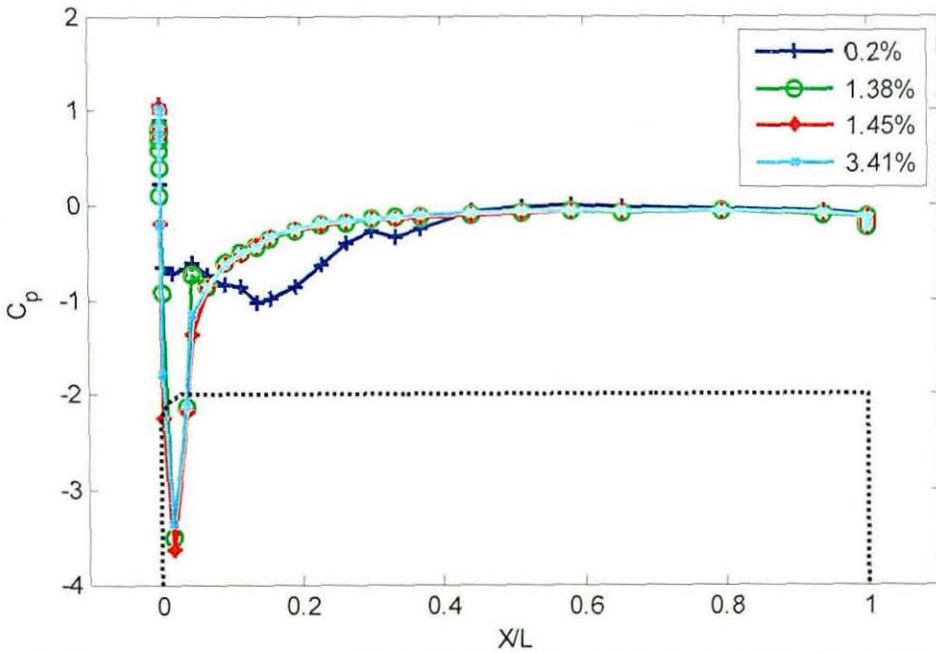
Figure 51 Top surface C_p results, 30mm radius at 40m/s with body profile shown (Tu as a parameter)

Figure 51 shows that broadly the same results occur at 40m/s ($Re_r=0.82*10^5$). No result is presented for 5.13% turbulence because it is not possible to run the tunnel at 40m/s with that grid installed. The C_D results are, for 0.2% turbulence 0.670, for 1.38% turbulence, 0.383, for 1.45% turbulence, 0.381 and for 3.41% turbulence 0.382. The drag coefficients are almost exactly the same in increased turbulence, and so are the pressure distributions. The drag reduction between 0.2% turbulence and the increased levels comes from the change from a separation on the radius to no or almost no separation, causing the large suction peaks on the radius that give rise to an increased component of pressure force pointing in the direction of travel, as well as strongly affecting the front lift. There is also some evidence of a change in the C_p over the rear half of the top surface between the clean tunnel and the turbulence grid results, which is due to a larger boundary layer in the separated case (Section 4.4.2).
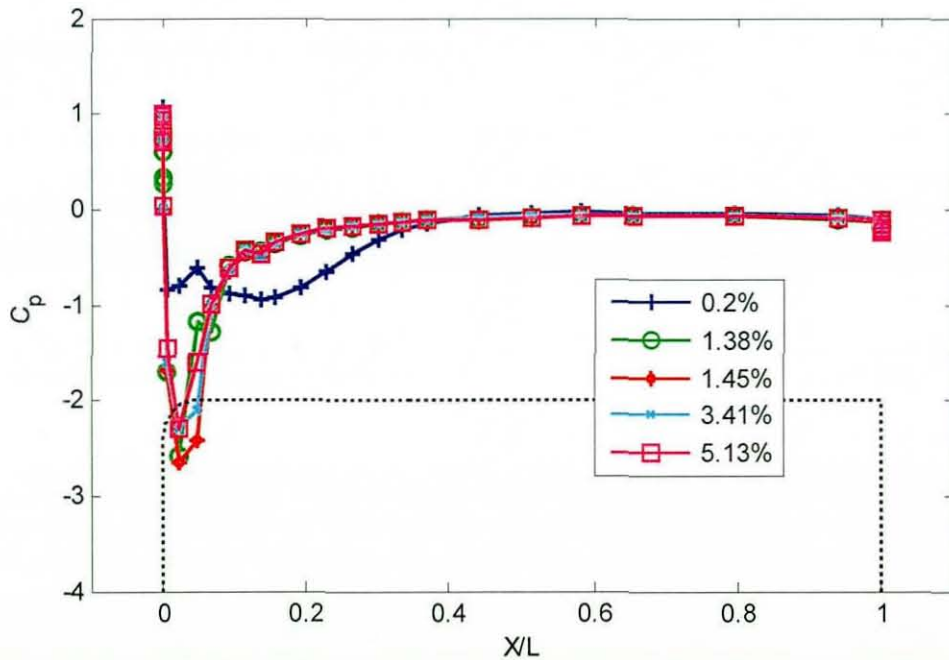
Figure 52 Top surface C_p results, 40mm radius at 30m/s with body profile (Tu as a parameter)

Figure 52 shows the results for the 40mm front radius at 30m/s. As expected, it is similar to the 30mm front radius at the same Reynolds number, but the acceleration over the front section is reduced, making the suction peak smaller in value but over a larger surface area. As for the 30mm front section, there is a separation shown at 0.2% turbulence, and then the flow is attached when the level of freestream turbulence is raised. This was expected from the C_D results as before.

For comparison, the pressure distribution over the 100mm radius is shown in Figure 53 at 30m/s. It is clear that a radius this large must have fully attached flow, and so it is seen in the figure. There is a suction peak on the radius which is then recovered as the flow moves downstream, with some variation in the pressure recovery and precise location of the suction peak with turbulence intensity. The differences between the curves are small, and so is the variation in C_D – in order of increasing turbulence, the drag coefficients for the 100mm radius at 30m/s are 0.347, 0.357, 0.355, 0.360 and 0.360, which show an initial increase due to skin friction and then almost no change with increasing turbulence, at this speed.
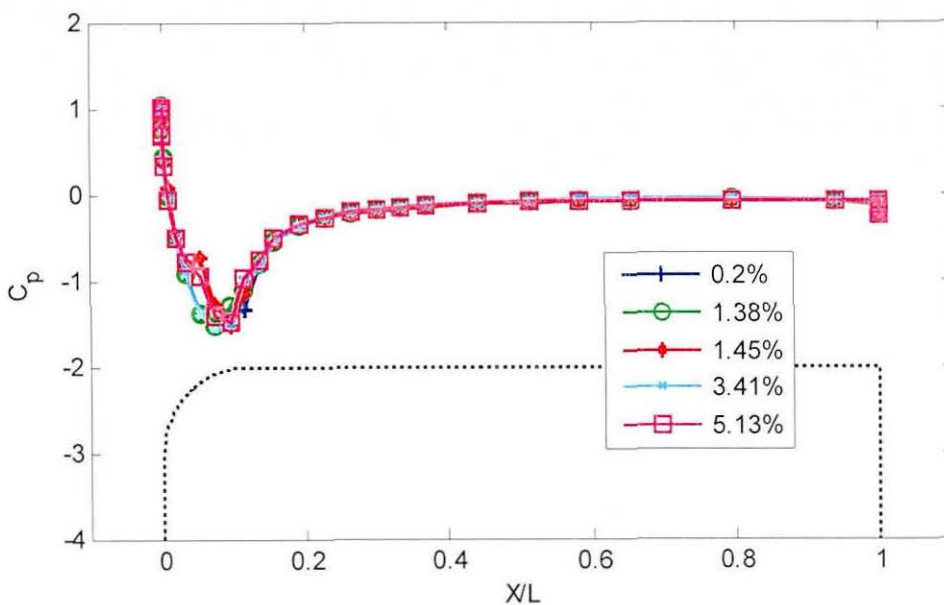
Figure 53 Top surface C_p results, 100mm radius at 30m/s with body profile (Tu as a parameter)

3.4.2   Base pressure distribution

The base pressure distribution shows a different perspective to the results from the average of 5 centrally placed tappings in Sections 3.2.1.2 and 3.2.3.5. The effect of the ground becomes clear, and it is shown that there is a difference between the effect of Reynolds number and turbulence on the top half of the model and the bottom half.

Figure 54 illustrates how the base pressure distribution changes for the 30mm front radius in the clean tunnel with increasing Reynolds number. The curves are typical of a road vehicle in ground effect, showing more suction between $Z/H = 0$ to 0.5 than between 0.5 and 1 due to the flow acceleration under the model. The base pressure distribution is similar at 20 and 30m/s, and at 40m/s the suction from $Z/H = 0$ to 0.7 becomes deeper. This repeats the result from the previous base pressure measurement

80

that showed an increase in base suction with increasing Reynolds number (increasing the base drag). From the top surface distributions it is known that for this radius there is a separation on the radius for all speeds tested in the clean wind tunnel configuration.
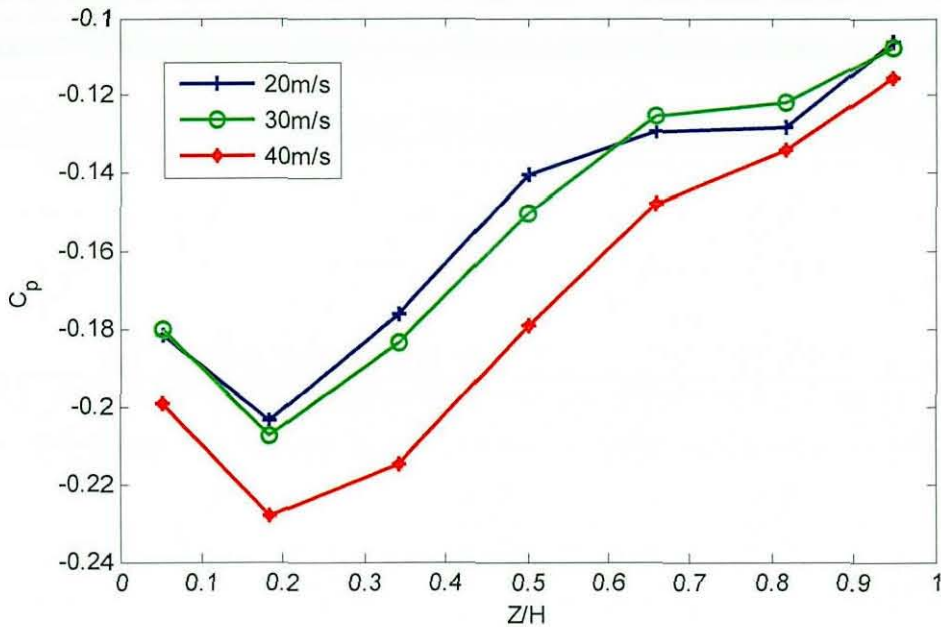
Figure 54 Variation in base pressure with vertical position for the 30mm radius in the clean tunnel (windspeed as a parameter)
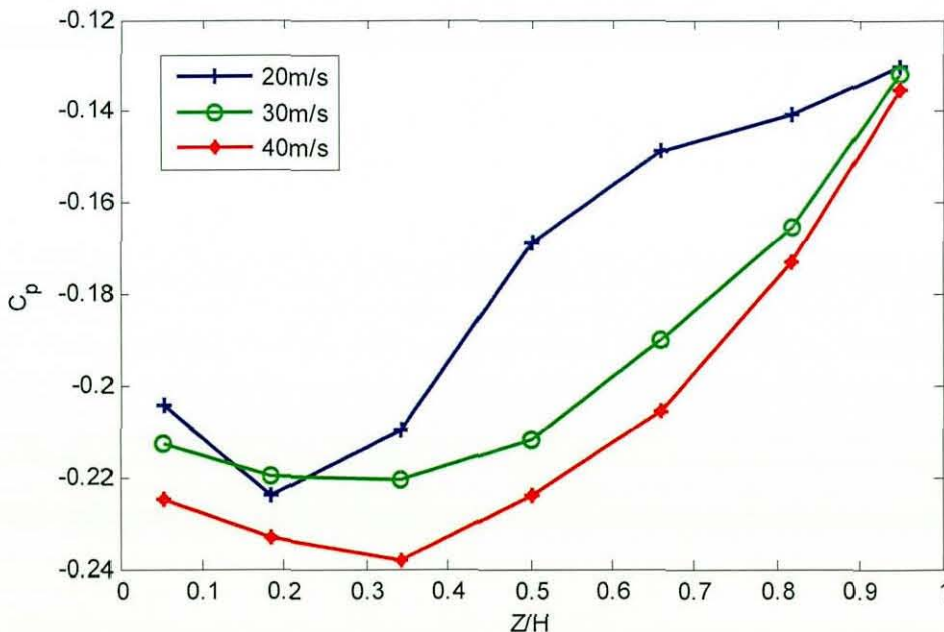
Figure 55 Variation in base pressure with vertical position, 30mm radius in 1.45% turbulence (windspeed as a parameter)

Figure 55 shows the base pressures with the turbulence intensity increased to 1.45%. Again referring to the over-body distribution (Figure 47), the flow shows a separation at 20m/s and then becomes attached or intermittently separated by 30m/s. The shape of the curve becomes quite different, with a much deeper suction over the top half of the base

(Z/H=0.4 to 1). Since this deeper suction is the result of a fully attached flow with a corresponding thin boundary layer, the comparatively reduced suction at 20m/s implies that even if the boundary layer reattaches, there is still a considerable thickened boundary layer developed by the separated region which persists as the flow moves downstream, which encourages mixing in the base and reduces the suction. This is seen in the PIV results in Section 4.4.
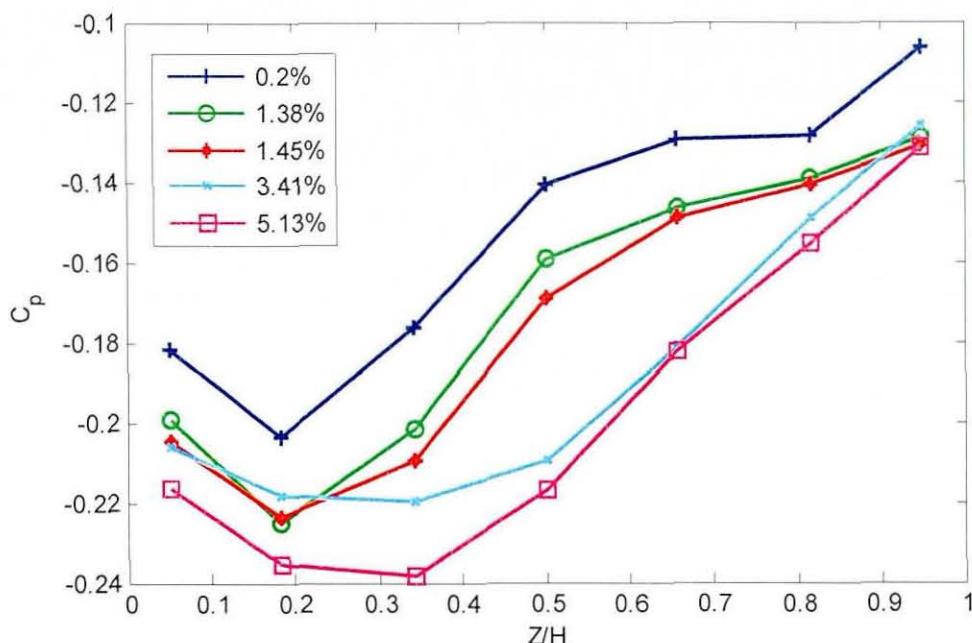
Figure 56 Variation in base pressure with vertical position, 30mm radius at 20m/s

Figure 56 shows the variation in the base pressure distribution for the 30mm radius at 20m/s as turbulence intensity changes. As has been previously seen for the upper surface results, the flow is separated in the clean tunnel, and for 1.38% and 1.45% turbulence, but becomes attached when the turbulence intensity reaches 3.41%. There is a clear progression in the curve as the turbulence intensity increases – the suction increases a little at the bottom of the model (Z/H=0 to 0.4), and when the flow becomes attached, it increases significantly at the top (Z/H=0.45-0.8). These changes appear to be similar to the changes caused by increasing the Reynolds number both in the clean tunnel and for the 1.45% grid, but the curves with the highest turbulence levels do not quite become the smooth parabolas that are shown for 30m/s and 40m/s at 1.45% in the figure above (and also for the 40mm radius in the clean tunnel at higher Reynolds numbers). This is because the 30mm radius is in the critical region at 20m/s even in 5.13% turbulence, as shown by Figure 26 and so there is still some intermittent separation around the radius.

82

Figure 57 shows the results at 30m/s. The flow is now attached at all increased levels of freestream turbulence, and there is a corresponding similarity in the distributions. There is evidence of a trend with turbulence in the base pressure near the top edge of the box, where a small amount of turbulence has had a large effect on the suction, but increasing turbulence further has brought the suction back towards the clean tunnel result. This could be a result of increased boundary layer thickness, as the clean tunnel base pressure here is the result of a thickened boundary layer that has propagated downstream from the separation on the leading edge radius. At the bottom-most point measured, there is very little difference in the base pressures once the turbulence intensity was raised from the clean tunnel result.
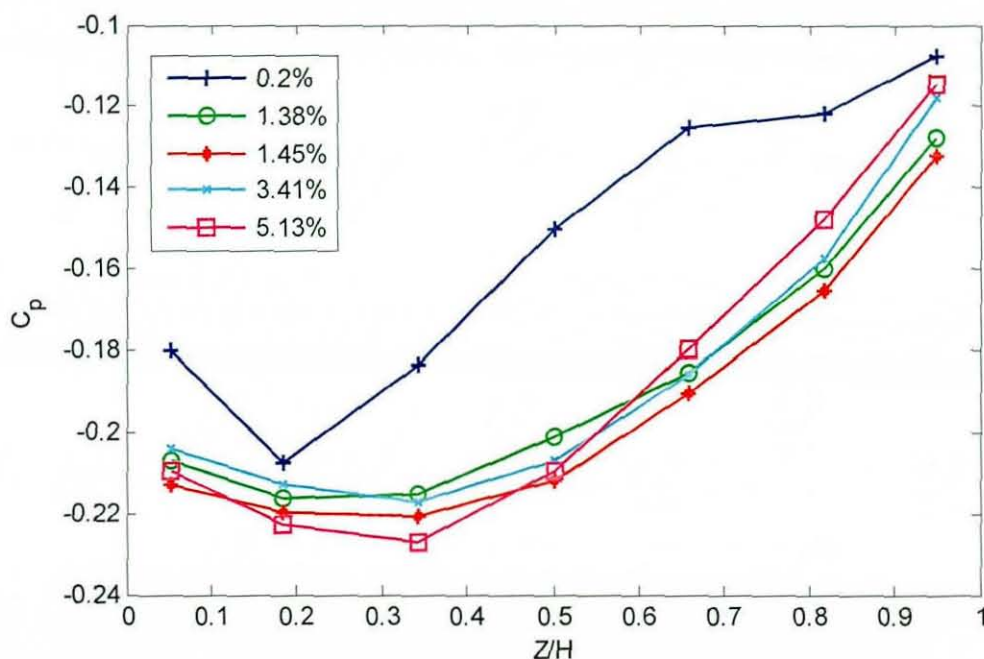
Figure 57 Variation in base pressure with vertical position, 30mm radius at 30m/s

Increasing the speed to 40m/s (Figure 58) shows a very similar pattern to that at 30m/s, with the result (expected from Figure 54) that increasing the Reynolds number has further reduced the suction near the bottom of the model.

The results for the 100mm front radius at 30m/s (Figure 59) show the base pressure distribution where the flow is fully attached around the front radius. This figure also shows the trend of a reduction in the suction near the top of the model when the turbulence intensity was raised above 1.4%.
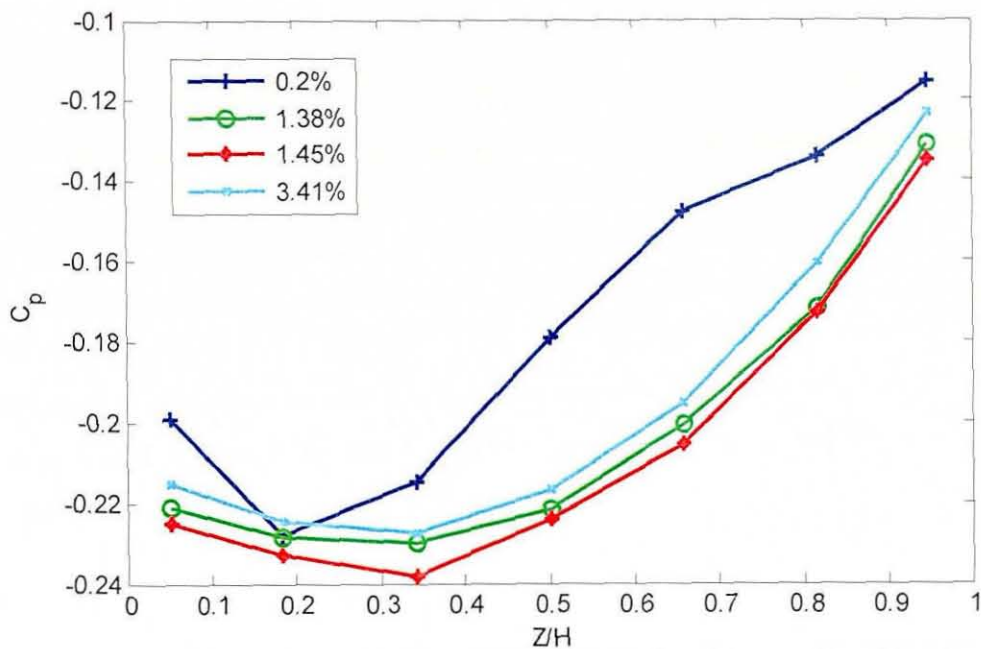
Figure 58 Variation in base pressure with vertical position, 30mm radius at 40m/s
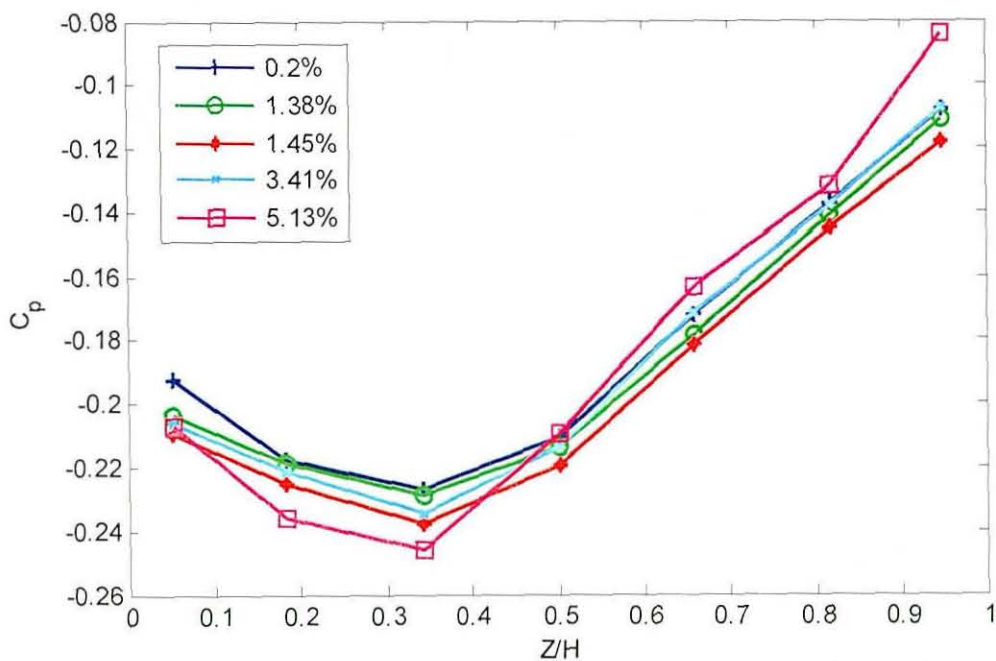
Figure 59 Variation in base pressure with vertical position, 100mm radius at 30m/s

All of the figures show a significant variation in base pressure with vertical position, and it is difficult to gain an understanding from the above figures of the effect of turbulence on the base drag. It may be that, given the conflicting effects of turbulence (depending also on the Reynolds number) between the base pressure on the top half of the base and the bottom half, that there is not just a single effect that can be easily identified as a rule of thumb for the effect of turbulence on the base pressure of a body with separation at the front, but in order to show the effect of turbulence on the base drag, an area weighted average was calculated. The results are shown in the following

figures as area weighted average base pressure C_{pb} against turbulence intensity, with leading edge radius as a parameter, for 20m/s (Figure 60), 30m/s (Figure 61) and 40m/s (Figure 62).
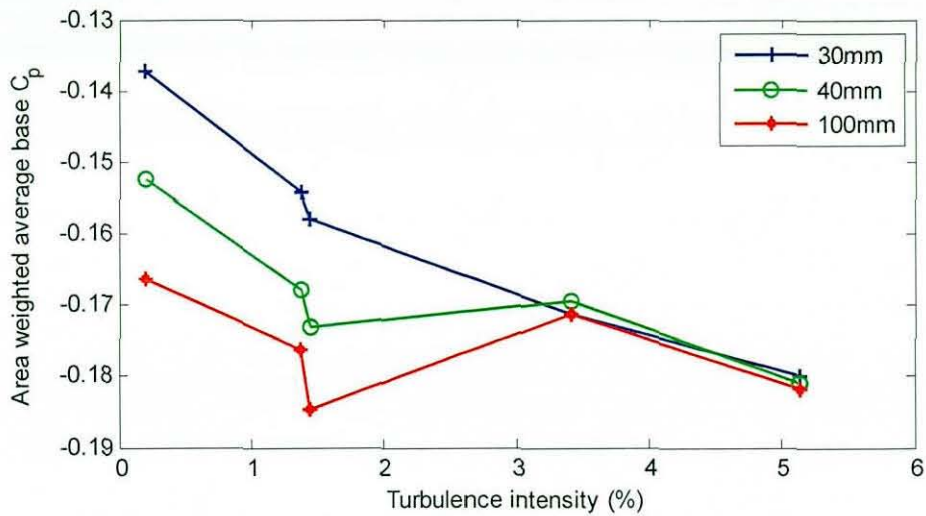
Figure 60 Variation in area weighted average C_{pb} with Tu at 20m/s (edge radius as a parameter)
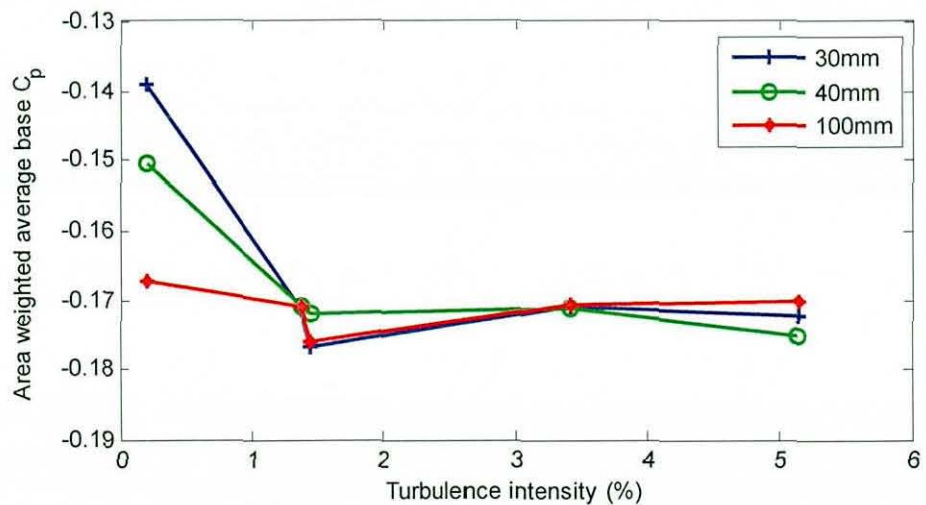
Figure 61 Variation in area weighted average C_{pb} with Tu at 30m/s (edge radius as a parameter)
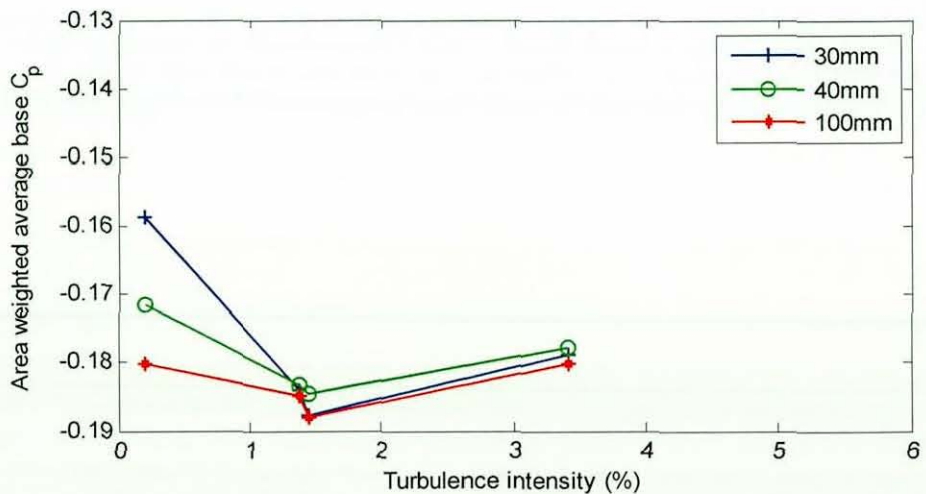
Figure 62 Variation in area weighted average C_{pb} with Tu at 40m/s (edge radius as a parameter)

85

The results show that, as might be expected from the C_D results, adding some additional turbulence to the flow over a body with a separation makes a large difference, and adding more turbulence makes a smaller difference. In general, adding turbulence reduces the base pressure, increasing the suction and therefore the drag. However, it should be remembered that the results are only indicative as they are distorted by the presence of the ground, and do not show the variation across the width of the base, only the height.

3.5   Summary

- The 1-box drag results showed that the transcritical Reynolds number based on edge radius is a constant, both in the clean tunnel and with increased freestream turbulence. Increasing the level of freestream turbulence reduced the value of the constant and the inverse relationship $Re_{rtcrit}=6.4*10^5*Tu^{-0.32}$ was found to match the results.

- Since the constant is dependent only on the edge radius, the results can be treated as a test of edge radius optimisation without reference to the model scale. A 40mm radius should perform the same in a full scale wind tunnel at a particular turbulence level as it does in the model scale wind tunnel, at the same Reynolds number based on edge radius and in the same freestream turbulence conditions.

- The concept of effective Reynolds number was found to be an inadequate description of what happens when the freestream turbulence level is increased. Instead, effective edge radius was proposed as a more representative model. It was shown that this concept gave a fair representation of the change in the trend of drag with Reynolds number at different turbulent intensities, but did not capture the difference in the values of C_D between one radius at an increased turbulence intensity and its equivalent in the clean tunnel, because of skin friction effects and the difference in acceleration around the radius.

- The model was shown to be sensitive to yaw, but the transcritical Reynolds number remained constant over the range of yaw angles tested ($0 - 15°$), both in the clean tunnel and with increased freestream turbulence. This was also reflected in Cooper's results [4].

- The post-critical C_D was shown to increase with increasing turbulence intensity. The increase was reasonably independent of edge radius and was shown to depend on the ratio between turbulence levels.

- The base pressures were also found to vary with Reynolds number, in a way that correlated to the presence of separation at the front of the model. The base pressure was considered to be controlled by the boundary layer thickness at separation. Increasing the turbulence intensity caused an increase in base suction (more negative base pressure) indicating that some of the increase in drag is caused by this change in the pressure field, as well as an increase in skin friction.

- Increasing the freestream turbulence completely eliminated the hysteresis loops that were seen in the clean tunnel for the 40mm and 50mm radii.

- The lift results broadly show the same effects as the drag results, in terms of the change in Re_{rtcrit} and the effect of the additional turbulence on post-critical front and rear lift coefficients.

- The most significant effects on lift occur around the front of the model, as would be expected, with additional effects at the rear of the model that most likely arise from shifts in the front stagnation point position.

- The centreline pressure results showed further evidence for the presence of separations in the clean tunnel for the smaller radii at low Reynolds numbers. The reduction in drag when the Reynolds number increased was shown to come from the sharp increase in suction on the leading edge radii, indicating that the separations had reduced, or that the flow had become fully attached.

- The addition of freestream turbulence also caused the pressure distribution around the radius to change, increasing the suction and indicating that the separation around the radius was reduced or absent.

- The base pressure distribution was seen to be affected by both changes in the Reynolds number and changes to the turbulence intensity. Increasing either Reynolds number or turbulence intensity increased the base suction.

Chapter 4

Flowfield measurement

In order to gain a fuller insight into the effect of turbulence around the radius of the 1-box model, it is desirable to make direct measurements of the flow. There are several ways to achieve this, all with advantages and disadvantages. The main tool that has previously been used to make measurements in boundary layers is the hotwire, but this is not suited to recirculating flows and would not provide an insight into changes in the separation bubble. What was needed is a non-intrusive measurement of the flow velocities around the radius, and for this reason Particle Image Velocimetry (PIV) was used, because it is capable of producing velocity vectors over a large area of flow that are synchronous with each other, giving a measurement of separation and vorticity that cannot be easily obtained using other techniques.

4.1   PIV technique

PIV is a method of measuring the velocity distribution of a flow on a plane (classic PIV), on and through a plane (stereoscopic PIV) or throughout a volume (full 3D PIV) in the test section. Only classic PIV was available for this experiment, and so only classic PIV will be described here.

A dual pulsed laser fires into the wind tunnel working section. The laser beam passes through optics, which spread the beam into a light sheet, which is then orientated and aligned to illuminate the plane of interest. A seeding system is used to introduce particles into the flow, which must be set so that the particles fill the plane of interest. A camera is mounted, ideally normal to the light sheet and outside the wind tunnel, and image pairs are taken of the particles as illuminated by the laser, with a very short delay between the two images in a pair. The basic setup is shown in Figure 63 (this diagram is a schematic only; the light sheet shown continues to the far wall, where it passes the model).

Figure 64 shows a cropped area of the field of view for a sample image pair taken at 15m/s, showing the model at the bottom and the seeding moving from right to left.
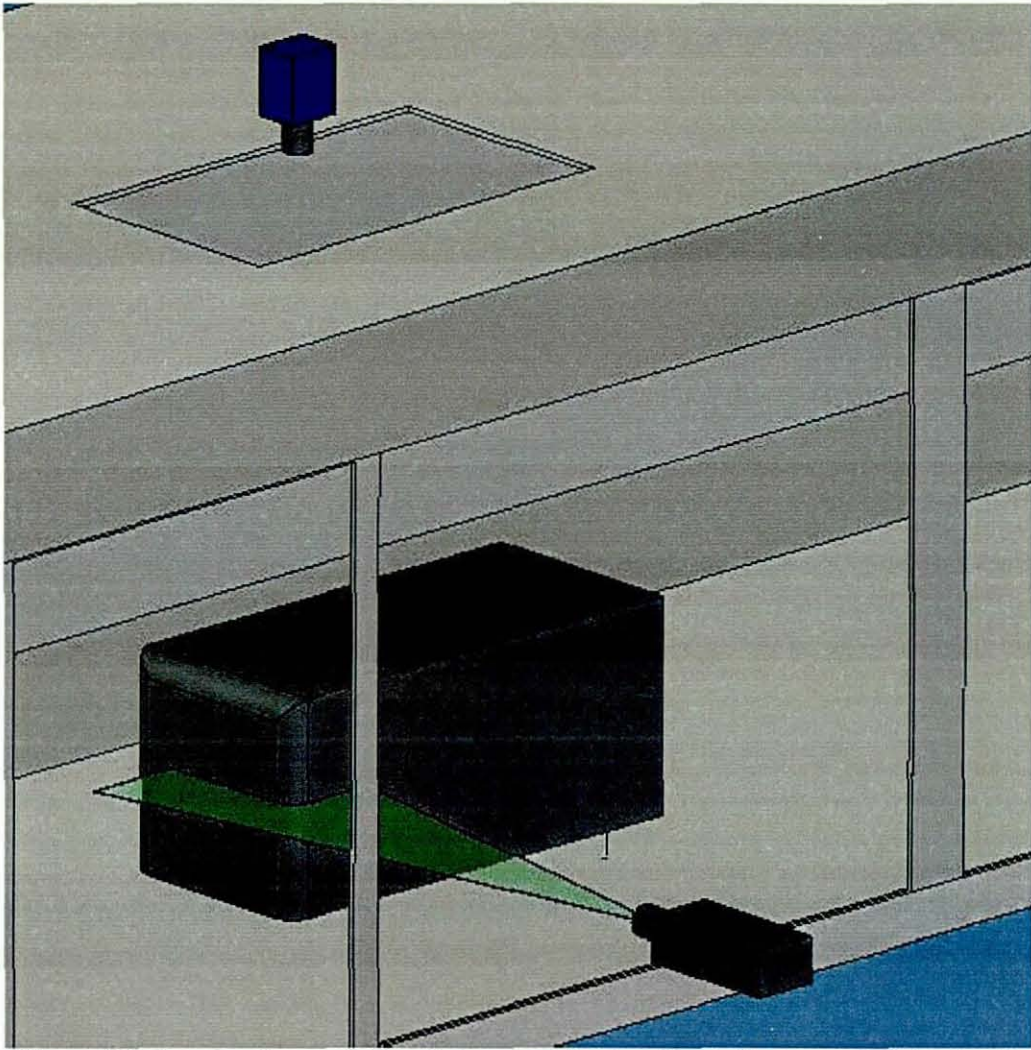
Figure 63 Setup showing model (centre) camera (top) and laser (bottom with light sheet)
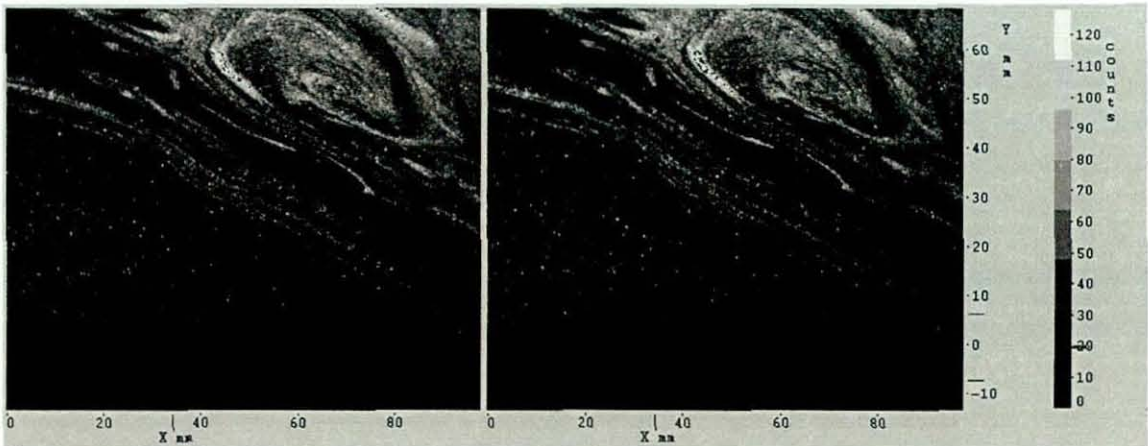
Figure 64 Example image pair (cropped) showing model (dark region) with seeding particles

PIV processing is then carried out on the image pairs. The software breaks the images down into many small interrogation cells and correlates the intensity of a cell in image 1 with the intensity of the corresponding cell in image 2 by moving the second interrogation window to different locations at a small distance from its original position in image 1. A map of correlations is then produced, and the displacement between the

cell in image 1 and the corresponding cell in image 2 where the correlation produces the highest peak then gives a displacement vector in pixels. This can be converted to mm or metres using a calibration image. The time delay between the two images is then used to calculate the velocity of the flow for that window. In practice, a multi-pass algorithm that starts with a large cell size and works down to smaller ones is used, and in the final passes the cells are overlapped. In between each pass, the software uses the results from *the previous pass to distort the grid of interrogation cells in the second image.*

- Starting with a large window and working down to smaller ones means that for the first vectors, although the spatial resolution is poor, a very large amount of data is being used to generate the correlation.

- The interrogation cells are distorted in the second image using the vectors generated in the previous pass, effectively moving and skewing the interrogation window in the second frame in the local flow direction in order to improve the correlation and reject correlated noise or random chance correlation with unrelated areas of seeding.

- 50% overlap is used on the final cells because it allows for a finer resolution without reducing the cell size (discussed in the next section). It also means that the data in the images is all used twice – the reason for this is discussed below.

In practice, settings were determined by experience and by inspecting the vector fields for obviously inconsistent vectors. Two passes were executed at the initial window size of 128x128 pixels, and the window size was then halved, and the process repeated, down to a final window size of 32x32 pixels, with 50% overlap for the final two passes.

Although the experimental parameters are carefully chosen and the image quality is the best possible, the vector field that is produced often has a very small number of inconsistent vectors. These vectors can be removed and replaced using a median filter, which tests each vector against its neighbours for consistency. Parameters are chosen based on experience, and vectors can be checked against the visible particle displacement between the original image pairs to give additional confidence. If a vector is discarded because it is obviously incorrect, for example, a single isolated vector of 70m/s with direction left to right in a freestream region where the flow is moving at 20m/s from right to left, then it can often be replaced by using the vector calculated

from the second, third or fourth highest correlation peak in the map, which are also then checked by the median filter. The choice of correlation peak is recorded with each vector. Vectors are also discarded based on the Q ratio, which is the ratio of the first correlation peak in the interrogation window to the second correlation peak. A very low Q ratio, for example less than 1.3, indicates a high noise floor. If a vector is discarded based on Q ratio, the likely cause is usually a small hole in the seeding field, which can be established by visual examination of the source images. Because of the overlap, it is considered legitimate practice to fill discarded vectors by interpolation, if there are sufficient surrounding consistent vectors, although this was not done in this investigation, and very few vectors were rejected based on Q ratio. In practice it was possible to achieve 98-99.9% first choice vectors, meaning that the quality of the images is very good. Further information on the PIV image processing parameters can be found in the LaVision product manuals [45].

4.2   Sources of error

Hollis [46] states that care must be taken when choosing experimental parameters. The seeding system must be carefully chosen. PIV is sensitive to both particle density and particle size. The particles must be small enough to be carried along by the air at the same speed, but large enough to show up as more than one pixel on the chosen camera. The size of the reflection from the particles then determines the largest achievable field of view. This is because the correlation uses a Gaussian curve fit to establish the location of the particle, and in order to do this accurately, each particle should be between 2 and 6 pixels on the image. If the particles are too small, then the velocities calculated tend towards integer pixel values, which is termed peak lock. This can be checked for by analysing the velocities as pixel displacements in a mod.1 number system (which essentially only shows the value after the decimal place). Figure 65 shows a sample PDF from one processed PIV image pair taken at 15m/s. Peak locking would be shown by a U shaped histogram, which clearly is not the case here. Instead the data is well spread across the range, indicating that the particles are sufficiently large. It is possible [45] to calculate the degree of peak lock by calculating the average centre of mass of the velocities ($\bar{U}_{mass}$):

$$\bar{U}_{mass} = \begin{array}{ll} U \bmod 1 & (\textit{if } U \bmod 1 < 0.5) \\ 1 - U \bmod 1 & (\textit{if } U \bmod 1 > 0.5) \end{array} \qquad \text{Equation 7}$$

$$\text{Peak lock} = 4*(.25 - \overline{U}_{mass}) \qquad \text{Equation 8}$$

In the example, the degree of peak locking is 0.027, which is much less than the estimated degree of accuracy of finding the centre of a particle, quoted as 0.1 pixels in the LaVision manual [45]. This is the normally quoted noise floor of the technique, so that provided the peak locking remains at or below 0.1, it can be said not to contribute significantly to the error.
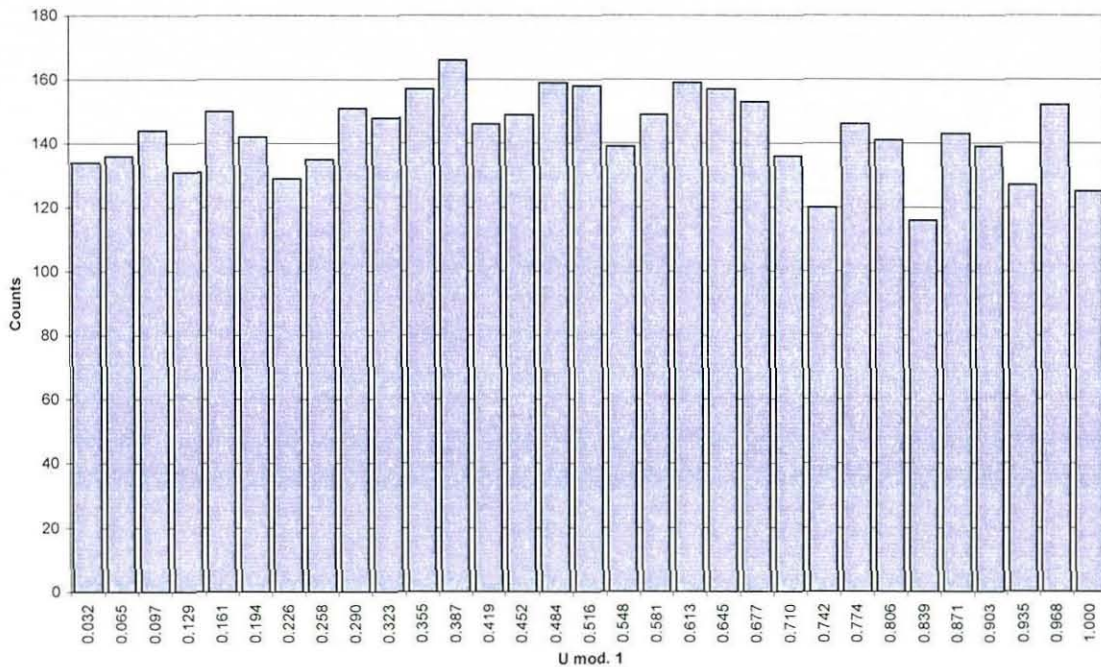
Figure 65 PDF of U mod.1 (from sample PIV image pair)

The inter-frame time, combined with the speed of the flow, effectively determines the displacement of the particles. There are a number of conflicting constraints on the ideal value of pixel displacement. The relative error on the velocity is determined by pixel displacement because the positional accuracy is calculated with a typical tolerance of ± 0.1 pixels [45]. However, in order to achieve a good correlation, Keane and Adrian [47] state that the displacement magnitude of each particle group, ie. within one interrogation cell, should be less than ¼ of the cell size. Increasing the pixel displacement also has the effect of smoothing the flow, by dynamically averaging the displacement. Since in this experiment one 32x32 pixel block is 7mm by 7mm, and so with a 50% overlap each vector represents 3.5mm by 3.5mm of the flowfield, the spatial averaging due to the desired frame size means that it is not possible to resolve

down to the Kolmogorov scales (likely in this type of flow to be sub-millimetre), and so accurate measurement of the turbulence intensity is not possible.

The objective here is to provide data that sheds light on the balance results by means of producing accurate vector maps of the flow around the radius, to show vortex shedding and recirculations, and for this reason accurate turbulence measurement will not be pursued, and spatial averaging will be accepted as an inevitable limitation of the technique. Further investigation of the state of the near model freestream and boundary layer, using a longer focal length lens, could be carried out as a follow-up to this work and would provide valuable insight into the effect of the model on the freestream turbulence, and the effect of freestream turbulence on the size of the boundary layer, but this would be a complex and time consuming experiment in its own right.

Since this experiment involves changing the Reynolds number by changing the wind speed, the inter-frame time was optimised for each tunnel velocity individually, and varied between 60-21µs for 15-45m/s respectively, with the aim at each speed being an r.m.s. pixel displacement of 6 pixels and a maximum of 8. For an example flowfield with a freestream velocity where 6 pixels equates to 22m/s, the error due to the uncertainty in locating the centre of a particle is 0.1 pixels, or 0.369m/s.

4.2.1 Statistical errors in mean and r.m.s vector fields

At each measurement point, 1000 images were recorded at 4.5Hz, and an average and r.m.s. vector field produced. The statistical accuracy of calculated mean and r.m.s. values can be determined using standard error estimation techniques, e.g. Montgomery and Runger [48].

$$\varepsilon_U = z\sigma\sqrt{\frac{1}{N}} \qquad\qquad \varepsilon_{u'} = z\sigma\sqrt{\frac{1}{2N}} \qquad\qquad \text{Equation 9}$$

where ε_U is the actual error in U, $\varepsilon_{u'}$ is the actual error in the r.m.s, z is a constant related to the confidence interval and σ is the standard deviation (r.m.s.)

The statistical percentage error in U is ε_U/U (which is problematic for an image with significant variation in velocity), and in the r.m.s. velocity it is $\varepsilon_{u'}/\sigma$ (which means that the percentage error in r.m.s. velocity is independent of the value of the r.m.s. and only depends on the sample size). For 99% confidence, z = 2.576, and so for example, the

actual error in U over 1000 samples, at 22m/s in 5.1% turbulence, is 0.091m/s. For the example freestream at 22m/s, the total error (including the uncertainty in particle centre location above) in the average velocity is therefore 0.3799m/s, with 99% confidence (from Hollis's method [46]). It is clear that in this case, the main source of error is in the ability of the PIV algorithm to determine an accurate fit to the data.

The r.m.s values in the region above the separated shear layer (see the results section) are much higher, and so the local error due to a lack of statistical convergence will be greater – if the r.m.s. is 10m/s, as it is in some separated regions, the error in the local mean is 0.8m/s, and the total error is 0.88m/s. The mean windspeed also varies throughout the flowfield, and so it is not very useful to calculate a single percentage error for U.

As indicated above, the error in the r.m.s itself is easier to calculate as a percentage, and for any of the average flowfields it will be 5.76%, with a total error of 5.99%. However, these estimates of the error do not take into account the spatial averaging that occurs due to having several particles in the same interrogation window, and so the actual error will be less (Hollis [46]). The above quoted errors are therefore the worst case.

4.3   PIV experimental setup

The experimental setup is shown in Figure 63, but it omits one important part of the system, which is the seeding system. For the Loughborough model tunnel, a commercially available seeding system based on atomising olive oil using a Laskin nozzle was selected. The particles produced are around 1μm in diameter. A seeding rake was then devised that distributes the olive oil particles in the tunnel settling chamber over a large enough volume that they fill any plane of interest chosen on the side of the model nearest the laser. The wake of the seeding rake causes streakiness in the seeding, in the clean tunnel (seen in Figure 64). The vortical structures visible in the seeding are stationary by the time they have passed through the settling chamber and the contraction and reached the model. The seeding density is sufficient to give good quality results despite this minor problem, which is typical of seeding for PIV in air. One useful side effect of installing the turbulence generating grids is that the seeding quality becomes excellent, because the streakiness is broken up completely by the turbulence and the seeding appears as a field of discrete and uniformly distributed particles.

The laser used is a dual pulsed Nd:YAG laser, producing 50mJ of light energy per laser pulse and operating at a maximum of 15Hz. In practice, because the maximum operating speed of the camera is 4.5Hz, the laser is set to operate at 9Hz to ensure image pairs are taken as quickly as possible. The experiment was set up so that the laser could always be operated at its maximum power setting, thus ensuring the brightest possible images of the seeding particles.

The camera is a 12-bit per pixel, 1.3 megapixel (1376 x 1040) device, that can take 2 frames in very close succession (down to approx. 5µs separation is possible). The firing of the laser and camera is synchronised by a timing unit in the data acquisition computer. Once one pair of images is taken, it is transferred from the camera to the RAM of the computer. Due to a limitation of Windows 2000, the computer is capable of grabbing 2Gb of images at a time. The images are compressed on the fly, which means that 334 image pairs can be taken at one go. For each measurement point (a particular radius in a particular turbulence intensity at a particular windspeed) 1002 image pairs were recorded. The images are then transferred to disk, and a pre-taken background image (with the laser but without the seeding) subtracted from each, and then more data can be taken. In this application, a 35mm lens was used, because this gave a sufficiently large field of view to be able to see the area of interest in one image, but avoided peak locking. A bandpass filter is used on the front of the lens that only permits light with a wavelength of 335nm ±5nm to pass through.

Since the area of principle interest is the flow around the leading edge radius, the laser was aimed at the mid-height of the model on the side (as shown in Figure 1). Using this configuration gave such strong scatter from the side of the model that, if the laser power had been turned up high enough to get good quality images of the seeding, damage to the camera would have occurred. In order to avoid this, several solutions were tried, including rhodamine (which absorbs green light and fluoresces orange, which should be rejected by the filter)), mirror finish paper to reduce diffuse reflection, and rolling the model over towards the laser to angle the reflections away from the camera. None were fully successful, and so it was decided to bolt a thin metal plate to the top of the model, which extended a few millimetres out to the side, to completely screen the reflection and approx. 2mm of the freestream from the camera's view. These plates had to extend forward to cover the radius, but did not follow the curve of the model, and therefore

will have introduced some additional complex flows. However, the plate is relatively far from the measurement plane at the mid model position, and therefore it is assumed that the important flow features of separation and reattachment will not be altered.

The laser sheet extends from just in front of the leading edge of the model to a point approximately 300mm from the leading edge. The laser sheet has a Gaussian power distribution, so it is difficult to see exactly where it stops, but by experimentation it was positioned so that the field of view shows the area from approximately 40mm in front of the model to 250mm from the front, along the left hand side of the model. The laser does not cover the whole field of view on the top side, away from the model, or at the far right edge (upstream) and so some areas are masked off, to prevent the PIV algorithm trying to create vectors out of correlated noise. The image is then 290mm wide (with the freestream flow running from right to left) and 220mm "high", overlapping the edge of the model by a bit more than 20mm to show the end of the leading edge radius.
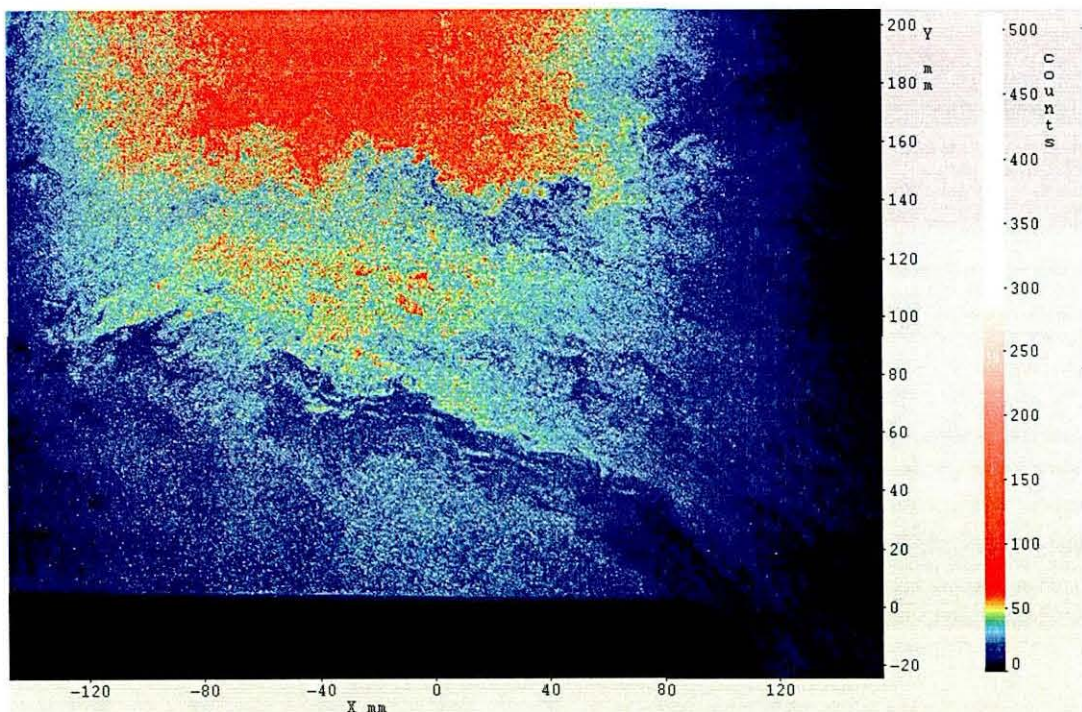
Figure 66 Example raw image showing the 30mm front at 15m/s in 1.45% turbulence, frame 1

A typical image showing the whole field of interest is shown in Figure 66. The flow is from right to left, and the dark area at the bottom is the model. As previously noted, this image, with the 1.45% turbulence grid, has much better quality seeding than the clean tunnel images (although both are sufficient to get high quality vectors). The colour

coding corresponds to the brightness levels recorded by the camera (out of a maximum of 4096 levels).

The image pairs were then post-processed using the parameters previously described to generate instantaneous velocity fields, and for each measurement point (a particular radius at a particular windspeed) average and r.m.s. vector fields were calculated using all 1002 image pairs.

4.4 Flow visualisation results

It is clearly impossible to reproduce the PIV results in detail here. There are far too many instantaneous velocity fields, and even too many average velocity fields to show all of them, since the images must be large to be of any use. As few results as possible are presented here to demonstrate the points being made, and to simplify the images, the vector resolution is reduced to show fewer vectors. This second step allows for longer, clearer arrows, but can make detailed flow features more difficult to identify. The degree of reduction is indicated in the figure caption.

The explanations made for the balance results will be examined using the PIV results, firstly by looking at sample individual vector fields, where the unsteadiness in the flow can be seen and compared between different Reynolds numbers and turbulence intensities, and then by examining the time averaged vectors, with the r.m.s. values displayed as a background to the image, which show the time-averaged structures in the flow-field that determine the time-averaged forces on the model.

4.4.1 Instantaneous flow fields

Several sets of instantaneous flow fields have been chosen to illustrate typical flowfield characteristics as Reynolds number and turbulence intensity varies. In all cases the measurements are presented for the 30mm radius.

In the clean tunnel at low Reynolds number a large separation bubble is seen. The following three sequential images show typical instantaneous flow fields for the clean tunnel at 15m/s. The images have been zoomed and cropped to show only the area of interest, with the freestream running from right to left and the side of the model at the bottom of the image (the black shape).
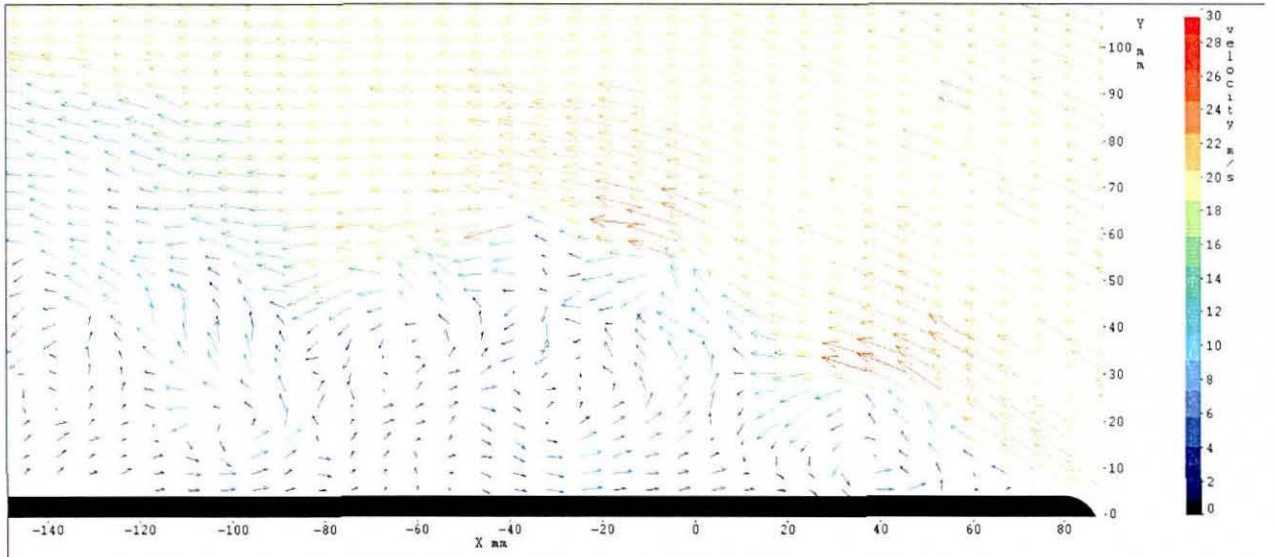
Figure 67 30mm front section, clean tunnel, 15m/s frame 152 (half horizontal resolution)
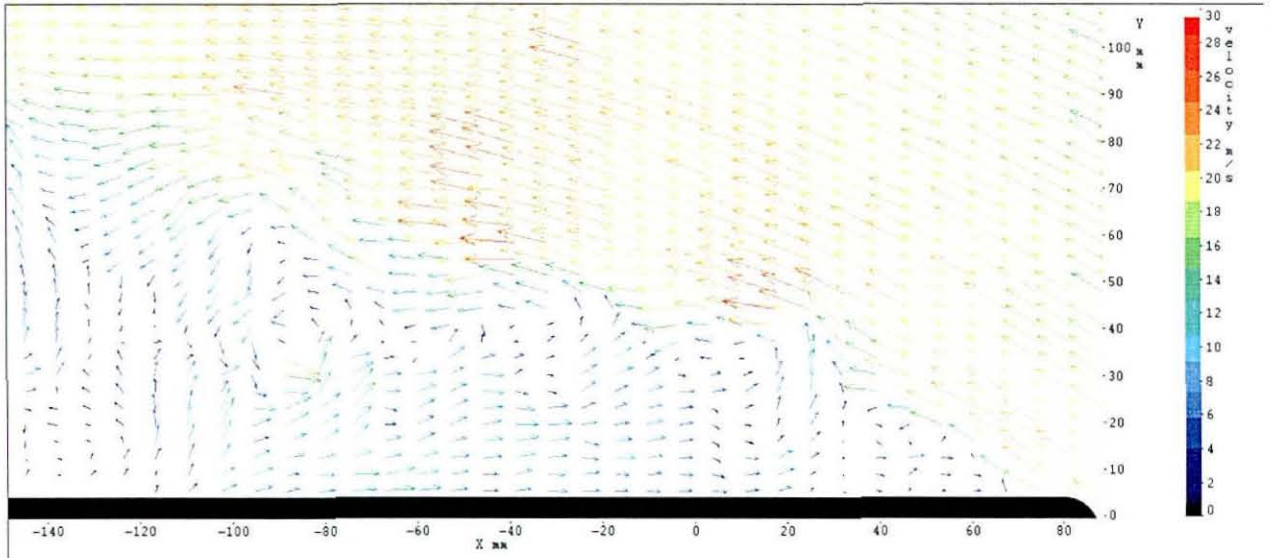
Figure 68 30mm front section, clean tunnel, 15m/s frame 153 (half horizontal resolution)
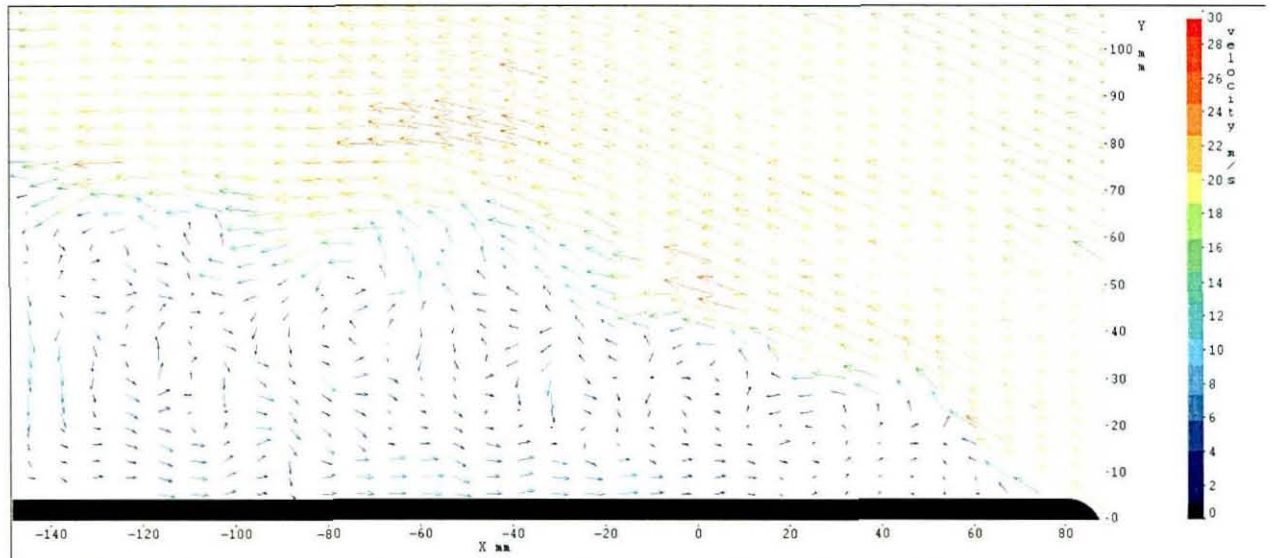
Figure 69 30mm front section, clean tunnel, 15m/s frame 154 (half horizontal resolution)

100

The vortices spinning off the radius can be clearly identified, and it can be seen that the shear layer is moved around by these vortices. The separated recirculating region near the model wall can also be seen. Because the frame rate is relatively slow at 4.5Hz, it is not possible to identify the same structures in consecutive frames, as an individual vortex of around 40mm diameter driven by the shear layer moves a considerable distance in 0.222s. For example, in Figure 67 the velocities inside the vortices would imply that a small volume of air in this region might move between 1.5 – 2.5m between image pairs.

The vortices can be seen to extend all the way to the wall in some areas, depending on the locations of the centres of the vortices in each frame. In each frame there are undisturbed regions of reversed flow, some larger than others. In the time-averaged flow-fields in the next section, a clearly delineated and identifiable separation region is seen, but in the instantaneous fields it is an unsteady region of separated flow containing regions with velocities in both upstream and downstream directions and high vorticity. These frames are representative of the dataset at 15m/s, but there is the occasional frame where the separation bubble collapses, which occurs in about 3 or 4 frames in the set of 1001. An example is shown in Figure 70.
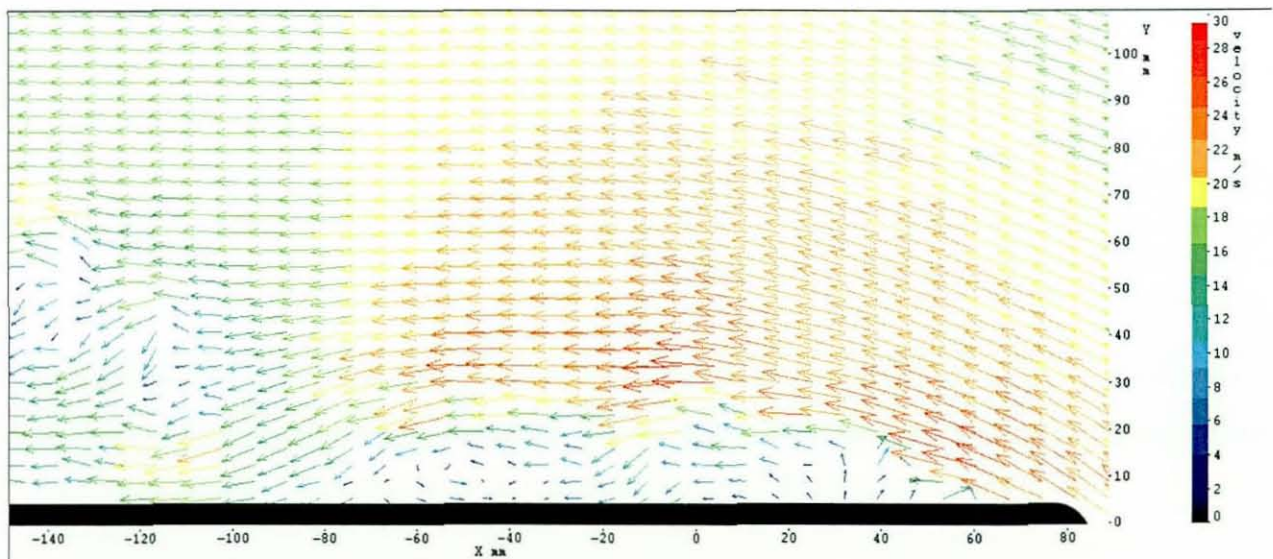
Figure 70 30mm front section, clean tunnel, 15m/s frame 157 (half horizontal resolution)

In this figure there is a separation region that begins near the end of the radius at x=60, with a small vortex-like structure. Downstream at x=-50 there is another distinct vortex, and then just downstream the flow becomes reattached, with flow entrained into the boundary layer at close to the freestream velocity and an isolated patch of vorticity

being transported away from the side of the model. This collapse of the separation bubble, where the flow becomes reattached briefly, is relatively infrequent in the clean tunnel but seen to occur at all speeds up until the separation bubble disappears at 40m/s. It is typical of the unsteady aerodynamics around a bluff body, even in very low turbulent flow.

An example instantaneous flowfield at 40m/s is shown in Figure 71. There is no separation at all at this speed.
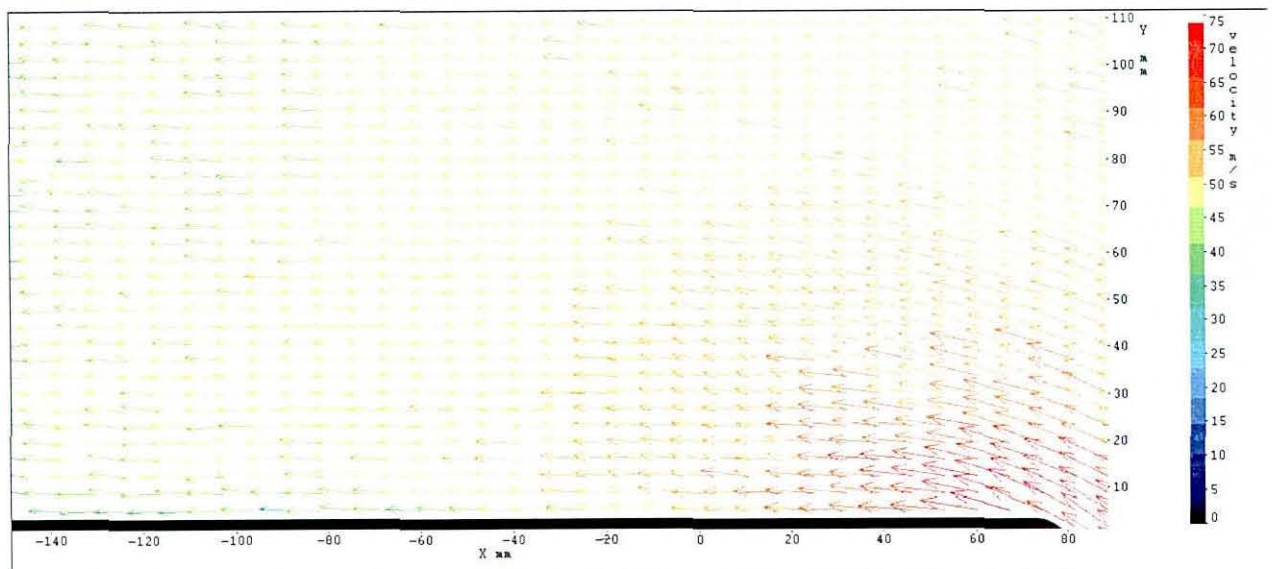
Figure 71 30mm front section, clean tunnel, 40m/s frame 120 (half horizontal resolution)

When the freestream turbulence intensity is raised to 1.38%, the separation bubble at 15m/s becomes more unstable. In some frames (e.g. Figure 72) there are clear, distinct vortex structures, with strong reverse flow against the wall of the model towards the separation point. One frame later (Figure 73) the vortices have become less distinct and there is a strong flow back towards the model in the left of the frame, pulling the flow back and causing it to reattach. The flow near the wall is entirely disturbed by the unsteadiness in the separated region. In the next frame, the shear layer has moved much closer to the model, with a delayed separation point about 30mm further downstream than in the previous frames, and much thinner but longer separated region (Figure 74). There are a couple of small vortices that can be identified. The separated region is highly disturbed and the reversed velocity near the wall at x=-20 to -120 is low.

Figure 72 30mm front section, 1.38% turbulence, 15m/s frame 52 (half horizontal resolution)

Figure 73 30mm front section, 1.38% turbulence, 15m/s frame 53 (half horizontal resolution)


Figure 74 30mm front section, 1.38% turbulence, 15m/s frame 54 (half horizontal resolution)
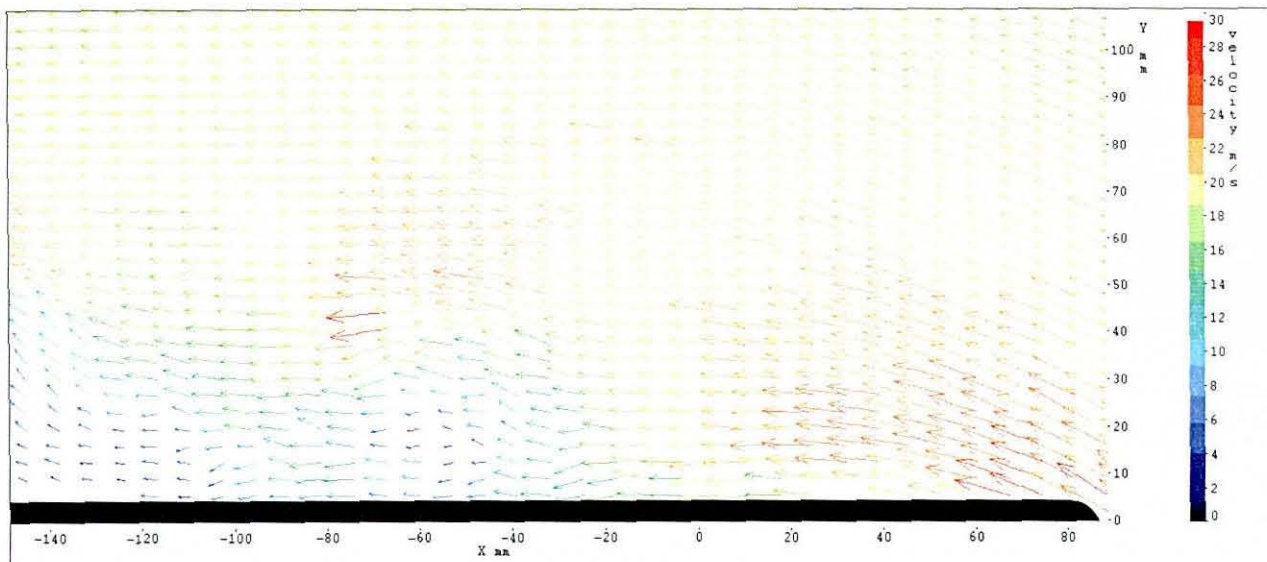
Figure 75 30mm front section, 1.38% turbulence, 15m/s frame 55 (half horizontal resolution)

The next frame in the sequence is Figure 75. The flow in this frame is fully attached around the radius but shows evidence that it was separated – there is a region of low velocity where the flow appears as a thick boundary layer, all moving in the same direction but much slower than the freestream. At this level of turbulence, the flow is usually separated and showing the characteristics of Figure 72 and Figure 73. It is difficult to be precise, but it is estimated that the conditions in Figure 75 occur in about 25% of the recorded frames.

Increasing the turbulence intensity to 3.4% increased the instability further. An intermittent separation exists in some frames, but in the majority of vector fields the flow is attached but with a thick unsteady region where vortices roll down the side of the model. The following three figures show a typical sequence. Figure 76 shows the flow separating at around x=70 as it did before. A number of strong vortices can be seen along with a body of flow that is returning up the side of the model and entraining into the shear layer at x=50, y = 30. The fluctuation in the freestream velocities due to the superimposed turbulence can also be seen. In the next frame (Figure 77) the separation point is the same but there is no clear recirculation volume and the unsteady region is much thinner. There are several vortices visible and some reversed flow at the model wall associated with the structures in the shear layer. Figure 78 shows the next frame. There is still a thick boundary layer visible with two weak vortical structures near the wall. There is no clear separation at the radius at all in this frame.

104
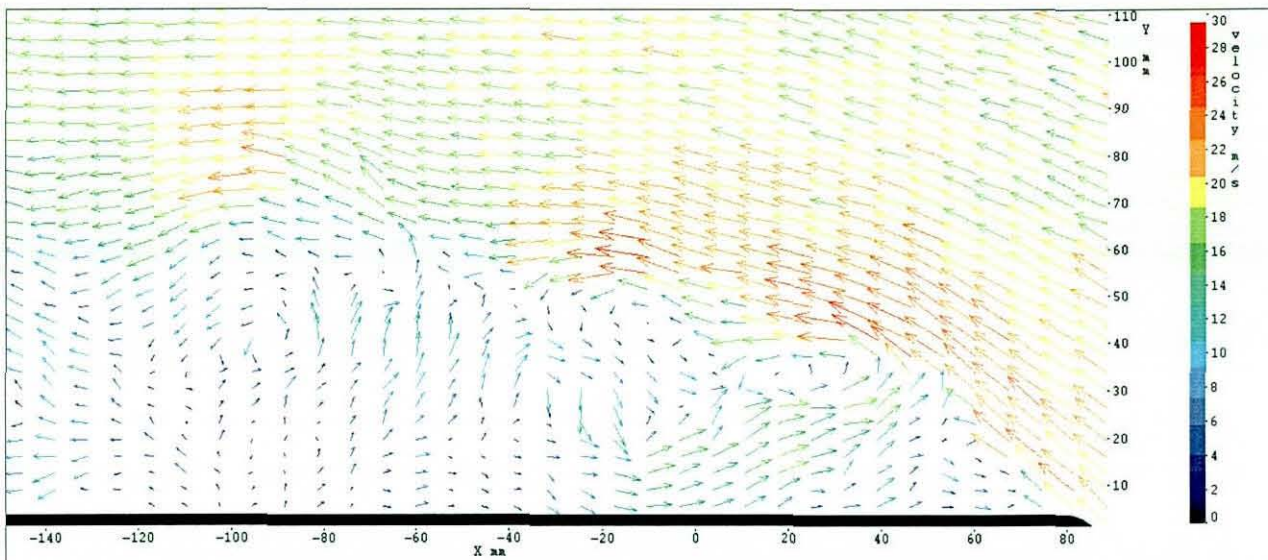
Figure 76 30mm front section, 3.4% turbulence, 15m/s frame 777 (half horizontal resolution)
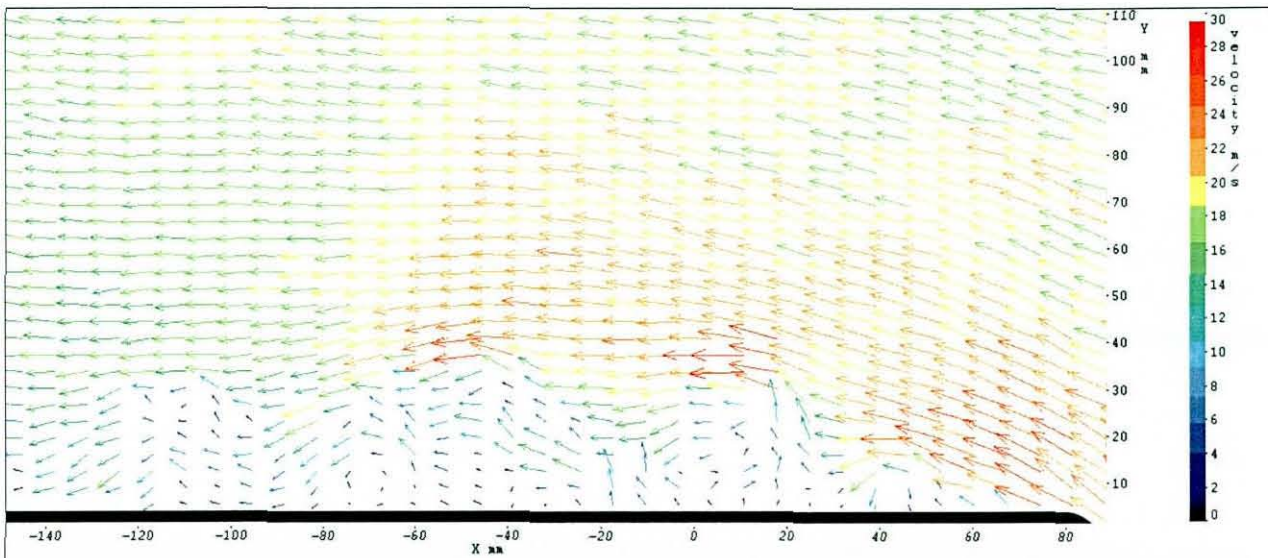
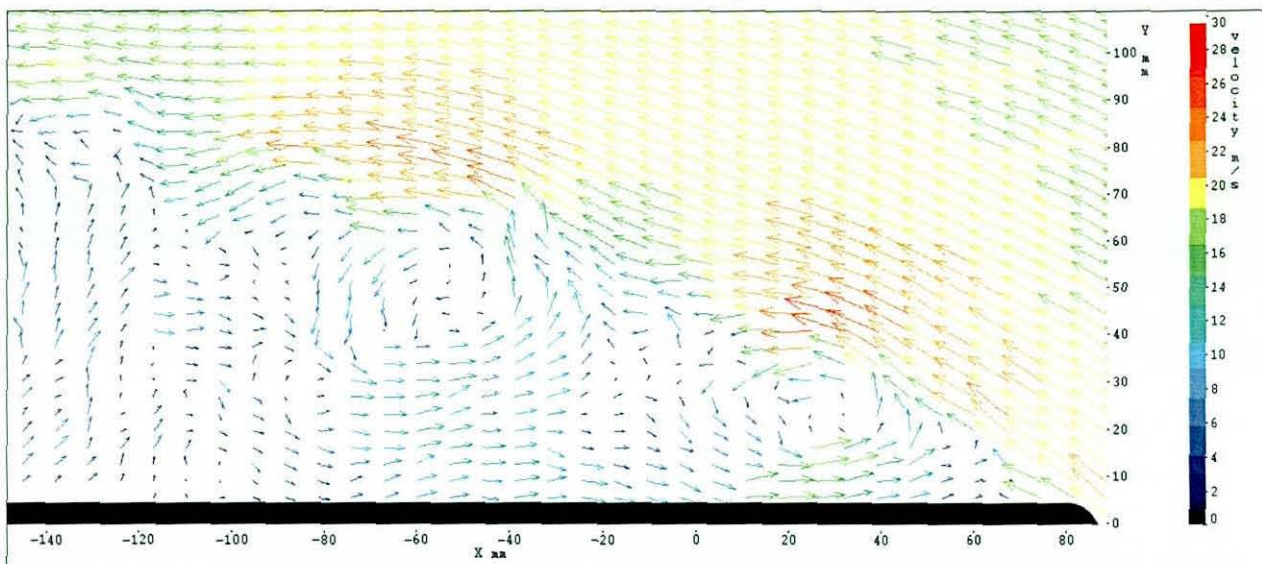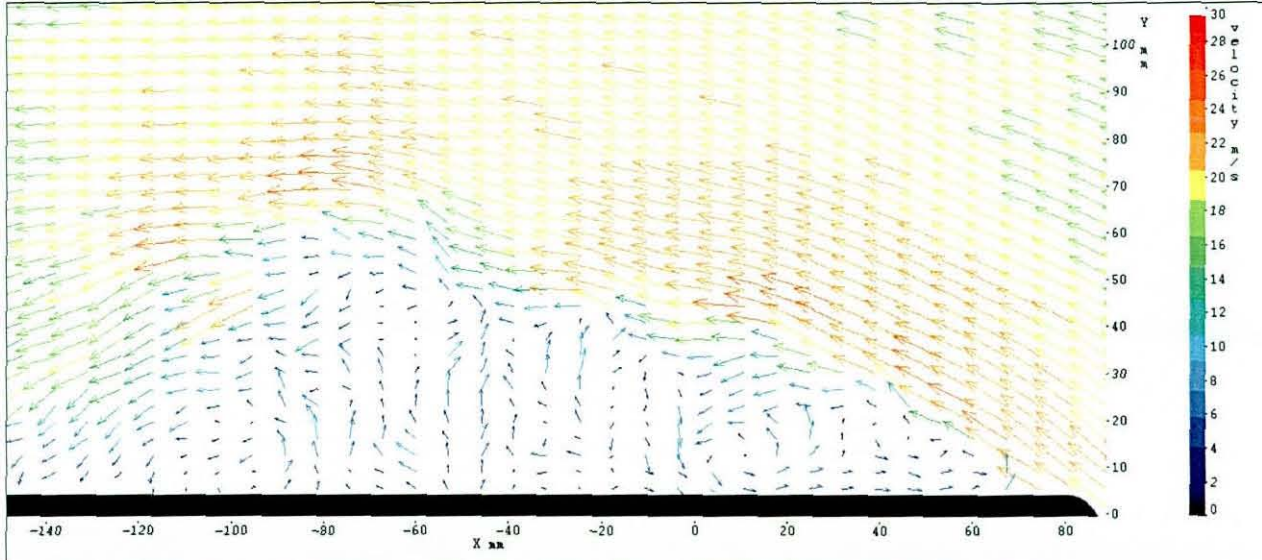Figure 77 30mm front section, 3.4% turbulence, 15m/s frame 778 (half horizontal resolution)
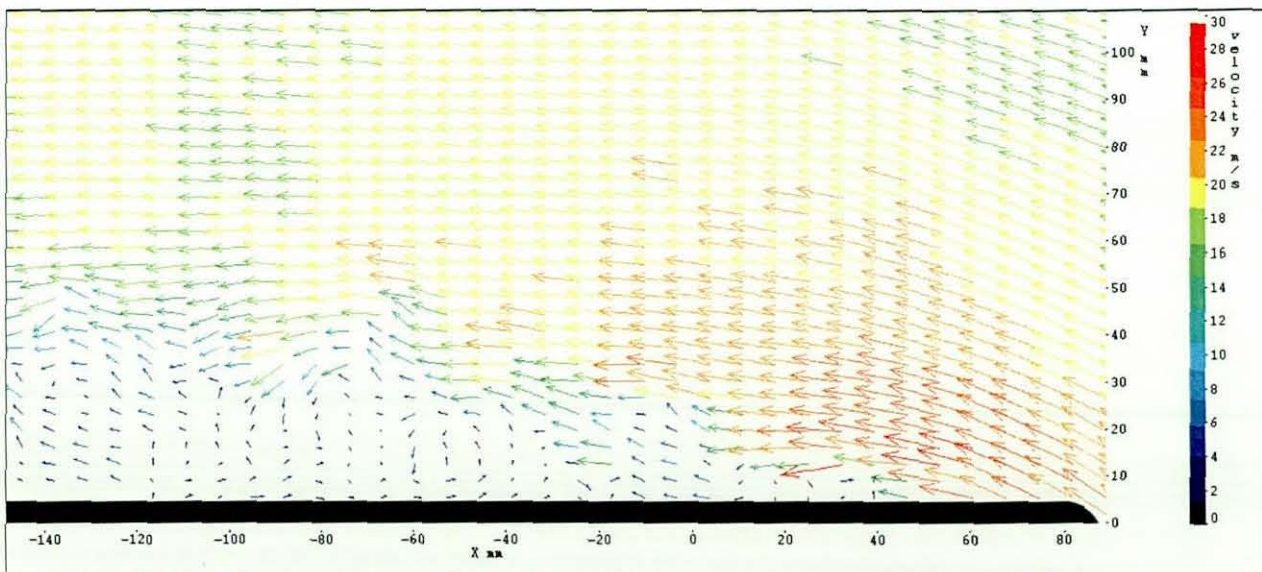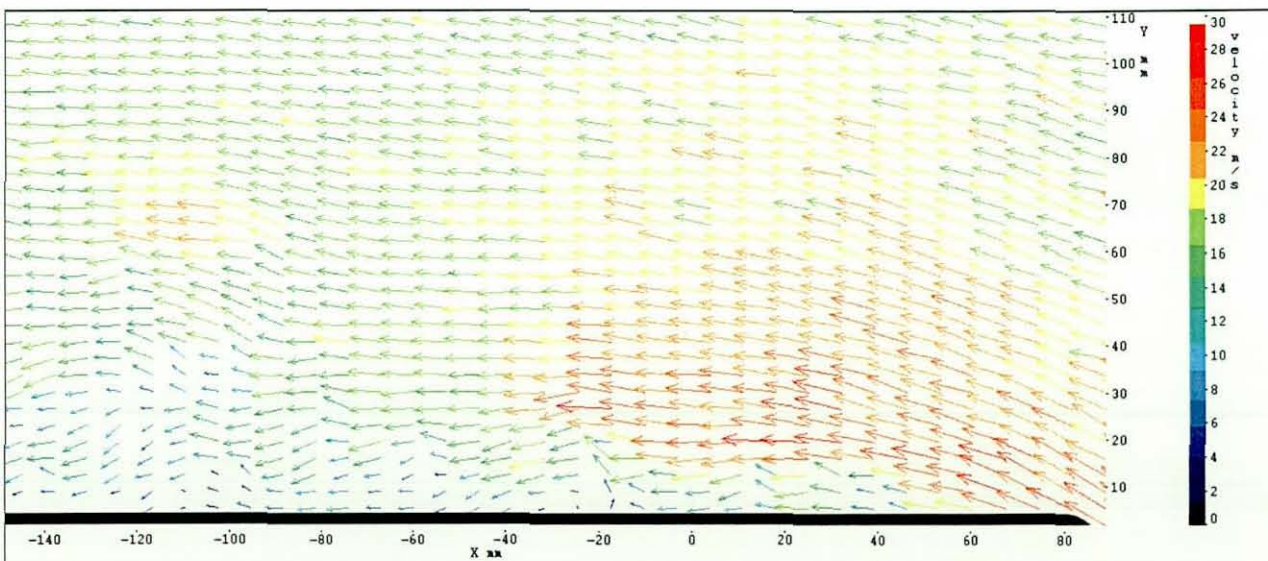

Figure 78 30mm front section, 3.4% turbulence, 15m/s frame 779 (half horizontal resolution)

The effect of the freestream turbulence is to collapse the separation bubble. When they are present, the vortices are clearly stronger when the freestream turbulence intensity is raised. It appears in the results that the additional freestream turbulence strongly affects the boundary layer or the free shear layer, as was shown by Hillier and Cherry [18], acting to increase the unsteadiness in the separated region. Bradshaw [40] stated that the interaction between freestream turbulence and a boundary layer on a flat plate is strongest when the eddy size in the freestream turbulence matches the thickness of the boundary layer. Here, where there are periodically shed vortices, it could be expected that the interaction is strongest when the local eddy size matches the vortex size. The integral length scales of the freestream turbulence of 15-37mm are similar to the vortex sizes seen in the images. When this happens, combined with a sufficiently high turbulence intensity, it is the likely cause of the collapse of the separation bubble, as the reinforced vortex draws more energetic flow across the shear layer.

4.4.2   Reynolds number effects

In Section 3.2, Figure 13 was used to indicate the presence of 2 distinct flow patterns; a separated flow with a high drag coefficient, termed pre-critical, and a fully attached, low drag coefficient flow pattern, termed post-critical. The 40mm front section was used in the figure, because, due to loading constraints on the balance, the 30mm front section did not undergo transition. For the PIV results, however, the model was bolted to the tunnel floor, and so it was possible to run the 30mm radius at the highest tunnel speed, and the flow did undergo transition, as seen in the following figures. The 40mm front section follows the same pattern, but the 30mm held the pre-critical flow up to higher Reynolds numbers – and also with a turbulent freestream – and is therefore more interesting.

The figures in this section are averages of 1000 vector fields at 4.5Hz. Figure 79 shows a big separation bubble on the radius, as expected. It is not possible to see the reattachment point, but the shear layer is clearly curving back in towards the model to the left of x=-80. The highest r.m.s. velocities are in the shear layer, where it was shown in the previous section that there is significant vortex shedding from the radius. Since there is some kind of periodicity to this shedding, the r.m.s. component here could be considered a mixture of turbulence and structured unsteady flow, rather than pure random turbulent eddies.
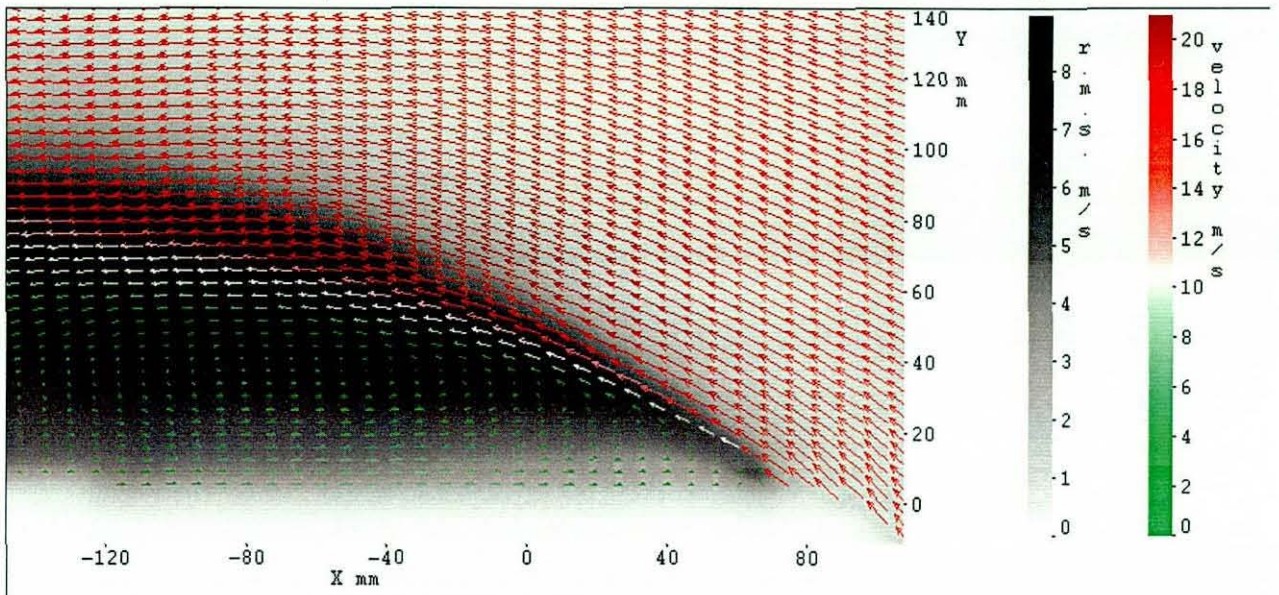
Figure 79 30mm front section in 15m/s flow, clean tunnel (half horizontal resolution) (Re$_r$ = 30,000)

Slightly increasing the tunnel speed to 20m/s gives the flowfield shown in Figure 80. Again, as expected, there is a separation bubble, of slightly smaller width (35mm instead of 40mm at its widest extent), and clearly shorter with the shear layer much closer to the model as it leaves the field of view.
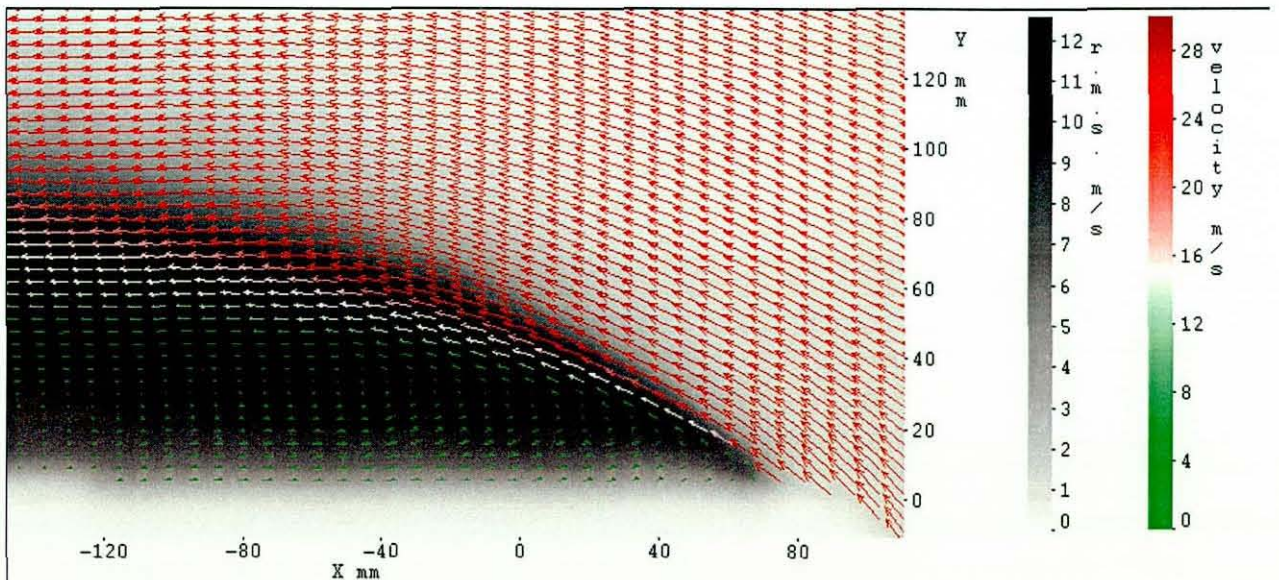
Figure 80 30mm front section in 20m/s flow, clean tunnel (half horizontal resolution) (Re$_r$ = 41,000)

As the Reynolds number is increased, the separation bubble continues to shorten, with the reattachment point appearing in the field of view, but does not get significantly narrower – the widest point moves upstream but remains at around 35mm from the side of the model. The separation bubble still persists at 35m/s, as shown in Figure 81, with

streamlines drawn in the background instead of r.m.s. velocities. The highest velocity reached with the balance was 37.5m/s, where the drag coefficient was still approx. 0.67.
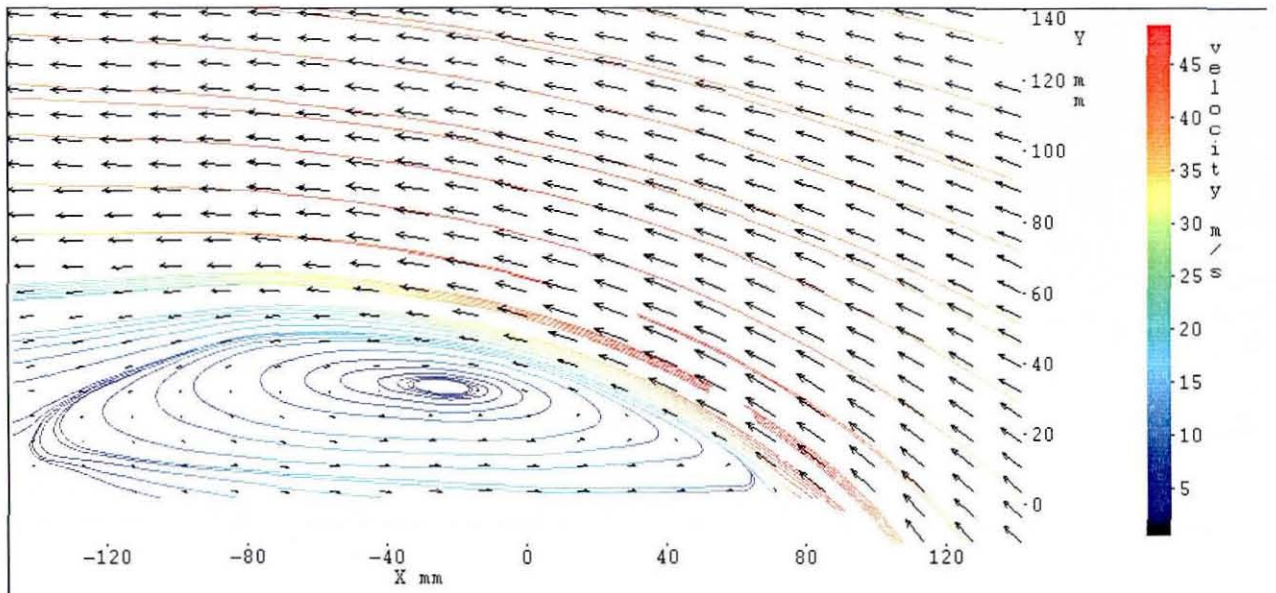
Figure 81 30mm front section in 35m/s flow, clean tunnel (quarter horizontal and half vertical resolution) (Re$_r$ = 72,000)
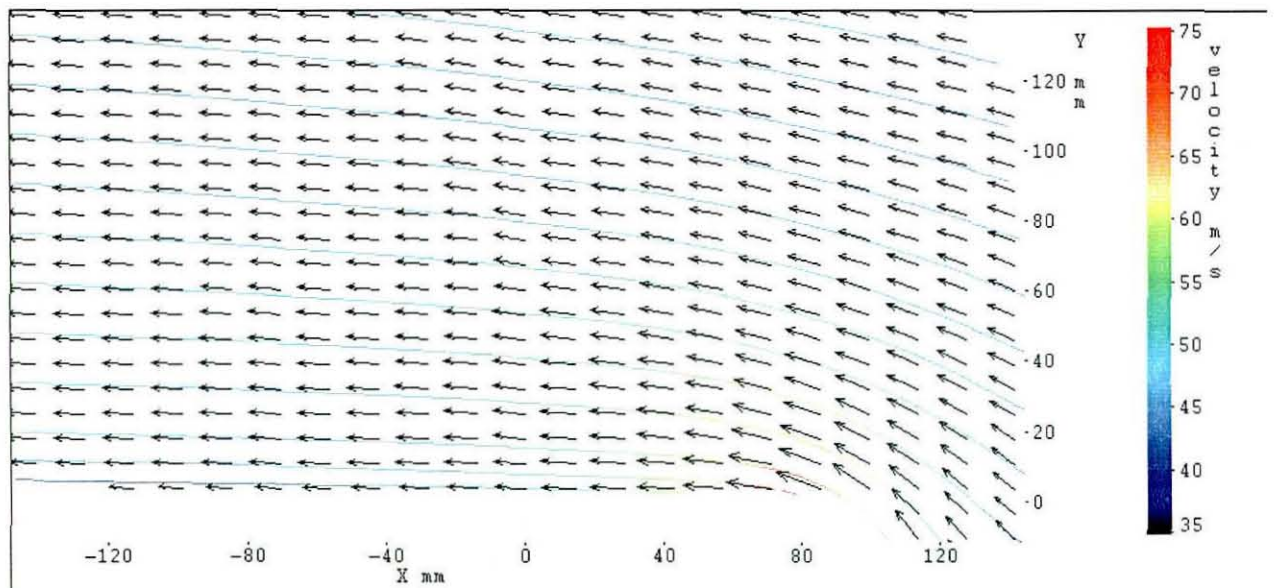
Figure 82 30mm front section in 40m/s flow, clean tunnel (quarter horizontal and half vertical resolution) (Re$_r$ = 82,000)

Figure 82 shows that at 40m/s, the separation bubble has collapsed and the flow is fully attached, as shown in the previous section. This did not occur in the pressure distribution tests, but it is already known that the critical region shows poor repeatability compared to fully pre-critical or post-critical Reynolds numbers. To compare against a radius which did show fully post-critical behaviour at this speed in the previous chapter, with a drag coefficient of 0.37, the 40mm radius is shown in

Figure 83. The small blob of high r.m.s velocity at x=-35, y= 25 is caused by a piece of tape on the tunnel floor, which even subtracting the background image from the images before processing them could not cure. It is clear from these results, and the previous research of Cooper [4] and others, that the drag coefficient is largely controlled by this separation region (with separation bubbles over the front quarter of the model length at low Reynolds numbers). It is known that increasing the Reynolds number causes the boundary layer to transition over a shorter length from the stagnation point on the front of the model, and it is assumed, based on previous research by Hoerner [5] and others, that this is the reason for the collapse of the bubble.
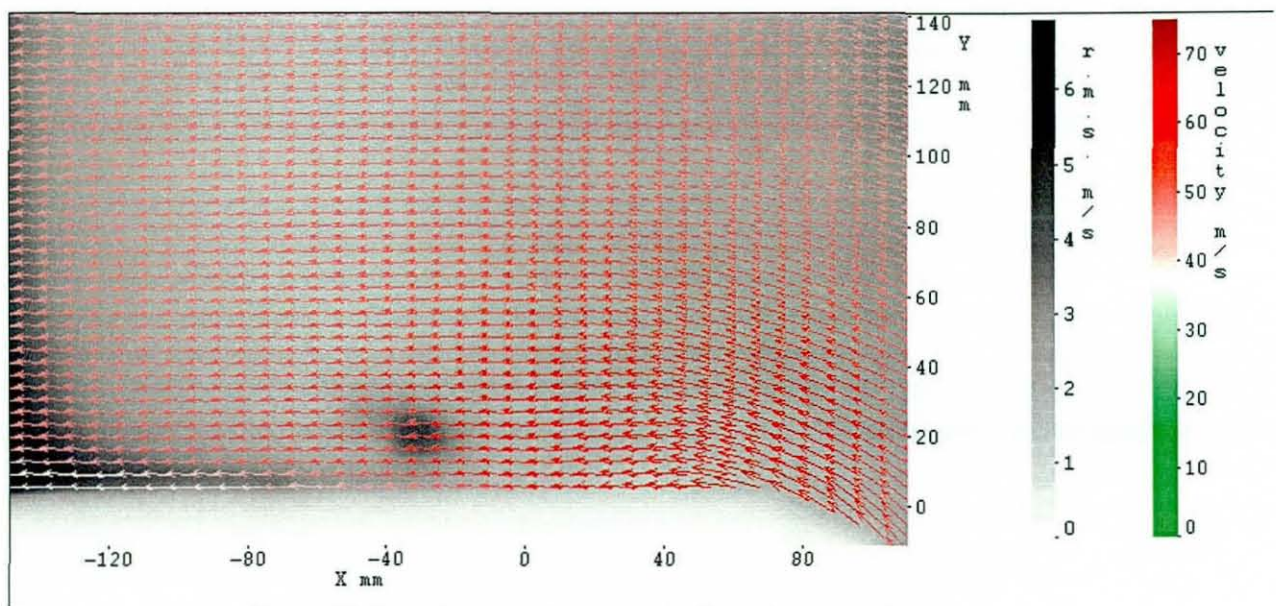
Figure 83 40mm front section in 40m/s flow, clean tunnel

It is difficult to determine the state of the separated shear layer from the time-averaged PIV results, because, as was seen in the previous section, there is vortex shedding and flapping in the shear layer as it comes off the leading edge radius. Given that the width of the separation bubble does not change much between 20m/s and 35m/s, it is suggested that the increased momentum of the flow being entrained into the shear layer is the controlling factor over the separation length, and the effect of Reynolds number on the boundary layer then causes the separation bubble to collapse when the transition point moves upstream of the end of the radius.

4.4.3   Freestream turbulence effects

The individual frames in Section 4.4.1 showed that additional turbulence had a strong effect on the flow around the radius where there were large separation regions. In order to examine the effect of turbulence on the time averaged flowfield, the flow around the

30mm radius will be examined, starting with Figure 84 showing the results in 1.38% turbulence, at 15m/s. Comparing this figure with Figure 79 shows that the separation bubble has been significantly reduced in size, with the separated shear layer now 20mm from the model and the reattachment point, which is not very clear in this image, at approximately x=-110mm. The reduction in the separation length was expected from the pressure results in Section 3.4.1. The peak r.m.s. velocity has also increased from 8.9m/s to 11.7m/s. It is useful to note that the freestream velocity in the U direction, in the very top left hand corner of the uncropped vector field is almost identical for the first turbulence grid, at 17.1m/s, and the clean tunnel case, where it was 17.4m/s. This gives additional confidence in the procedure of setting the reference velocity using a pitot tube upstream of the turbulence grid.
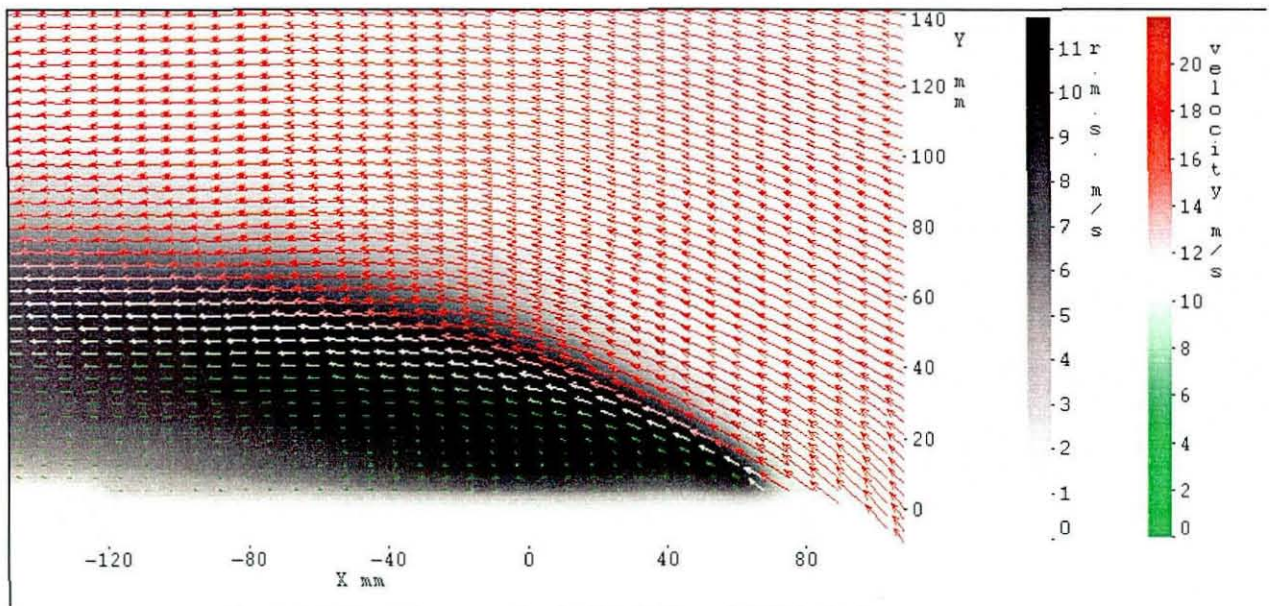
Figure 84 30mm front section in 15m/s flow, 1.38% turbulence

In the balance results, it was often seen that the second turbulence grid, at 1.45%, produced higher drag coefficients than the first turbulence grid. Figure 85 shows that the separation bubble was bigger for this turbulence level, with the separated shear layer at a maximum of 35mm from the model as it was at higher Reynolds number in the clean tunnel case, and the reattachment point out of the field of view. The peak r.m.s velocity of 9.0m/s is barely raised above that of the clean tunnel case. The reason why this grid produces turbulence that has less effect than would be predicted is still unclear. The results for 1.38% and 1.45% turbulence for the 40mm front at the same speed, which show evidence of intermittent separation and a very thick time averaged

boundary layer, are almost indistinguishable, with a maximum difference between velocity vectors of around 1m/s in the recirculation region.
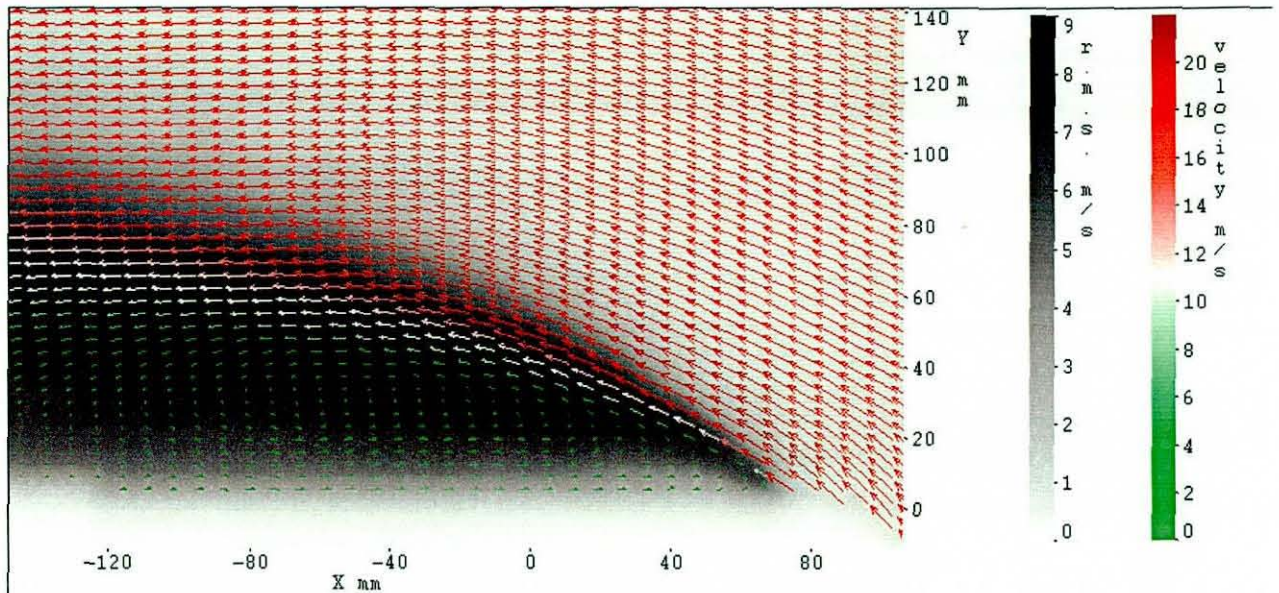
Figure 85 30mm front section in 15m/s flow, 1.45% turbulence
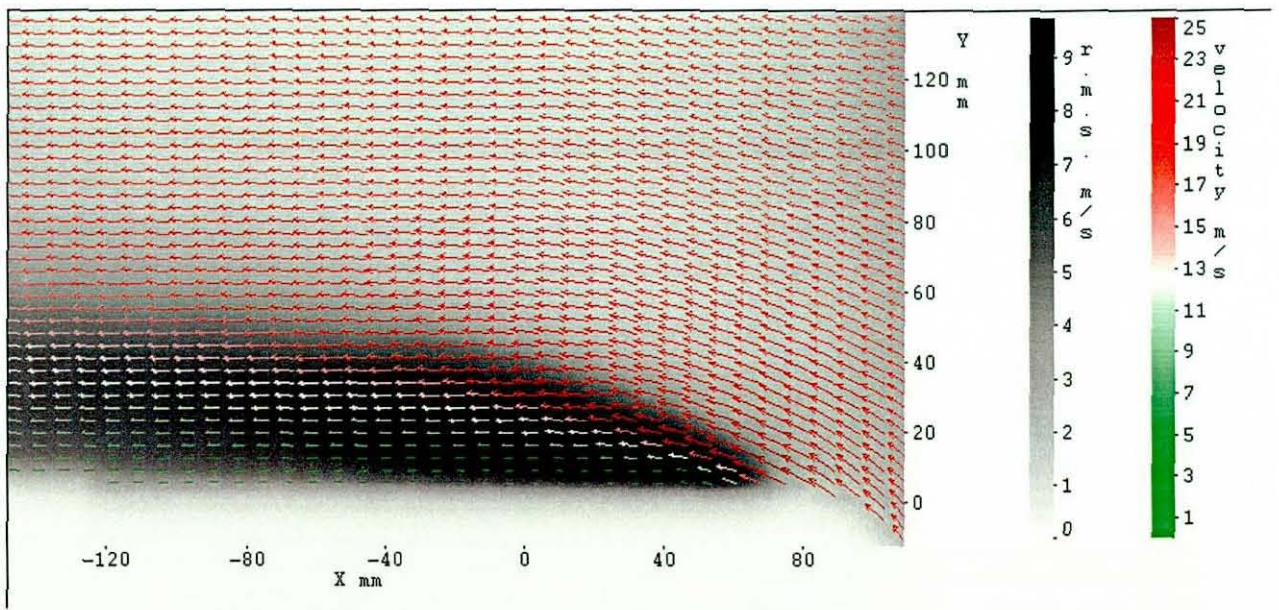
Figure 86 30mm front section in 15m/s flow, 3.41% turbulence

When the turbulence intensity is raised to 3.41% as shown in Figure 86, the 30mm radius also has evidence of only intermittent separation, with high r.m.s. values of up to 9.7m/s in the time averaged boundary layer. The drag results in Figure 25 indicate that the time averaged drag coefficient is just pre-critical at this speed, and the PIV results support this – the flow is neither smooth nor fully attached.

The results in Figure 26 for the 30mm front section with 5.13% turbulence show that the 15m/s case falls right in the middle of the critical region, between the high C_D pre-

111

critical results and low C_D post-critical results – which means that it is likely to display an intermittent separation. The time averaged flowfield for the 30mm radius in 5.13% turbulence (Figure 87) shows a similar result to the 3.41% grid, but with a smaller region of high r.m.s. velocities, and a lower peak r.m.s. value of 7.3m/s. The high r.m.s values are evidence of the expected intermittent separation, and the flowfield still does not show the fully attached characteristic of the high Reynolds number clean tunnel results in Figure 83.
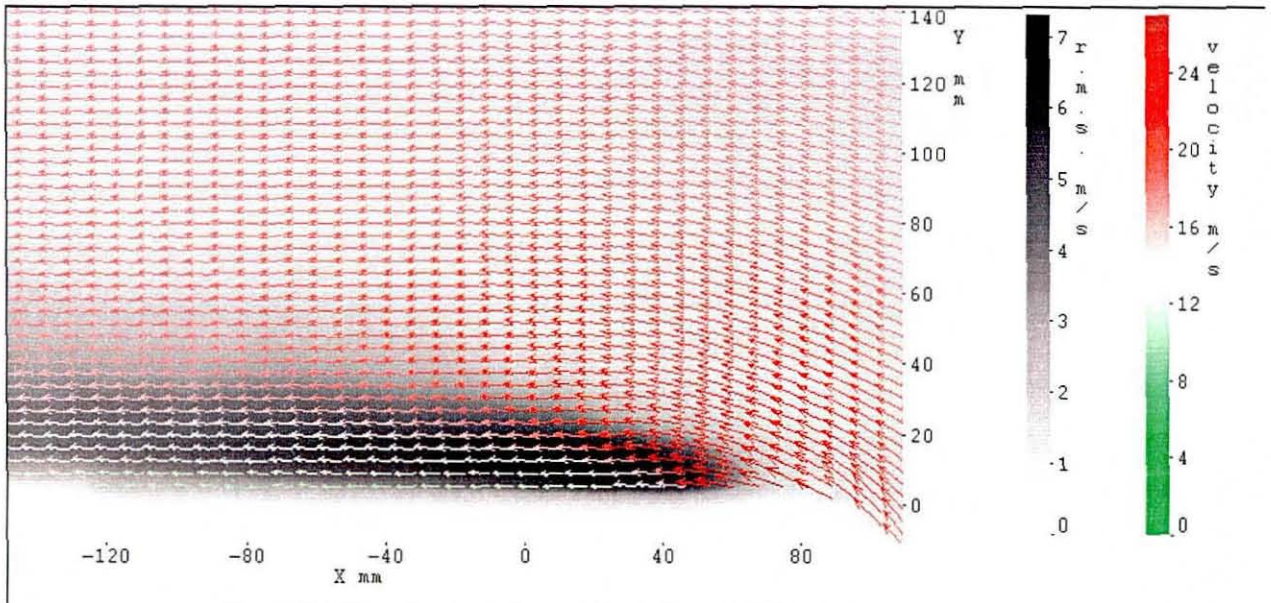
Figure 87 30mm front section in 15m/s flow, 5.13% turbulence

As was indicated by the instantaneous flowfields, the time averaged results show that increasing the turbulence level increases the unsteadiness in the free shear layer, leading to up to a 30% increase in r.m.s. velocities for the lowest turbulence level. As the turbulence intensity rises, the instability in the separation region becomes greater, leading to smaller separation bubbles in the time-averaged flowfields, and correspondingly lower peak r.m.s. values (but still higher than in the clean tunnel, up to and including in the 3.41% case). The additional turbulence is adding significantly more energy into the separated shear layer, causing earlier reattachment and ultimately forcing the flow to undergo transition at the highest turbulence level, intermittently at 15m/s for the 30mm, but fully for the 40mm radius and for the 30mm at higher Reynolds numbers.

112

4.5 Summary

- The PIV results showed that the 1-box model is sufficiently long that there is separation and reattachment along the side of the model at low Reynolds numbers. As the Reynolds number increased, the separation bubble became shorter, and at a sufficiently high Reynolds number the separation bubble collapsed and the flow became fully attached around the radius, for both the 30mm and 40mm front radii. This confirmed the general analysis put forward in Section 3.2.1 where the flowfield was described as having a pre-critical phase with separation and reattachment, a short critical region where the separation bubble collapsed, and a post-critical region with fully attached flow around the radius.

- In the instantaneous results for the clean tunnel, it was seen that there is a significant amount of vortex shedding from the point of separation, which occurred at the end of the radius. There was some evidence of unsteadiness even at low Reynolds numbers, but the vast majority of the frames recorded a relatively stable separation bubble with recirculating flow at the model surface and vortices in the shear layer.

- Increasing the freestream turbulence caused the unsteadiness to increase, and frames where the flow had become attached around the radius were more frequent. The vortices more often reached the wall of the model causing increased unsteadiness and interrupting the reversed flow. Further increases in turbulence intensity caused more flapping of the free shear layer and its intermittent collapse.

- The time averaged results with increased turbulence also showed increased unsteadiness in the separated region, with up to 30% increases in the r.m.s velocities. The time-averaged separation bubble was seen to get shorter, acting to reduce the pressure recovery length (Section 3.4.1).

Chapter 5

Edge radius optimisation with different models

This chapter describes the extended edge radius tests that were carried out with a 2-box model at model scale, and the MIRA reference vehicle at full scale. The 2-box model results extend the research in the Loughborough model scale tunnel to a more representative vehicle. This model is used to investigate the effect of raised freestream turbulence on the optimisation of leading edge radius in the presence of a pressure gradient on the bonnet. The MIRA reference model is used to validate the effect of turbulence on transcritical Reynolds number based on edge radius, using the turbulence grid technique in the MIRA full scale tunnel, against the 1-box and 2-box results at model scale.

5.1   2-box model

5.1.1   Model details and test method

The 2-box model has the same width as the 1-box model in order to reuse the top half of the front sections, but uses a shorter roofline and longer body more typical of a modern SUV. These decisions set the scale at 1:5. The model details are given in Table 9.

	2-box
Length L	960mm
Width W	390mm
Height H	320mm
Front cross-sectional area A	0.1248m^2
Blockage ratio	4.99%
Front edge radii	10mm – 100mm in 10mm steps

Table 9 Details of 2-box model sizing

Figure 88 2-box model mounted in the Loughborough wind tunnel

116

Figure 88 shows the 2-box model in the Loughborough wind tunnel, and Figure 89 is a detailed drawing of the model with dimensions. The test method for the 2-box model was the same as for the 1-box, but no data was captured for the model at yaw, as little value was seen in following up the results for the 1-box where the transcritical Reynolds number was insensitive to yaw.
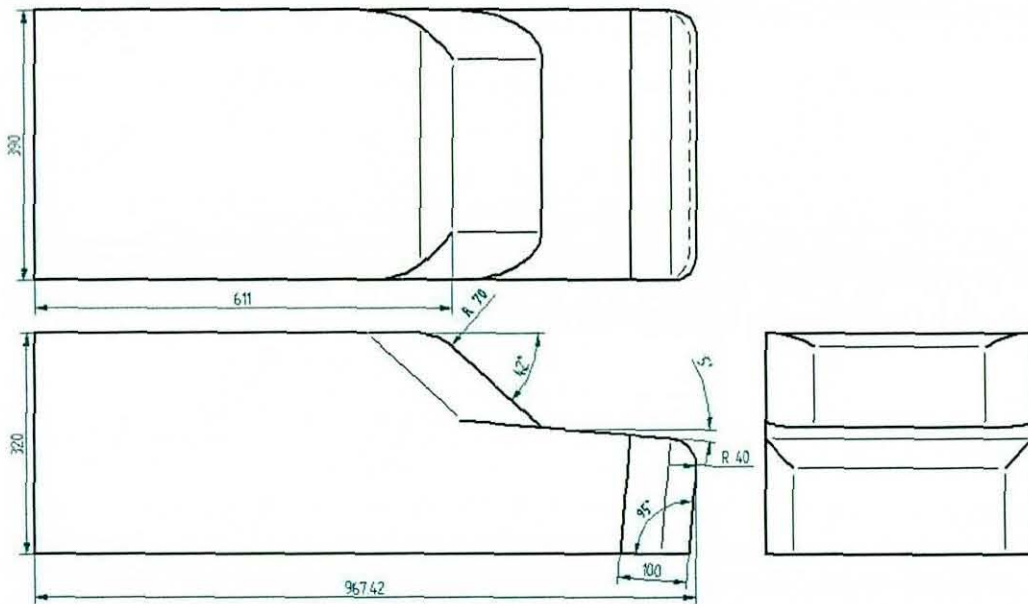
Figure 89 Dimensioned drawing of the 2-box model (40mm front section fitted)

5.1.2   Clean tunnel drag results

The drag results for the 2-box model are presented as C_D against Reynolds number based on frontal area in Figure 90. In comparison with the results for the 1-box model (Figure 11), the most obvious difference occurs for the largest radii. For the 1-box model, the curves for the 80, 90 and 100mm radii smoothly curved towards the approximately constant post-critical drag coefficient, whereas they do not here. The transition for the 70mm radius is a lot sharper and the reduction in C_D greater. The radii on the A-pillars and windscreen-roof edge (downstream of the front section) were set at 70mm to prevent significant separations, but it is possible that this transition region is partly due to those radii. The increased streamlining of the 2-box model gives lower drag coefficients throughout the range of Reynolds numbers tested, comparing like radii with the 1-box model.

117
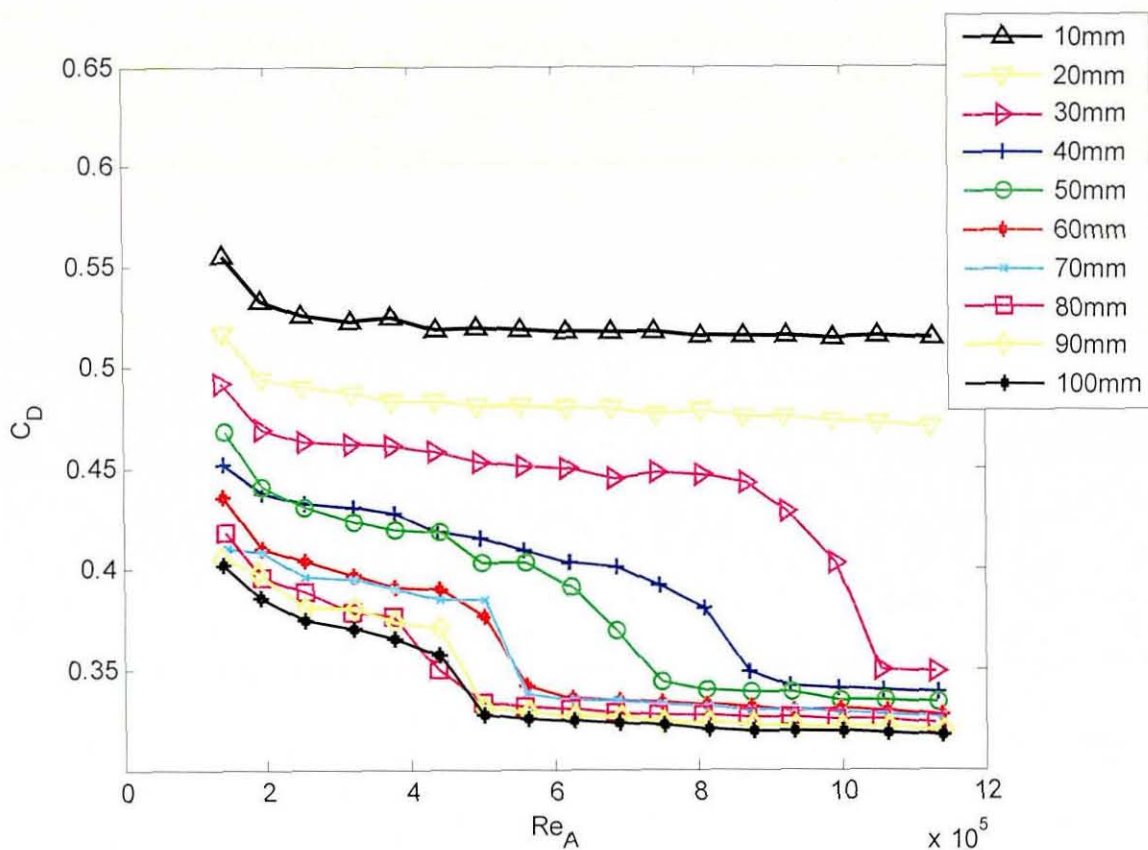
Figure 90 Variation in drag coefficient with Reynolds number based on frontal area for the 2-box model (edge radius as a parameter)
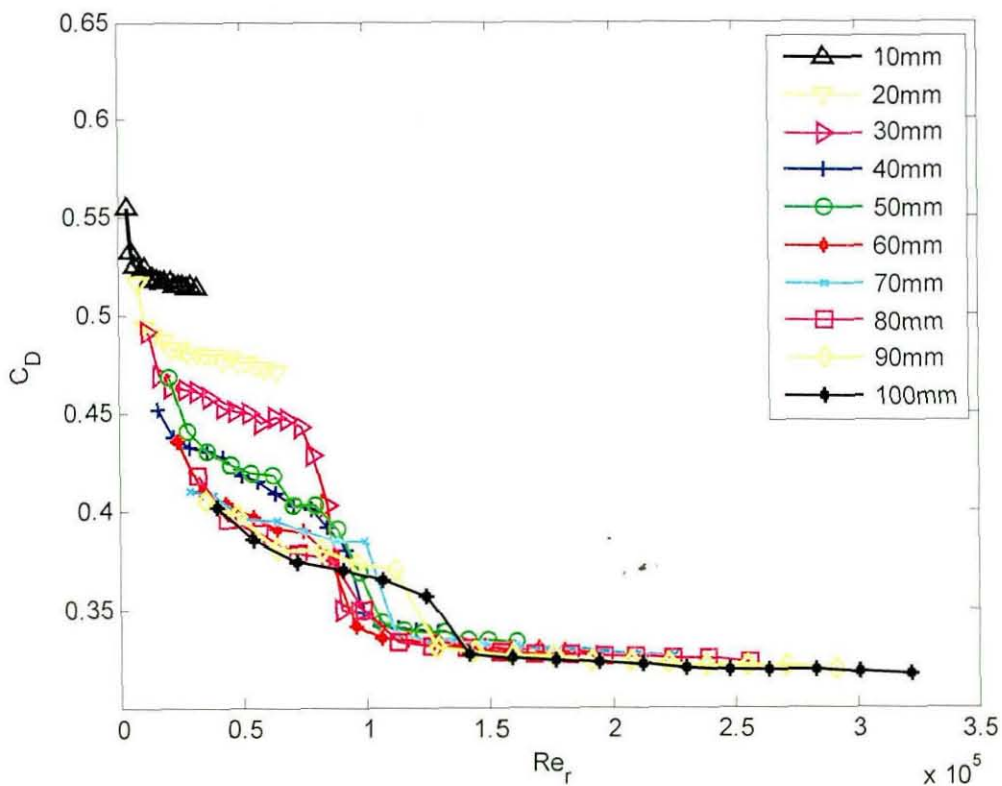
Figure 91 Variation in drag coefficient with Reynolds number based on edge radius for the 2-box model (edge radius as a parameter)

Figure 91 shows the drag results for the 2-box model plotted against Re_r. The transition for the 90 and 100mm radii is slightly delayed, supporting the idea that the A-pillars may be causing some effect on C_D, which would give a higher than expected transcritical Reynolds number. However, the delay is only by a small amount, and there is no obvious similar effect on the 80mm radius. There is a positive pressure gradient on the bonnet and the results indicate that this may cause the formation of a separation bubble which persists up to the critical Reynolds number even for the larger radii, and then collapses in a similar way to the separation bubbles on the smaller radii that were also apparent on the 1-box model.
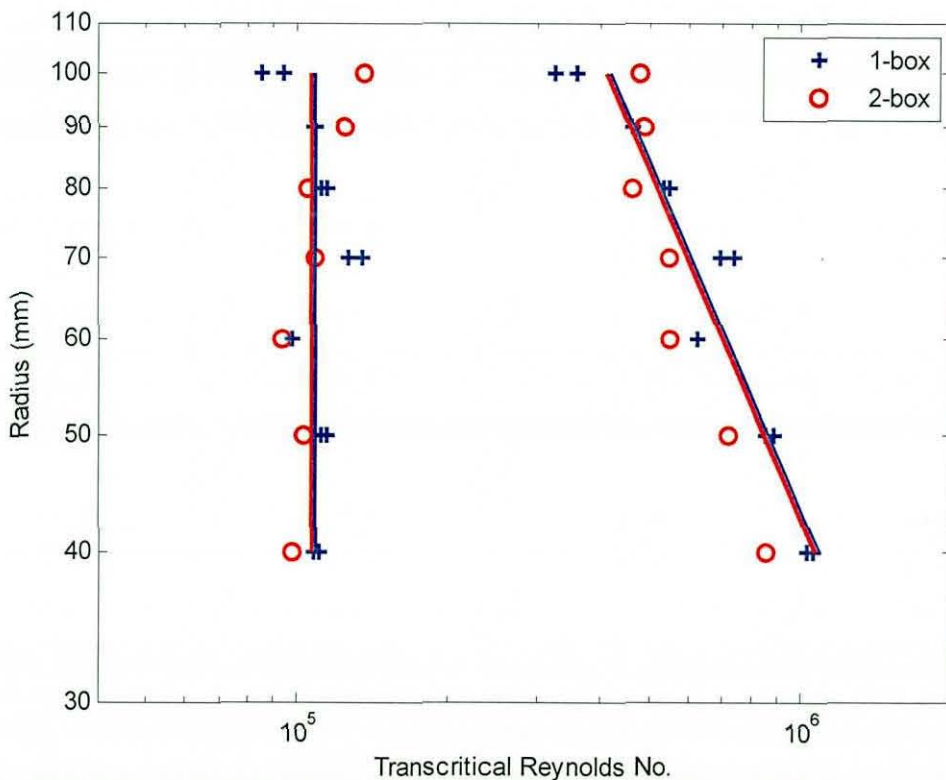
Figure 92 Variation of transcritical Reynolds number with edge radius (model as a parameter)

Figure 92 shows the results plotted as transcritical Reynolds number against radius, as they were for the 1-box model with the transcritical Reynolds numbers based on the square root of frontal area on the right, and on edge radius on the left. The average transcritical Reynolds number based on edge radius for the 2-box model was calculated as $1.07*10^5$ using the same method as before, which is almost exactly the same as the value of $1.08*10^5$ for the 1-box, and compares well with Cooper's[4] value of $1.30*10^5$.

The results show that the 2-box model performs very similarly to the 1-box model. The main difference was that a clearly identifiable transition region occurred for the biggest

radii as well as the 40, 50 and 60mm radii, probably due to a combination of bonnet to windscreen pressure gradient and changes in the flow around the A-pillar. The larger radii (80 – 100mm) still show the same constant Reynolds number based on edge radius, which indicates that the flow around the leading radii still dominates, and the A-pillars are not thought to have a significant effect on the results.

5.1.3 Drag results with increased freestream turbulence

Figure 93 shows the variation in drag coefficient for the 2-box model with the 2nd turbulence grid installed. The curves are quite similar to the curves for the 1-box model (Figure 33). For the larger radii (>40mm) the curves drop rapidly towards the low drag post-critical condition, without showing the pre-critical condition where the drag stays high. This implies that when the turbulence is added, above very low Reynolds numbers there is no longer a separation bubble on the bonnet, because the increased turbulence provides a strong enough effect on the boundary layer to cause the flow to become attached above a Reynolds number (based on $\sqrt{A}$) of around 300,000. The 2-box shape responds to the addition of turbulence in exactly the same way as the 1-box, so, for these types of simple shapes, the mechanisms that cause the different states – pre-critical, transition, post-critical – are similar, and are caused by the same interactions with the boundary layer on each model.

The average transcritical Reynolds numbers were calculated for the 2-box model using the method described above for the 1-box results. The results are shown in Table 10 and are substantially the same in both cases, apart from the 3.41% case, which is put down to errors in determining the transcritical Reynolds number because the variation of C_D with Reynolds number is smaller, and therefore the transcritical Reynolds number is harder to identify.

Turbulence intensity (%)	1-box model	2-box model
0.2	$1.08 * 10^5$	$1.07 * 10^5$
1.38	$0.54 * 10^5$	$0.56 * 10^5$
1.45	$0.56 * 10^5$	$0.58 * 10^5$
3.41	$0.44 * 10^5$	$0.29 * 10^5$
5.13	$0.41 * 10^5$	$0.38 * 10^5$

Table 10 Comparison of transcritical Reynolds number for the 1-box and 2-box models
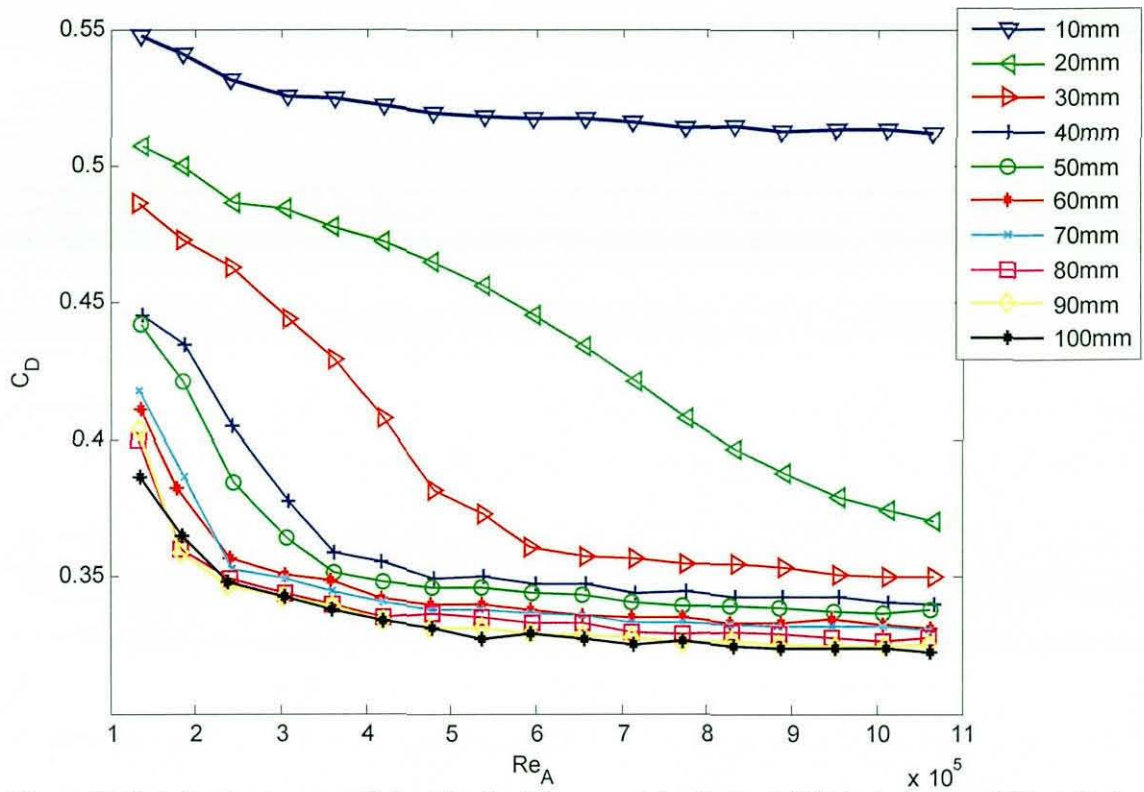
Figure 93 Variation in drag coefficient for the 2-box model with the 1.45% turbulence grid installed with Reynolds number based on frontal area (edge radius as a parameter)

5.2 Full scale model tests

5.2.1 Model details and test procedure

Tests were conducted in the MIRA tunnel using the MIRA reference car with a modified front end. The MIRA model has a number of possible rear end geometries, but the estate car configuration was employed in order to be most similar to the model scale geometry. Wooden additions were used to reduce the radius on the leading edge of the bonnet from 152mm to between 25mm and 100mm. The additional pieces extended across the front of the bonnet to the extent of the single radius so as to avoid the complication of the corners where 3 radii meet. Reynolds sweeps from 9 to 36m/s were used to identify the Reynolds sensitivity of the smaller radii, having previously established that the baseline MIRA reference model was not very sensitive to Reynolds number, in its estate car configuration.

Figure 94 shows the model in the tunnel with one of the wooden edge radii modifications fitted and a detailed drawing of the MIRA model is shown in Figure 95 (the estate car configuration is labelled option C).

Figure 94 MIRA reference vehicle with leading edge radius modification fitted in the MIRA full scale tunnel

Because the additional pieces only cover the main leading radius on the top of the front of the model, there is a sharp edge at the ends of each piece. An experiment where the

ends of the wooden radius piece were crudely faired into the corners of the model using shaped paper taped onto the ends found that it made no measurable difference to the results. Modifying only one radius also means that there will be significantly less variation in C_D over the range of Reynolds numbers tested.
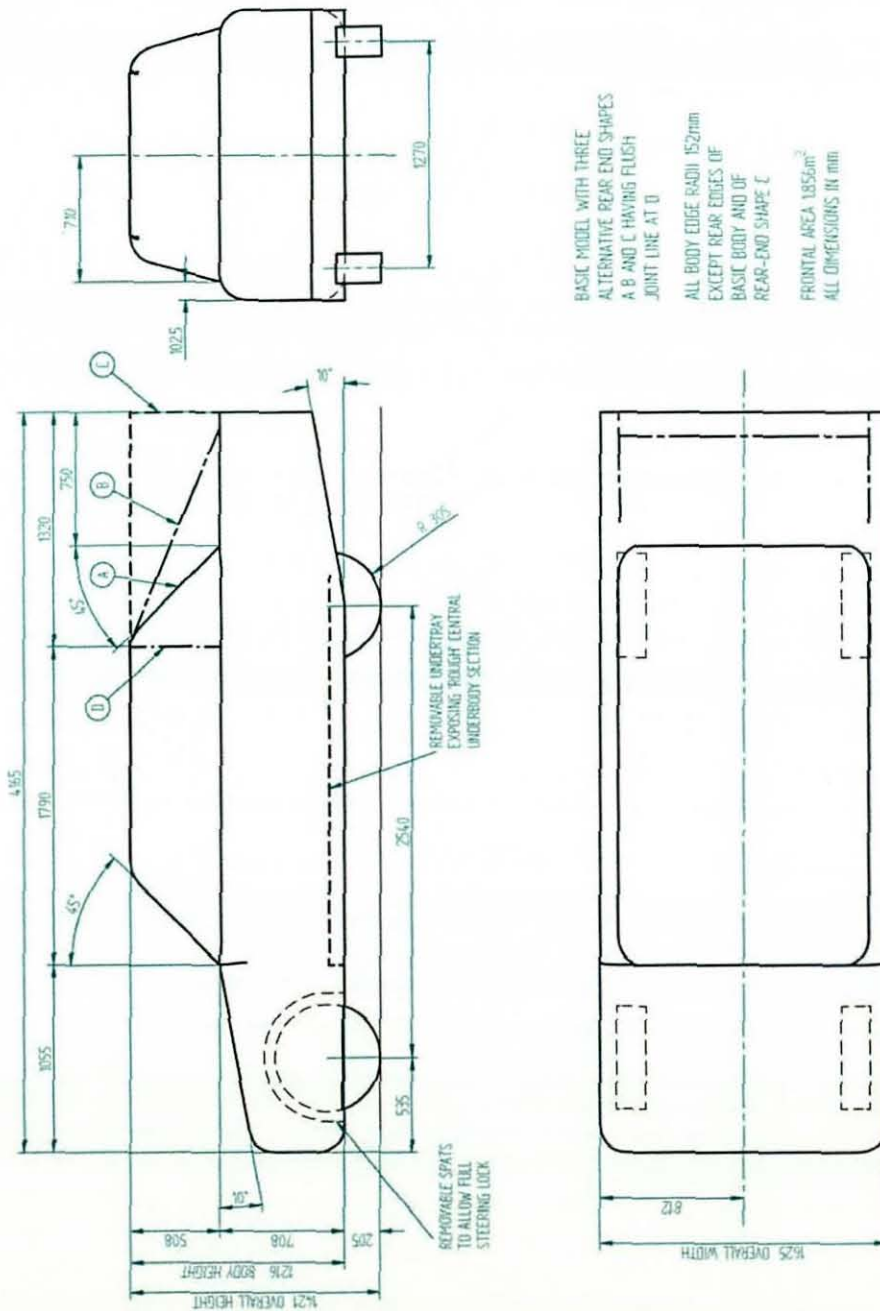
Figure 95 Dimensioned drawing of the MIRA reference model

5.2.2   Clean tunnel drag results

The aim of the full scale tests, as previously stated, is to show the applicability of the techniques used at model scale. The reference vehicle used is designed to show very little separation. Since it has a bigger radius on the leading edges than any tested at

123

model scale, no Reynolds sensitive separation would be expected for the baseline MIRA reference model with 152mm leading edge radii.
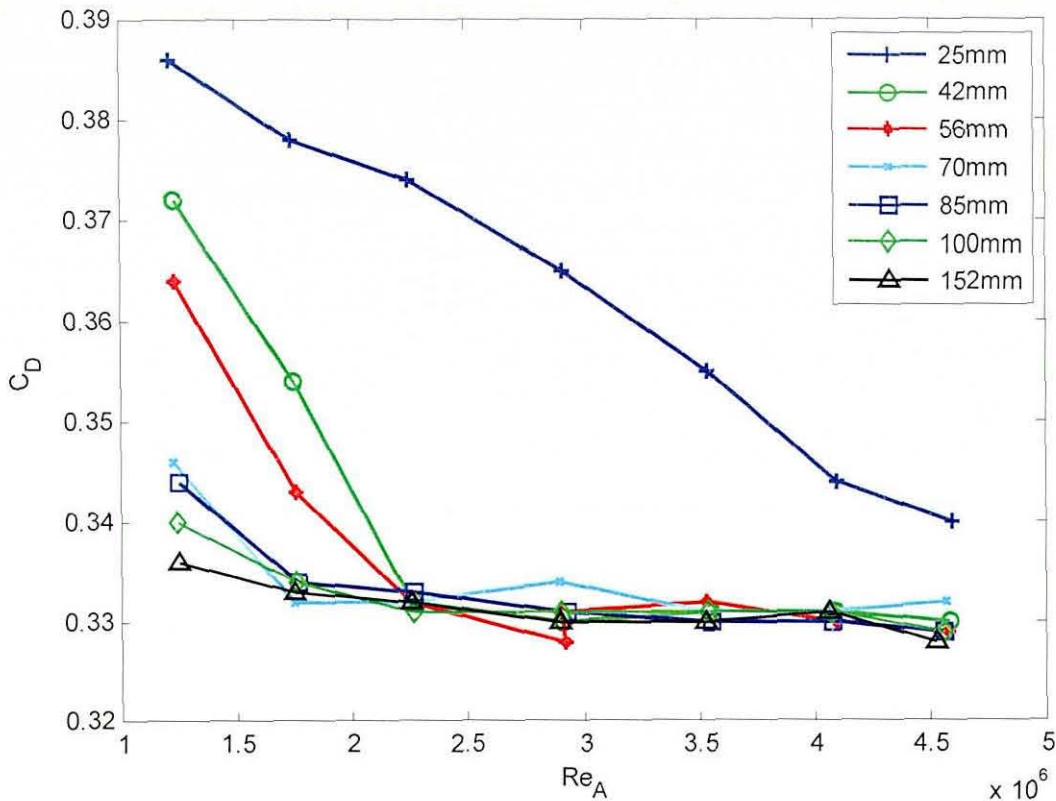
Figure 96 Variation of C_D with Reynolds number R_A for the MIRA model, Tu=1.8% (edge radius as a parameter)

Figure 96 shows the C_D results for the MIRA reference vehicle in the clean tunnel (turbulence intensity 1.8%) for all radii against Reynolds number based on the square root of frontal area. The smaller radii show some Reynolds sensitivity. The 42mm and 56mm front sections show a transition from higher drag to lower drag over a short Reynolds number range, and then a relatively constant post-critical drag coefficient, whilst the 25mm radius has a falling drag coefficient but does not undergo a full transition to the low constant value of the others. The overall variation of the drag coefficient at full scale is much less than at model scale, but the change made is also much less significant, affecting only one leading edge of the car rather than three as for the models. The MIRA reference model is also a more complex geometry. On the 2-box model with the 30mm radius on 3 leading edges, the C_D fell from 0.47 to 0.33. On the MIRA model with the 25mm radius the C_D fell from 0.39 to 0.34, and the post-critical C_D was around 0.33, which is approximately 2.3 times less variation in C_D. Since the top radius is the longest, this is approximately as expected. In terms of transcritical Reynolds numbers and the characteristic sensitivity to Reynolds number shown by the

shape of the curves, these results are similar to the results for the 1.45% turbulence results at model scale (Figure 93).
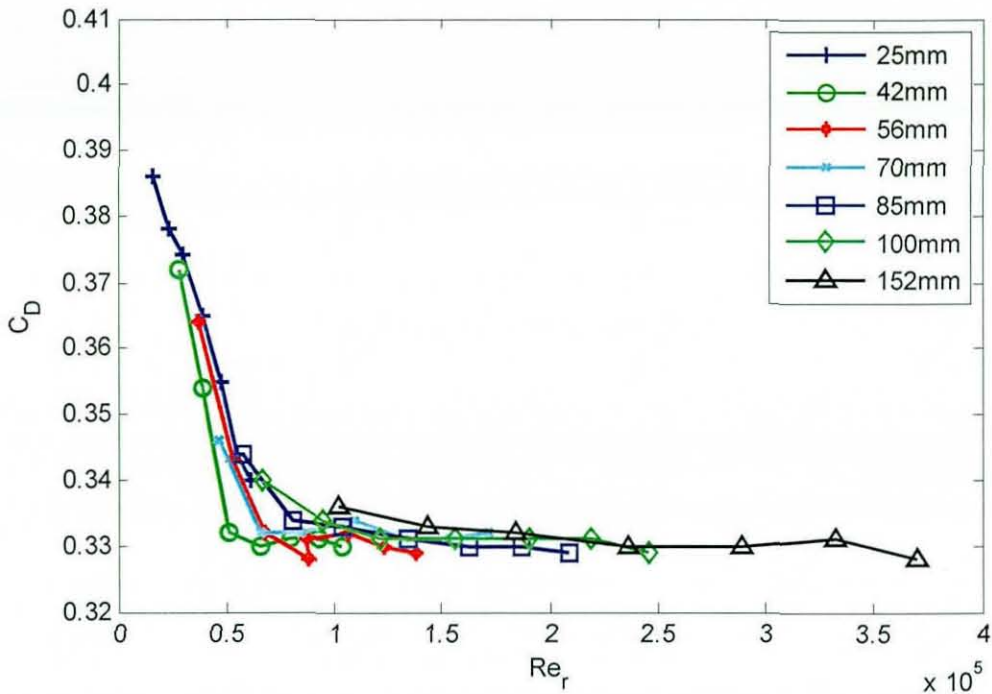
Figure 97 Variation in C_D with Reynolds number Re_r for the MIRA model, Tu=1.8% (edge radius as a parameter)

When the results are replotted against Reynolds number based on edge radius (Figure 97) there is a much clearer similarity with the model scale results at raised freestream turbulence (for example Figure 93). The level of turbulence in the MIRA tunnel was measured as 1.8%, which is slightly higher than the 2nd turbulence grid produced at model scale. The transcritical Reynolds number Re_{rtcrit} is calculated to be $0.52*10^5$, which compares well with the 2-box result of $0.58*10^5$ at 1.45% turbulence.

There is therefore a good level of confidence from the clean tunnel results that, as predicted, an individual edge radius, for example 70mm, has the same characteristic variation with Reynolds number mounted to the full scale model as the 70mm radius did on the 1-box and 2-box models in the model scale tunnel.

5.2.3   Results with increased freestream turbulence

The model scale results showed that the largest effects were seen when the turbulence was increased from the initial very low level. At full scale the lowest level is relatively high at 1.8%, and the full scale grids produce turbulence intensities of 3.4% and 4.3%. It is therefore expected that the changes that occur will be less pronounced, but that significant effects will be possible.
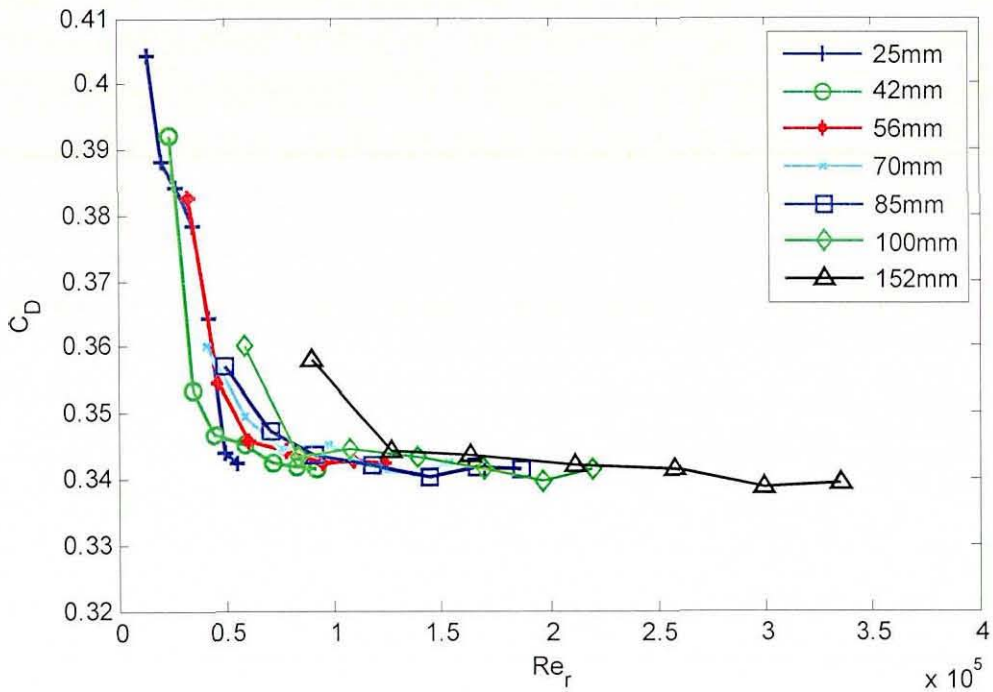
Figure 98 Variation of C_D with Reynolds number Re_r for the MIRA model, Tu=3.4% (edge radius as a parameter)
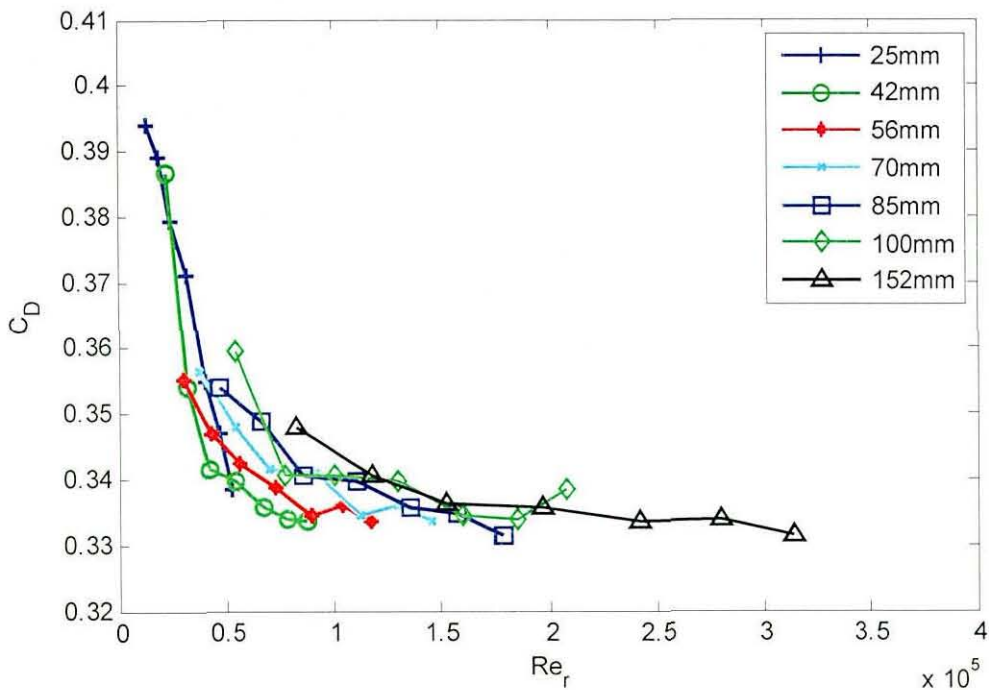
Figure 99 Variation of C_D with Reynolds number Re_r for the MIRA model, Tu=4.3% (edge radius as a parameter)

Figure 98 and Figure 99 show the results for the 3.4% grid and 4.3% grid respectively. As expected from the model scale results, there is some reduction in the transcritical Reynolds number, but it is a relatively small change compared to Figure 97. There is a problem of lower resolution of the data, because the full scale tunnel can only be operated at seven distinct speeds. This makes accurate identification of Re_{tcrit} more

difficult. Ignoring the two largest radii, which do not show a convincing transition region (only the lowest point, where the tunnel speed is at its least stable, is at all higher than the others), Figure 98 shows a very tight group of trancritical Reynolds numbers for the various radii, while the spread is larger for Figure 99.

The transcritical Reynolds numbers were extracted from this data using the same method as previously described, and the results are plotted in Figure 100. This figure shows the results for both model scale vehicles and the MIRA reference model, and it is clear that they all fall on the same curve. A best fit is plotted for all the data using the fit $Re_{rtcrit}=6.4*10^5*Tu^{-0.33}$. This is almost exactly the same as the fit to the 1-box data alone, which was found to be $Re_{rtcrit}=6.4*10^5*Tu^{-0.32}$ in Section 3.2.3.
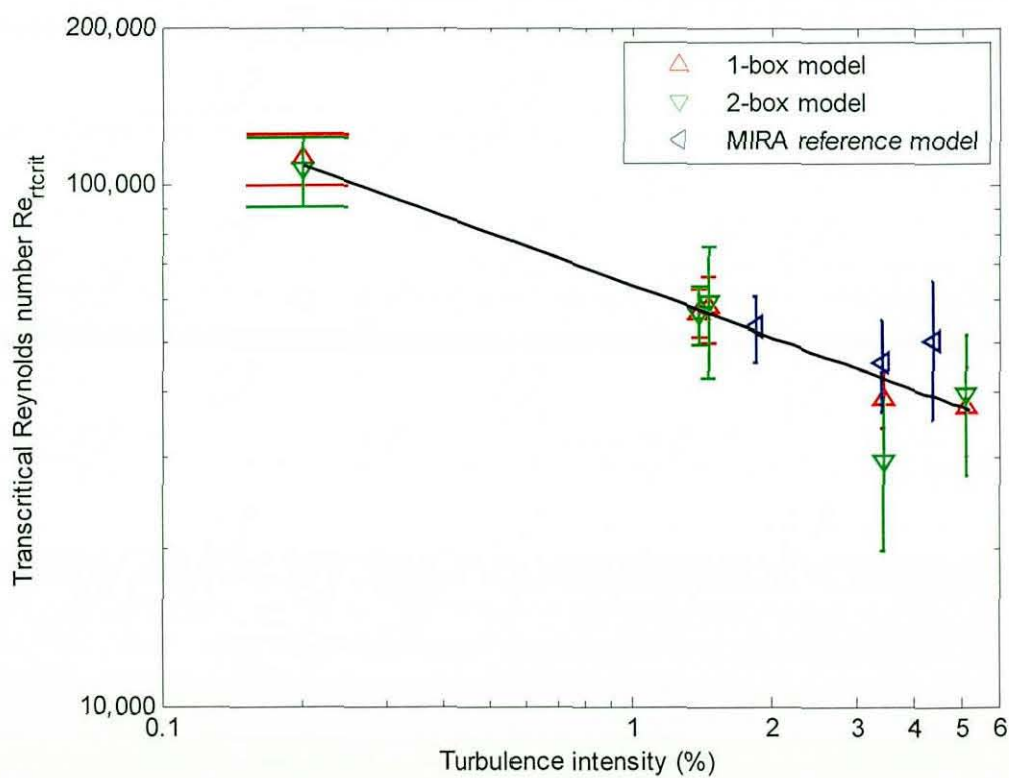
Figure 100 Variation in average transcritical Reynolds number with turbulence intensity for all three models (error bars show ±1s.d.)

As was seen for the 1-box model alone, Figure 100 shows that the biggest change in transcritical Reynolds number at model scale occurs between the clean tunnel result and the first two turbulence grids. This means that finding any difference between one turbulence case and another in the full scale tunnel is more difficult. However, this result has implications for the comparison of data recorded in different tunnels, where the turbulence intensities are dramatically different. The MIRA tunnel also appears to offer, in its standard configuration, a turbulence environment that would produce results

127

less sensitive to typical variation in on-road turbulence intensity than would be the case in a tunnel with very low turbulence – which is normally considered to be the ideal scenario.

It is worth noting that only 5 of the 7 radii tested at full scale showed convincing transcritical Reynolds number, and it is suggested that a useful extension to this work would be to increase the number of radii tested in the range that do go through the transcritical Reynolds number within the speed range available in the MIRA tunnel.

5.2.4 Effect of turbulence on the post-critical drag coefficient
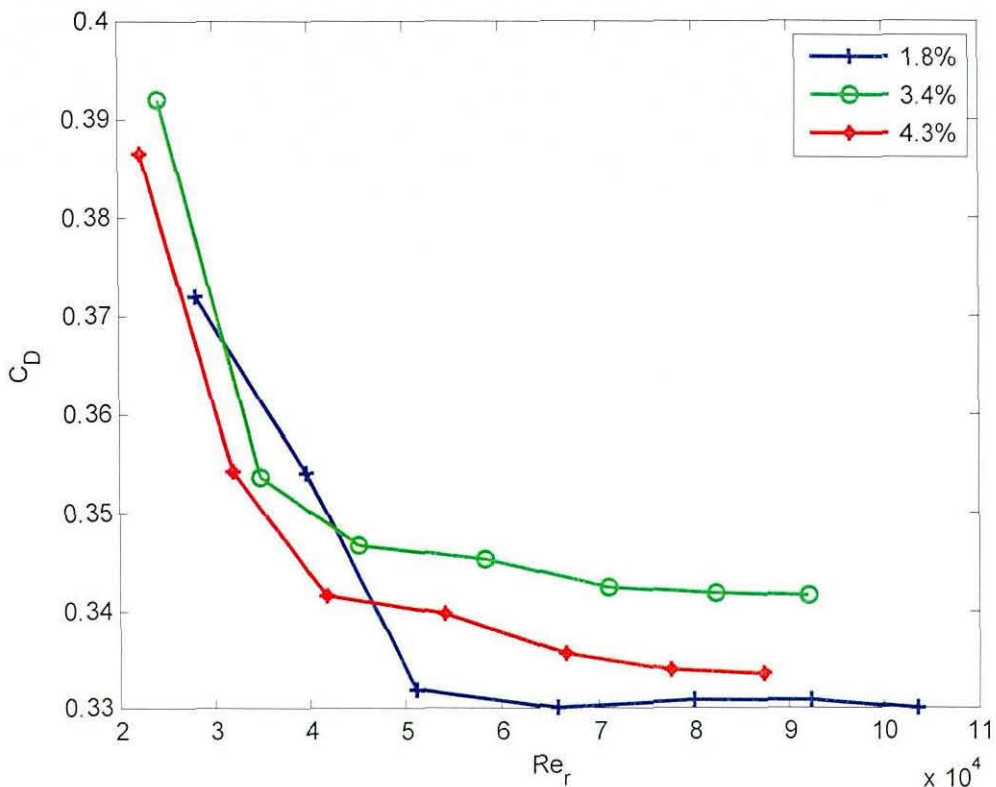
Figure 101 Variation of C_D with Reynolds number for the 42mm front radius at full scale

The three full scale turbulence levels are compared in Figure 101 for the 42mm front section only. In a similar manner to the model scale results, the C_D values for raised levels of freestream turbulence drop below the clean tunnel result, and then cross over and remain higher by up to 12 counts. The post-critical C_D is higher for the 3.4% grid than the 4.3% grid. This result was repeated in every test made at full scale, and the magnitude of the difference is significantly larger than the correction for the reference velocity, giving some confidence that it is a real effect.

128

5.2.5   Clean tunnel lift results

In the full scale tunnel there were some subtle differences in the results, compared to the 1-box and 2-box results. The first of these was that the overall lift results (Figure 102) had a more obvious divide between pre-critical and post-critical flows than at model scale.
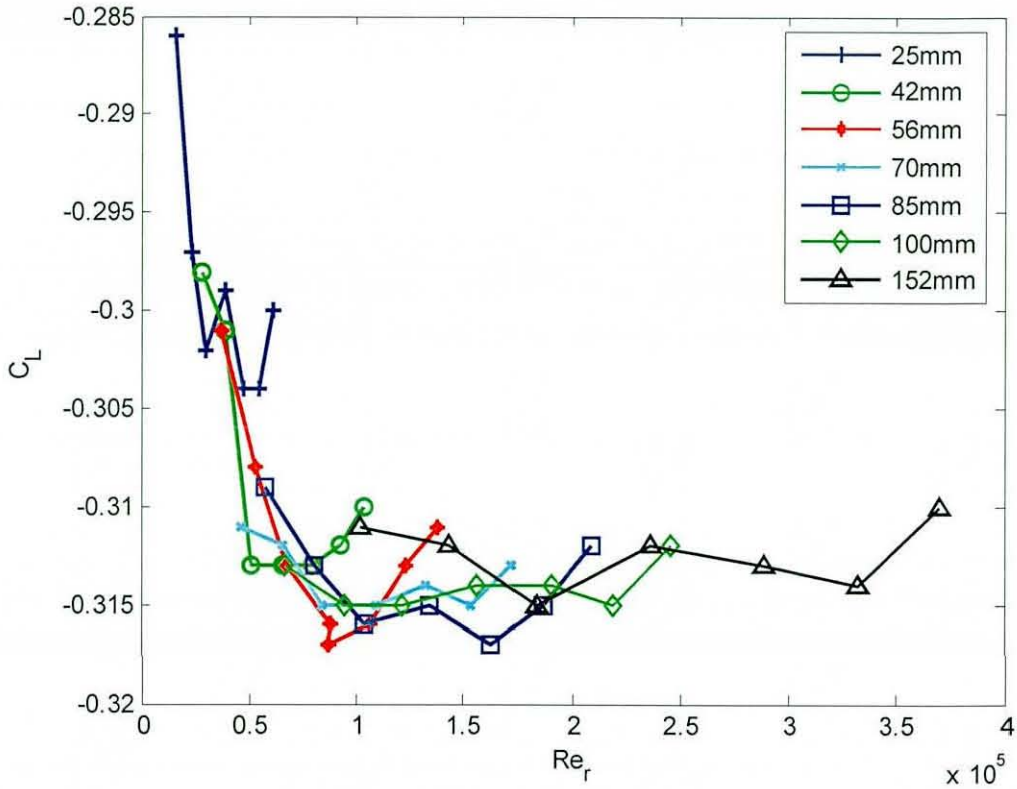
Figure 102 Variation of lift coefficient with Reynolds number based on edge radius for the full scale model (edge radius as a parameter)

At model scale the overall lift coefficient varied significantly between front sections at high Reynolds numbers, but on the MIRA reference car this is not the case – the final lift coefficient for each radius is broadly similar, and the trends are also quite close. There is a much clearer distinction between the critical and post-critical regions in this figure compared with Figure 37. It is still of value to split the lift between front and rear, as shown in Figure 103 and Figure 104.
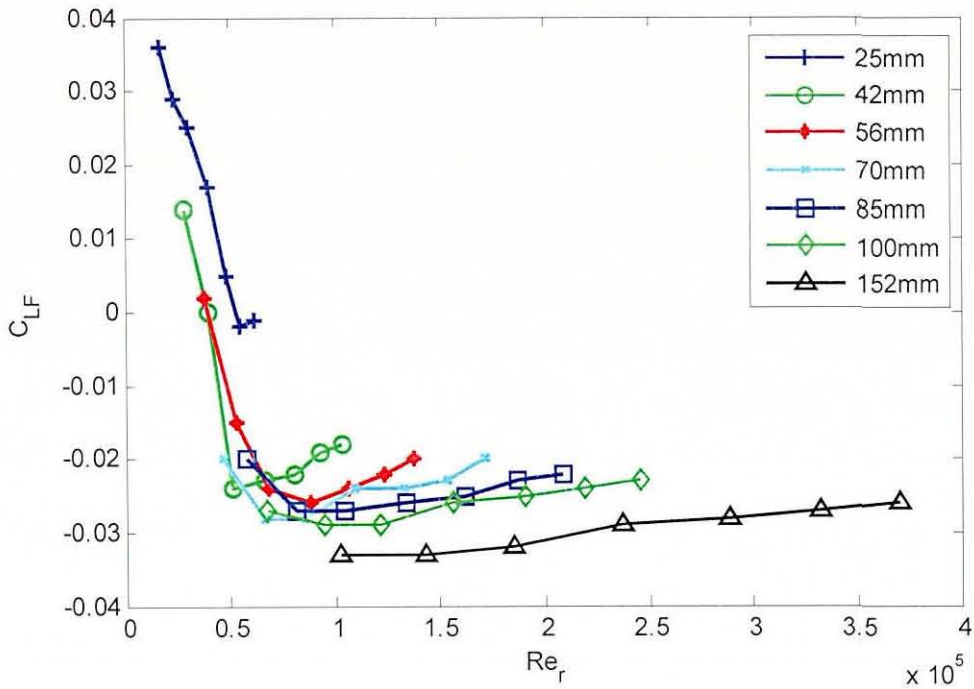
Figure 103 Variation in front lift coefficient with Reynolds number at full scale (edge radius as a parameter)

The variation in front lift is much smaller than it was at model scale, as would be expected, over a generally higher Reynolds number range. The final trend in post-critical front lift is slightly positive, where in Figure 38 it was slightly negative.
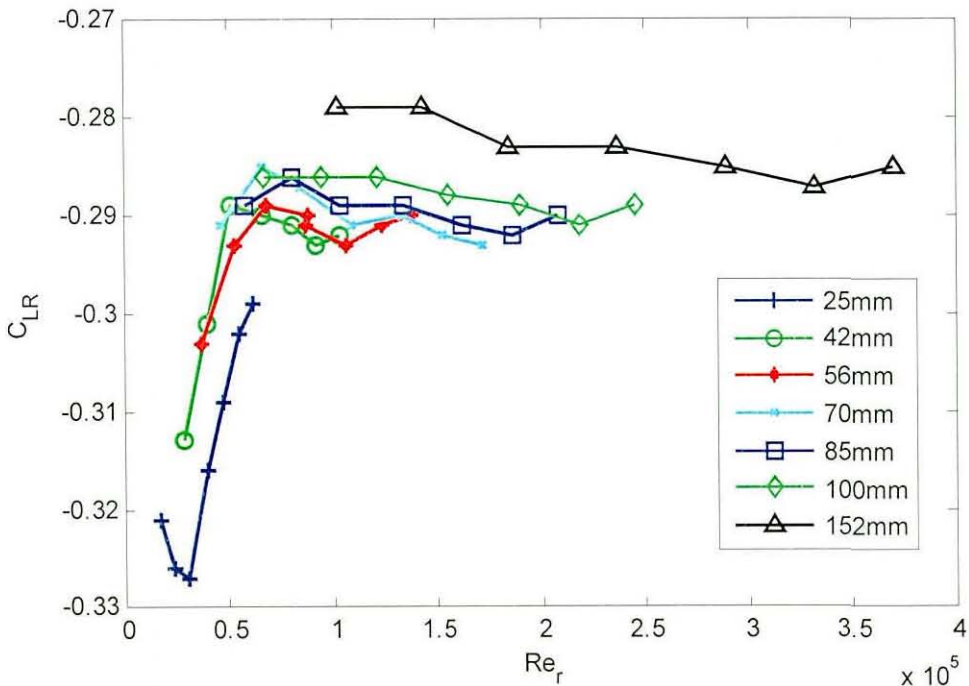
Figure 104 Variation in rear lift coefficient with Reynolds number at full scale (edge radius as a parameter)

The variation in rear lift is also smaller than it was at model scale. The post-critical lift has a slight negative trend, as it does in Figure 39, and the values are lower than they

were at model scale, which is probably due to the presence of the diffuser on the MIRA reference car. The fact that both front and rear lift vary only slightly and in opposite directions at full scale is probably the main driver for the relative stability of the overall lift coefficient at higher Reynolds numbers.

5.2.6   Effect of increased freestream turbulence on lift

The front and rear lift results at full scale are shown in Figure 105 for the 42mm radius only. They follow the same general trend as the model scale results in Section 3.3. The effects on front and rear lift seem similar to each other, as they did before. The rear lift is not so dramatically affected as to suggest that the diffuser performance was significantly changed by the addition of turbulence (for the specific diffuser on the MIRA model).
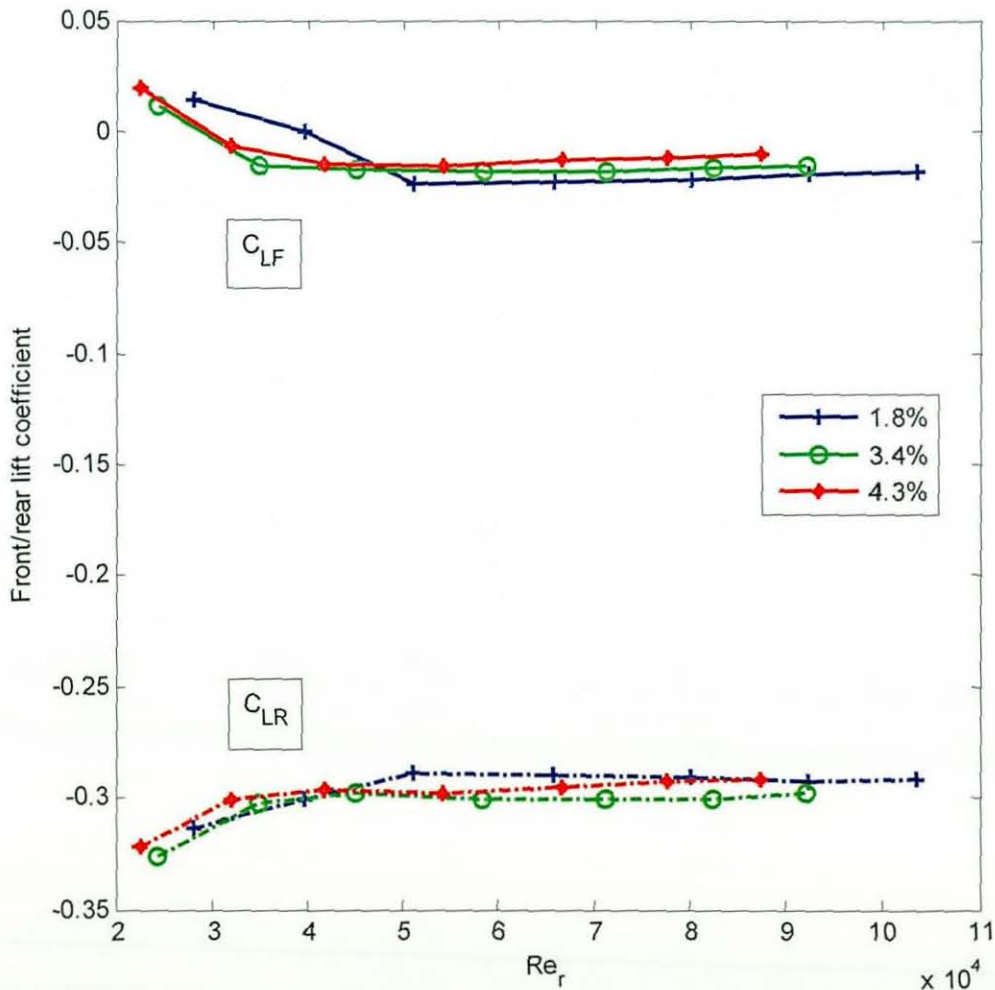
Figure 105 Variation in front and rear lift coefficients at full scale for the 42mm radius only (turbulence intensity as a parameter)

5.3 Summary

- The transcritical Reynolds numbers of the 2-box model are almost identical to the results of the 1-box model, leading to the conclusion that the model geometry was not the key factor, and the results can be carried forwards to more complex shapes. The full scale model in the MIRA tunnel also reproduced a very similar result, and a best fit line was drawn for the variation of transcritical Reynolds number with turbulence intensity that fits the data from all 3 models.

- In the clean tunnel, the pressure gradient over the bonnet of the 2-box model created a sustained separation bubble at low Reynolds numbers for even the largest radii, which then disappeared at high Reynolds numbers, giving a clear transition region.

- In raised levels of freestream turbulence, the clear transition region did not appear for radii larger than 50mm, and so the 2-box model results did not support the effective edge radius model. This was the only significant effect of using the more complex geometry model.

- The post-critical drag of the MIRA model was increased by the two raised levels of freestream turbulence, but 3.4% turbulence produced a larger increase in drag than 4.3% turbulence.

- The lift results for the full scale MIRA model also matched the results for the 1-box model, which supports the conclusion that the dominant features in the flowfield at full scale are the same as those which dominate the model scale results.

Chapter 6

The influence of freestream turbulence on the effects of backlight angle

The effect of basic parametric rear end shape changes has been widely reported [7-9, 21]. In particular there has been a significant body of work relating to the backslant geometry on fastback car shapes. In this geometry the interaction between 3D vortex flows and the more 2D base flows produces a particularly characteristic drag and lift response, which makes it an ideal test case for an investigation into the effect of additional freestream turbulence on that characteristic.

6.1   Model details and test method

The model used was the Windsor model, a simple bluff body with a replaceable rear section that allows for a range of 11 different back angles from 0 degrees to 40 degrees. The leading edges of the model had a radius of 50mm, but the radius is blended out to a sharp edge on the roof and floor (Figure 106), and the rear edges are all sharp.

Figure 106 The Windsor model installed in the Loughborough model scale tunnel

Figure 106 shows the Windsor model with the 35° backlight angle. The Windsor model has been used by Rover and Land Rover for many years, providing a good basis for comparison.

The test programme consisted of a Reynolds sweep from 5m/s to the maximum available tunnel speed, and a yaw sweep from -15° to +15° at the normal tunnel test speed of 40m/s, where possible, and the maximum tunnel speed where this was lower, for each back angle tested. The results are presented using Reynolds number based on

the square root of frontal area (Re_A). Re_A at 40m/s is $9.41*10^5$, and at 34m/s (the maximum speed with the highest turbulence grid) it is $7.5*10^5$, which is reasonably comparable. The turbulence was generated with the same grids as for the edge radius tests, giving turbulence intensities ranging from 0.2% (clean tunnel) to 5.1% (highest turbulence grid).

6.2   Results

The results are divided into 3 sections – the effect of Reynolds number, the effect of turbulence on the drag and lift vs. back angle characteristic at zero yaw, and the effect of turbulence on the yaw moment.

6.2.1   Reynolds number effects
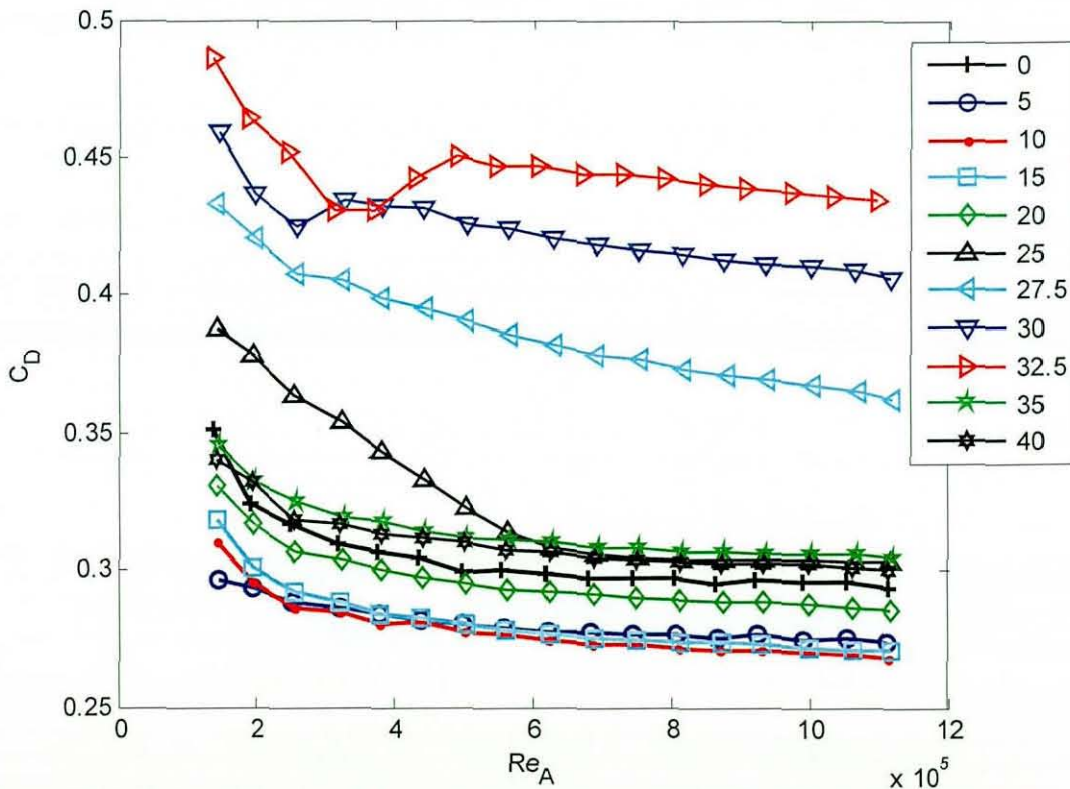
Figure 107 Variation of drag coefficient with Reynolds number for the clean tunnel (back angle as a parameter)

Figure 107 shows that there is little variation with Reynolds number for most back angles. The reduction in drag coefficient from the lowest Reynolds number over the first few steps is characteristic of this type of model (see also Chapter 3 and Cooper [4]). For the angles that approach the critical angle (27.5, 30 and 32.5) there is a continuous slow reduction in drag coefficient over the Reynolds number range, which can be attributed to the separation on the back angle, shown by Ahmed's [8] schematic of the flow at high back angle. There is however no identifiable pre-critical and post-

135

critical Reynolds number sensitivity with a change from high drag to low drag as there was with the front radius experiments. Above a Reynolds number of $7*10^5$ there is no Reynolds sensitivity for any of the other back angles, which is in agreement with the SAE standard recommendation of a minimum Reynolds number of $10*10^5$. Even for the back angles near the critical angle, there is less than 10 counts variation between $7*10^5$ and $10*10^5$. This pattern was repeated at all turbulence levels and no Reynolds number effects were seen, as expected for this type of model where the leading edge radii were selected to be reasonably Reynolds number independent. All further tests were carried out at a minimum Reynolds number of $7.5*10^5$ as this has been shown to be sufficient for this model, including for the highest turbulence level where the maximum Reynolds number, due to the pressure loss across the grid, is $7.7*10^5$.

6.2.2   Drag and lift results with increased freestream turbulence

In order to validate the results of these tests a comparison was made with previous data. Figure 108 shows a comparison between Newnham (from the current study) and Windsor [49]. Windsor's results were obtained in the MIRA model tunnel, which had a closed working section at the time.
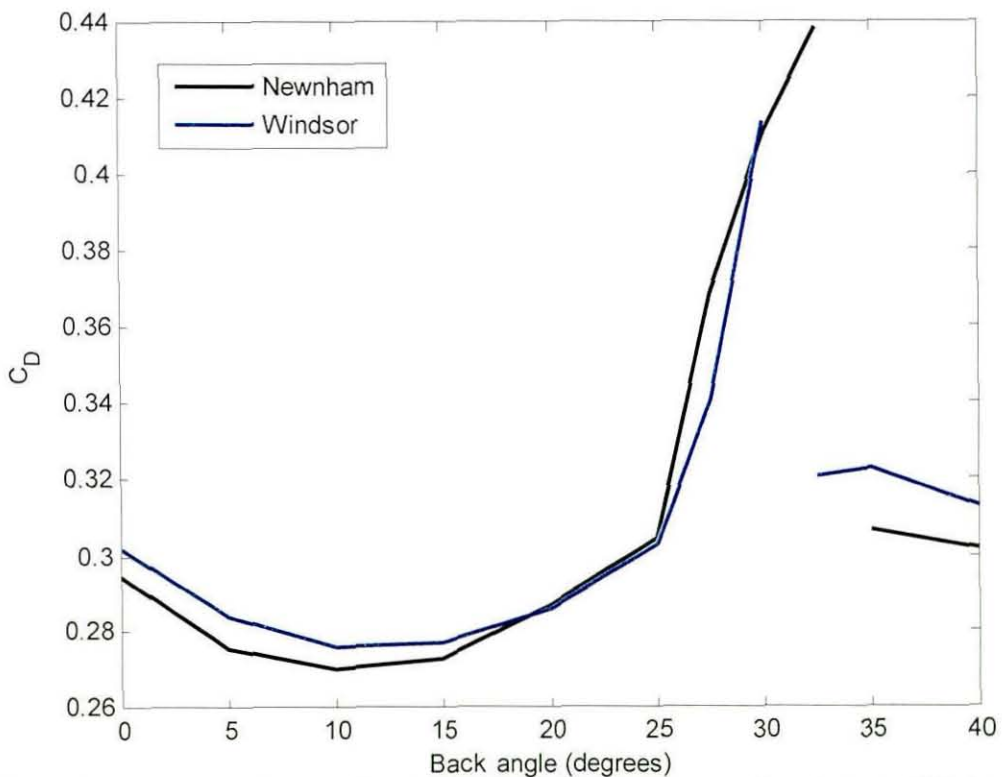
Figure 108 Variation in drag coefficient with back angle to compare Newnham and Windsor

The trend is accurately matched apart from the 32.5 degree back angle, which shows the high drag case in the Loughborough tunnel and the low drag case in the MIRA tunnel. This could be for a number of reasons but it is most likely to be a tunnel effect due to less blockage in the Loughborough tunnel. As widely reported [8, 9], there is a peak in drag around 30°, which is the point where the backlight flow switches between the two states that were described by Ahmed [8] – either a semi-attached flow with two trailing vortices, or a flow that separates fully at the end of the roof. In fact there are two competing effects, described by Ahmed, which appear in the results in Figure 108. The reduction in the size of the base, as backlight angle increases, reduces the base pressure linearly, which dominates the overall drag at low angles, between 0° and 10°. The second effect is that the vortex drag increases in a non-linear way as backlight angle increases, and this begins to take over above 10°, and beyond 25° this is the dominant effect, giving the dramatic rise in C_D. Bearman's results [10] showed that the variation of C_D with backlight angle is a function of vortex strength. At 35 degrees the backlight flow again separates cleanly at the roofline, as shown by Ahmed with wake surveys of the low drag case. This causes the drag coefficient to fall back to similar levels to those for 0°.
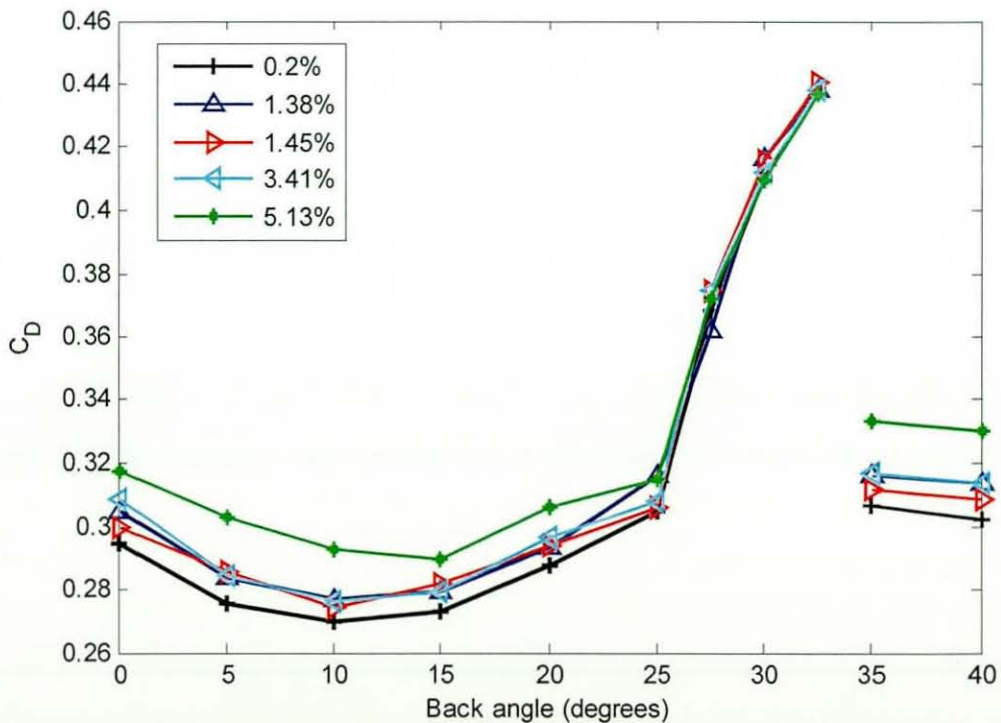
Figure 109 Variation in drag with back angle (Tu as a parameter)

With the introduction of freestream turbulence (Figure 109) the trends remain largely unchanged, and there is no change in the critical back angle, but there is an apparently

systematic increase in drag, which is largest for the highest turbulence level (5.13%). At low angles (0 – 20°) and very high angles (>35°) there is a drag increase of around 20 counts compared to the clean tunnel case. This is large in comparison to the change caused by the other turbulence levels. Between 20° and 27.5° the results with increased turbulence progressively reduce until they match the clean results.

Figure 110 shows the drag results as ΔC_D relative to the 0.2% turbulence case. It becomes clear in the figure that the effect of turbulence is shape dependent for all turbulence levels. For the 0° back angle, additional turbulence increases drag, by around 7 counts for the first two turbulence levels, 15 counts for 3.41% turbulence and 25 counts (approximately 8% more than the clean tunnel result) for 5.13%. As back angle increases, the drag increase gets smaller for the two highest turbulence levels, at first gradually and then more rapidly until they match the clean result for a back angle of 32.5°. The trend is the same for the first two turbulence levels but the effect is weaker and the results much noisier for the critical back angles approaching 32.5°.
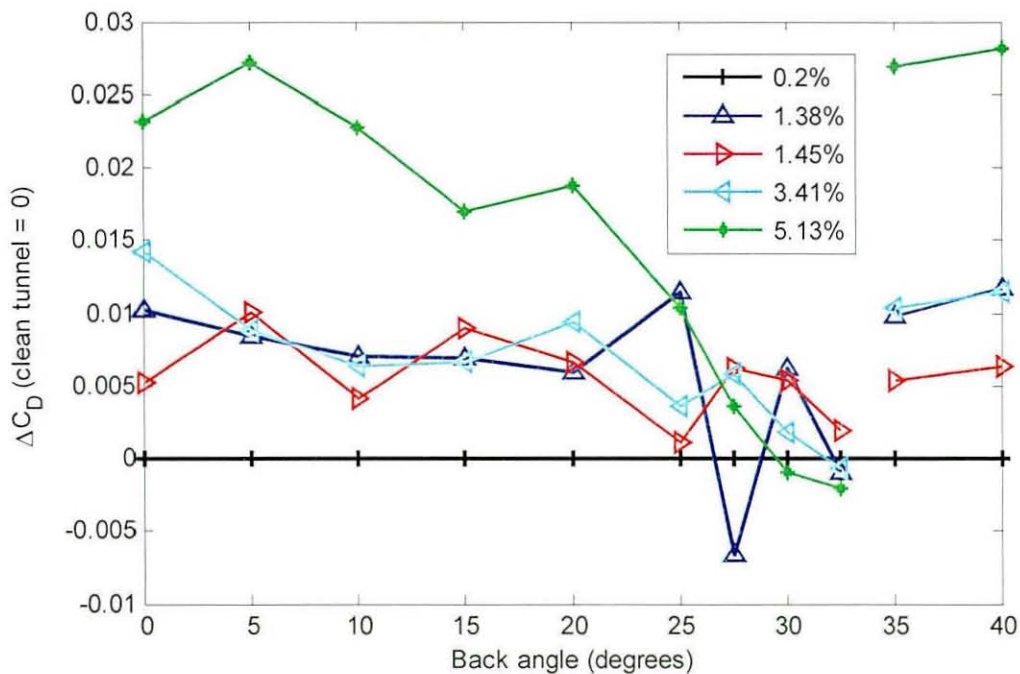
Figure 110 Variation in drag with back angle as ΔC_D values (Tu as a parameter, Tu = 0.2% as a baseline)

It is suggested that the increase at small or 0° back angles is due to increased skin friction, as was the case for the 1-box model. The additional shape dependent reduction appears for the higher back angles where the vortices are strongest, and so, following Bearman's results in the clean tunnel that showed a strong correlation between vortex

138

strength and drag coefficient, this shape dependent reduction is ascribed to a weakening of the trailing vortices.
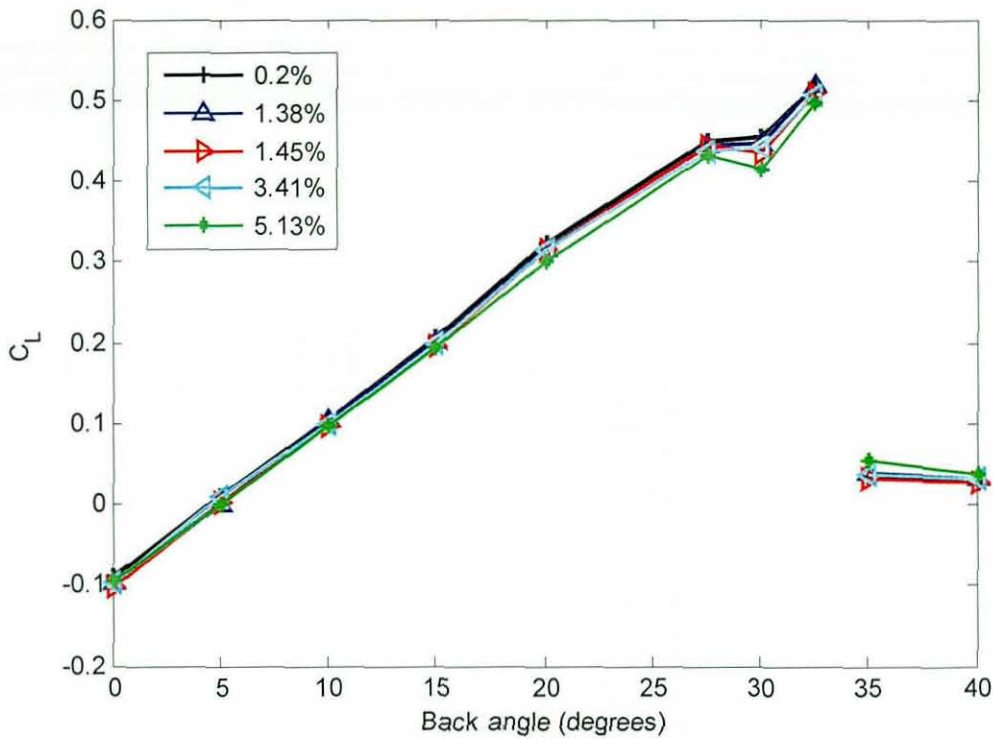
Figure 111 Variation in lift coefficient with back angle (turbulence intensity as a parameter)

The variation in lift with back angle shown in Figure 111 is much larger than the variation in drag, and therefore the differences between turbulence levels are difficult to identify, except around the critical angle. However, it is seen in the figure that the highest turbulence grid shows the same trend as the others for total lift.

To show the variation caused by the turbulence more clearly, the lift data is replotted as ΔC_L relative to the clean tunnel in Figure 112. As the results approach the critical angle, there is considerably more noise in the data. Although the lift results for the 25° back angle do not alter the conclusions, they confuse the figures, and are therefore excluded. At low angles, there is a reduction in total lift with increased turbulence, which becomes greater with increasing back angle, although the trend is not stable near the critical back angle. At higher angles (35° and 40°), there is an increase in lift with additional turbulence. More turbulence generally gives a greater effect on lift.

The conclusion drawn from the drag results was that the effect of turbulence is shape dependent and related to the trailing vortex strength. There is an indication in the total lift results that there is an effect of turbulence on lift as the angle approaches 32.5°, but

to identify the changes in the flowfield that cause the change in drag the pitching moment is used to calculate the front and rear lift, so that they can be examined separately.
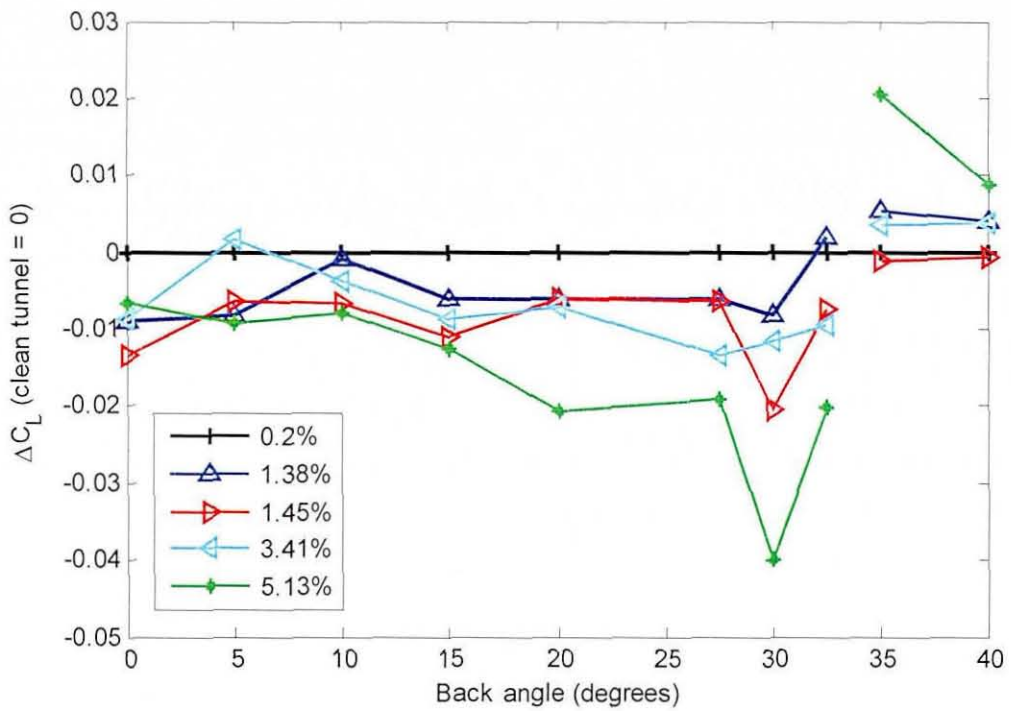
Figure 112 Variation in lift with back angle as ΔC_L values (Tu as a parameter, Tu = 0.2% as a baseline)
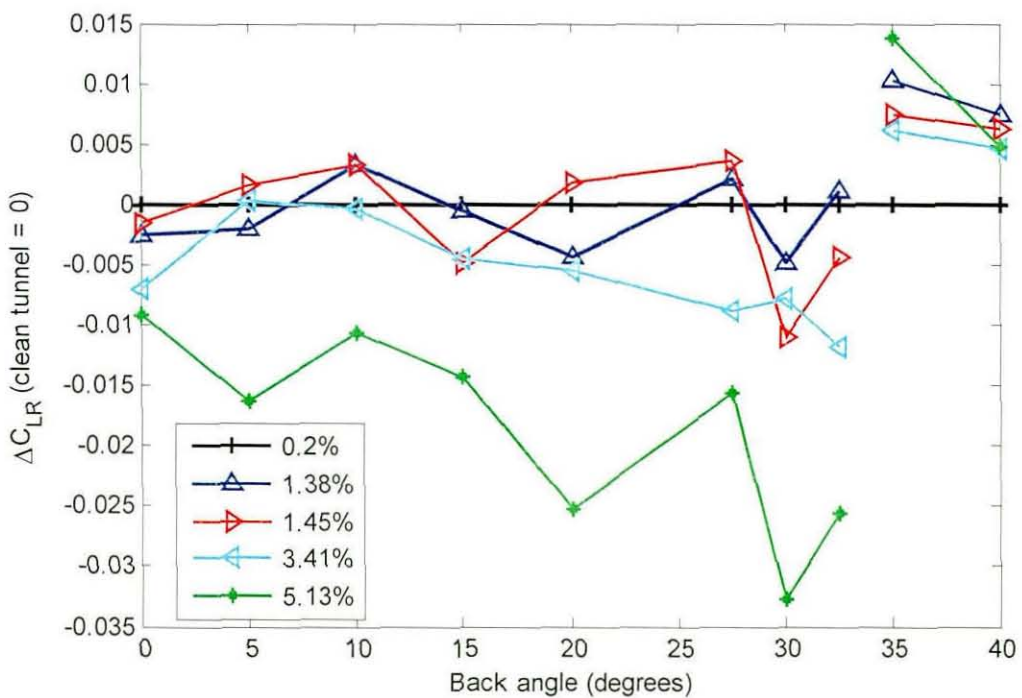
Figure 113 Variation in rear lift with back angle as ΔC_{LR} values (Tu as a parameter, Tu = 0.2% as a baseline)

Since the geometry change is at the rear, the largest effect should be on rear lift. Figure 113 shows ΔC_{LR} relative to the clean tunnel results plotted against back angle. As for the drag results, the two highest turbulence grids show the strongest effect, causing a reduction in rear lift for the 0° back angle that increases consistently with increasing back angle up to 32.5°, although there is significant variation in the results as the critical angle approaches. The two lowest turbulence levels show a much weaker effect, but there is still some evidence of a trend of reducing lift with increasing back angle. It is suggested that there is a reduction in vortex strength, and from the 1-box results it would be expected that there is also an effect of turbulence on the separation over the backlight at high back angles. It could be that these two effects are in competition, with the vortex strength affected more strongly by increased turbulence intensity and/or length scale, as the length scales are around 15mm for the first two grids, 24mm for the 3.41% grid and 37mm for the 5.13% grid. A reduction in vortex strength would cause a small reduction in the downwash over the backlight, increasing the local pressures and reducing the acceleration over the backlight, reducing rear lift and drag, while a reduction in the separation length could produce an opposing effect.

For all turbulence levels, there is a significant increase in rear lift at 35° and 40° back angle. Since the critical angle remains the same, the flow must separate at the end of the roof, and so it is expected that these changes must be as a result of a turbulence driven increase in the base suction, as was seen on the 1-box model (Section 3.4.2), which in this case acts to increase both drag and rear lift, as the top half of the base is at an angle.

The results for front lift show a much smaller effect (Figure 114) as would be expected. For the two highest turbulence levels, there is no change or a slight increase in front lift for the 0° back angle, which then reduces with increasing back angle up until 30°, although it increases again for 32.5°. This shape reduction is likely to be driven by the changes at the rear, as the acceleration reduces over the backlight causing the front stagnation point to rise, reducing front lift. The two lower turbulence levels produce a reduction in front lift at 0° back angle, which rises only slightly with increasing turbulence as back angle increases up to 30°. This appears consistent with the idea that the trailing vortices are less strongly affected by these lower turbulence intensities. The result at 32.5° appears to show some slightly different effect, but the flow must be very

close to critical at this angle and therefore strongly affected by unsteadiness in the flowfield.
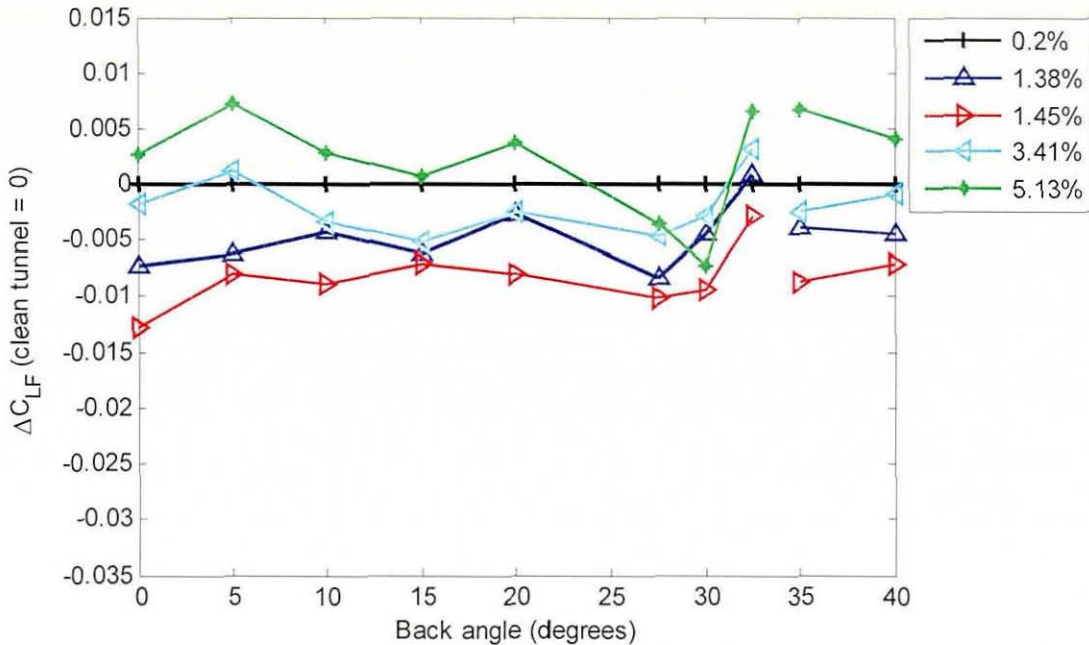
Figure 114 Variation in front lift with back angle as ΔC_{LF} values (Tu as a parameter, Tu = 0.2% as a baseline)

6.2.3 The effect of turbulence on yaw moment

The yaw moment derivatives were established by calculating the gradient of the yaw moment as it varies with yaw angle between ±10 degrees, in order to use as much of the recorded data as possible and so reduce the error. Over this range the gradient was approximately constant. Figure 115 shows the yaw moment derivatives plotted against back angle with turbulence intensity as a parameter. The trend of yaw moment coefficient with back angle matches that shown by Howell [9] for the yaw moment of the same model at a constant yaw angle (15°). The effect of additional turbulence is seen to be small and spread around the clean tunnel results, with some levels giving increases in yaw moment and some levels reducing it.

Figure 116 shows the yaw moment derivative plotted with the clean tunnel as a baseline. In this plot, as before for the other results, a shape dependency does appear for the angles closest to the critical angle, around 20° to 32.5°, although the difference is very small – equivalent to a change of 3 counts of yaw moment at 10 degrees yaw angle. Increasing the level of freestream turbulence does not appear to have a significant effect on yaw moment for this model.
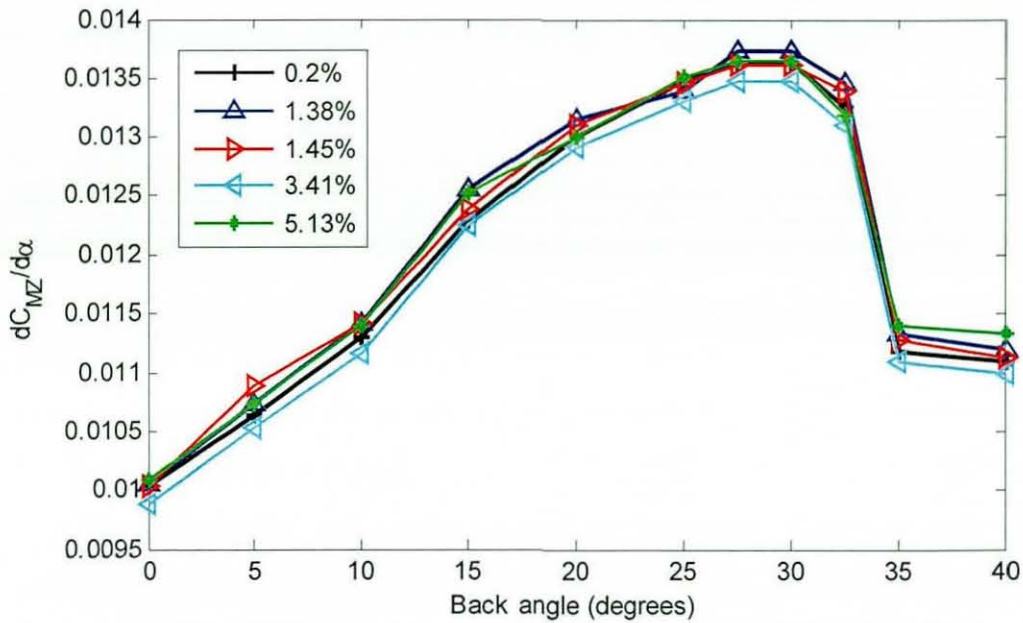
Figure 115 Variation of yaw moment derivative with back angle (turbulence intensity as a parameter)
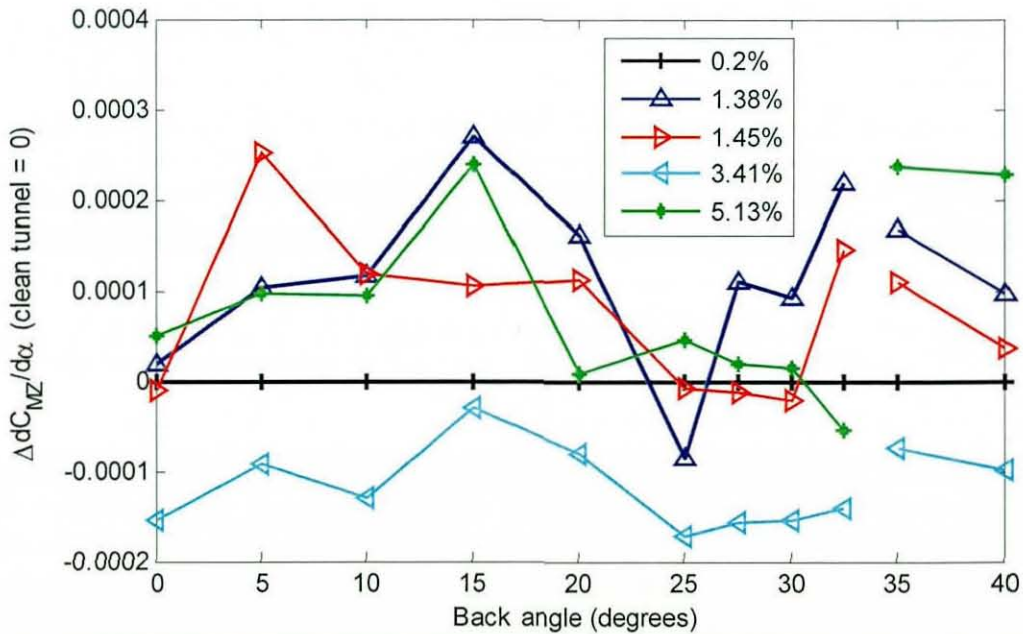
Figure 116 Variation in yaw moment derivative with back angle as $\Delta dC_{MZ}/d\alpha$ values (Tu as a parameter, Tu = 0.2% as a baseline)

6.3   Summary

- The Windsor model has a typical drag characteristic with back angle, which was repeated in the Loughborough wind tunnel and matched previous results with the same model. The drag initially falls as the base gets smaller, and then rises with increasing vortex strength up to a critical angle, in this case 32.5°. At higher angles this flow breaks down and the drag falls to the same value as for 0° back angle, with a separation at the end of the roof.

- Increasing the freestream turbulence gave an increase in drag for 0° back angle, which was strongly dependent on the turbulence intensity. As the back angle increased, there was a shape dependent reduction in drag which reduced the drag back to the clean tunnel result for all turbulence levels at 32.5° back angle.

- For higher back angles there was an increase in drag at higher turbulence levels, as was seen for the lowest back angles. The 1-box results demonstrated that this was partly due to raised base pressure.

- The rear lift results also showed a shape dependent reduction up to the critical with increased turbulence. It was suggested that the additional turbulence reduced the vortex strength and affected the separation over the roof, and that higher levels of turbulence had a stronger effect on the vortex strength.

- At back angles above the critical angle, the rear lift was higher with increased turbulence. The 1-box results showed that increasing freestream turbulence increased the base pressure, resulting in increases in drag and lift in this case because the upper half of the base is at an angle to the vertical.

- Tests at different yaw angles showed that the yaw moment was not significantly affected by the addition of freestream turbulence.

Chapter 7

Effect of freestream turbulence on practical vehicle development

There are many subtle aerodynamic devices available to the vehicle aerodynamicist that can have large effects on the flowfield around the vehicle, and consequently on the body forces. Typically, full width front and rear spoilers, wheel spoilers, and variations in air intake sizes and internal cooling flows may be employed to reduce drag and control lift. This chapter presents an investigation into the changes caused by additional freestream turbulence on front, rear and wheel spoilers and cooling drag. The MIRA reference model is used to show the effect of very simple spoilers on a generic model, and it is also possible to make crude adjustments to the backlight angle by testing the notchback, fastback and estate car configurations (A, B and C in Figure 95) which can then be examined in the context of the results from the previous chapter. Two production vehicles are then used to further investigate the effect of turbulence on front, rear and wheel spoilers and cooling drag, and on one the effect of turbulence on the A-pillar vortex was investigated using flourescene.

7.1   Further tests on MIRA reference model

The MIRA reference model was tested at all 3 turbulence levels in the full scale wind tunnel in its 3 baseline configurations of notchback (A), fastback (B) and estate car (C) (which is a repeat of the 152mm radius test in Section 5.2). Front and rear spoilers were also fitted, and for these tests, the MIRA reference car was in its notchback configuration. The front spoilers consisted of a series of rectangular strips of foam, 20mm high by 50mm deep under the full width of the front of the car where the flat underfloor starts.

Figure 117 Schematic diagram of front and rear spoiler locations

The total spoiler height varied from 20mm to 80mm. The rear spoilers were 50mm deep and varied in height from 20mm to 48mm at the rear edge, with a triangular cross section and a sharp leading edge which was taped to the reference car across the rear bootlid, with the rear face of the spoiler flush with the back of the car. Figure 117 shows the front spoiler location under the chin of the nose on the left, and the rear spoiler location on the rear of the boot deck on the right.

146

7.1.1 Notchback, fastback and estate back results

Figure 118 shows that increasing the turbulence intensity increased the drag, but that 4.3% turbulence gave a lower drag coefficient than 3.4%, as was the case for the estate back with different leading edge radii in Section 5.2. The variation in C_D with turbulence is around 10 counts (0.01) which would be a significant change in the vehicle development process. The back angle of the fastback is approximately 22°, and the notchback 45° (actual backlight angle), but with an extended boot deck, giving the same effective back angle as the fastback but with a significant separated region. This is why the notchback has a lower C_D than the estate back but higher than the fastback. The estate back shows the 0° case. A reduction in drag between the 0° and 22° back angle was also shown in the results from the previous chapter.
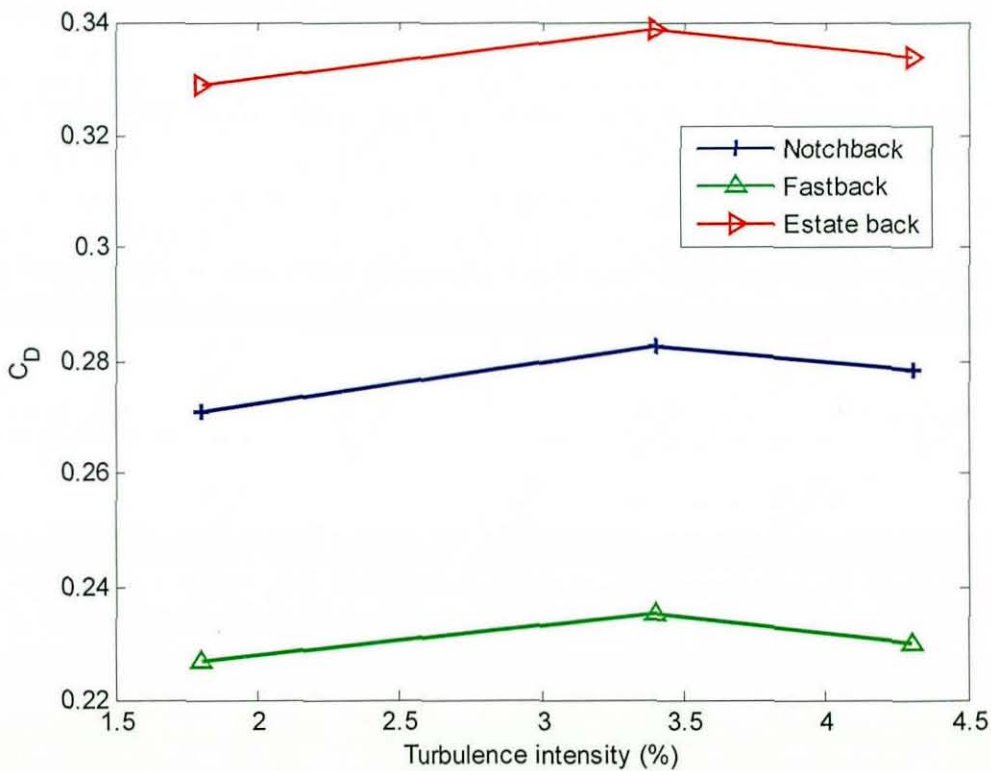
Figure 118 Variation of C_D with drag coefficient for the MIRA model (configuration as a parameter)

Figure 119 shows the variation in lift coefficient with turbulence and configuration. There is a large increase in rear lift between the estate back and the other two back angles, as also seen on the Windsor model. The difference of around 0.35 is approximately the same as the difference between 0 degrees and 20 degrees for the Windsor model.

147
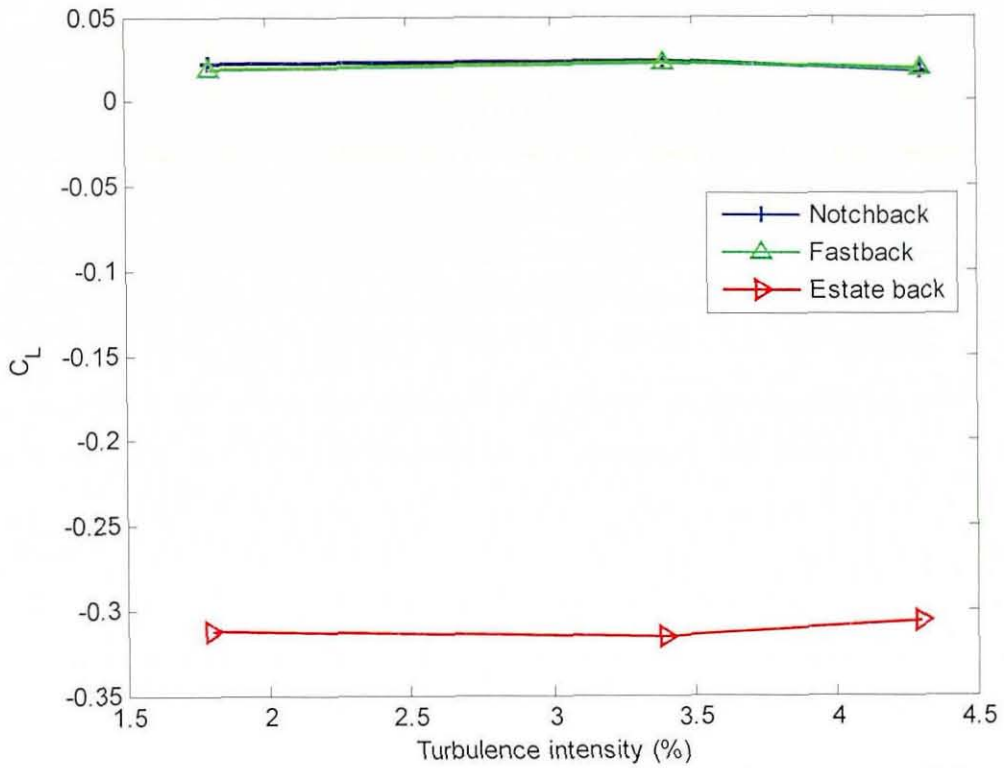
Figure 119 Variation in C_L with turbulence intensity (configuration as a parameter)

In order to examine the effect of turbulence on the lift, the front and rear lift coefficients are plotted separately and as ΔC_{LF} and ΔC_{LR} from the 1.8% baseline turbulence case in Figure 120 and Figure 121.
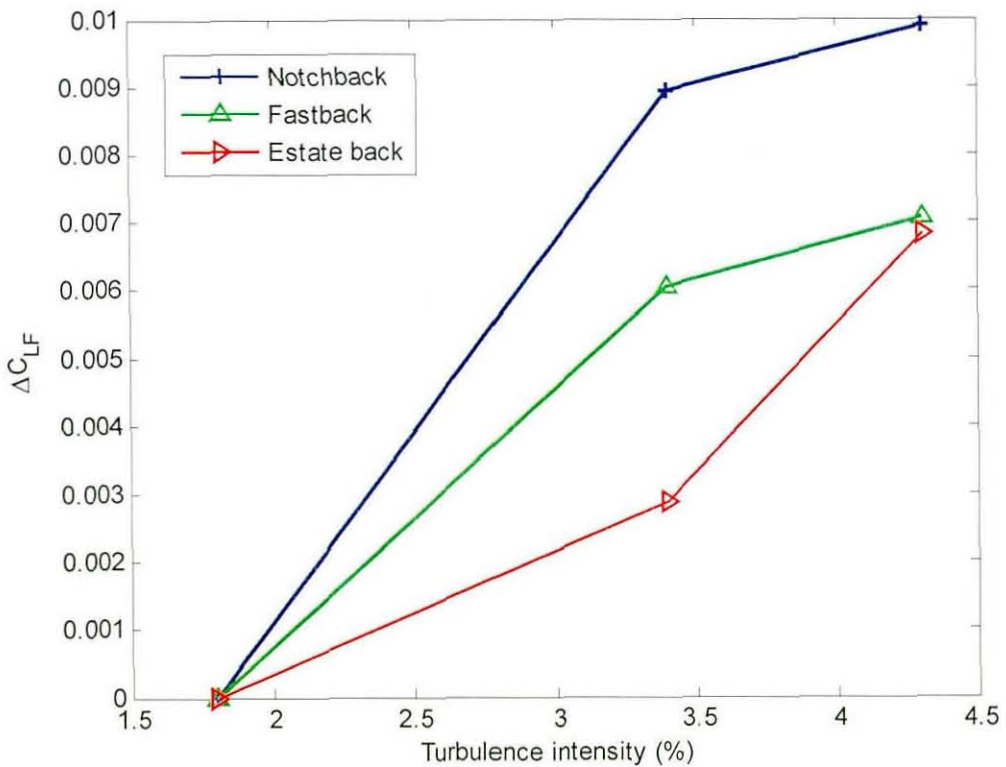
Figure 120 Change in C_{LF} with turbulence intensity (configuration as a parameter)
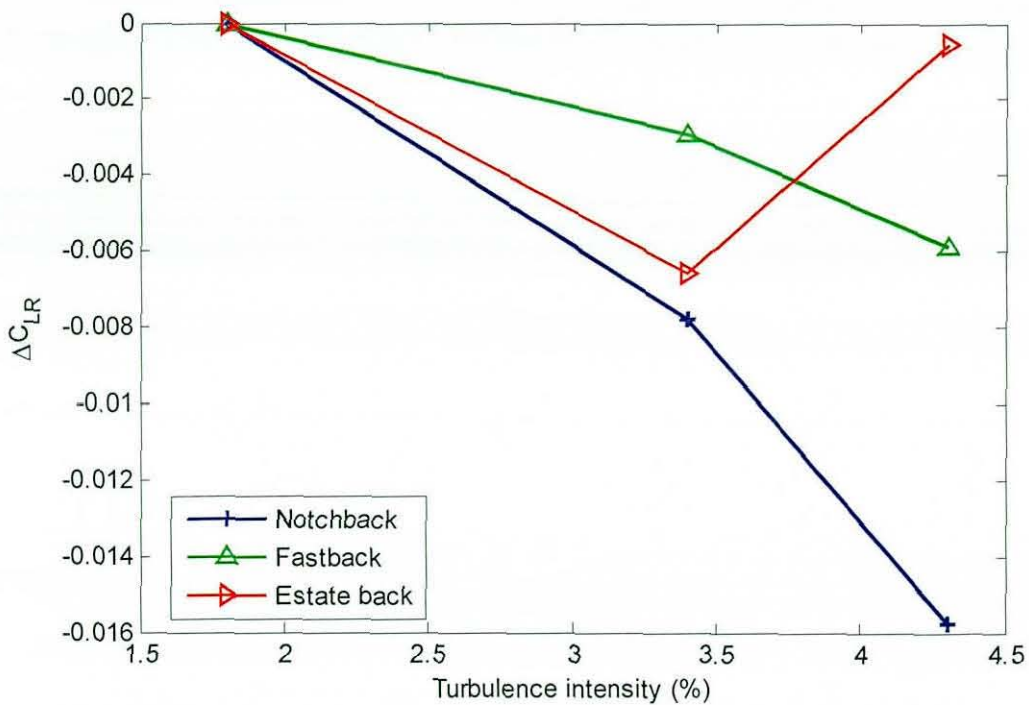
Figure 121 Change in C$_{LR}$ with turbulence intensity (configuration as a parameter)

The increase in front lift and decrease in rear lift seen for the Windsor model when the turbulence intensity is raised is repeated here. The changes are comparable in magnitude to that seen in the Windsor model results between 1.4% and 5.13% turbulence.

7.1.2 Front spoiler results

Figure 122 shows the variation in front lift with front spoiler depth. Although the increments in spoiler depth were rather coarse, the results suggest that there is some change in the shape of the curve that means that the optimum spoiler depth for maximum front downforce is dependent on the turbulence intensity. In the clean tunnel, the most downforce is produced by the 40mm spoiler, and when the freestream turbulence was increased to 4.3%, the 60mm spoiler produced the most. There is a visible shift from left to right of an imagined best fit parabola. Based on the discussion of how separated flows are affected by turbulence in Section 4.4.3, it is expected that the separation bubble is made smaller by the turbulence, which may reduce the blockage caused by the spoiler and therefore increase its effectiveness.

Figure 123 shows the effect of front spoiler height on rear lift. Additional turbulence seems to mitigate the increase in rear lift, giving as much as 15 counts less rear lift for the highest turbulence intensity. The increased effectiveness of the deeper front spoiler must come from a reduction in separation, reducing the blockage effect of the spoiler,

which will shift the front stagnation point upwards and cause a resultant reduction in rear lift. There may also be a change in the diffuser performance but it is not possible to identify this here.
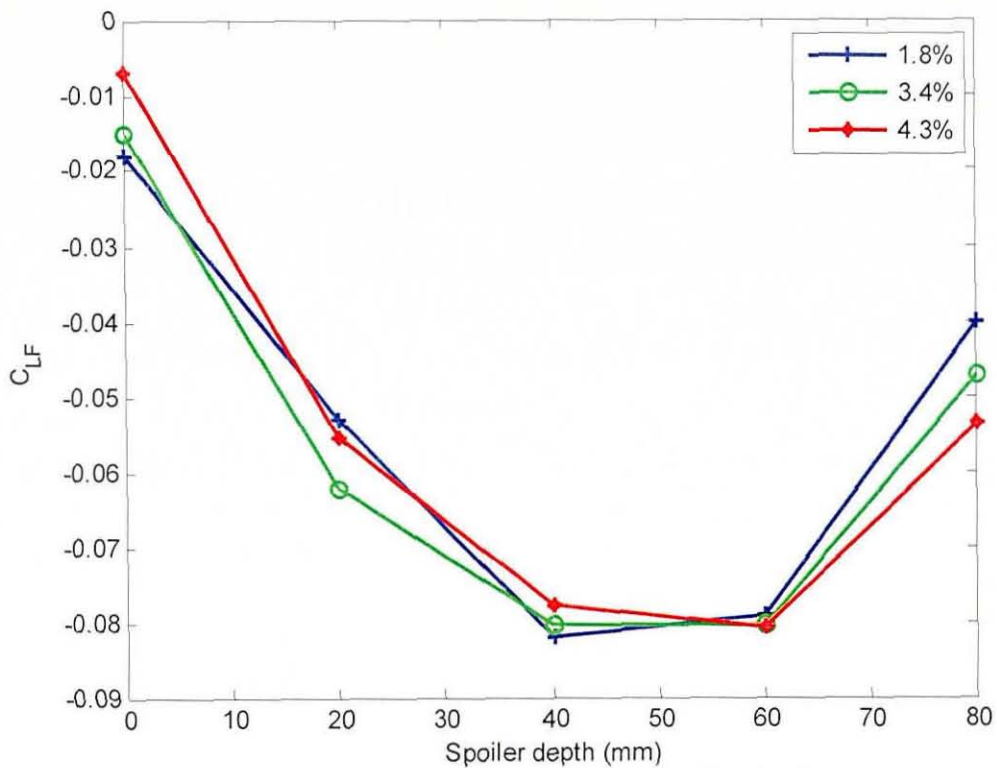
Figure 122 Variation in front lift with front spoiler depth
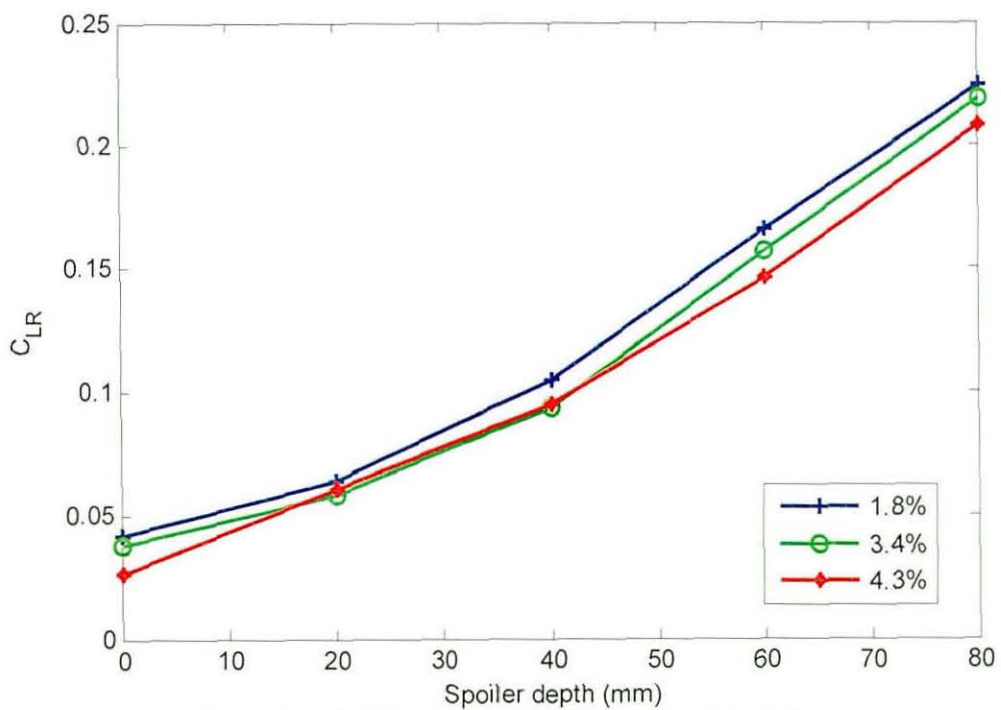
Figure 123 Variation in rear lift with front spoiler depth
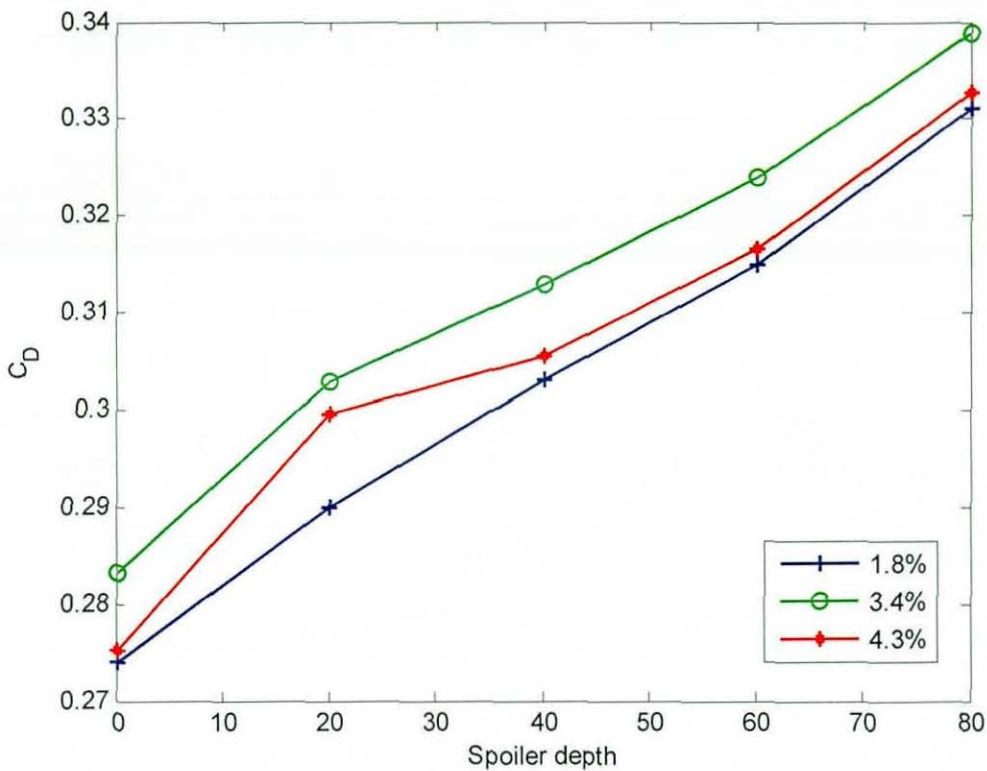
Figure 124 Variation in C$_D$ with front spoiler depth

Figure 124 shows the variation in drag with front spoiler depth. There is a drag penalty from the front spoiler which increases with spoiler depth. For small spoilers there is an additional drag penalty in increased freestream turbulence, but for deeper front spoilers the change in C$_D$ between clean tunnel and increased turbulence is the same as for the baseline model. The increased drag is small and the reason for it is not clear. As in most cases tested, the 3.4% turbulence level gives the highest drag increase, significantly more than the other two cases.

7.1.3   Rear spoiler results

The effect of turbulence on the trend with varying rear spoiler height of front (Figure 125) and rear (Figure 126) lift was investigated by testing four spoilers. Increasing turbulence to 3.4% caused very little change on the unmodified MIRA model, but gave an additional reduction at the rear of up to 20 counts when a rear wing was added. Increasing the turbulence to 4.3% gave a reduction in rear lift of around 15 counts with or without a rear spoiler fitted. At the front there was very little change with a turbulence intensity of 3.4%. When the turbulence was increased to 4.3% there was a 15 count increase in front lift. Increasing the turbulence to 3.4% made the rear spoiler more effective, but increasing it to 4.3% changed the balance by 30 counts with or without the rear spoiler.

151
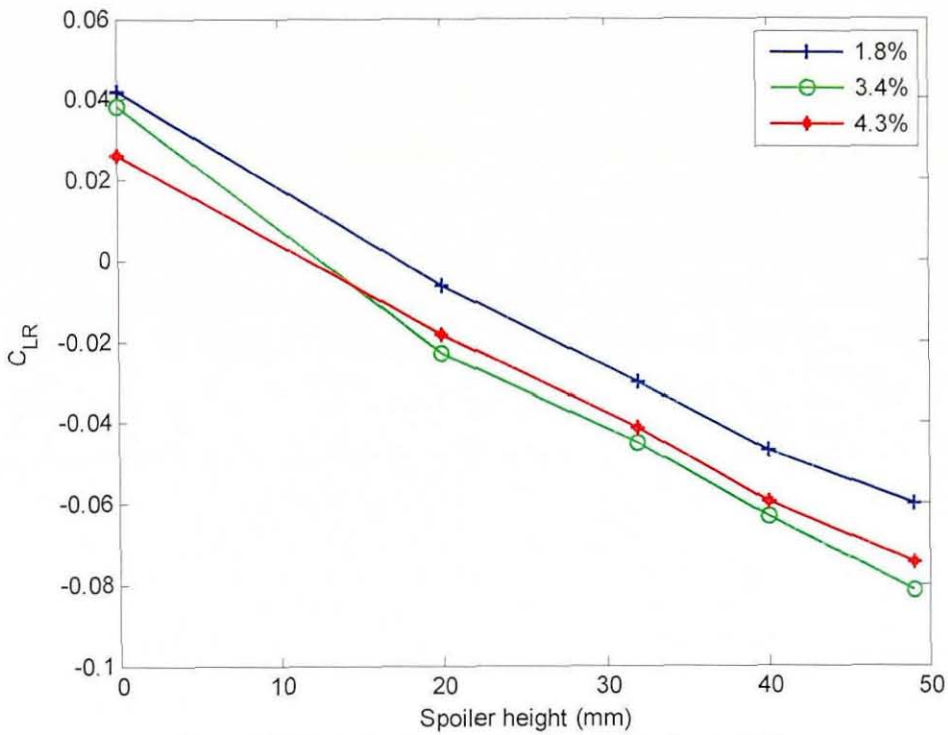
Figure 125 Variation in rear lift with rear spoiler height
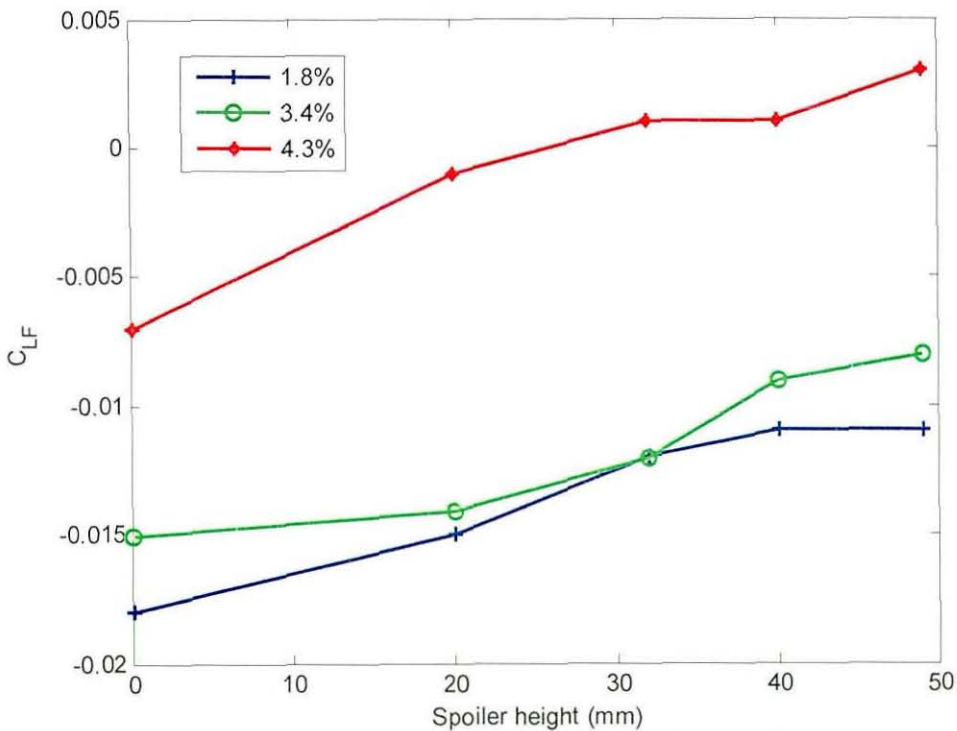
Figure 126 Variation in front lift with rear spoiler height

The rear spoiler increased the C_D of the baseline vehicle, which is unusual – the common result for a rear spoiler is a drag reduction for these small spoilers [50]. The drag increase implies that for this model the increase in the wake size due to deflection of the flow was more significant than any induced effects on the backlight, probably because at 45°, the backlight itself is likely to be in a separation region and an effect of

the spoiler on the pressure on the flat boot deck will not affect drag. Adding more turbulence did not significantly change the trend of C_D with spoiler height. The difference between the result for 1.8% turbulence and 3.4% turbulence remained at approximately 20 counts for all spoiler heights tested.
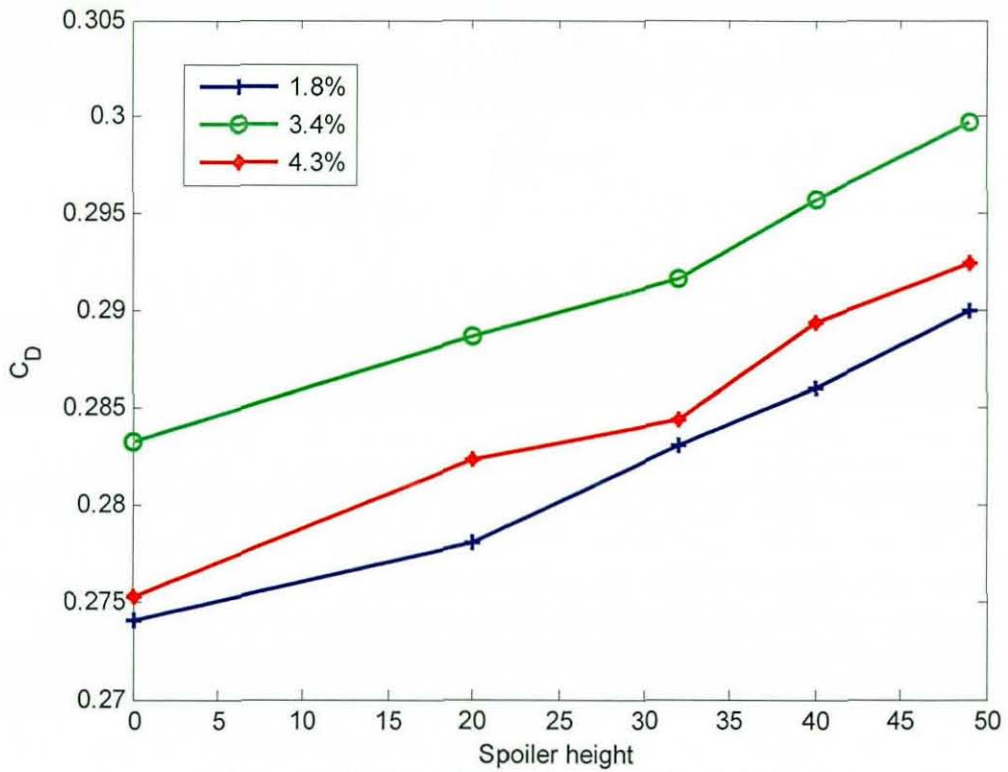
Figure 127 Variation in C_D with rear spoiler height

7.2 Simple modifications to real vehicles (full scale)

Two production vehicles, a Jaguar XJ8 (X350) and Land Rover Discovery 3 (L319) were used to investigate the effect of additional freestream turbulence on simple vehicle modifications. In addition to testing the baseline vehicle and each modification at 0° yaw, a yaw sweep was conducted for the baseline vehicle and for one of the rear spoilers, to give an indication of the effect of turbulence on yaw moment and sideforce. Figure 128 shows the wooden beams of the turbulence grid and the X350 installed on the balance and Table 11 shows the test details for the X350. Figure 129 shows the Discovery as it was installed on the balance in its baseline configuration and Table 12 shows the test details for the Discovery.

Figure 128 Jaguar XJ8 (X350) in the MIRA full scale wind tunnel, with the turbulence grid installed

These two photos show the rear spoilers installed. The spoilers were triangular sections of foam 20mm, 25mm and 30 mm high at the rear edge and installed across the trailing edge of the boot deck.
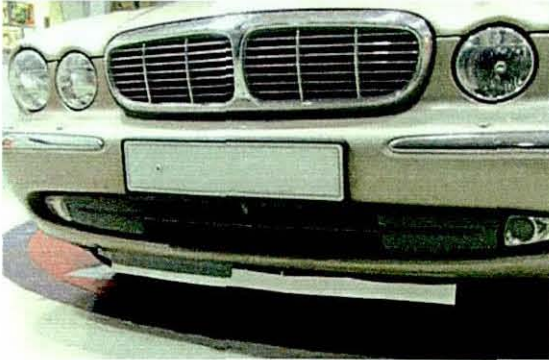
The front chin spoiler extension was 900mm wide and 50mm deep, and attached so that its top edge rested against the underside of the car, at the top edge of the much smaller spoiler fitted to the standard vehicle.
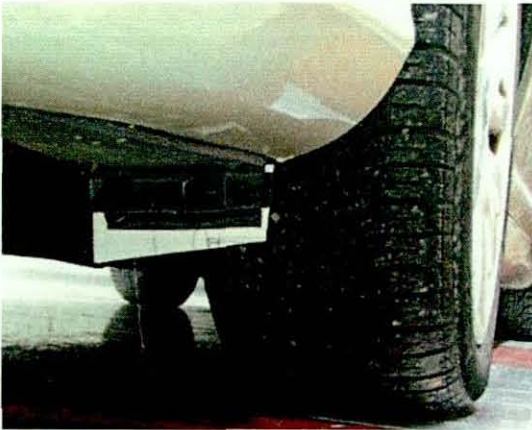
The wheel spoiler extension was designed to double the size of the existing wheel spoiler. The original wheel spoiler is also deeper on the inside edge than on the outside, and part of the wheel-arch moulding which made it impossible to remove.

The cooling inlets were fully blocked.

Table 11 Test details for the XJ8

155

Figure 129 Land Rover Discovery 3 (L319) in the MIRA full scale wind tunnel

The rear spoiler fitted to the Land Rover Discovery. The 20mm spoiler made a significant difference to the vehicle drag, and so a 15mm spoiler was used along with the 25mm spoiler to give three heights, as the 30mm spoiler used on X350 would have been too extreme.

Discovery with the Land Rover made 40mm wheel spoilers fitted.

Wheel spoilers extended to a depth of 65mm.

As a final test, the cooling intakes (seen in Figure 129) were blocked completely.

Table 12 Test details for the Discovery

7.2.1   Baseline results at 0° yaw
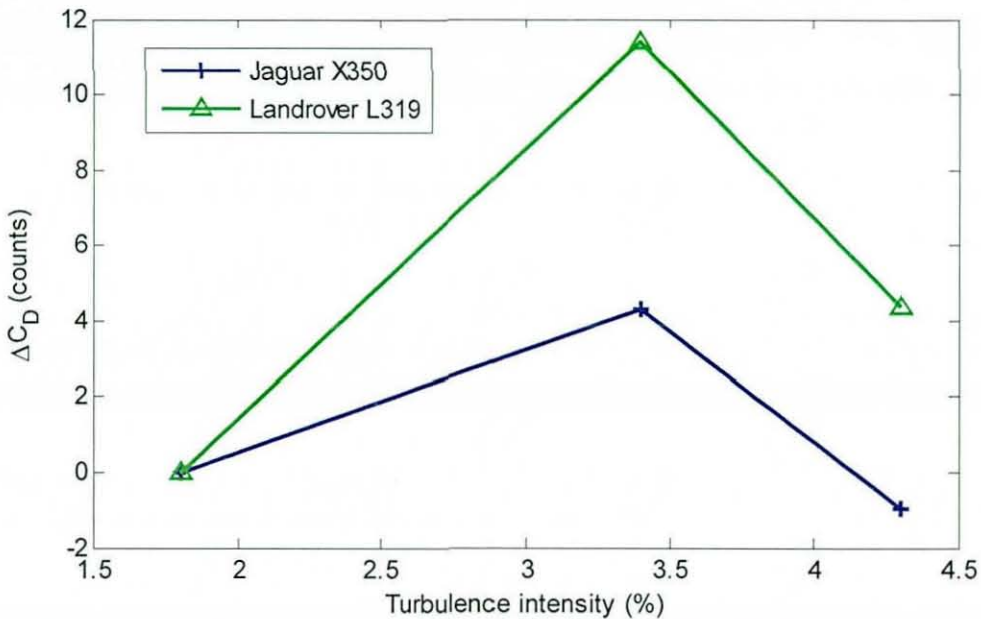
Figure 130 Change in baseline vehicle drag coefficient with turbulence intensity

Figure 130 shows that for the baseline configurations the drag for both vehicles increased when the turbulence intensity was increased to 3.4%, in line with expectations from the previous work reported here (Sections 5.2.4 and 7.1.1) and previously published work (e.g. Cogotti [51]). The results also show that at 4.3% turbulence, the drag increase for the Discovery is reduced, and the C_D of the X350 is the same as it was for the clean tunnel, within the repeatability of the experiment. The backlight angle of the X350 is approximately 27 degrees (angle of the rear screen not including the boot deck effective angle, as measured from a photo), and examination of the Windsor model results shows that the likely change in C_D around this angle between 1.38% and 5.13% (a larger change in Tu than in the full scale tunnel) is small and unpredictable, close to the critical back angle of 35 degrees where the drag is highest. As was the case

157

with the MIRA notchback the X350 also has a significant boot deck which will give a different flowfield to the Windsor model – this is often represented by considering the effective back angle to be between the top edge of the backlight and the rear edge of the boot. It is also probable on a more complex vehicle that there are more competing effects due to turbulence, as the drag increase from skin friction is balanced by drag reduction from reduced vortex strength at the rear. There is unlikely to be significant separation on a production vehicle as it has already been through an aerodynamic optimisation process.
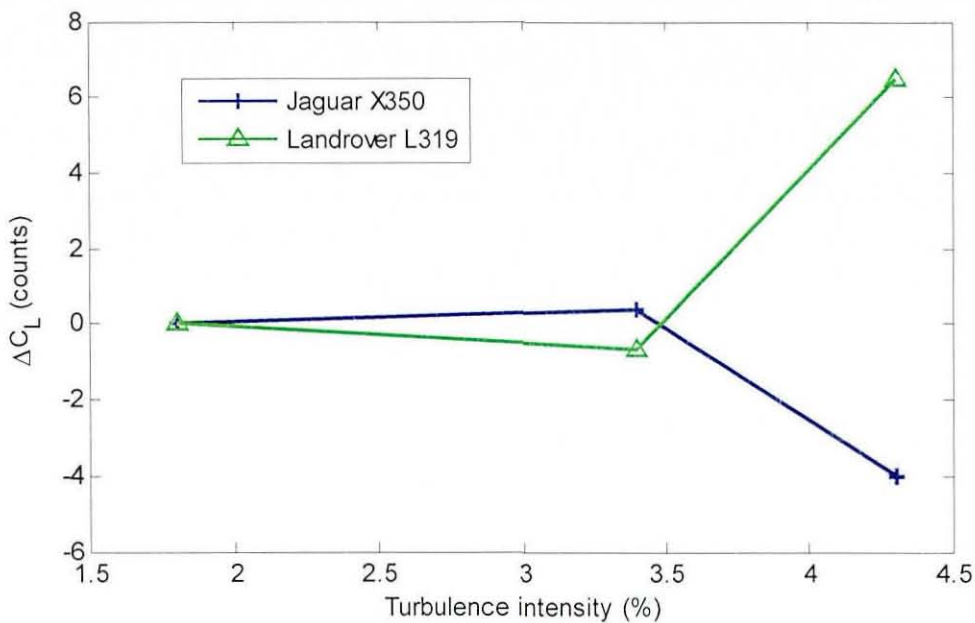
Figure 131 Variation in baseline vehicle overall lift with turbulence intensity

Figure 131 shows the variation in total lift. The main points of interest here are that the medium level of turbulence had no effect on the total lift of either vehicle, and that with a further increase of turbulence intensity the two vehicles experience opposite changes in overall lift. In both cases the lift change is small, between 4 and 6 counts. This small change repeats the results for the MIRA reference model, where the estate back vehicle showed an increase in total lift and the fastback and notchback showed a decrease in total lift.

7.2.2   Yaw sweep results

Figure 132 shows the variation in drag coefficient for the X350 with yaw angle at each turbulence intensity and Figure 133 shows the same results for L319. For both vehicles, raising the freestream turbulence increases the drag at yaw, but the largest increase is still for 3.4%, around 12-15 counts.
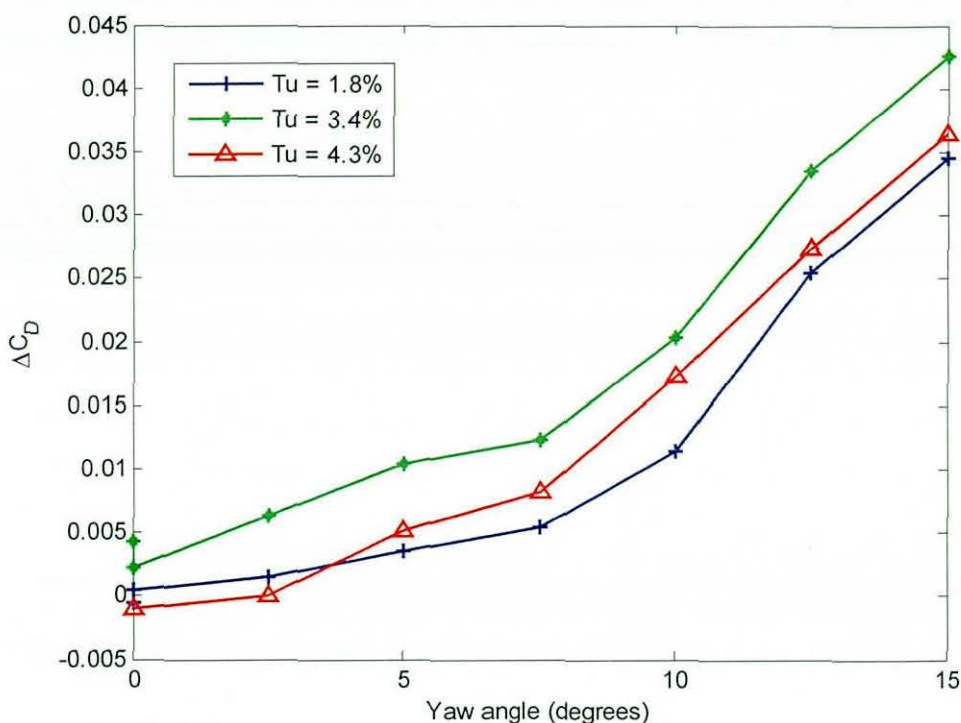
Figure 132 Variation in drag coefficient with yaw angle for the baseline X350
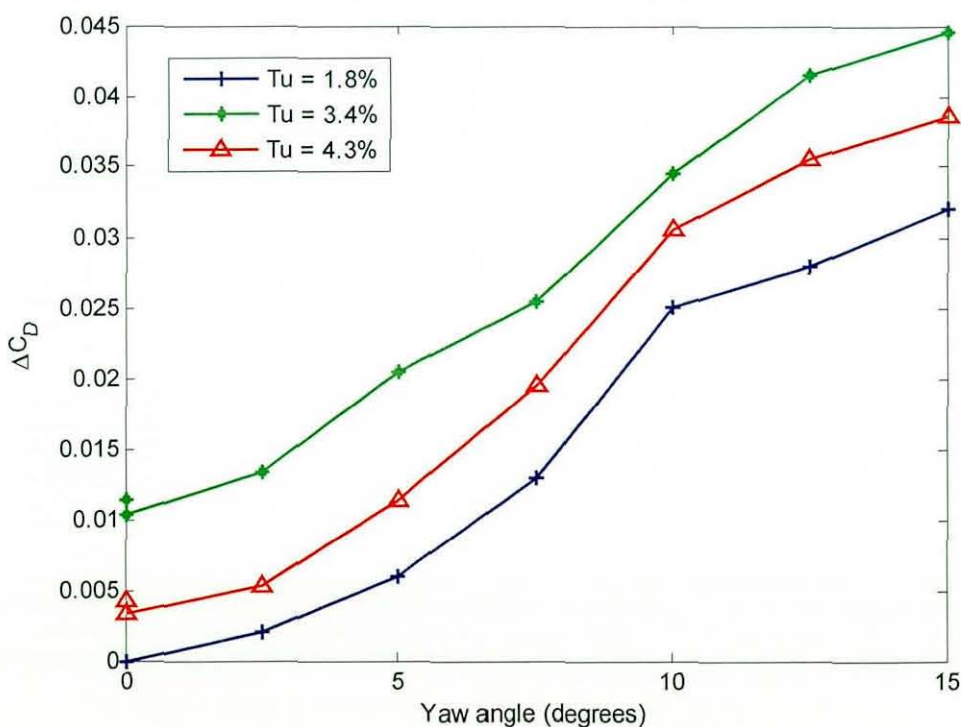
Figure 133 Change in drag coefficient for the baseline L319

7.2.3   Rear spoilers

Figure 134 and Figure 135 show the change in rear lift and drag coefficients for the X350 with the rear spoiler. In comparison with the results for the MIRA model, there is a much more significant improvement in rear downforce with additional turbulence. However, in this case the rear spoiler reduced the drag compared to the baseline vehicle

rather than increased it, and the effect of additional turbulence was to mitigate the reduction in drag. Achieving a drag reduction with a spoiler is the more common result (eg. Schenkel [50]) ascribed to an increase in pressures on the backlight and boot deck. It is not clear why this effect should be reduced by the additional turbulence.
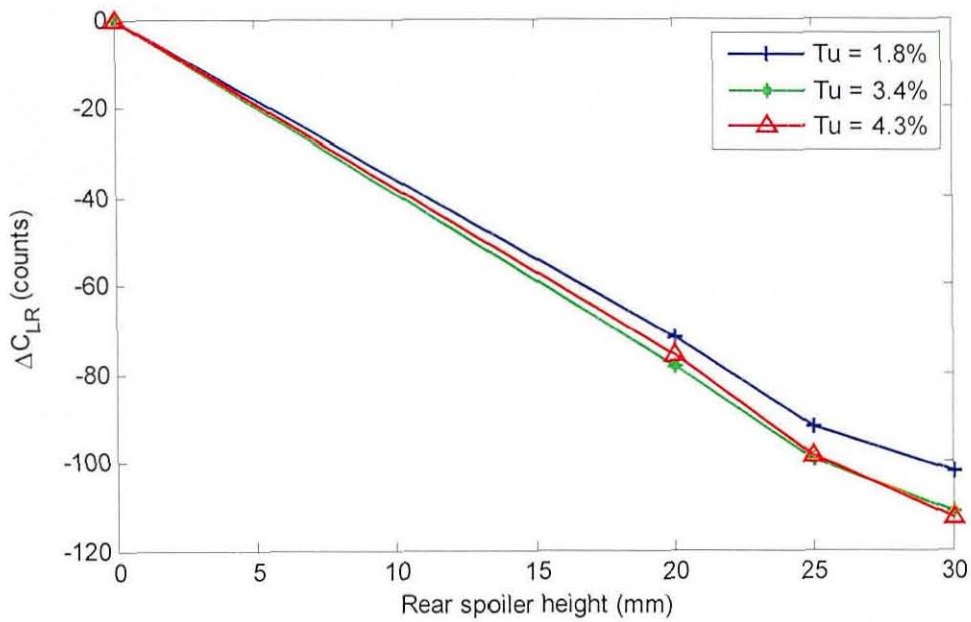
Figure 134 Change in rear lift coefficient with rear spoiler height for X350
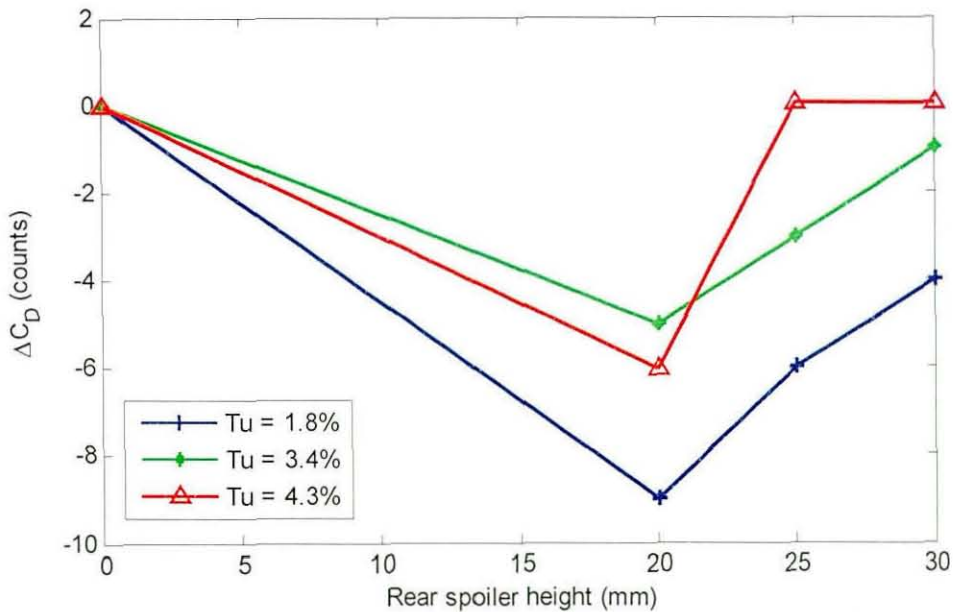
Figure 135 Change in drag coefficient with rear spoiler height for X350

Figure 136 and Figure 137 show the same results for the L319. The rear lift results show a similar improvement in rear lift reduction for the medium turbulence level over the clean tunnel, but the highest turbulence grid produces results that are very close to the clean tunnel. The addition of turbulence reduces the drag penalty slightly, which

may be due to improved mixing in the free shear layer after the spoiler or a reduction in the wake size.
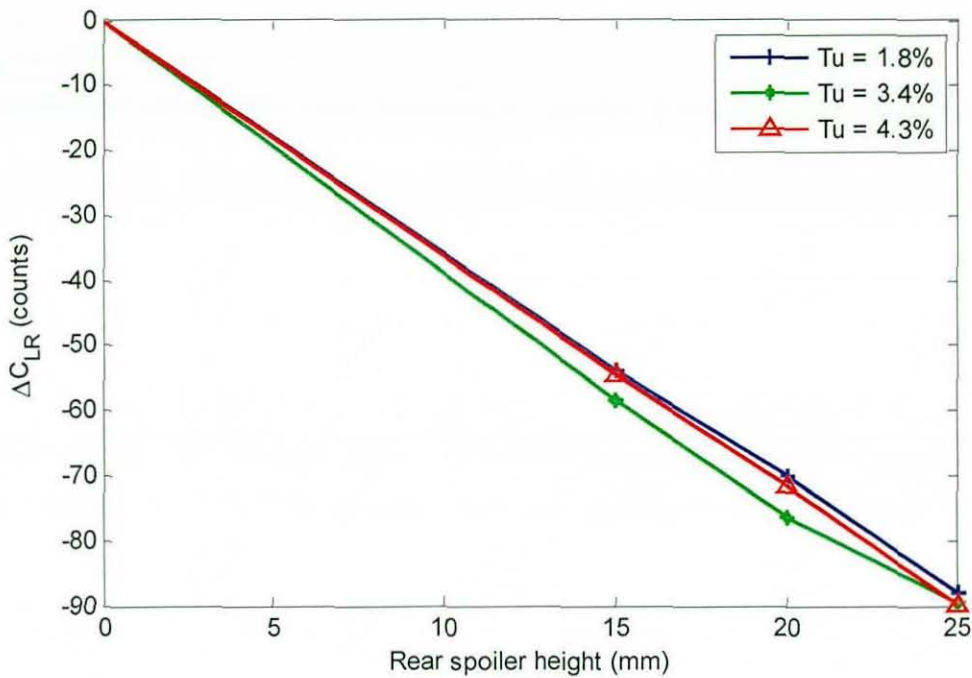
Figure 136 Change in rear lift coefficient with rear spoiler height for L319
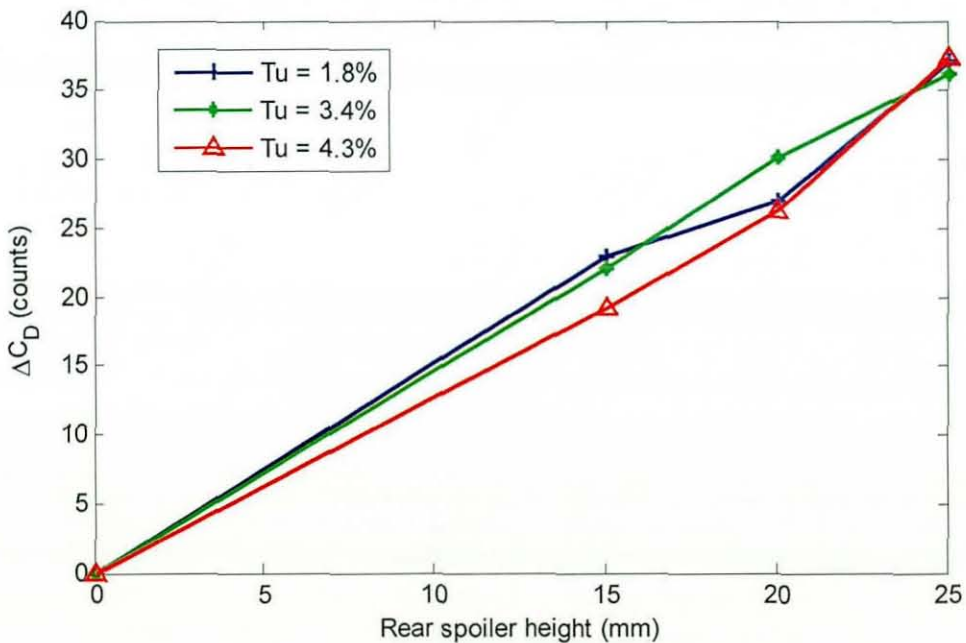
Figure 137 Change in drag coefficient with rear spoiler height for L319

7.2.4   Front spoilers, wheel spoilers and cooling drag

Figure 138 and Figure 139 show the change in lift and drag for the wheel spoilers, front spoiler and cooling drag with turbulence intensity, where the difference is based on the value for the baseline vehicle at each turbulence intensity. The front spoiler increased drag and overall lift, but did reduce the front lift. With additional turbulence, there was

161

an small additional downforce benefit but also a drag penalty, matching the results for a similar sized spoiler on the MIRA reference model above.
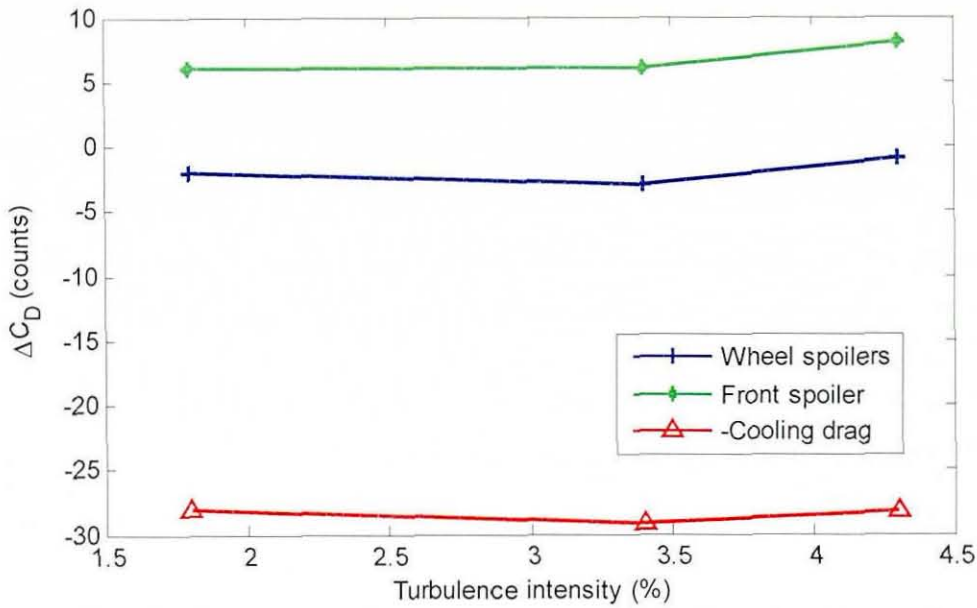
Figure 138 Variation in drag with turbulence intensity for the wheel spoilers, front spoiler and cooling drag for the X350
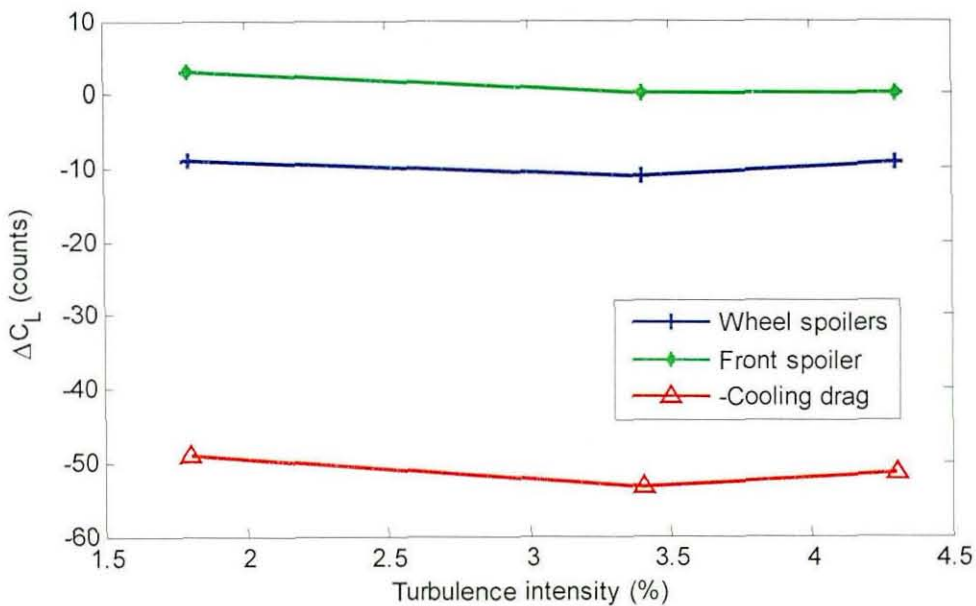
Figure 139 Variation in lift with turbulence intensity for the wheel spoilers, front spoiler and cooling drag for the X350

The wheel spoilers reduced the drag and the lift, and increasing the turbulence had very little effect – at 3.4% the drag was slightly reduced, and at 4.3% slightly increased. Cooling drag is shown as a negative change, because it is calculated as the change in drag for the modification, i.e. the blocked air intakes. Additional turbulence has little effect on drag, only increasing it slightly, but reduces the lift with inlets blocked by a small amount. Closing cooling intakes can force a small separation around the bonnet

radii because more flow is diverted over the bonnet (eg. as shown by Wolf [52]) and therefore the changes due to turbulence may be due to reductions in any induced separation.

Figure 140 and Figure 141 show the same results for the L319 (on a larger scale). The variation in drag is still small in most cases, and the 65mm spoiler shows no significant variation at all. The lift results also show fairly small variations. The wheel spoilers show a reduced drag benefit when the turbulence level is raised, and a very small effect on lift. Wheel spoilers work by creating flow spillage that then misses the front wheels, and so a reduction in separation due to increased turbulence is likely to reduce their effectiveness. It is likely that the 65mm spoiler is too big for the turbulence to make any difference. Cooling drag is lower for the medium turbulence grid than the clean tunnel, but for the highest turbulence grid it is very close to the clean result. The change in lift due to blocking up the air intake is quite small and in a similar way to that on the X350 it may be due to a reduction in any separation induced by blocking the inlets.
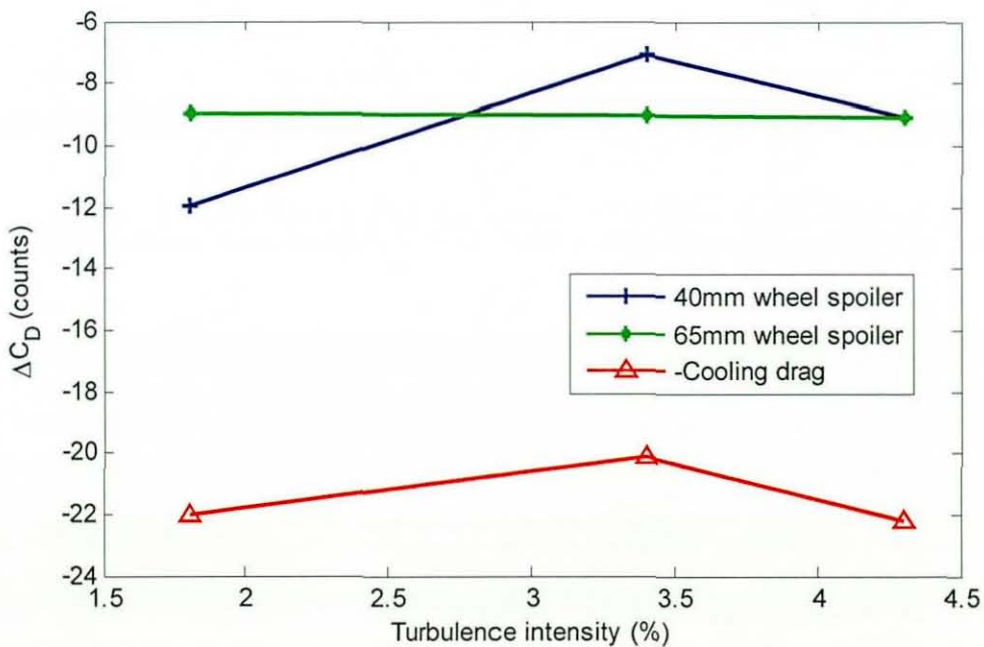
Figure 140 Variation in drag with turbulence intensity for wheel spoilers and cooling drag for the L319
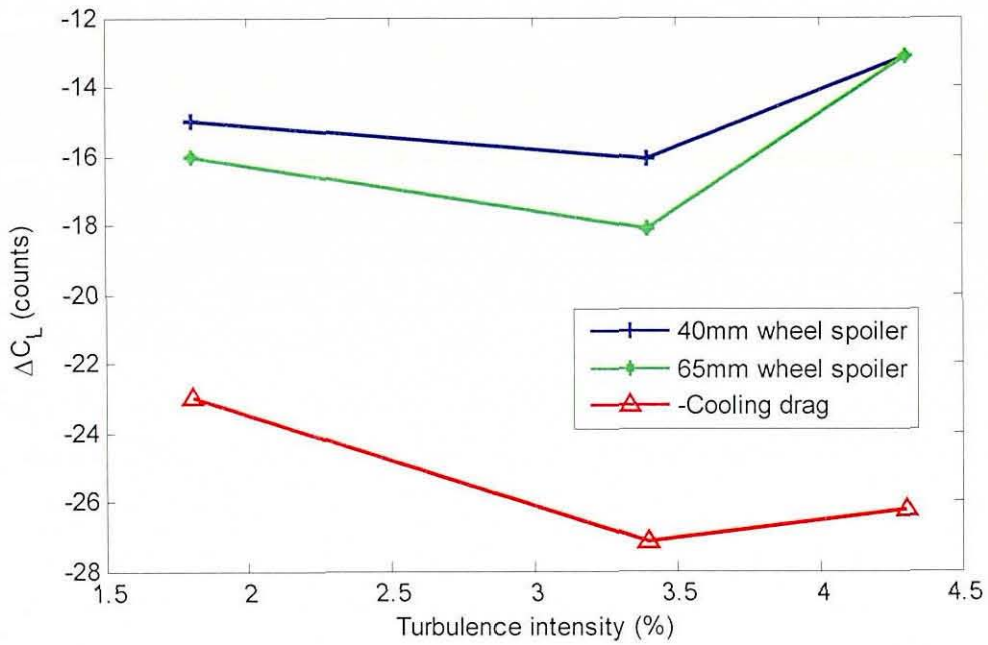
Figure 141 Variation in lift with turbulence intensity for wheel spoilers and cooling drag for the L319

7.2.5 A-Pillar Vortices

An investigation was carried out into the variation in A-pillar vortex size using wool tufts. The following figures show the wool tufts as seen from the front passenger seat.

Figure 142 Wool tuft photo, clean tunnel

Figure 143 Wool tuft photo, 3.4% grid

Figure 144 Wool tuft photo, 4.3% grid

In Figure 142, Figure 143 and Figure 144 the first visible row of wool tufts has been numbered for ease of comparison between turbulence cases. There is clearly a small effect on the flow around the A pillar and over the wing mirror. In comparison to the clean tunnel, in the first turbulence case tufts 10 to 12 look less vertical, and tufts 5 to 8 are much more agitated by the flow. For the highest turbulence grid, tufts 10-12 are visible to the right of the tape, and tufts 5-8 are less agitated. This shows that the

165

vortical flows in these areas are affected by the turbulence, as was suggested for the trailing vortices on the Windsor model. On the side glass of a road vehicle, this may have implications for wind noise. Repeating the photographs for the two turbulence grid cases appeared to show the same features.

Surface flow visualisation using flourescene paint was carried out on the A-pillar flow to further extend these tests. The areas of interest identified by the wool tuft experiment were the A-pillar vortex itself, and the flow around the top of the wing mirror.

Figure 145 Flourescene visualisation of A-pillar vortex, 1.8% turbulence vs. 3.4%

Figure 145 shows a comparison of the A-pillar vortex for the clean tunnel against the A-pillar vortex with 3.4% turbulence in the freestream. Increasing the turbulence has made the reattachment line move slightly further from the A-pillar, and also further from the roofline as the vortex propagates downstream.

The wing mirror flow is shown in Figure 146. The jet flow behind the wing mirror is affected by the turbulence with a bigger recirculation on the glass just above the door line (enough to cause a small dribble in the middle of the recirculating flow where the flourescene did not fully dry out) and a stronger imprint of the jet flow between the wing mirror and the A-pillar.
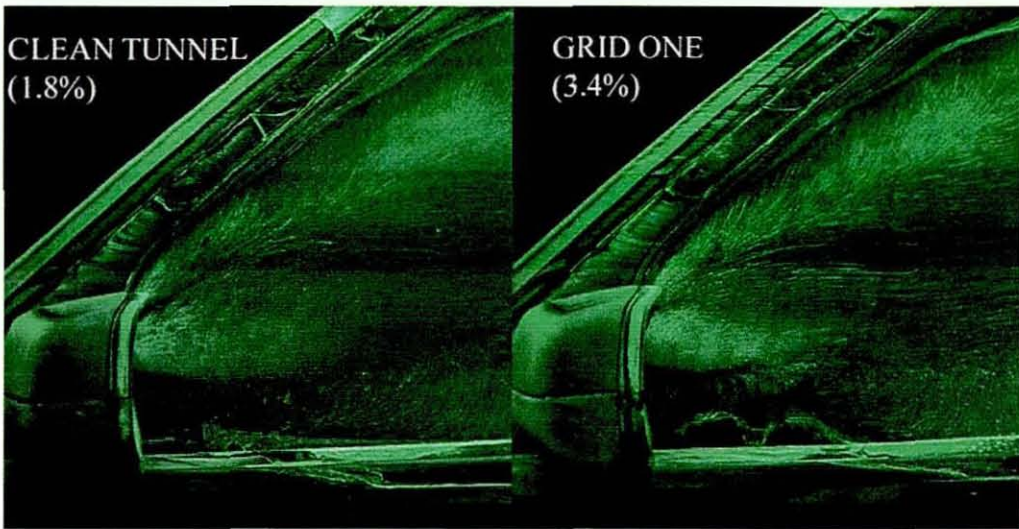
Figure 146 Flourescene visualisation of wing mirror flow, 1.8% turbulence vs. 3.4%
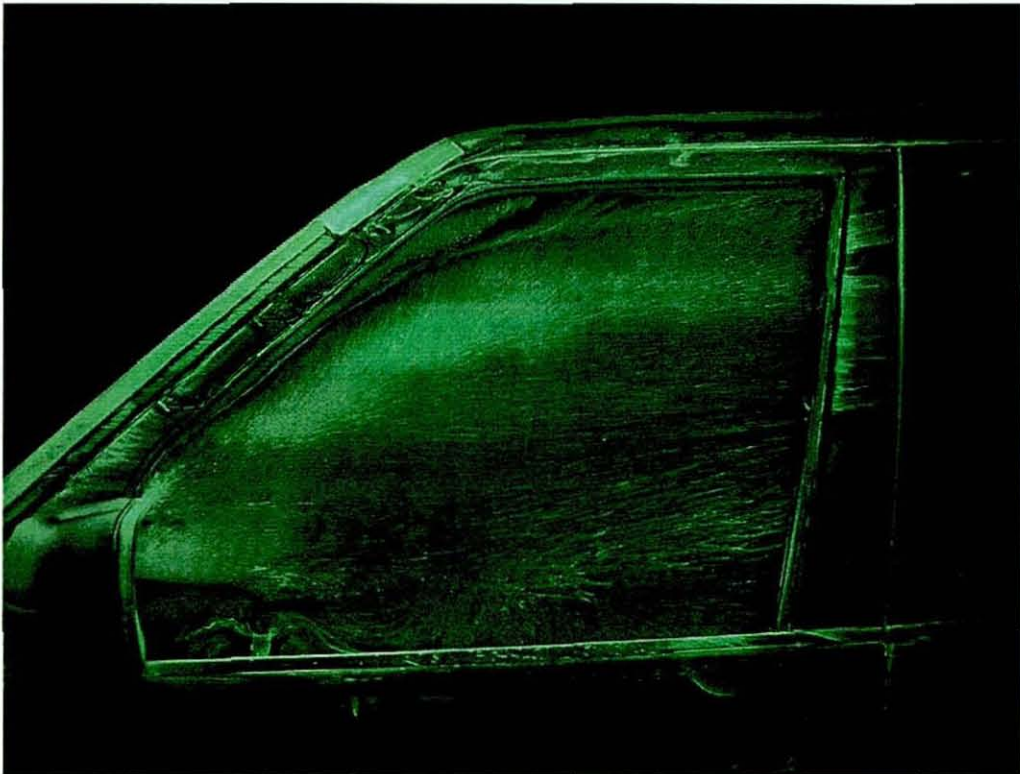
Figure 147 Flourescene sideglass flow visualisation, 4.3% turbulence

Figure 147 shows the result at 4.3% turbulence. The A-pillar vortex is a little smaller than in the 3.4% turbulence, and the reattachment line going back along the glass by the roof is much less distinct. The recirculation region at the bottom of the glass near the wing mirror and door line is again large with a small dribble of flourescene, and the imprint of the jet flow is stronger than it was in the clean tunnel. In the previous chapter it was suggested that increasing the freestream turbulence reduces the C-pillar vortex strength. Although it is not possible to determine the strength of the A-pillar vortex from flourescene pictures, the spreading and smearing of the reattachment line suggests

167

that the vortex is bodily disturbed and possibly weakened by the addition of freestream turbulence. Further experimentation is required to show what effect this has on the wind noise, and whether the measurement of inferred wind noise from pressure tappings [32] could be improved using turbulence grids.

7.3   Summary

- Tests were carried out on the MIRA full scale reference model, and good comparison was made between the baseline model and the Windsor model in the Loughborough tunnel.

- Front and rear spoiler tests were carried out, and additional freestream turbulence was found to improve the performance of the spoilers in lift but by a small amount. Following the 1-box results it was suggested that the separation was smaller around the front spoiler and that lead to the increased optimum spoiler size in raised freestream turbulence.

- This result was repeated for two production vehicles, and the effect of freestream turbulence on wheel spoilers and cooling drag was also investigated. The performance of small wheel spoilers was shown to be adversely affected by additional turbulence, which may be because they are intended to produce a large separation that then pushes the flow around the front wheels, and increased turbulence is known to reduce the size of separated regions. There was very little effect of turbulence on cooling drag.

- An investigation was also carried out into the flow over the sideglass, paying particular attention to the A-pillar vortex. It was suggested, following the Windsor model results from the previous chapter, that the A-pillar vortex had become weaker with the additional turbulence, and it was seen that the area of glass affected by the vortex became larger and the reattachment line less distinct, indicating that the vortex might be deflected by the turbulent eddies as well as any possible weakening (that could not be measured).

- The individual differences that were measured on the MIRA reference model and the production vehicles are all very small, but it is possible that added

together they could produce a significant difference in overall lift and drag, if a vehicle was entirely designed at a higher level of freestream turbulence.

Chapter 8
Further work

The method used in this project was specifically designed to investigate the effects of small scale turbulence, by making the assumption that a principle of superposition could be adopted, and that some level of small scale turbulence does exist in the real world. Reference was made to studies that measured the turbulence intensity in the real world in order to establish what levels should be tested, but the turbulence intensity on the roads under normal driving conditions is still not well understood, and most studies that make reference to road vehicles filter the atmospheric spectrum to only include what is considered relevant, i.e. the higher frequency end of the spectrum. An in depth study of on road turbulence under many different driving conditions (eg. traffic, road type, car speed etc.), during varied atmospheric conditions (calm days, windy days, etc.) and with varied levels of roadside obstructions would be a very useful project to aid the understanding of the environment that road cars experience. The challenge of choosing, cataloguing and understanding the data that would be collected is left to the investigator taking this on.

A useful future experiment would be to look in detail at the flow over the backlight of the Windsor model with increased freestream turbulence using the PIV system, or by measuring the pressure distribution over the backlight in detail. A set of measurements of the pressure distribution across both the width and length of the backlight of several of the large back angles approaching 32.5° in different levels of freestream turbulence would provide useful insight into the changes in separation and reattachment and vortex strength that have been suggested in this work.

Further investigation of the behaviour of the A-pillar vortex under increased freestream turbulence would also be of interest, considering the flow visualisation results for the Land Rover Discovery side glass. Considering that the turbulence greatly increased the unsteadiness in the flow, measurements of the unsteady pressure distribution on the A-pillar and local side of a representative model with tight A-pillar radii would be very useful in extending the understanding of how vortical flows are affected by turbulence.

Further study that may also lead on from these investigations is the effect of raised freestream turbulence on the aeroacoustic characteristics of the vehicle. It is known that wind noise is often under-predicted, and that customers complain of more wind noise on the road than was noticed during vehicle development. Measuring wind noise is generally done in a very low turbulence environment because reducing freestream

turbulence usually goes hand in hand with reducing background noise levels, but recently developed techniques using fluctuating surface pressure measurement to imply noise levels could be used in conjunction with raised freestream turbulence to investigate whether the small scales generated by grids do cause more problems, and to look for solutions.

Chapter 9
Conclusions

Various model geometries and turbulence levels have been used to show that there is an effect of turbulence on the aerodynamic optimisation process. In general it is seen that although small, this effect is of a similar order of magnitude to the differences seen when rolling roads were first used in wind tunnels. The following specific conclusions arose from the work:

- The 1-box drag results showed that the transcritical Reynolds number based on edge radius is a constant, both in the clean tunnel and with increased freestream turbulence. Increasing the level of freestream turbulence reduced the value of the constant and the inverse relationship $Re_{rtcrit}=6.4*10^5*Tu^{-0.32}$ was found to fit the results. The experiment was extended to a 2-box model and the MIRA full scale reference vehicle, and the result was repeated. The best fit line for the results of all 3 models was given by the equation $Re_{rtcrit}=6.4*10^5*Tu^{-0.33}$, essentially the same as for the 1-box model alone. This showed that the transcritical Reynolds number did not depend on model geometry.

- Since the constant is dependent only on the edge radius, the results can be treated as a test of edge radius optimisation without reference to the model scale. The 70mm radius was seen to have the same transcritical Reynolds number based on edge radius in the full scale wind tunnel at a particular turbulence level as it did in the model scale wind tunnel, at the same Reynolds number based on edge radius and in similar freestream turbulence conditions. This showed that the edge radius optimisation experiment was not scale dependent and could be extended to full scale models simply by comparing like radii in millimetres.

- In the clean tunnel, the pressure gradient over the bonnet of the 2-box model created a sustained separation bubble at low Reynolds numbers for even the largest radii, which then disappeared at high Reynolds numbers, giving a clear transition region. In raised levels of freestream turbulence, the clear transition region did not appear for radii bigger than 50mm. This was the only significant effect of using the more complex geometry model.

- The concept of effective Reynolds number was found to be an inadequate description of what happens when the freestream turbulence level is increased. Instead, effective edge radius was proposed as a more representative model. For

the 1-box model, it was shown that this concept gave a fair representation of the change in the trend of drag with Reynolds number at different turbulent intensities, but did not capture the difference in the values of C_D between one radius at an increased turbulence intensity and its equivalent in the clean tunnel, because of skin friction effects and the difference in acceleration around the radius. It was not possible to extend this concept to the 2-box model because of the effect of the pressure gradient on the bonnet, but it is still felt to be a useful description of the way turbulence affects the flow around a radius on a simple bluff body.

- The post-critical C_D of the 1-box model was shown to increase with increasing turbulence intensity. The increase was reasonably independent of edge radius and was shown to depend on the ratio between turbulence levels. The post-critical drag of the MIRA model was increased by the two raised levels of freestream turbulence, but 3.4% turbulence produced a larger increase in drag than 4.3% turbulence.

- The 1-box model was shown to be sensitive to yaw, but the transcritical Reynolds number remained constant over the range of yaw angles tested (0 – 15°), both in the clean tunnel and with increased freestream turbulence. This was also reflected in Cooper's results [4].

- The base pressures were also found to vary with Reynolds number, in a way that correlated to the presence of separation at the front of the model. The base pressure was considered to be controlled by the boundary layer thickness at separation. Increasing the turbulence intensity caused an increase in base suction (more negative base pressure) indicating that some of the increase in drag is caused by this change in the pressure field, as well as an increase in skin friction.

- The lift results for the 1-box model broadly show the same effects as the drag results, in terms of the change in Re_{rtcrit} and the effect of the additional turbulence on post-critical front and rear lift coefficients. The most significant effects on lift occur around the front of the model, as would be expected, with additional effects at the rear of the model that most likely arise from shifts in the

position of the front stagnation. The lift results for the full scale MIRA model also matched the results for the 1-box model, which supports the conclusion that the dominant features in the flowfield at full scale are the same as those which dominate the model scale results.

- The centreline pressure results showed further evidence for the presence of separations in the clean tunnel for the smaller radii at low Reynolds numbers. The reduction in drag when the Reynolds number increased was shown to come from the sharp increase in suction on the leading edge radii, indicating that the separations had reduced, or that the flow had become fully attached. The addition of freestream turbulence also caused the pressure distribution around the radius to change, increasing the suction and indicating that the separation around the radius was reduced or absent.

- The base pressure distribution was seen to be affected by both changes in the Reynolds number and changes to the turbulence intensity. Increasing either Reynolds number or turbulence intensity increased the base suction.

- The PIV results showed that the 1-box model is sufficiently long that there is separation and reattachment along the side of the model at low Reynolds numbers. As the Reynolds number increased, the separation bubble became shorter, and at a sufficiently high Reynolds number the separation bubble collapsed and the flow became fully attached around the radius, for both the 30mm and 40mm front radii. This confirmed the general analysis put forward for the 1-box model where the flowfield was described as having a pre-critical phase with separation and reattachment, a short critical region where the separation bubble collapsed, and a post-critical region with fully attached flow around the radius.

- In the instantaneous PIV results for the clean tunnel, it was seen that there is a significant amount of vortex shedding from the point of separation, which occurred at the end of the radius. There was some evidence of unsteadiness even at low Reynolds numbers, but the vast majority of the frames recorded a relatively stable separation bubble with recirculating flow at the model surface and vortices in the shear layer. Increasing the freestream turbulence caused the

178

unsteadiness to increase, and frames where the flow had become attached around the radius were more frequent. The vortices more often reached the wall of the model causing increased unsteadiness and interrupting the reversed flow. Further increases in turbulence intensity caused more flapping of the shear layer and intermittently collapsed the shear layer.

- The time averaged PIV results with increased turbulence also showed increased unsteadiness in the separated region, with up to 30% increases in the r.m.s velocities. The time-averaged separation bubble was seen to get shorter, acting to reduce the pressure recovery length.

- The Windsor model has a typical drag characteristic with back angle, which was repeated in the Loughborough wind tunnel and matched previous results with the same model. The drag initially falls as the base gets smaller, and then rises with increasing vortex strength up to a critical angle, in this case 32.5°. At higher angles this flow breaks down and the drag falls to the same value as for 0° back angle, with a separation at the end of the roof.

- Increasing the freestream turbulence did not have an effect on the critical angle. It gave an increase in drag for 0° back angle, which was strongly dependent on the turbulence intensity. As the back angle increased, there was a shape dependent reduction in drag which reduced the drag back to the clean tunnel result for all turbulence levels at 32.5° back angle. For higher back angles there was an increase in drag, as was seen for the lowest back angles. From the 1-box results it was seen that the rise in drag for the 0° back angle and highest back angles was partly due to raised base pressure and partly due to skin friction.

- The rear lift results also showed a shape dependent reduction up to the critical angle with increased turbulence. It was suggested that the additional turbulence reduced the vortex strength and affected the separation over the roof, and that higher levels of turbulence had a stronger effect on the vortex strength. At back angles above the critical angle, the rear lift was higher with increased turbulence. The 1-box results showed that increasing freestream turbulence increased the base pressure, resulting in increases in drag and lift in this case because the upper half of the base is at an angle to the vertical.

- Tests at different yaw angles showed that the yaw moment was not significantly affected by the addition of freestream turbulence.

- Further tests were carried out on the MIRA full scale reference model, and good comparison was made between the baseline model and the Windsor model in the Loughborough tunnel. Front and rear spoiler tests were carried out, and additional freestream turbulence was found to improve the performance of the spoilers in lift but by a small amount. Following the 1-box results it was suggested that the separation was smaller around the front spoiler and that led to the increased optimum spoiler size in raised freestream turbulence.

- This result was repeated for two production vehicles, and the effect of freestream turbulence on wheel spoilers and cooling drag was also investigated. The performance of small wheel spoilers was shown to be adversely affected by additional turbulence, which may be because they are intended to produce a large separation that then pushes the flow around the front wheels, and increased turbulence is known to reduce the size of separated regions. There was very little effect of turbulence on cooling drag.

- An investigation was also carried out into the flow over the sideglass, paying particular attention to the A-pillar vortex. It was suggested, following the Windsor model results from the previous chapter, that the A-pillar vortex had become weaker with the additional turbulence, and it was seen that the area of glass affected by the vortex became larger and the reattachment line less distinct, indicating that the vortex might be deflected by the turbulent eddies as well as any possible weakening (that could not be measured).

- The individual differences that were measured on the MIRA reference model and the production vehicles are all very small, but it is possible that added together they could produce a significant difference in overall lift and drag, if a vehicle was entirely designed at a higher level of freestream turbulence.

Chapter 10

References

1. L. F. Richardson. Weather Prediction by Numerical Process. Cambridge University Press. 1922

2. J. Howell. Private communication regarding the process of vehicle design and development. 2007

3. W. H. Hucho, L. J. Janssen and H. J. Emmelmann. The Optimization of Body Details - A Method for Reducing the Aerodynamic Drag of Road Vehicles. 760185. SAE Transactions pp.865-882, 1976

4. K. R. Cooper. The Effect of Front-Edge Rounding and Rear-Edge Shaping on the Aerodynamic Drag of Bluff Vehicles in Ground Proximity. 850288. SAE Transactions pp.2.727-2.757, 1986

5. S. F. Hoerner. Fluid-Dynamic Drag. 1958 (Published by the author)

6. R. H. Barnard. Road Vehicle Aerodynamic Design. MechAero, 2001

7. R. Buchheim, K. -R Deutenbach and H. -J Lueckoff. Necessity and Premises for Reducing the Aerodynamic Drag of Future Passenger Cars. 810185. SAE Technical Paper Series 1985

8. S. R. Ahmed, G. Ramm and G. Faltin. Some Salient Features of the Time-Averaged Ground Vehicle Wake. 840300. SAE Technical Paper Series 1984

9. J. P. Howell. Shape features which influence crosswind stability. Ride and Handling Conference, I Mech E, NEC Birmingham 1993

10. P. W. Bearman. Some Observations on Road Vehicle Wakes. 840301. SAE Technical Paper Series 1984

11. S. Watkins, J. W. Saunders and P. H. Hoffmann. Turbulence experienced by moving vehicles. Part I. Introduction and turbulence intensity. J.Wind Eng.Ind.Aerodyn. Vol. 57, Iss. 1, pp.1-17, 1995

12. S. Watkins and J. W. Saunders. Review of the wind conditions experienced by a moving vehicle. SAE Paper 981182 pp.211-218, 1998

13. P. J. Richards, R. P. Hoxey and J. L. Short. Spectral models for the neutral atmospheric surface layer. J.Wind Eng.Ind.Aerodyn. Vol. 87, Iss. 2-3, pp.167-185, 2000

14. P. Bradshaw. An Introduction to Turbulence and its Measurement. Pergamon, 1971

15. J. Howell. Real Environment for Vehicles on the Road. Euromotor Conference 2000, Aachen

16. P. W. Bearman and T. Morel. Effect of Free Stream Turbulence on the Flow Around Bluff Bodies. Prog. Aerospace Sci. Vol. 20, pp.97-123, 1983

17. G. I. Taylor. Statistical Theory of Turbulence - Part V. Proc. Roy. Soc. London A Vol. 156, pp.307-317, 1936

18. R. Hillier and N. J. Cherry. The effects of stream turbulence on separation bubbles. J.Wind.Eng.Ind.Aerodyn. Vol. 8, pp.49-58, 1981

19. Q. S. Li and W. H. Melbourne. An experimental investigation of the effects of freestream turbulence on streamwise surface pressures in separated and reattaching flows. J. Wind Eng. Ind. Aerodyn. Vol. 54/55, pp.313-323, 1995

20. Q. S. Li and W. H. Melbourne. The effect of large-scale turbulence on pressure fluctuations in separated and reattaching flows. J.Wind Eng.Ind.Aerodyn. Vol. 83, pp.159-169, 1999

21. X. J. Xia and P. W. Bearman. An experimental investigation of the wake of an axisymmetric body with a slanted base. Aero. Quart. Vol. 34, pp.24-45, Feb. 1983

22. S. Watkins, J. W. Saunders and P. H. Hoffmann. Comparison of road and wind-tunnel drag reductions for commercial vehicles. J.Wind Eng.Ind.Aerodyn. Vol. 49, Iss. 1-3, pp.411-420, 1993

23. J. Wiedemann and B. Ewald. Turbulence Manipulation to Increase Effective Reynolds Number in Vehicle Aerodynamics. AIAA Journal Vol. 27, Iss. 6, pp.763-769, 1989

24. H. L. Dryden and A. M. Kuethe. Effect of turbulence in wind tunnel measurements. NACA Report No. 342 1931

25. MA Passmore, S. Richardson and A. Imam. An experimental study of unsteady vehicle aerodynamics. Proc.Inst.Mech.Eng.Part D J.Automob.Eng. Vol. 215, Iss. 7, pp.779, 2001

26. A. Cogotti. The Evolution of the Testing Environment in the Pininfarina Wind Tunnel: The new Turbulence Generation System. Vol. Proceedings of BBAA 5, 2003

27. P. Hong, B. Marcu, F. Browand and A. Tucker. Drag Forces Experienced By Two Full Scale Vehicles At Close Spacing. SAE Transactions ref. 980396 1998

28. C. J. Baker. Flow And Dispersion In Ground Vehicle Wakes. J.Fluids Struct. Vol. 15, Iss. 7, pp.1031-1060, 2001

29. D. B. Sims-Williams, R. G. Dominy and J. P. Howell. An Investigation into Large Scale Unsteady Structures in the Wake of Real and Idealized Hatchback Car Models. Society of Automotive Engineers Technical Paper 2001-01-1041

30. A. Cogotti. Flow Field of a Car moving in the far wake of another Car. Preliminary Information and Interpretation. 38th Annual SATA International Conference, Monash University 2002

31. C. Peric, S. Watkins, E. Lindqvist and J. Saunders. Effects of On-Road Turbulence on Automotive Wind Noise: Comparing Wind-Tunnel and On-Road Tests. 970406. SAE Technical Paper Series 1997

32. M. Burnett and A. Lock. Aeroacoustic Testing in MIRA's Full Scale Wind Tunnel. Proceedings of the 5th MIRA International Vehicle Aerodynamics Conference 2004

33. B. R. Gilhome and J. W. Saunders. The Effect of Turbulence on Peak and Average Pressures on a Car Door. SAE Paper 2001-01-0253 2001

34. G. Johl, M. Passmore and P. Render. Design Methodology and Performance of an In-Draft Wind Tunnel. The Aeronautical Journal pp.465-473, Sept. 2004

35. M. Gad-el-Hak and S. Corrsin. Measurements of the nearly isotropic turbulence behind a uniform jet grid. J. Fluid Mech. Vol. 62, Iss. 1, pp.115-143, 1974

36. B. J. Vickery. On the flow behind a coarse grid and its use as a model of atmospheric turbulence in studies related to wind loads on buildings. NPL Aero Report 1143, National Physical Laboratory, Teddington, England March 1965

37. J. H. M. Fransson, M. Matsubara and P. H. Alfredsson. Transition induced by free-stream turbulence. J. Fluid Mech. Vol. 527, pp.1-25, 2005

38. W. T. Mason and G. Sovran. Ground plane effects on the aerodynamic characteristics of automobile models - an examination of wind tunnel test technique. Advances in Road Vehicle Aerodynamics pp.291-309, 1973

39. E. L. Houghton and P. W. Carpenter. Aerodynamics for Engineering Students. pp.368, 1993

40. P. Bradshaw. Effect of Free-Stream Turbulence on Turbulent Shear Layers. Vol. ICAERO7410; ARC35648; N75206698, pp.18, 1974

41. P. S. Newnham, M. A. Passmore and A. Baxendale. An experiment to investigate the influence of free stream turbulence on edge radius optimisation. 5th MIRA International Vehicle Aerodynamics Conference 2004

42. H. U. Meier and H. P. Kreplin. Influence of freestream turbulence on boundary-layer development. AIAA Journal Vol. 18, Iss. 1, pp.11-15, 1980

43. W-H. Hucho (ed). Aerodynamics of Road Vehicles (Fourth Edition). SAE. 1998

44. P. J. Saathoff and W. H. Melbourne. Freestream turbulence and wind tunnel blockage effects on streamwise surface pressures. J. Wind Eng. and Ind. Aero. Vol. 26, pp.353-370, 1987

45. LaVision GmbH. DaVis 6.2 manuals. 2001

46. D. Hollis. Particle Image Velocimetry in Gas Turbine Combustor Flow Fields (PhD Thesis). 2004

47. R. D. Keane and R. J. Adrian. Optimisation of Particle Image Velocimeters. Part I: Double Pulsed Systems. Meas. Sci. Technol. Vol. 1, pp.1202-1215, 1990

48. D. C. Montgomery and G. C. Runger. Applied Statistics and Probability for Engineers. 2003

49. S. Windsor. Private communication; results taken from the MIRA model scale wind tunnel. Land Rover 2006

50. F. K. Schenkel. The origins of drag and lift reductions on automobiles with front and rear spoilers. 770389. SAE Transactions 1977

51. A. Cogotti. Update on the Pininfarina "Turbulence Generation System" and its effects on the car Aerodynamics and Aeroacoustics. 2004-01-0807. SAE Technical Paper Series 2004

52. T. Wolf. Minimising the Cooling System Drag for the New Porsche 911 Carrera. 5th MIRA International Vehicle Aerodynamics Conference 2004

Appendix A - Hotwire

The constant temperature anemometer system used in this thesis was a Dantec Dynamics Streamline system used with Streamware software. A single wire was used, of Dantec type 55P11, connected to a Dantec long single wire support (55H21) that was connected to the Streamline system by a 4m long cable. The data were acquired using a National Instruments 16 bit general purpose DAQ card (NI-6052E) controlled and configured by the Streamware software to the correct settings for the Streamline kit. The Streamline kit has internal filters, offset and gain controls, which were used to set up the wire for the range of values expected both in the amplitude and frequency domains. The wire was calibrated by mounting it in the tunnel and recording the wire voltage against the pitot windspeed, both sampled for 10s and averaged. The ambient pressure and temperature were also recorded in the calibration process. A fourth order polynomial was then fitted to the calibration curve results, because the Streamline kit uses the voltages as recorded, post signal conditioner offset and gain, and so it is not possible to use King's Law. However, the polynomial is a very good fit to the recorded data, and the results were always checked to make sure that they fell within the bounds of the calibration.

The traverse was always mounted so that the hotwire was on the centre of the model position both longitudinally and laterally, and the wire was traversed in the vertical plane over a greater height than the model. The standard sampling period was 104.8576s at 10kHz. The results were analysed using software coded in Labview which calculated turbulence intensities, autocorrelation, spectra and pdf results by breaking up each sample into 8 blocks and ensemble averaging to reduce the noise.

The following formulae describe the calculations that were performed by Labview (using built in functions):

Turbulence intensity Tu = r.m.s / mean velocity

Autocorrelation $R_{xx}(t) = R_{uu} = \int_{-\infty}^{\infty} u(\tau)u(t+\tau)dt$

      where u is the fluctuating component of velocity, t is time, and τ is the shift
      away from the starting time for the autocorrelation.

Power spectrum = (FFT* (u) * FFT (u)) / N^2
      where FFT is the fast Fourier transform, * indicates the complex conjugate, u is
      the fluctuating component of velocity and N is the number of samples.

Appendix B – PIV

The PIV system used in this thesis was a LaVision supplied system based around a LaVision Imager Intense camera and a New Wave dual pulsed Nd:YAG laser producing 50mJ per pulse. The system was controlled by DaVis 6.2 software. The seeder was a LaVision olive oil based seeder and the rake was designed by a process of trial and error, by first designing a rake and then using a single point smoke source to identify where the rake should be extended to seed unseeded flow in the measurement area.

The results were post processed using DaVis software with the settings as described in the thesis and all the figures were produced using DaVis. Photoshop was used to draw the outline of the model on the time varying flow fields for clarity.

The final seeding rake design is shown below with approximate dimensions:
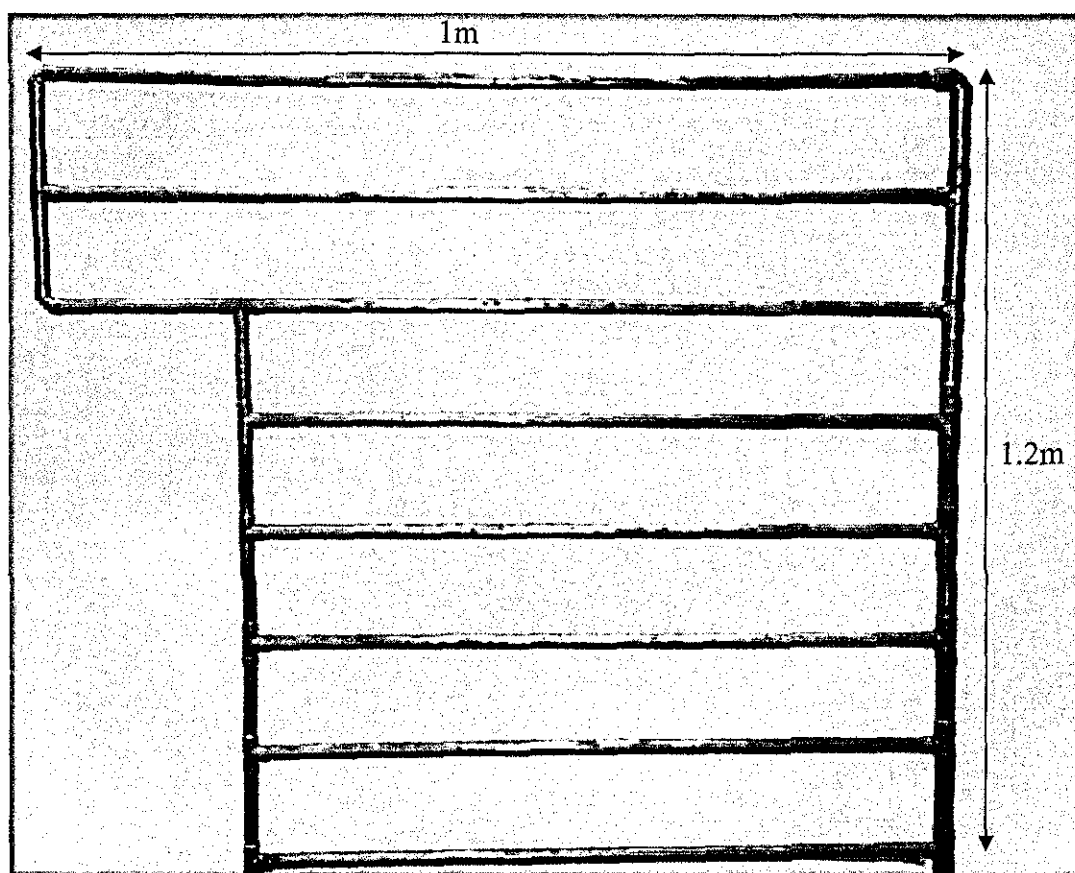
The tube is standard 22mm copper pipe for the right hand vertical pipe and 15mm for all other pipework. 5mm diameter holes for the seeded air to exit through were placed on the top and bottom of each horizontal section at 25mm spacing.